



**HAL**  
open science

# Exploring the phase diagram of electrolyte solutions under extreme conditions

Adriaan-Alexander Ludl

► **To cite this version:**

Adriaan-Alexander Ludl. Exploring the phase diagram of electrolyte solutions under extreme conditions. Physics [physics]. Université Pierre et Marie Curie - Paris VI, 2015. English. NNT : 2015PA066303 . tel-01597902

**HAL Id: tel-01597902**

**<https://theses.hal.science/tel-01597902>**

Submitted on 29 Sep 2017

**HAL** is a multi-disciplinary open access archive for the deposit and dissemination of scientific research documents, whether they are published or not. The documents may come from teaching and research institutions in France or abroad, or from public or private research centers.

L'archive ouverte pluridisciplinaire **HAL**, est destinée au dépôt et à la diffusion de documents scientifiques de niveau recherche, publiés ou non, émanant des établissements d'enseignement et de recherche français ou étrangers, des laboratoires publics ou privés.

# Université Pierre et Marie Curie

Ecole doctorale de physique et chimie des matériaux – ED 397

Institut de minéralogie, de physique des matériaux et de cosmochimie – UMR 7590

Physique des systèmes simples en conditions extrêmes

## Étude du diagramme de phases des solutions d'électrolytes sous conditions extrêmes

Par Adriaan-Alexander Ludl

Thèse de doctorat de Physique

Dirigée par Livia Eleonora Bove et Antonino Marco Saitta

Présentée et soutenue publiquement le 28 septembre 2015

Devant un jury composé de :

Mme. Livia Bove	Chargée de Recherches	Directrice de thèse
Mme. Isabelle Daniel	Professeur	Examineur
Mme. Paola Gallo	Professeur	Rapporteur
M. Thomas Loerting	Professeur	Examineur
M. Alfonso San Miguel	Professeur	Rapporteur
M. Rodolphe Vuilleumier	Professeur	Examineur





# High Pressure Salty Ice

—

Exploring the phase diagram of electrolyte  
solutions in extreme conditions

Adriaan-Alexander Ludl

Institut de minéralogie, de physique des matériaux et de cosmochimie  
Université Pierre et Marie Curie  
Paris, France

3rd November 2015



# Abstract

Salty solutions are present on terrestrial planets and form an integral part of all living organisms. Moreover amorphous solutions are used for cryopreservation of biomolecules and tissues. The study of amorphous and crystalline phases of these solutions gives essential insight on the behaviour of water under conditions relevant for biology and planetary science.

The aim of this work is the exploration of the phase diagram of common electrolyte solutions (LiCl-water, LiBr-water, NaCl-water) under the pressure and temperature conditions (temperatures from  $\approx 77$  K to  $\approx 330$  K and pressures up to 5 GPa) relevant for icy bodies such as Europe and Ganymede. In experiments and simulations we search for crystalline phases of ice at high-pressure, which can contain considerable amounts of salt in their lattice (up to 10 % of by weight). We probe the existence of these salty ices, and characterize two exotic (pressure-induced) properties, such as polyamorphism and ionic inclusions in the ice lattice. We performed these studies by the combined use of neutron and X-ray diffraction, classical Molecular Dynamics and ab-initio calculations.

We have produced highly concentrated amorphous solutions of NaCl in water by fast quenching to liquid nitrogen temperature. Our neutron and X-ray diffraction experiments showed that local structure of this amorphous solution at ambient pressure is very similar to the high density amorphous (HDA) structure of pure water. Our high pressure experiments with the Paris-Edinburgh cell and our calculations with classical Molecular Dynamics show only smooth structure and density changes during compression up to 4 GPa. We discuss the possibility of salt (NaCl) inclusions in the ice VII lattice at high pressure. To this end we combine data from the above neutron experiments and the computational structure searching based on Density Functional Theory and ab-initio molecular dynamics. The structure of the ice VII which crystallized in our experiments indicates that it is either pure ice or that it contains only a small fraction of the ions from the solution. It may be possible that ions can be included in larger quantities at higher pressures, as suggested by from other experiments of the group.



To my family



Was die Menschen treibt ist stärker als jede Vernunft.

Christa Wolf (\*1929, †2011), Medea Stimmen

I love deadlines. I love the whooshing noise they make as they go by.

Douglas Noel Adams (\*1952, †2001), The Salmon of Doubt



# Acknowledgements

I thank my thesis advisors Livia Bove and Marco Saitta for have allowed me to pursue this project and the Laboratoire d'Excellence MATISSE for their funding. They enabled me to learn from the best and participate in international conferences. I would also like to thank them both for their guidance, Marco who helped me with first principles simulations and the concepts of condensed matter physics, and Livia for introducing me to the experimental techniques and her untiring motivation to perform experiments under extreme conditions, both for reading the manuscript and for their constructive criticism.

Thank you Mathieu Salanne for your patient help with molecular dynamics simulations and inviting me to the PHENIX lab, and your corrections on this thesis. Thank you Dario Corradini for your invaluable help for the generation of myriads of crystal structures, your advice on the analysis. I thank Stefan Klotz for his having shared his knowledge, teaching me the nuts and bolts of high pressure experiments and the times we spent producing samples. I am very grateful to Karel Kunc, Robert Pick and Catherine Dreyfus for having shared their knowledge and experience with me and for many discussions about research and researchers over lunches and tea times.

I sincerely thank the members of the jury, Isabelle Daniel, Paola Gallo, Alfonso San Miguel and Rodople Vuilleumier, for having accepted to evaluate this manuscript and taking the time to read it in depth.

Many thanks to Zamaan and Gopal for being fine officemates, discussing science in the office, over lunch and tea. Frederico for sharing his energy and transforming the office when he joined. Terry for long winding discussions about science and the nature of the universe. Betül for serious discussions about water ice and science, and fun discussions about anything. Special thanks to Katrin for sharing her knowledge about astrophysical ices from far far away. Thank you Raffaello, Flora, Thomas and the above for hanging around and cheering me up. Thank you Sara and Adrien for your patience and help with thermodynamics teaching. Thank you Myrtille, Clémence, Axelle, Sara, Antoine, Nicolas, Vincent and the other students for fun times. I thank all of you for making my time in the lab enjoyable one and good memories. Un grand merci à Tijana pour son cours d'aikido et aux aikidokas pour

des entrainements qui m'ont permis de progresser et de me vider l'esprit.

Finally, I thank my family and friends for having shown their love to me and given me their support at all times. Vielen Dank meine lieben Freunde Sophia und Thomas, alias Good et Hidalgo, Mathilde et Arthur, Alice, Xinyi und Raphael für fröhliche gemeinsame Abendessen, euren Beistand und eure Aufmunterungen, die mir geholfen haben durchzuhalten. Merci aussi Christophe et Célesté, Clément, Flora, Antoine, Frédéric, Édouard, Praxitelis, j'ai beaucoup apprécié votre compagnie durant ces trois années. Merci Louise d'insister pour me faire jouer au go de temps en temps, quand je ne voyais plus comment en trouver le temps, et les discussions à propos de la grammaire et des langues. Vielen Dank an Ria und Werner für guten Rat und dass ihr mich an die Geduld erinnert habt. My parents, Elisabeth und Toni, in gratefulness for allowing me to pursue the career that I chose, for believing in me and always helping me as much as they can.

# Contents

<b>1</b>	<b>Introduction</b>	<b>15</b>
1.1	Water and ice . . . . .	16
1.2	Aqueous solutions . . . . .	23
1.3	Outline of this work . . . . .	26
<b>2</b>	<b>Experimental techniques</b>	<b>29</b>
2.1	Diffraction . . . . .	29
2.1.1	Scattering theory . . . . .	29
2.1.2	X-ray experiments . . . . .	36
2.1.3	Neutron experiments . . . . .	37
2.1.4	Structure refinement . . . . .	41
2.2	High pressure devices . . . . .	42
2.2.1	Historical high pressure techniques . . . . .	42
2.2.2	Paris-Edinburgh cell . . . . .	42
2.2.3	Diamond anvil cells . . . . .	47
2.2.4	Pressure gauges . . . . .	48
<b>3</b>	<b>Atomistic calculations</b>	<b>53</b>
3.1	Atomic interaction models . . . . .	53
3.1.1	Density Functional Theory . . . . .	54
3.1.2	Classical interaction potentials . . . . .	56
3.2	Structure searching . . . . .	62
3.2.1	Random search . . . . .	62
3.2.2	Structure optimisation . . . . .	63
3.3	Molecular Dynamics . . . . .	65
3.3.1	Simulation of the NaCl-water system . . . . .	66
3.3.2	<i>Ab initio</i> Molecular Dynamics . . . . .	67
3.4	Evaluating structural properties . . . . .	68
3.4.1	Thermodynamic sampling . . . . .	68
3.4.2	Microscopic structure . . . . .	69

<b>4</b>	<b>Producing aqueous glasses</b>	<b>73</b>
4.1	Quenching techniques . . . . .	74
4.1.1	Quenching and amorphising solutions . . . . .	74
4.1.2	Experimental set-up . . . . .	78
4.2	Sample preparation . . . . .	80
4.2.1	Solutions . . . . .	80
4.2.2	Amorphous powder . . . . .	83
4.3	Structure characterisation at ambient pressure . . . . .	84
4.3.1	Fraction of amorphous material . . . . .	84
4.3.2	Transformation upon annealing at ambient pressure . . . . .	95
4.4	Summary . . . . .	99
<b>5</b>	<b>High pressure Phases of NaCl · 10.2D<sub>2</sub>O</b>	<b>101</b>
5.1	Compression of amorphous NaCl · 10.2D <sub>2</sub> O . . . . .	101
5.1.1	High-pressure neutron diffraction experiments . . . . .	101
5.1.2	Densification under compression . . . . .	105
5.1.3	The role of Na <sup>+</sup> ions . . . . .	109
5.1.4	Conclusion . . . . .	117
5.2	Crystalline phases . . . . .	118
5.2.1	Crystallisation upon annealing . . . . .	118
5.2.2	Proposed structures of salty ice VII . . . . .	130
5.2.3	Stability of salty ice VII . . . . .	137
5.2.4	Conclusion . . . . .	142
<b>6</b>	<b>Conclusion</b>	<b>143</b>
<b>A</b>	<b>Additional data from experiments and simulations</b>	<b>147</b>
A.1	Fits of diffraction data . . . . .	147
A.1.1	Profile functions for fitting diffraction data . . . . .	147
A.1.2	Fit of sample 3 with peak positions . . . . .	147
A.1.3	Fit of sample 3 with salty ice VII . . . . .	147
A.2	Simulations of salty ice VII . . . . .	149
A.2.1	Distribution of dipoles in the set of salty ice boxes . . . . .	149
A.2.2	Fitted equations of state for pure and salty ice . . . . .	149
A.3	Thermal average . . . . .	153
A.4	Multipolar expansion . . . . .	154
A.5	X-ray form factors . . . . .	154
A.6	List of abbreviations . . . . .	155

---

<b>B Résumé en français</b>	<b>157</b>
B.1 L'eau et la glace . . . . .	158
B.2 Les solutions aqueuses . . . . .	163
B.3 Aperçu des travaux . . . . .	165
B.4 Conclusion . . . . .	166
 <b>List of Figures</b>	 <b>171</b>
 <b>List of Tables</b>	 <b>185</b>
 <b>References</b>	 <b>187</b>



# Chapter 1

## Introduction

« ubi materia, ibi geometria »

Johannes Kepler (1601) \*

*De Fundamentis Astrologiae Certioribus*

The relationship between matter and geometry must have become apparent to the first humans who tried to represent by drawing and writing what they had observed. Regular geometrical patterns emerge naturally, a common example are snowflakes. Incidentally, Kepler attempted to explain the hexagonal symmetry of snowflakes by the stacking of “the smallest natural unit of a liquid like water” in *De Nive Sexangula* (1611) (Ball, 2011). It has been shown by X-ray diffraction experiments that the crystal structure of common ice ( $I_h$ ) is indeed hexagonal, although not close-packed as Kepler conjectured.

The work presented in this thesis is concerned with the structure of aqueous electrolytic solutions and the phase transitions which arise when the local and long range structure of the material change upon compression and upon changes of temperature. The solutions investigated here are mostly rock salt (NaCl) in water ( $H_2O$  or  $D_2O$ ). The structure of these solutions at ambient pressure and temperature is built by elementary geometrical units which are tetrahedra and octahedra (Figure 1.1). The tetrahedra are formed by the first neighbours of water molecules. While the first hydration shells of  $Na^+$  cations in liquid water typically form octahedra (Enderby and Neilson, 1981). Both structural elements are deformed as pressure increases.

In the next section a brief discussion of the physical properties of water and ice as they appear in nature is given. This is followed by a discussion of the structure of aqueous solutions of electrolytes. The last section gives the outline of the work presented in the subsequent chapters.

---

\*This translates as “ where there is matter, there is geometry ”.

## 1.1 Water and ice

**Water** on Earth is intimately linked to life and human civilisation. Water may be found in liquid, crystalline and gaseous state in our everyday lives. This is due to the fact that the conditions of atmospheric pressure ( $1 \text{ atm} = 1.01325 \times 10^5 \text{ Pa}$ ) and ambient temperature ( $\approx 300 \text{ K}$ ) are close to the triple point water ( $273.16 \text{ K}$  and  $611.73 \text{ Pa}$ ), where all three phases coexist in thermodynamic equilibrium (NIST, IAPWS) (NIST, 2015, Wagner, 1999, Wikipedia, 2015). This relatively low triple point, the thermodynamic properties of water are consequences of the interaction between water molecules. The latter also gives rise to the hydrogen bond network formed by the water molecules in the liquid and solid phases. (DeBenedetti, 1996) Water is a peculiar substance which displays many unexpected “anomalous” properties when compared to other liquids. The anomalies observed in the supercooled regime are presented on page 20.

**Ice** at ambient pressure floats on water, because the density of the liquid is larger than that of the crystalline ice  $I_h$ . This may be the most striking property of water which contrasts with many other substances, *e.g.* simple liquids such as argon. It is one of the reasons why water greatly affects the climate on Earth (Koop, 2015). However, this is not a universal property of ice. At higher pressure ice becomes more dense than the liquid and will sink, this is the case for ices VI and VII.

In this thesis we are concerned mostly with high pressures ( $p > 1$ ) GPa. In this pressure range and the temperature range of  $77 \text{ K}$  to  $\approx 350 \text{ K}$  the phase diagram of pure water reveals a surprising variety of distinct solid phases (Figure 1.2). Today 16 crystalline phases of ice have been reported, which are traditionally identified by roman numerals, and three amorphous phases have been identified. The existence of these many phases is a consequence of the structure of the water molecule and the hydrogen bonds between molecules. The equilibrium configuration of an isolated water molecule is an isocetes triangle. In ices this triangle is distorted. The geometry and the environment of a water molecule in the ice  $I_h$  phase are shown in Figure 1.1. The  $\widehat{\text{HOH}}$  angle is about  $106^\circ$ . This value is close to the angle at the center of an ideal tetrahedron and it remains so in all molecular ice phases. Hence a water molecule “likes” to form four hydrogen bonds with its neighbours in most phases, which leads to the so-called “ice rules” (Bernal and Fowler, 1933)

- (i) each oxygen atom has four hydrogen bonded neighbours,
- (ii) between any pair of neighbouring oxygen atoms sits exactly one hydrogen atom, which occupies one of the two available positions,
- (iii) any oxygen atom has exactly two hydrogen atoms within the intramolecular

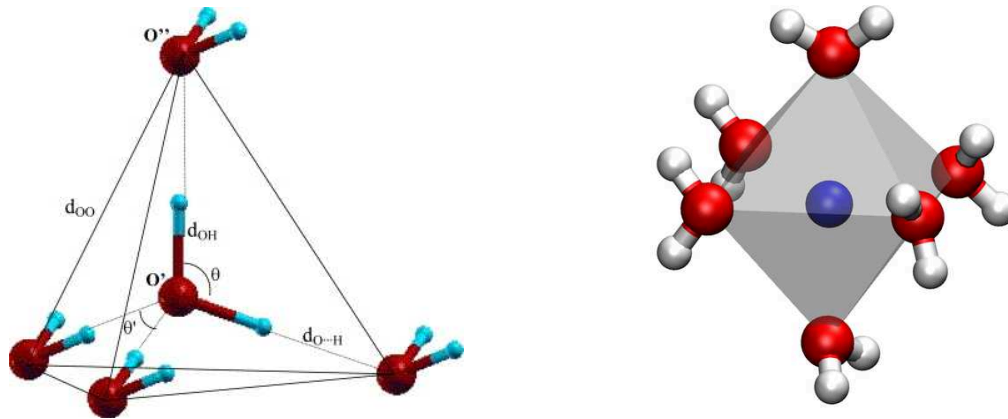


Figure 1.1: Left: Geometry of the water molecule and its local tetrahedral environment in ice  $I_h$  from Casassa et al. (2005). The structural properties of  $H_2O$   $d_{OO} \approx 2.7 \text{ \AA}$ ,  $d_{OH} \approx 0.95 \text{ \AA}$ ,  $\theta \approx 106^\circ$ , the average distance to nearest neighbour is  $d_{Hbond} \approx 1.75 \text{ \AA}$ . Right: Octahedron of nearest neighbours of a  $Na^+$  ion at ambient pressure  $d_{ONa} \approx 2.5 \text{ \AA}$ , from Ludl et al. (2015).

distance of  $\approx 1 \text{ \AA}$ .

These rules are respected in the crystalline molecular ice phases, except on defects such as Bjerrum defects which are rare (Bjerrum, 1952). In bulk phases this gives rise to a network containing large voids at low pressure. This network is modified when pressure is applied, it densifies and its structure changes (Bartels-Rausch et al., 2012). This H-bond network also partially survives in the liquid and it has been suggested that this percolating network gives rise to the anomalies of water (see below and Geiger et al. (1979)).

Four crystalline<sup>†</sup> ice phases will be mentioned in the later chapters. These are hexagonal ice I (ice  $I_h$ ), “cubic” ice I (ice  $I_c$ ), cubic ice VII, and tetragonal ice VIII.

The ices  $I_h$  and  $I_c$  are low pressure polymorphs. Ice  $I_h$  is the predominant phase at on the Earth’s surface. Its structure is made of a hexagonal oxygen lattice (space group  $P6_3/mmc$ ) and was determined in the 1920s (Dennison, 1921). It was first suggested by Pauling (1935) that the hydrogen atoms in ice  $I_h$  should be disordered to account for the measured residual entropy in low temperature experiments (Giauque and Ashley, 1933). The structure of the disorder in ice  $I_h$  has been studied in great detail in the past (Kuhs and Lehmann, 1986, 1987). Ice  $I_c$  would be strictly cubic (space group  $Fd\bar{3}m$ ), if it did occur in pure form. So far it has been impossible to verify this experimentally as all samples containing ice  $I_c$  also contained a fraction of hexagonally structured ice (Hansen et al., 2015, Kuhs et al., 2012). This is ex-

<sup>†</sup>In a *crystal* the particles (atoms or molecules) are disposed on a periodic lattice (Kittel and McEuen, 1976). Crystals are classified in seven lattice systems and 14 Bravais lattices. There are 230 distinct groups of isometries of periodic lattices in three-dimensional Euclidean space. They are known as space groups and are given in the International Tables for Crystallography (Hahn, 2006).

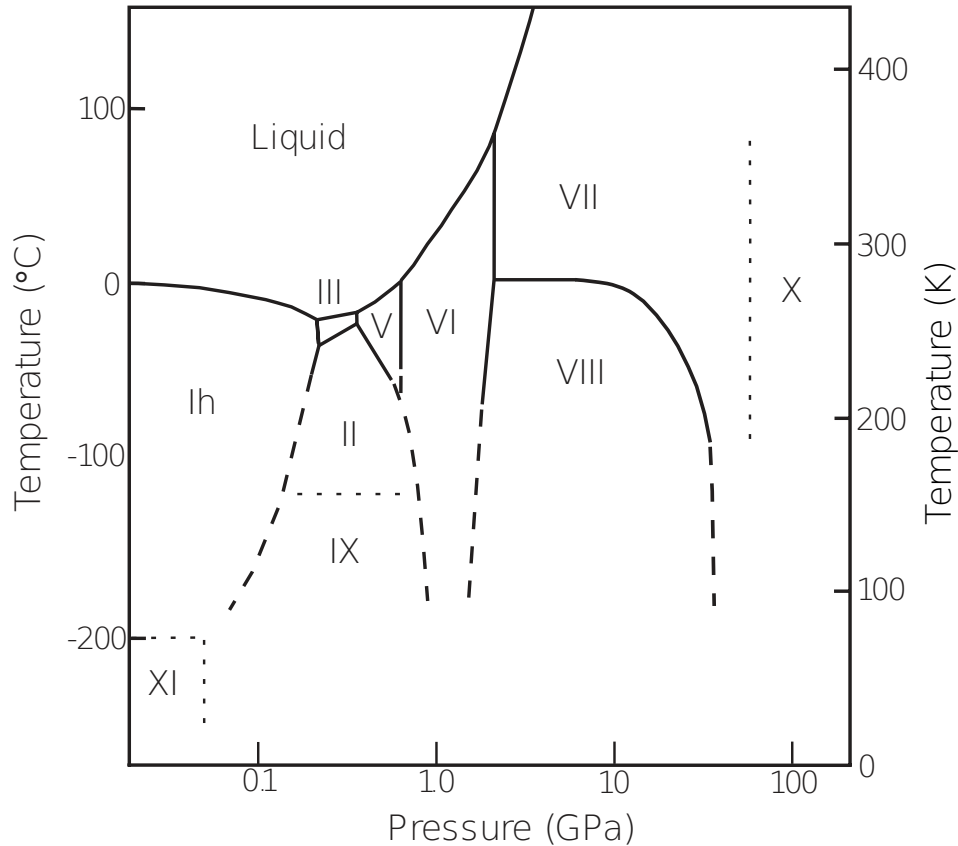


Figure 1.2: The temperature-pressure phase diagram of water and crystalline ices. The stability domains of ices I to XI ices are shown, those of ices XII to XVI are not indicated in this figure. Dashed lines indicate phase boundaries across which metastability has been observed. (Finney et al., 1998).

plained by the fact that the two phases differ solely by the stacking order of lattice planes along the  $c$  axis of the crystal. It has been suggested that cubic ice would always contain stacking faults and hence a fraction of hexagonally ordered material (Hansen et al., 2008a,b, Malkin et al., 2015). This form occurs at low temperatures and converts to ice  $I_h$  above 190 K.

Ice VII and VIII are high pressure phases (stable above  $\approx 1.5$  GPa). Ice VII is cubic and displays hydrogen disorder. Its structure is made of two interpenetrating lattices of ice  $I_c$ . Its space group is  $Pn\bar{3}m$ , the full structure can be found in (Jorgensen and Worlton, 1985, Kuhs et al., 1984). The corresponding low temperature phase is tetragonal ice VIII, with space group  $P4_2nm$ . This phase is (partially) hydrogen ordered (Johari, 1974, Kuhs et al., 1984). For crystalline ice phases, the general rule for hydrogen ordering appears to be that “(all) phases that share phase boundaries with liquid water (ices  $I_h$ , III, V and VI and VII) have disordered hy-

drogen bonding”, according to (Chaplin, 2015, Holzappel, 1972, Johari, 1974, Kuhs et al., 1984, Pauling, 1935).

Some of the hydrogen ordered phases are difficult to obtain in experiments even at low temperatures. They can be stabilised by doping of ice with ions. For ice XI, KOH (in 10 mM concentration) was used to dope ice  $I_h$  at ambient pressure and low temperature ( $T \approx 72$  K) (Fukazawa et al., 1998, Matsuo et al., 1986, Pamuk et al., 2015). Ices XIII and XIV were formed by doping with HCl (Salzmann, 2006). It is interesting to note that this simple acid and this simple base promote hydrogen ordering, while other salts (alkali-halides such as LiCl and NaCl) tend to promote disorder of the hydrogen bond network. This is likely to be due to a favoured interaction of  $H_3O^+$  and  $HO^-$  defects with water molecules.

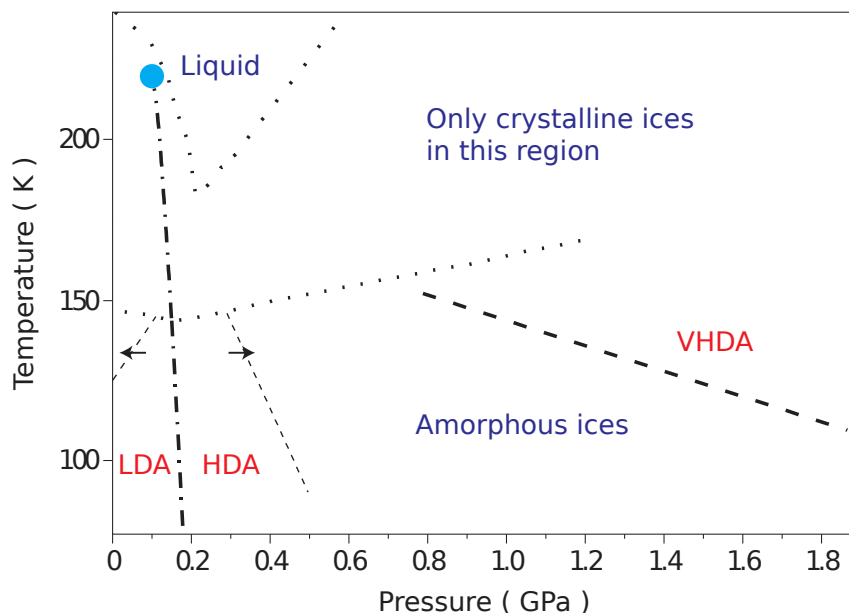


Figure 1.3: The stability domains of the three metastable amorphous phases of ice (LDA, HDA, VHDA). The “no man’s land” is the region where only crystalline ices are stable. The blue circle is the proposed second critical point of pure water. The dot-dashed line emanating from it, is the line of proposed first order transitions in (inaccessible) water. (Nelmes et al., 2006)

**Amorphous ices:** Three distinct amorphous structures of pure water ice (Loring et al., 2011). Figure 1.3 shows their temperature and pressure stability domains. Five different amorphous states are distinguished according to their method of preparation. The first is amorphous solid water (ASW) which is formed by vapour deposition on a substrate at liquid nitrogen temperature. Next is hyper-quenched glassy water (HGW) which is obtained by hyper-quenching liquid droplets. Both of them are low density amorphous states whose structures are very similar to that of the low density amorphous (LDA) form which can be produced by annealing the

high density form at ambient pressure (Kohl et al., 2005). The latter most resembles ice  $I_h$  in its tetrahedral short-range structure. The high density form (HDA) is formed above 0.2 GPa by compressing low pressure phases (ice  $I_h$ ,  $I_c$  or LDA) and is metastable at ambient pressure and low temperature. A more relaxed form called expanded HDA (eHDA) is obtained by annealing HDA to about 125 K at moderate pressure (Winkel et al., 2008, 2011b). The very-high-density form (VHDA) is formed upon annealing HDA at pressures of about 1 GPa or more, it can also be recovered to ambient pressure due to hysteresis (Nelmes et al., 2006). The structure factors of these amorphous ices are shown in Figure 1.4 taken from Bowron et al. (2006). The vertical arrows exemplify that the first diffraction peak shifts to larger  $q$  in denser phases. In chapter 4 the quenching techniques employed to obtain amorphous ices in laboratory experiments will be discussed.

The phenomenon of polyamorphism consists in the coexistence of two amorphous states of different density and local arrangement of molecules. The transition between two such states, which corresponds to the change in structure and density, will be more or less sudden depending on the external parameter which provokes it. For instance the transition from HDA to LDA upon annealing at 0.2 GPa is reversible and abrupt (Mishima, 1994). There is however significant hysteresis upon decompression of HDA and VHDA at 77 K, as mentioned above.

**Supercooled water** is water below the freezing point ( $0^\circ\text{C}$  at 1 atm). This is a metastable state in which ice should nucleate. The temperature to which water can be supercooled depends on the purity. Very pure samples, can be supercooled to the homogeneous nucleation temperature ( $T_H \approx 235 \text{ K} = -38^\circ \text{C}$  at 1 atm), at which water freezes without need for preferred nucleation sites (impurities or perturbations) (Koop, 2015). Under suitable experimental conditions water can persist in this metastable liquid state (Debenedetti, 1996).

The region of the temperature-pressure diagram, below the line of homogeneous nucleation temperature and above the glass transitions of the amorphous ices, in which neither liquid nor amorphous phases have been observed experimentally, has been called “no man’s land”. This is to say that it is impossible to observe the glass transition in pure water over an extended range of temperature as in other glass forming systems. Speedy and Angell (1976) found that the isothermal compressibility appears to diverge as temperature decrease is extrapolated just below  $T_H$ . Further divergences of a number of thermodynamic coefficients (heat capacity, viscosity, coefficients of thermal expansion and of self-diffusion, thermal conductivity, various relaxation times) have been suggested from extrapolations of numerous experiments (Angell et al., 1982, Mishima, 2000, Stanley and Mallamace, 2015). These divergences are unexpected and several explanations have been invoked (Holten et al.,

2012, Speedy and Angell, 1976). As the amorphous phases of water were discovered and the transitions between them became better characterised, it was suggested that a first order liquid-liquid phase transition (LLPT) might prolong the transition between LDA and HDA at higher temperatures. There would be a low density liquid (LDL) and high density liquid (HDL) corresponding to the two amorphous phases. The existence of a second critical point terminating the LLPT below  $T_H$  has been proposed as an explanation of the apparent divergences. (Stanley and Mallamace, 2015, Stanley and Mishima, 1998).

A recent study tries to probe the dynamics and structure of water at the upper edge of the no man's land (down to  $\approx 227$  K) at short time scales using X-ray free electron laser techniques (Sellberg et al., 2014). In another study this region is approached from the low temperature side (Amann-Winkel et al., 2013). Nevertheless the no man's land still remains largely unexplored in experiments. Simulations, however, allow to probe the behaviour of water in this region, this has given rise to a lively debate recently (Limmer and Chandler, 2013, Palmer et al., 2014).

A different approach to the study of the no man's land is to use nano-confined water (Chen et al., 2006, Mallamace et al., 2006), for instance porous minerals (such as zeolites) or cells which will not freeze at the  $T_H$  of the bulk (Nigro et al., 2015), or aqueous solutions which can be supercooled in this region (see the next section).

**Astrophysical ices** Water is an abundant molecule in outer space. It is produced during star formation and can be found in stellar atmospheres and interstellar clouds. When these clouds cool the gases, including water vapour and others such as CO, condense and ice forms on the surface of dust grains. This happens in the region beyond the ice line,  $\approx 3$  A.U.<sup>‡</sup> from the Sun in the case of the early solar system. Since grains are typically cold (less than 200 K) this ice is usually amorphous (ASW or LDA) or cubic ice (Ciesla, 2014, Hogerheijde et al., 2011). Amorphous ice may be the most common form of ice in interstellar space (Jenniskens and Blake, 1996). Moreover the total mass of all types of ices is expected to be about twice that of the rocky material in the solar system (Lodders, 2003). In protoplanetary disks surrounding young stars, these grains collide and accrete to pebbles, comets, planetesimals and in the long run form planets such as those in our solar system. Ice is expected to play a crucial role in the accretion process. Experimental and theoretical studies have shown that coagulation of dust particles is frustrated by bouncing and fragmentation (Gundlach et al., 2011a,b, Wada et al., 2008). Ros and Johansen (2013) have demonstrated in a numerical model that condensation of vapour is an efficient growth mode towards the formation decimeter sized pebbles.

Violent collisions between increasingly large planetesimals are expected to occur

---

<sup>‡</sup>Astronomical Units, 1 A.U. =  $1.4960 \times 10^{11}$  m

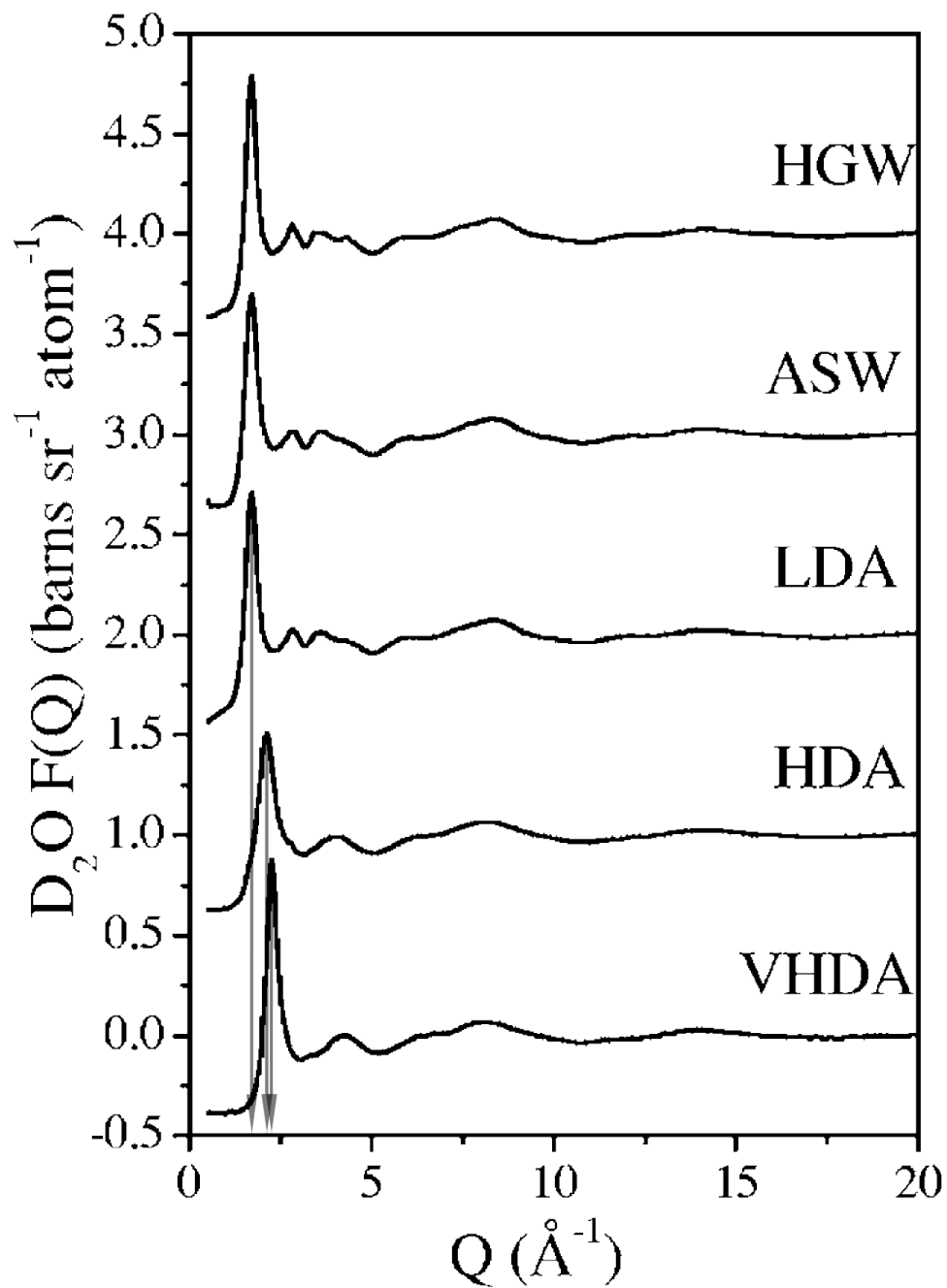


Figure 1.4: The structure factors of LDA, HDA, VHDA, HGW and ASW prepared from  $D_2O$ . The data were obtained by neutron diffraction experiments at 80 K and ambient pressure (Bowron et al., 2006). The grey arrows indicate the positions of the first peak in the diffraction patterns of LDA, HDA and VHDA.

frequently during accretion. If these events happen to objects beyond the ice line, these bodies will contain considerable fractions of ice. Hence ices will experience extreme thermodynamic conditions of temperature and pressure. The macroscopic properties of these ices (such as density, viscosity and stickiness) are highly relevant for models of planet formation (Gundlach et al., 2011a,b, Wada et al., 2008, Wettlaufer, 2010). Since these ices occur in heterogeneous extreme environments, their interaction with other elements in these conditions must be taken into account. Salts are an excellent probe for this interaction, because they are naturally abundant and soluble in water. Thus the question whether these ices can include ions ought to be addressed. If the structure of these ices is understood, it may provide the opportunity to gain further insight into the structure of a variety of bodies containing sizable fractions of water. The latter include the moons of the Jovian systems (Europa, Ganymede, Callisto, Enceladus, Titan amongst others), in whose interiors pressure reaches the Giga Pascal range, and the ice giants (Neptune and Uranus), in whose interiors pressure goes beyond 100 GPa. Under these conditions Ice VII and X should exist, and their properties (density, EoS, and more) are relevant in models of the internal structure (Bezacier et al., 2014b, Choukroun et al., 2013, Fortes and Choukroun, 2010, Frank et al., 2004, 2008, Journaux et al., 2013, Sohl et al., 2010, Tobie et al., 2009, Vance et al., 2014). In particular, the discovery that ice VII can include LiCl at high concentration (Klotz et al., 2009), encourages the search for ices including other salts.

Furthermore, circumstellar ice has also been proposed as a locus for the development of organic molecules and prebiotic chemistry (Modica et al., 2014), and it has been suggested that sea ice on Earth may be linked to the origins of life (Trinks et al., 2005).

**Note:** In the following we will use the word “ice” alone to refer to crystalline phases only. If the amorphous phase is mentioned it will be explicitly stated. The latter may also be called “amorphous state” or “amorphous ice”.

## 1.2 Aqueous solutions

Electrolytic aqueous solutions, such as LiCl and NaCl water solutions, occur spontaneously in nature and are studied in diverse fields of science ranging from geology to energy technology. In these systems water molecules are under the influence of Coulomb forces due to the charged species. The limit on the number of ions which can be dissolved is called solubility. The properties of ions in solutions and those of their hydration shells have been studied extensively (Bankura et al., 2013, Mancinelli et al., 2007, Neilson and Enderby, 1979) as they are crucial for the understanding of

a variety of chemical and biological processes. The concepts of structure-breaking and structure-making have been widely used to provide at least a qualitative understanding of the effect of ions on the structure of water. The idea is that ions are supposed either to disrupt the hydrogen-bond network or to form ionic hydration structures in water (Gallo et al., 2011, Leberman and Soper, 1995, Mancinelli et al., 2007, Winkel et al., 2011a).

LiCl solutions have been studied in depth since the early 1970s in the attempt to address the thermodynamic and structural properties of water in the deep undercooled regime (Angell and Sore, 1970, Kanno, 1987, Prével et al., 1995), the stability of which is extended by the addition of ions in water.

The high-pressure phases of this solution have been explored by calorimetry and Raman spectroscopy (Mishima, 2005, 2011, Suzuki and Mishima, 2000, 2009b, Yoshimura and Kanno, 2002), and the possibility of a relation between the liquid-liquid transition in the solutions has been addressed (Kanno, 1987, Mishima, 2007). Other solutions such as KCl have also been investigated (Gallo et al., 2014, Yoshimura et al., 2004). Detailed knowledge of the non-equilibrium phase diagram of common electrolyte aqueous solutions, such as LiCl, NaCl and KCl-water solutions, and of the structural properties of the hydration shells of their ions has been achieved, at least at ambient and moderate ( $p < 2$  kbar) pressures. A variety of techniques have been employed to this end individually and in combined studies. They include X-ray diffraction, extended X-ray absorption fine-structure spectroscopy (EXAFS), neutron diffraction with isotopic substitution, and simulation techniques. (Bankura et al., 2013, Ben Ishai et al., 2013, Le and Molinero, 2010, Mancinelli et al., 2007, Migliorati et al., 2013, Neilson and Enderby, 1979, Prével et al., 1995, Tazi et al., 2012, Winkel et al., 2011a) In NaCl solutions the effects of concentration on the thermodynamics of the supercooled liquid, as well as the link to water anomalies have been explored using molecular dynamics simulations (Corradini et al., 2010, 2009). While  $\text{Na}^+$  ions are octahedrally coordinated in the crystalline phase, they show large variations in the coordination number in solution, ranging from 4 to 6, depending on the anion and the salt concentration. (Enderby and Neilson, 1981, Mantegazzi et al., 2013, Neilson and Enderby, 1979, Valenti et al., 2012)

Not only bulk properties of these solutions, but also the interaction of ions with interfaces has been probed. For instance, the adsorption of ions on interfaces and its effects on solvation has been investigated using techniques such as second harmonic generation (D.E. and R.J., 2015, Mishra et al., 2012). Crystallisation and phase equilibria in bulk and in droplets, which are of relevance to atmospheric science, have been investigated in detailed atomistic simulations (Bogdan et al., 2013, 2014, Bullock and Molinero, 2013, Hudait and Molinero, 2014, Pummer et al., 2015).

A common feature of most electrolytic solutions is that ions are not included

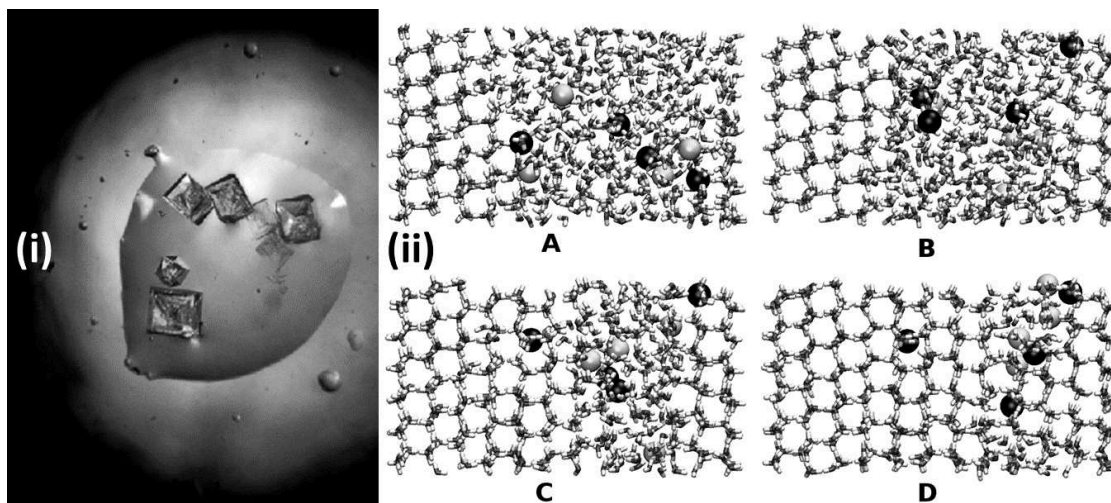


Figure 1.5: Left: (i) Photograph of rocksalt (NaCl) crystallising from an evaporating drop of saturated brine. Right: (ii) Brine rejection of NaCl from the ice lattice in a simulation using Molecular Dynamics. The snapshots A, B, C, D were taken every 200 ns (Vrbka and Jungwirth, 2006).

in ice that crystallises from these solutions. Depending on concentration ions may be expelled from the ice into a highly concentrated solution (brine), or they form hydrates of well defined composition or pure salt precipitates. (Elarby-Aouizerat et al., 1983, Kessis, 1965, Klewe and Pedersen, 1974, Vrbka and Jungwirth, 2006) This is the main reason why the solid domain of the phase diagram of these solutions has barely been explored at high pressure.

The behaviour of LiCl-water solutions under high pressure has been investigated more recently by neutron diffraction experiments and atomistic simulations (Bove et al., 2011b, Klotz et al., 2009, Ruiz et al., 2014). A polyamorphic transition between a high-density and a very-high-density structure has been observed under high-pressure (Bove et al., 2011b). This transition is similar to that observed in pure water. Furthermore, evidence has been provided for the existence of high-pressure ice phases including considerable amounts of salt in their lattice (Klotz et al., 2009).

The high-density relaxed state was produced by cooling the eutectic solution  $\text{LiCl} \cdot 6\text{D}_2\text{O}$  (Dupuy-Philon et al., 1992) at ambient pressure. It is highly similar to the eHDA state of pure water as shown in the left panel of Figure 1.6. This HDA-like state undergoes a polyamorphic transition to the very-high-density state upon annealing the solution under high pressure (right panel of Figure 1.6). The latter state has been shown to be very stable up to multi-GPa pressures. Of note is the fact that the  $\text{Li}^+$  ion is octahedrally coordinated at high-pressure in both the amorphous and the crystalline phase (see next paragraph). The observed polyamorphic transition (eHDA to VHDA) is due to the change of the coordination around the  $\text{Li}^+$  ion from four-fold at ambient pressure to six-fold at high pressure (Bove

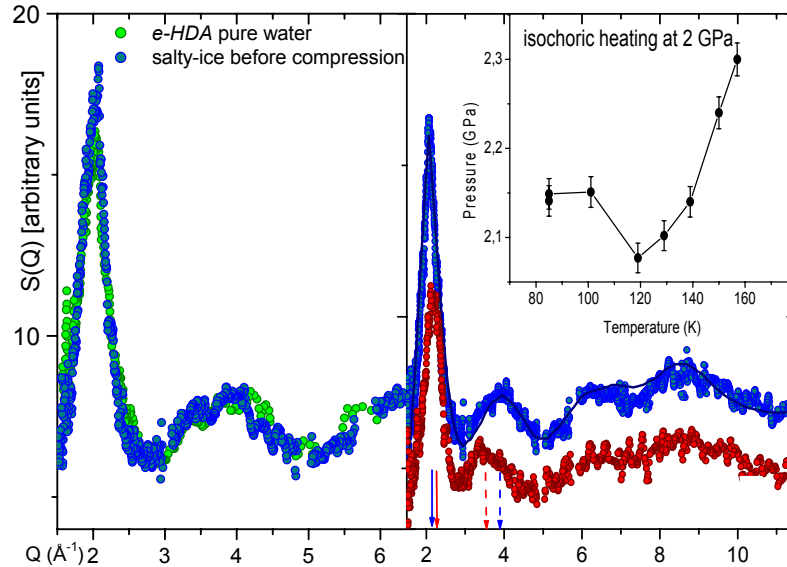


Figure 1.6: Left: Comparison between the diffraction pattern of the HDA form of amorphous  $\text{LiCl} \cdot 6\text{D}_2\text{O}$  at 80 K and ambient pressure (blue dots) and that of pure ice eHDA (light green). Right: Comparison of salty HDA (blue) and salty VHDA (red) both recovered to ambient pressure. Arrows indicate the position of the first and second diffraction peaks. The inset shows the pressure under isochoric annealing, measured from the lead calibrant. (Bove et al., 2011b)

et al., 2011b). Whether the existence of a polyamorphic transition is a common feature of electrolytic aqueous solutions, and whether it is linked to the polyamorphic transition observed in pure water (Klotz et al., 2005), as suggested by recent Raman studies (Suzuki and Mishima, 2009a), still remains to be established. In this work we contribute to this by studying NaCl solutions.

The ice VII phase which crystallised upon annealing of the VHDA state at 4 GPa, was found to incorporate LiCl into its lattice by substitution of  $\text{Cl}^-$  for water molecules, and inclusion of  $\text{Li}^+$  in the octahedral interstices of the body centered cubic (*bcc*) oxygen lattice of ice VII. This structure shows an expansion of the unit cell of 8% by volume at 4 GPa and displacement factors five times larger than those measured in pure ice VII. This appears as a strong attenuation of peaks with increasing  $q$  in the diffraction pattern shown in Figure 1.7 (Klotz et al., 2009).

### 1.3 Outline of this work

NaCl is biologically and geochemically more important than LiCl and the existence of new amorphous and crystalline phases of NaCl water solutions could be of high relevance for the physics of both living organisms and celestial icy bodies (Bezacier et al., 2014a, Frank et al., 2006). Up to now NaCl di-hydrate is the only known solid

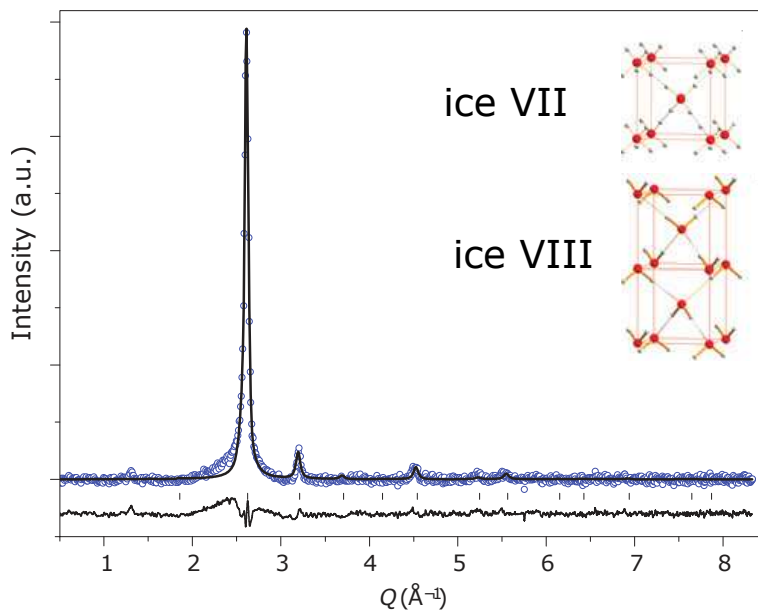


Figure 1.7: The neutron diffraction pattern of  $\text{LiCl} \cdot 6\text{D}_2\text{O}$  at 4 GPa and 280 K is shown by blue circles. The line through the data is a Rietveld fit based on the ice VII structure with interstitial  $\text{Li}^+$  and substitutional  $\text{Cl}^-$  ions. The inset shows the structures of ice VII (hydrogen disordered, body centered cubic) and VIII (hydrogen ordered, tetragonal). (Klotz et al., 2009)

compound formed by the  $\text{NaCl}$  and  $\text{H}_2\text{O}$  system. No phase transition in the solid state has been found (Klewe and Pedersen, 1974), in contrast to the  $\text{LiCl}$  and  $\text{H}_2\text{O}$  system where several hydrates are formed, depending on the salt concentration and pressure conditions (Elarby-Aouizerat et al., 1983).

Here we investigate the high-pressure (metastable) amorphous and crystalline phases of  $\text{NaCl}$  aqueous solutions close to the eutectic composition. We have combined high-pressure neutron diffraction and molecular dynamics simulations in order to obtain detailed structural information. Our experiments follow the paths in Figure 1.8, which also shows the metastable phase diagram of  $\text{LiCl}$  solution. Path 1 is the quench of the solution. Path 2 is annealing at ambient temperature. Path 3 is compression of the sample to 4 GPa at 80 K. Path 3' is the compression at 140 K performed in simulations only. Path 4 is the annealing of the amorphous phase to 140 K. Path 5 is the annealing of the solution to 300 K at 4 GPa. Path 6 is the cooling of the crystalline phase to 80 K at 4 GPa. Path 7 is the decompression to ambient pressure at 80 K. Path 8 is the annealing of the recovered sample at ambient pressure, which was performed in experiments but is not discussed here. Experiments with  $\text{NaCl} \cdot 10.2\text{D}_2\text{O}$  samples were performed along all paths except path 3'. Simulations were performed along paths 1, 3, 3', 4 and 5.

The experimental techniques of X-ray and neutron diffraction, as well as high-

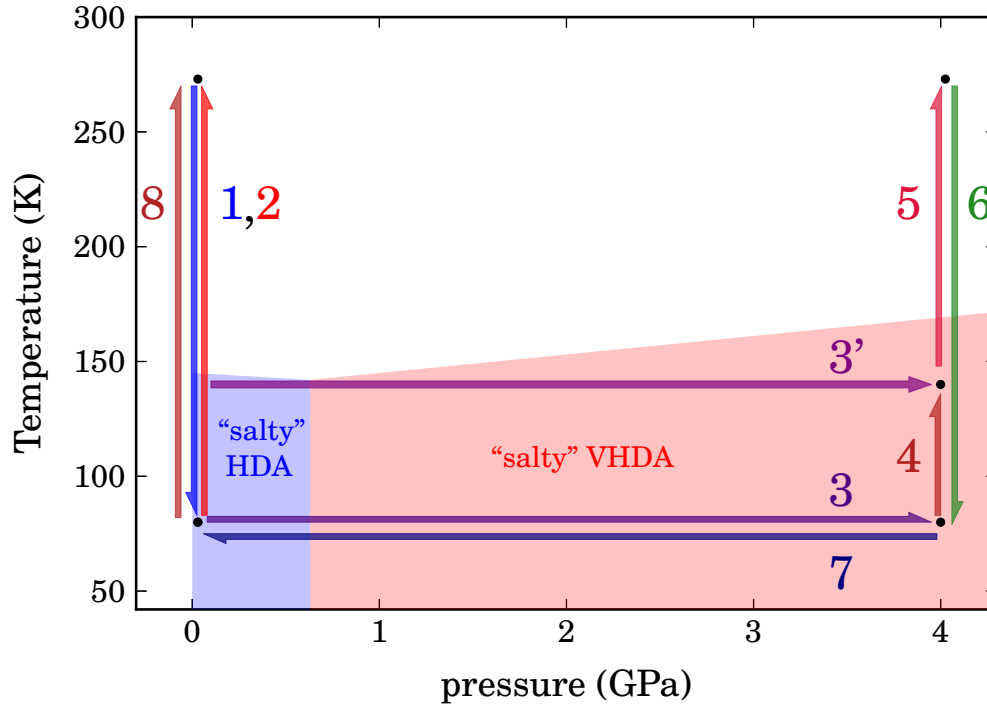


Figure 1.8: The thermodynamic path along which  $\text{NaCl} \cdot 10.2\text{D}_2\text{O}$  has been studied, by neutron diffraction and MD simulations. The coloured regions indicate the boundaries of amorphous phases of previously studied  $\text{LiCl} \cdot 6\text{D}_2\text{O}$ . (Bove et al., 2011b) Arrows: 1: hyper-quench at ambient pressure, 2: warming at ambient pressure (Figure 4.16), 3: compression at 80 K (Figure 5.1), 3': compression at 140 K (MD simulations only), 4: annealing at 4 GPa (MD and neutron diffraction experiments), 5: annealing to 300 K at 4 GPa, 6: quench to 80K at 4 GPa, 7: recovery to ambient pressure (decompression), 8: annealing at ambient pressure of the recovered sample .

pressure are presented in chapter 2. The methods of the atomistic simulations which we have employed are exposed in chapter 3. The quenching technique and the amorphous structure obtained at ambient pressure are presented in chapter 4. The results concerning the compression of  $\text{NaCl} \cdot 10.2\text{D}_2\text{O}$  at low temperature and its annealing at high pressure in experiments and simulations are presented in chapter 5. Certain details referred to in the text have been grouped in the appendix at the end of the manuscript.

# Chapter 2

## Experimental techniques

Here we present the techniques which were used in our experimental study of the NaCl-water system. First, the methods of diffraction used to study crystalline and amorphous materials are presented. Second, the high-pressure techniques employed are described.

### 2.1 Diffraction

#### 2.1.1 Scattering theory

In 1912 M.T. Von Laue discovered that X-rays are scattered in precise patterns by crystals. (Laue, 1913) \* The same year W.L. and W.H. Bragg proposed a formalism to calculate diffraction spectra. † They showed that

$$2 d \sin \theta = n \lambda \quad (2.1)$$

where  $n$  is an integer  $d$  is the spacing between lattice planes as shown in Figure 2.1,  $\theta$  is the angle between the incident beam and the scattering plane,  $\lambda = h/p$  is the de Broglie wavelength of the particle, and  $p$  is its momentum (Bragg and Bragg, 1913). This formula can be derived by considering the path difference of two rays scattered on successive planes (Figure 2.1). A peak in the diffraction spectrum arises when two such rays interfere constructively, which happens when the path difference is an integer multiple of the wavelength. (Warren, 2012) This is known as coherent elastic scattering. (Squires, 2012) Equation (2.1) can be rewritten as

$$q d = 2 \pi \quad (2.2)$$

---

\*Von Laue was awarded the Nobel prize in physics in 1914 for “for his discovery of the diffraction of X-rays by crystals” (Nobel Foundation, 2015).

†W.L. Bragg and W.H. Bragg were awarded the Nobel prize in physics in 1915 for “for their services in the analysis of crystal structure by means of X-rays” (Nobel Foundation, 2015).

where  $\|\mathbf{q}\| = 4\pi \sin(\theta)/\lambda$  is the momentum transfer. The object  $\mathbf{q}$  is a vector of the reciprocal space. In a cubic crystal system the lattice spacing is related to the lattice parameter  $a$  by the formula

$$d = \frac{a}{\sqrt{h^2 + k^2 + l^2}} \quad (2.3)$$

where  $h, k, l$  are the Miller indices of the Bragg plane. For other crystal systems the expression depending on  $h, k, l$  in the square root changes (Prince, 2006). For a given crystal symmetry there are selection rules which prescribe which combinations of integers  $h, k, l$  are allowed.

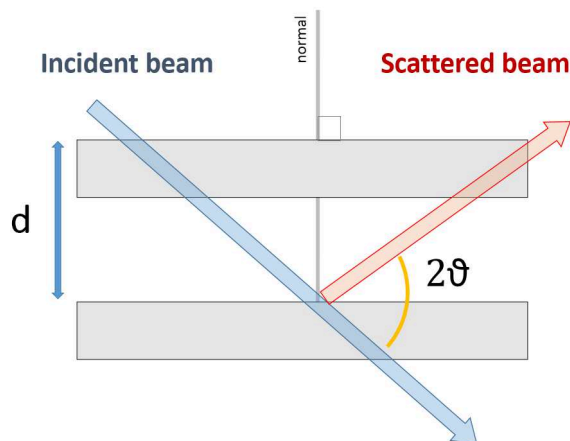


Figure 2.1: Sketch of the geometry of a diffraction experiment. The spacing between lattice planes is  $d$ , the angle between the incident and the scattered beam is  $2\theta$ ,  $\lambda$  is the wavelength of incoming radiation.

Diffraction can be observed in any system where a wave encounters a slit or obstacle, and the wavelength of incident radiation is comparable to the size of the obstacle. Surface waves on water are diffracted by macroscopic objects. Red laser light ( $\lambda \approx 700$  nm) can be diffracted on human hair ( $\varnothing \approx 100$   $\mu\text{m}$ ), here the integer  $n$  in (2.1) is quite large. A diffraction experiment usually measures intensity as a function of angles or time of flight. These diffractograms are then proportional to the structure factor (defined below) and are characteristic of the structure of the material.

For crystalline and amorphous phases of matter where typical distances are of the order of the Ångström ( $10^{-10}$  meters) X-rays, electrons and neutrons are commonly used in diffraction experiments. X-rays and electrons are diffracted by electronic clouds of atoms with which they interact strongly. Electrons being charged only penetrate the first few layers of material depending on their energy and are used as

surface probes. X-rays will scatter strongly from materials with high electron densities (good signals from  $Z > 4$ ). Neutrons interact with nuclei. The cross-sections for this process are small and therefore neutrons penetrate all ordinary matter. Hence large samples (typically more than 10 mm<sup>3</sup>) and long counting times (minutes to hours) are needed for good statistics (Pynn, 1990). The specific advantages of X-ray and neutron diffraction are discussed in sections 2.1.2 and 2.1.3 respectively.

General scattering theory relates the microscopic structure of the material (crystalline solid, glass or liquid) to the intensity profile measured in a diffraction experiment. The time dependent pair correlation function  $G(\mathbf{r}, t)$  is

$$G(\mathbf{r}, t) = \frac{1}{(2\pi)^3} \int \frac{1}{N} \left( \sum_{j,j'} \langle e^{-i\mathbf{q}\cdot\mathbf{R}_{j'}(0)} e^{-i\mathbf{q}\cdot\mathbf{R}_j(t)} \rangle \right) \exp(-i\mathbf{q}\cdot\mathbf{r}) d\mathbf{q} \quad (2.4)$$

$$S(\mathbf{q}, \omega) = \frac{1}{2\pi\hbar} \int G(\mathbf{r}, t) \exp(i(\mathbf{q}\cdot\mathbf{r} - \omega t)) dt \quad (2.5)$$

where  $\mathbf{R}_j(t)$  is the position vector of the  $j$ th nucleus at time  $t$  in the case of nuclear scattering,  $N$  is the number of atoms in the lattice and angular brackets denote the thermal average of an operator given in A.3. The scattering function  $S(\mathbf{q}, \omega)$  is the Fourier transform of  $G(\mathbf{r}, t)$ . The static structure factor  $S(\mathbf{q})$  is the zeroth energy moment of  $S(\mathbf{q}, \omega)$

$$S(\mathbf{q}) = \int_{-\infty}^{+\infty} S(\mathbf{q}, \omega) d(\hbar\omega). \quad (2.6)$$

Scattering theory and correlation functions are discussed in detail in Squires (2012) and Marshall and Lovesey (1971).

The cross section for coherent scattering from a crystal is

$$\left( \frac{d\sigma}{d\Omega} \right)_{\text{coh el}} = N \frac{(2\pi)^3}{v_0} \sum_{\boldsymbol{\tau}} \delta(\mathbf{q} - \boldsymbol{\tau}) |F_N(\mathbf{q})|^2 \quad (2.7)$$

$$F_N(\mathbf{q}) = \sum_j \bar{b}_j \exp(i\mathbf{R}_j \cdot \mathbf{q}) \exp(-W_j) \quad (2.8)$$

where  $F_N(\mathbf{q})$  is the unit cell structure amplitude for a non-Bravais crystal. This is a discrete sum of  $\delta(\mathbf{q})$  peaks which gives rise to the typical crystalline diffraction patterns of large numbers of sharp peaks. The term  $\exp(-W_j)$  is the Debye-Waller or atomic temperature factor, given by  $2W_j = U^2 = \langle (\mathbf{q} \cdot \mathbf{u}_0(0))^2 \rangle$  where  $\mathbf{u}_0(0)$  is the displacement of the atom from its equilibrium position. It describes the weakening of the intensities due to the atomic thermal motions and atomic disorder (Kuks and Lehmann, 1987).

In the following we consider the case where  $G(\mathbf{r}, t)$ ,  $S(\mathbf{q}, \omega)$ ,  $S(\mathbf{q})$  depend only on the norms  $r = \|\mathbf{r}\|$  and  $q = \|\mathbf{q}\|$ . This corresponds to the powder diffraction

method in which intensities are averaged over the angular dependence.

Glasses and amorphous phases are states of solid matter in which short range order exists but no long range order. This short range order is the structure of the shells of nearest neighbours of a particle in the glass. This ordering gives rise to oscillations of the radial distribution functions  $g(r)$  (RDFs), which give the probability of finding a second particle at a distance  $r$  from any given particle (Marshall and Lovesey, 1971). The formula to calculate these RDFs in a multi-component system is given in (3.25) in section 3.4.2. The structure factor  $S(q)$  is the Fourier transform (FT) of the radial distribution function (in the case of a multi-component system it is the FT of a linear combination of RDFs). How to compute  $S(k)$  from  $g(r)$  is discussed in more detail in section 2.1. An example of the RDF  $g(r)$  and SF  $S(q)$  and a sample configuration for a simple liquid or a glass are shown in Figure 2.3. The broad structure of the RDF and SF shown is in contrast to that of the narrow crystalline peaks shown in Figure 2.2. In the glass first peak of  $g(r)$  indicates the most probable location of a particle in the first coordination shell, the same holds for the  $n^{\text{th}}$  peak and  $n^{\text{th}}$  coordination shell (Chandler, 1987). It should also be noted that while in a crystal  $g(r)$  goes to zero between peaks, this is not the case in the glass, which means that a particle can be found in between shells, although this is rare.

In Figure 2.4 the diffraction patterns of crystalline ice  $I_h$ , amorphous phases LDA and e-HDA of pure water and  $\text{NaCl} \cdot 10.2\text{D}_2\text{O}$  solution are shown. Crystalline peaks are well defined sharp features and can be refined using Rietveld fitting in order to obtain atomic positions and mean square displacements for a given structural model. Amorphous features are broader due to the lack of long range order of the material, their interpretation requires a different approach than crystallography. The third spectrum shows a superposition of the diffraction patterns of e-HDA and ice  $I_h$ .

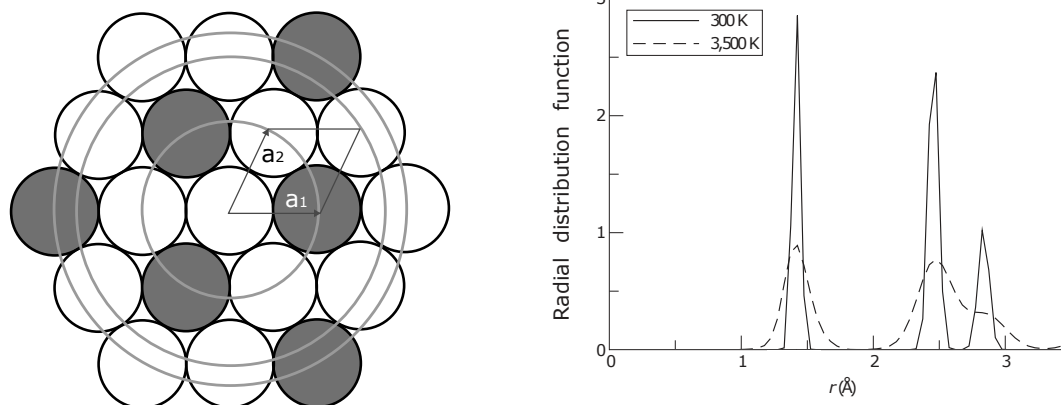


Figure 2.2: Left: Structures of a two-dimensional hexagonal lattice. The unit cell and the vectors  $a_1$  and  $a_2$  are shown. The distances corresponding to the shells of first, second and third neighbours are shown by circles. The sites which are empty in graphene and ice  $I_h$  are filled grey circles (graphic made with Inkscape 0.91 [www.inkscape.org]). Right: The radial distribution function  $g(r)$  for graphene, the two dimensional hexagonal polymorph of carbon, at 300 K and 3500 K showing the peaks corresponding to the first, second and third neighbours (Fasolino et al., 2007).

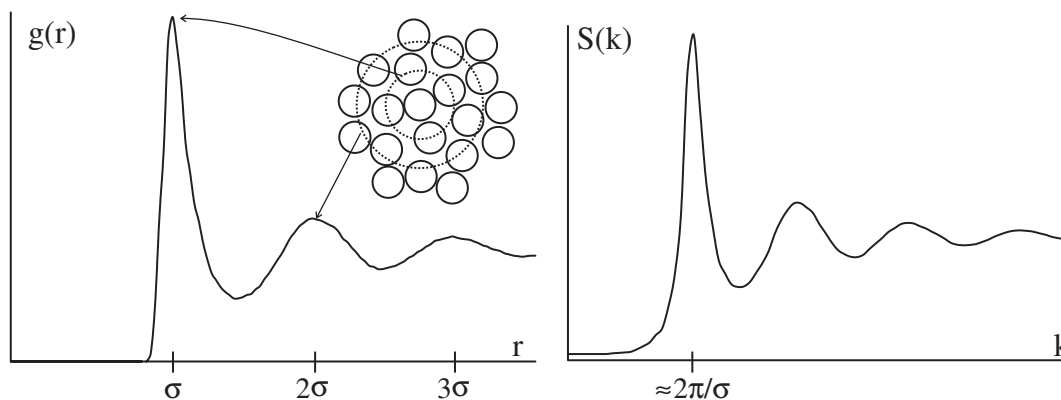


Figure 2.3: Right: the radial distribution function  $g(r)$  of an amorphous configuration of atoms. The dashed circles indicate the positions of first and second neighbour peaks of the  $g(r)$ . Right: the corresponding structure factor  $S(k)$ . (Reichman and Charbonneau, 2005)

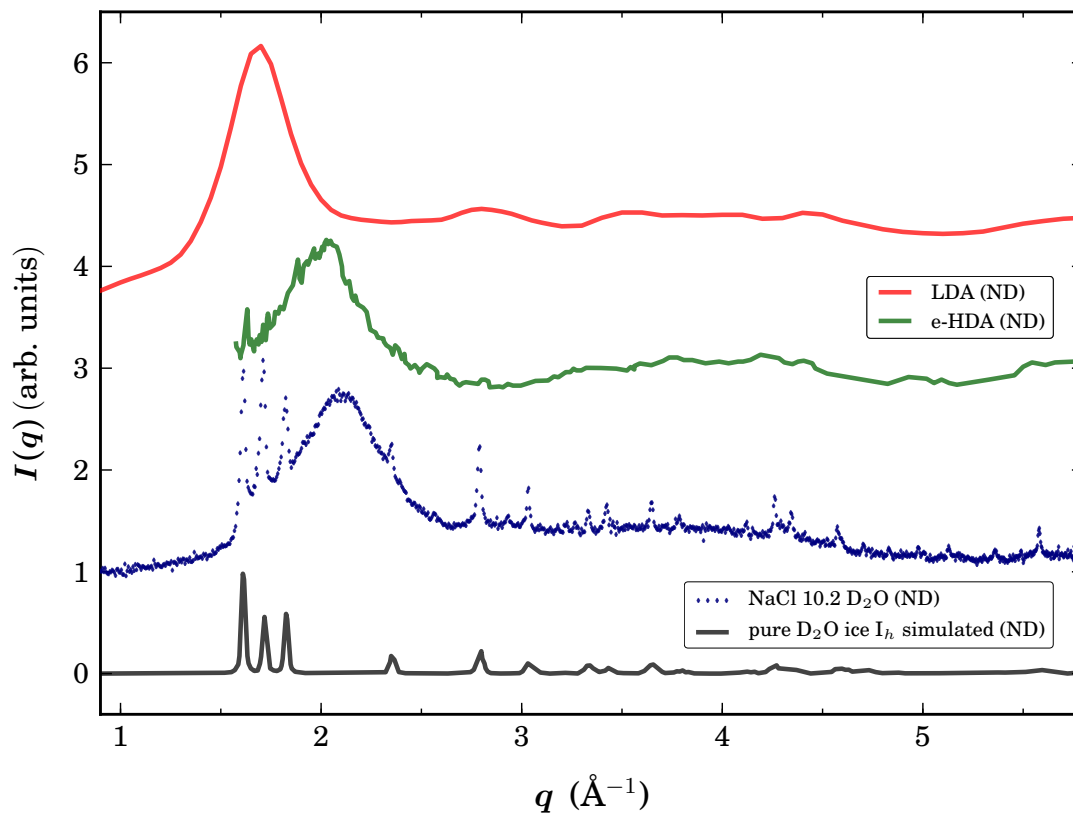


Figure 2.4: Measured neutron diffraction patterns and simulated structure factors  $S(q)$ . From bottom to top: Simulation of ice  $I_h$  pattern with FullProf, and amorphous LDA and e-HDA of pure water pure water e-HDA (dark green) (Nelmes et al., 2006) at 0.18 GPa and LDA (Bellissent-Funel et al., 1987) at 0.1 GPa, and  $\text{NaCl} \cdot 10.2\text{D}_2\text{O}$  pattern measured at ILL (Ludl et al., 2015).

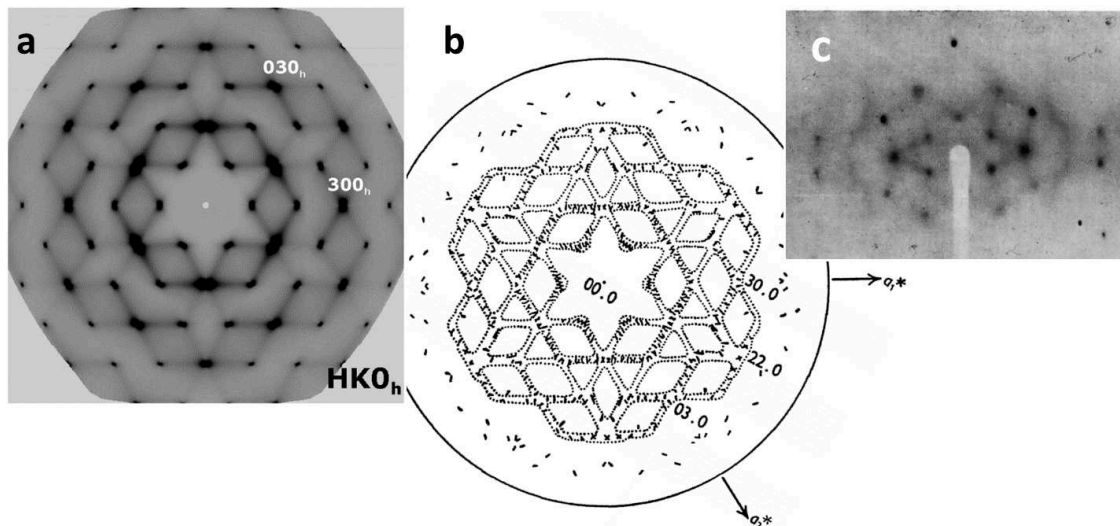


Figure 2.5: Diffraction data for single crystals of ice  $I_h$ . (a) Diffuse X-ray scattering intensity map of  $H_2O$  ice  $I_h$  at 175 K in the  $L = 0$  ( $HK0_h$ ) plane from Wehinger et al. (2014). (b) Positions of the diffuse spots (heavy lines) and approximate positions of the diffuse streaks (dotted lines) in the layer  $L = 0$ , (c) experimental recording of X-ray diffraction data along the hexagonal axis (4 hour exposure,  $-5^\circ\text{C}$ ), this recording is rotated  $30^\circ$  around the normal to the plane with respect to (a) and (b). (b) and (c) are taken from Owston (1949).

**Single crystal and powder diffraction** For a three dimensional single crystal reciprocal space is of the same dimension. In order to solve the crystallographic problem all Bragg peaks of this space have to be measured and indexed. Single crystal diffractometers use either 3 or 4 circle goniometers to rotate the sample crystal, and two dimensional detectors. This technique is used in many fields, notably solid state physics and protein crystallography. Figure 2.5 shows single crystal data of ice  $I_h$ . Panel (a) shows a measurement on a single crystal from lake Vostok measured by Wehinger et al. (2014) using X-rays at ESRF. The analysis of the diffuse scattering, which is the signal between the crystalline spots in the figure, shows that this sample is a single crystal showing no signs of stacking faults, and the signal is almost exclusively due to thermal diffuse scattering by phonons. Panel (c) shows data recorded by Owston (1949) using photographic plates and  $\text{Cu } K\alpha$  radiation. The reconstruction of the diffuse spots and streaks in panel (b) is rather crude compared to panel (a), but captures the overall structure of the diffraction spots remarkably well.

In powder diffraction intensities are reported as a function of only the  $2\theta$  angle. This is equivalent to averaging over concentric circles on a two dimensional detector. An ideal powder is a (possibly crystalline) material composed of grains whose orientations are distributed isotropically. Diffraction on an ideal powder will

indeed produce concentric circles instead of distinct peaks. If the lattice planes of a significant fraction of grains tend to be oriented along a common direction, the relative intensities of diffraction peaks in the powder spectrum are altered compared to the ideal powder. This is called texture.

When modeling a crystal's structure the space group, unit cell, and placement of atoms have to be guessed and refined. In this thesis we use the Hermann–Mauguin or “international notation” for the space groups, where the first letter stands for Bravais system. P for primitive, I body centered, F for face centered, A centered on A faces only, B centered on B faces only, C centered on C faces only, R for rhombohedral. As an example the symbol for the space group of hexagonal ice I is  $P6_3/mmc$ , with six-fold rotational symmetry. The number of this group is 194.

The unit cell is defined by three vectors and their coordinates (or their lengths and angles between them), the atomic positions are defined by coordinates, the occupancies and Debye-Waller factors. Only isotropic displacements were considered in this work.

### 2.1.2 X-ray experiments

X-rays are scattered by electrons, hence diffraction gives access to the electron density  $\rho(\mathbf{r})$  of the material, which is the Fourier transform of the structure amplitude

$$\rho(\mathbf{r}) = \frac{1}{(2\pi)^3} \int F(\mathbf{q}) e^{i\mathbf{q}\cdot\mathbf{r}} d\mathbf{q}. \quad (2.9)$$

Materials with high electron densities are good scatterers, whereas elements with few electrons such as H and Li produce very weak scattering signals. Therefore it is not possible to obtain full information about the ice lattice from X-ray diffraction. However, since the oxygen atoms do scatter, information about long range order can be deduced from such measurements. Since X-rays interact with charges they can be produced relatively easily and measured directly by dedicated CCD detectors<sup>‡</sup>.

The term  $\bar{b}_j = f_j(\lambda)$  in equation (2.8) is wavelength dependent and called the form factor (see appendix A.5). This is a major difference with neutron scattering and one reason of the complementarity of the two techniques.

Our X-ray diffraction experiments were performed at IMPMC on a commercial X-PERT powder X-ray diffractometer equipped with a low-temperature Anton Paar chamber. A sample holder made of nickel plated copper was used. The X-ray source was copper contained in a ceramic tube, which produces an incident wavelength of  $\lambda = 1.5418 \text{ \AA}$  (Cu  $K\alpha$ ). During the measurement the X-ray source and the detector were set up in Bragg-Brentano ( $\theta - 2\theta$ ) geometry. The sample was kept in fixed

<sup>‡</sup>Charge-coupled device, developed in the 1970s at Bell Labs.

position, while the bulb emitting the incident beam and the detector measuring the diffracted beam rotated. The angle between them being  $2\theta$ . The detector was a sealed linear silicon detector. A spectrum of sufficient quality to detect amorphous material could be measured in about 20 minutes. At synchrotrons such as ESRF X-rays are produced by accelerating electron beams. Common insertion devices include bending magnets, undulators and wigglers, which give much higher intensities. Winick (1994) Given the higher flux good spectra can be recorded in a few minutes.

### 2.1.3 Neutron experiments

Neutrons are neutral baryonic particles of spin  $\frac{1}{2}$  which interact weakly with ordinary matter and penetrate into the bulk. The neutron mass is  $\approx 1.6749 \times 10^{-27}$  kg (2010 CODATA recommended values) and its mean square radius  $\approx 0.8 \times 10^{-15}$  m, or 0.8 fm. They are unstable, their mean life time is  $\approx 881$  s. Since the neutron has a non zero magnetic moment it can be used to determine magnetic structures. (Nakamura, 2010) The scattering lengths vary largely between isotopes of an element. Hydrogen is the emblematic example since  $^1\text{H}$  scatters mostly incoherently while in deuterium ( $^2\text{H}$  or D) coherent scattering is stronger (see Table 2.1). Therefore the isotopic composition of the samples must be controlled to allow for correct interpretation of the data. While it is often more costly to use isotopically pure samples, the sensitivity of neutron scattering to isotopic composition allows experiments which could not be done with X-rays alone. One example is isotopic substitution which allows to determine partial structure factors of each element present in the sample, if all possible isotopic compositions are measured separately. In practice this technique is difficult to employ for samples with complex composition, however substituting H and D is often done to determine the structures of organic materials. (Pynn, 1990) Since  $^1\text{H}$  and  $^2\text{H}$  scatter neutrons strongly which makes neutrons an essential tool for the study of hydrogenated materials such as water, hydrogen storage materials and certain proteins.

For the elements of the  $\text{NaCl} \cdot 10.2\text{D}_2\text{O}$  solution scattering lengths and cross sections are reported in Table 2.1. The cross section  $\sigma_{\text{tot}}$  for scattering by a fixed single nucleus is

$$\sigma_{\text{tot}} = 4\pi b^2 \quad (2.10)$$

where  $b$  is the scattering length of the nucleus. It is typically of the order of a few femtometers. Since beam intensities are around  $\approx 10^7$  neutrons  $\text{s}^{-1}\text{cm}^{-2}$  this means that the number of neutrons scattered by a sample in an hour is of the order of a few thousand for a typical sample of a few milliliters. Depending on the sample, data collection times needed to get reasonable statistics range from minutes to a

few hours for a single scan. Neutron scattering experiments are a signal limited technique. (Pynn, 1990)

Scattering is due to the strong interaction between the neutron and nuclei. In neutron experiments where a sample is exposed to a flux of incoming neutrons  $\Phi$ , cross sections are the quantities measured. The partial differential cross section is the number of neutrons with final energy in  $[E', E + dE']$  scattered per unit time into the solid angle  $d\Omega$  (in a given direction) divided by  $\Phi d\Omega dE'$ . These cross sections are related to the correlation functions discussed above by a non-relativistic quantum mechanical treatment of neutron scattering (Squires, 2012). The state of the neutron depends only on the wave vector  $\mathbf{k}$ . The coherent cross section is proportional to the scattering function  $S(\mathbf{q}, \omega)$  defined in (2.5)

$$\left( \frac{d^2\sigma}{d\Omega dE'} \right)_{\text{coh}} = \frac{\sigma_{\text{coh}}}{4\pi} \frac{k'}{k} N S(\mathbf{q}, \omega) \quad (2.11)$$

where  $k$  is the norm of the wave vector of the incoming neutron, and  $k'$  that of the outgoing neutron, the scattering vector is  $\mathbf{q} = \mathbf{k} - \mathbf{k}'$ . In these terms Bragg's law requires that the scattering vector be equal to a reciprocal lattice vector  $\boldsymbol{\tau}$

$$\mathbf{q} = \mathbf{k} - \mathbf{k}' = \boldsymbol{\tau}. \quad (2.12)$$

Isotope	[ $c$ ]	Coherent b fm	Incoherent b fm	Coh xs barn	Inc xs barn	Scatt xs barn	Abs xs barn
H	—	−3.7390	—	1.7568	80.26	82.02	0.3326
<sup>1</sup> H	99.985	−3.7406	25.274	1.7583	80.27	82.03	0.3326
D or <sup>2</sup> H	0.015	6.671	4.04	5.592	2.05	7.64	0.000519
Li	—	−1.90	—	0.454	0.92	1.37	70.5
<sup>6</sup> Li	7.5	2.00 − 0.261 <i>i</i>	−1.89 + 0.26 <i>i</i>	0.51	0.46	0.97	940.(4.)
<sup>7</sup> Li	92.5	−2.22	−2.49	0.619	0.78	1.4	0.0454
O	—	5.803	—	4.232	0.0008	4.232	0.00019
<sup>16</sup> O	99.762	5.803	0	4.232	0	4.232	0.0001
Na	100	3.63	3.59	1.66	1.62	3.28	0.53
Cl	—	9.5770	—	11.5257	5.3	16.8	33.5
<sup>35</sup> Cl	75.77	11.65	6.1	17.06	4.7	21.8	44.1
<sup>37</sup> Cl	24.23	3.08	0.1	1.19	0.001	1.19	0.433

Table 2.1: Neutron scattering lengths and cross sections from NIST for thermal neutrons ( $\approx 300K$ ) NIST [NIST neutron scattering Lengths].  $c$  is the relative abundance of an isotope of the respective element. (1 barn =  $10^{-28}$  m<sup>2</sup>)

**Detecting neutrons** The low energy neutrons (few meV) used for diffraction experiments can be detected either via gaseous ionization detectors or scintillation detectors. In gaseous ionization detectors the neutron is absorbed by a nuclide such as  $^3\text{He}$ , which has an absorption cross section for thermal neutrons ( $v = 2200 \text{ m/s}$ ) of 5333 barn. The decay of the excited nuclide produces a ionized particles (a  $^1\text{H}$  and  $^3\text{H}$  ions in the case of  $^3\text{He}$ ) which can be detected by the proportional counter. Since its interaction with gamma rays is weak,  $^3\text{He}$  is convenient for neutron detection. From the count rate the number of neutrons can be deduced. (Alberi et al., 1975, Knoll et al., 1988)

Scintillation detectors use glass fibres doped with  $^6\text{Li}$  and  $\text{Ce}^{+3}$ . The interaction of a neutron with  $^6\text{Li}$  produces tritium ions and alpha particles, leading to an excitation of  $\text{Ce}^{+3}$  ions and emission of photons. Although the absorption cross section of  $^6\text{Li}$  (940 barn) for thermal neutrons is smaller than that of  $^3\text{He}$ , the density of the glass is higher than that of the gas, hence the output of these detectors per neutron is comparable to gaseous ionization detectors. Atkinson et al. (1987)

**Facilities and beamlines** To carry out neutron diffraction a beam of neutrons is needed. There are two kinds of sources of neutrons: nuclear reactors and high energy particle accelerators (spallation sources). Reactor sources such as the one at ILL provide a stable high flux beam which is moderated to give a fixed energy spectrum. For diffraction experiments this “white” beam has to be reduced to one of well defined energy using a monochromator, usually a large single crystal of highly reflective material. At spallation sources such as ISIS (Didcot, UK) and J-PARC (Tokai, Japan) neutrons are produced when a high energy proton beam hits a target of heavy metal. These beams are typically pulsed and contain more high energy neutrons than those at reactors. At spallation sources the time of flight (TOF) of neutrons is measured. This gives access to the neutron velocity  $v = l/t$ , where  $l$  is the length of the primary or secondary beam. From this the wave vector and wavelength can be deduced using the de Broglie equation  $\hbar\mathbf{k} = m\mathbf{v}$  for the momentum of the neutron. (Pynn, 1990)

Our experiments were carried out on D20 at ILL, PEARL at ISIS, and PLANET at J-Parc. The characteristics of these beamlines are given below.

**D20:** The ambient pressure study of our solution was carried out at the high-intensity two axis diffractometer D20 at the high-flux reactor of the Institut Laue-Langevin (ILL in Grenoble, France). The setup is shown in Figure 2.6. We used the (115) reflection of the germanium monochromator for a wavelength of  $1.87 \text{ \AA}$  with average resolution of  $\delta d/d = 3 \cdot 10^{-3}$  and a flux of  $1 \cdot 10^7 \text{ s}^{-1}\text{cm}^{-2}$ . The maximum beam dimensions are 50 mm (height) and 30 mm (width). A number of sample environments are available for low temperature (helium flow orange cryo-

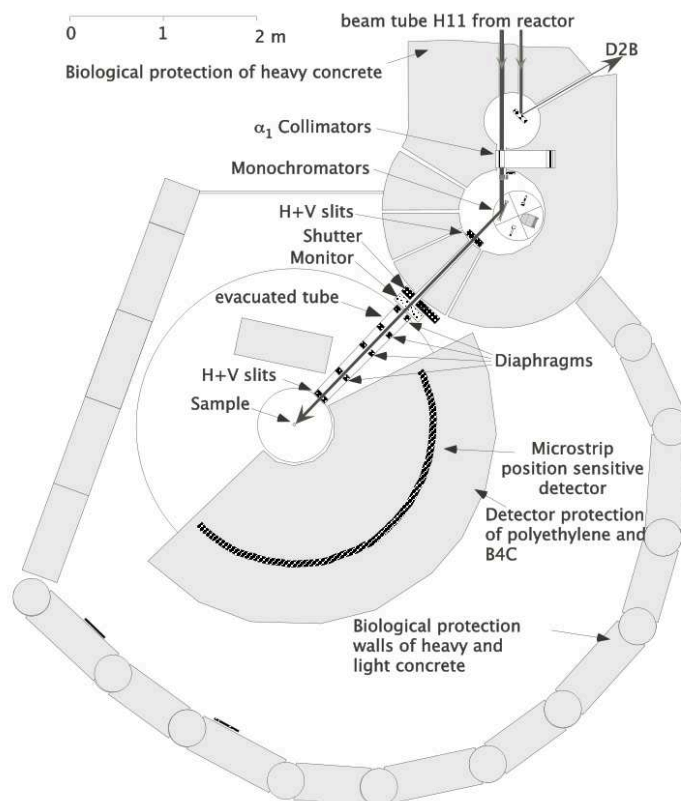


Figure 2.6: Setup of the D20 diffractometer at ILL after Hansen et al. (2008c).

stat) and high pressure (Paris-Edinburgh press) experiments. The detector bank is a one-dimensional position-sensitive detector based on the “microstrip” gas chamber technology. Hansen et al. (2008c), Oed (1988)

**PEARL:** The high-pressure diffraction experiment was carried out at the time-of-flight PEARL beamline on target station 1 of the ISIS Facility pulsed neutron source in Didcot (United Kingdom). The proton beam current is  $150 \mu\text{A}$ . The beam is moderated by 100 K methane ( $\text{CH}_4$ ). For the standard (through-anvil) scattering geometry of the Paris-Edinburgh pressure cell (versions V3, V4 and V7) the main transverse detector bank is used. It is composed of nine modules, each consisting of 78 ZnS scintillator elements. They cover  $81.2^\circ < \theta < 98.8^\circ$ , giving a 20 ms frame  $d$ -spacing range of 0.5 to 4.1 Å, with resolution  $\delta d/d \approx 0.65\%$ . (PEARL, 2015)

**PLANET:** The experiment on LiBr was done on the PLANET high-pressure beamline at the spallation source of J-Parc in Tokai (Japan). The proton beam characteristics are 3 GeV,  $333 \mu\text{A}$ , 25 Hz. The neutron beam arrives from the decoupled moderator. Its pulse width is  $33 \mu\text{s}$ , its flux on the beamline is  $1 \cdot 10^8 \text{s}^{-1}\text{cm}^{-2}$ , and the beam size is 15 mm x 15 mm.  $^3\text{He}$  detectors are used on the  $2\theta$ -range  $90 \pm 11.3^\circ$  with radial collimators. The  $d$  range for a single frame measurement is  $0.2 < d < 4.1 \text{Å}$ , with resolution:  $\delta d/d \approx 0.6\%$ . A Paris Edinburg press VX4 (20 GPa at 300 K), a Mito cell (10 GPa at 77 to 470 K), and ATSUHIME 6 axis

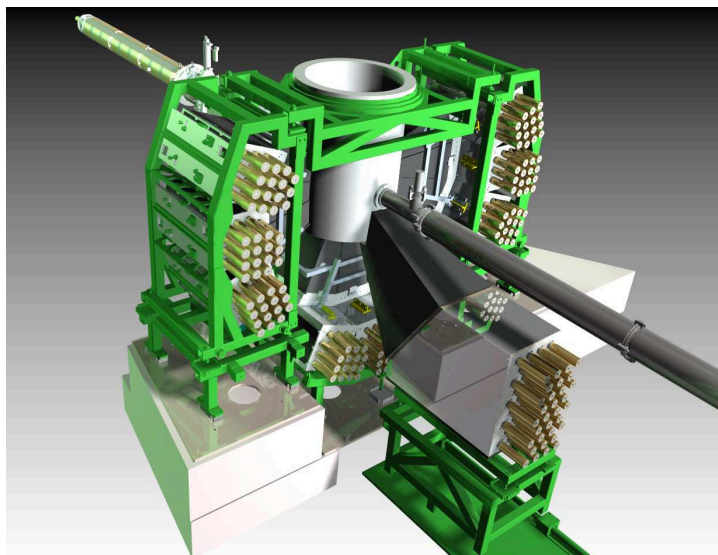


Figure 2.7: Setup of the PEARL diffractometer at ISIS after PEARL (2015).

multi-anvil press (20 GPa, 2000 K) are available as sample environments. (Arima et al., 2010, Komatsu et al., 2013)

#### 2.1.4 Structure refinement

Crystallography seeks to establish the microscopic structure of the material from the measured data. According to equation 2.9 the electron or nuclear density is the inverse Fourier transform of the structure factor. Only intensities are measured in practice, hence the problem lies in the determination of the phase of the particles measured at each peak. This phase is needed in order to perform the inverse Fourier transform. The phase problem can be solved in multiple ways. A mathematical direct method exists for some cases. There are also a number of experimental methods of recovering the phase, (Hendrickson and Ogata, 1997)

One possible method is the Rietveld method which relies on the guess of an *a priori* structural model of the crystal. It proceeds as follows, given the structural model the Bragg peaks are computed and a least squares optimisation procedure seeks the best fit of the sum of the peaks to the intensity at each of the recorded data points. The parameters of the fit are the lattice constants, angles, atomic positions and Debye-Waller factors, peak shape parameters, preferred orientation correction (texture) and background. The order in which these parameters are refined must be chosen with care. This method is implemented in the FullProf, GSAS and other programs for powder diffraction. (Will, 2006)

We used FullProf and its graphical interface WinPlotr to fit the powder data measured on D20 at ILL, because this program was developed to deal with continuous beam data, where the diffractogram is a function of the  $2\theta$  angle (Rodríguez-

Carvajal, 1993, Roisnel and Rodríguez-Carvajal, 2001). GSAS and its graphical interface EXPGUI was used to fit the data obtained on PEARL, because the profile functions it uses are more adapted for TOF data (Larson and Von Dreele, 1994, Toby, 2001).

## 2.2 High pressure devices

### 2.2.1 Historical high pressure techniques

Under pressure atoms explore the repulsive part of their interaction. The volume per atom decreases and electronic orbitals are deformed. Thus high pressure experiments give important information on the interactions of atoms in materials.

The first investigation of the effects of pressure on materials was concerned with compressibility of water and other liquids. Early experiments were performed by the Florentine Academy and John Canton in England in the 1760s. In the 1820s Perkins reached pressures above (2000 kg/cm<sup>2</sup>) by sinking an apparatus into the sea at known depths showed that water is indeed compressible at moderate pressures. Subsequent milestones were the development pumps by Andrews (1861) and Cailletet (1870) and packing techniques by Amagat (1893). The end of the 19th century saw development of further areas of high pressure research. Roentgen and Schneider (1881) investigated the compressibility of dilute solutions and pure NaCl. In Goettingen Tammann (1893, ZS Phys Chem 11.) studied these solutions under pressure, and proposed the idea of equivalent pressure of the solutes in dilute solutions. He observed transitions in ice under pressure (ice II and III). (Bridgman, 1952)

In the first half of the 20<sup>th</sup> century Bridgman developed techniques that eventually could reach as far as 10 GPa. <sup>§</sup> He also applied them to the study of ices.

The main tool for high pressure research today are presses which allow to maintain a static pressure on the sample. However these have a limited range. For pressures of more than megabars other, often destructive techniques, such as laser ablation and explosions which generate shock waves and large dynamic pressures have been used (Nellis, 2006).

### 2.2.2 Paris-Edinburgh cell

The Paris-Edinburgh cell (PEC) or Paris-Edinburgh press is a hydraulic large volume press which can be used with multiple kinds of anvils. It was developed in collaboration by Besson at Université Pierre et Marie Curie and Nelmes at the University

---

<sup>§</sup>P. W. Bridgman was awarded the Nobel prize in physics in 1946 for “for the invention of an apparatus to produce extremely high pressures, and for the discoveries he made therewith in the field of high pressure physics” (Nobel Foundation, 2015).

of Edinburgh in the 1990s with a view to enabling high pressure neutron diffraction in the range of tens of GPa. (Besson et al., 1992) Several models exist which can sustain loads from 50 to 500 tons, sample volumes range from 1 to 100 mm<sup>3</sup>. Depending on its size a press weighs between 10 and 100 kg. Today the presses are available at a number of neutron sources (ILL, ISIS, SNS, SINCQ, to name a few) as well as X-ray sources. They are used for applications ranging from diffraction, to inelastic and quasi-elastic neutron scattering (QENS). The description below is based on Klotz (2012).

**Load frames** There are two types of load frames of PECs. The original four-column V-design is used at pulsed neutron sources for measurements at constant  $2\theta$  diffraction angle. The two-column VX-design with two horizontal openings of 160° is used at continuous neutron sources where a large contiguous  $2\theta$ -range is needed.

The load frames of PECs are made of high tensile aeronautic steel (819AW produced by Aubert & Duval, France). Its yield strength is 1.4 GPa and its tensile strength 1.7 GPa. Forging is beneficial for its strength. Given the production procedure 300°C is the upper limit to which a press can be heated and avoid irreversible reduction of its performance. The material is very reliable even used at temperatures below 4 K, although at it unavoidably embrittles at such low temperatures as all other steels. The only exception is a VX1 press used at ILL which was built entirely of CuBe.

The experiments on our samples at ISIS were performed using a V3 press. Its capacity is 250 tonnes. For which a fluid pressure of 1 kbar generates a force of 100 tonnes on the piston ( $A=100\text{ cm}^2$ ). The anvils are locked in between the hydraulic ram (piston) and the breech (Figure 2.8).

**Anvils:** The mechanics of anvils and gaskets still relies on trial-and-error and empirical recipes, because they operate under severe conditions of pressure and shear, considerable plastic deformation and friction, and most of the parameters are unknown.

In the majority of neutron experiments toroidal anvils with central cups are used. Single toroidal (also called Los Alamos) anvils can go up to 13 GPa and double toroidal anvils go routinely up to 25 GPa although for 2 times smaller sample volume. (Khvostantsev et al., 1977, 2004).

The tensile strength of the anvil material determines the pressure range accessible in an experiment. Cemented Tungsten Carbide (TC) and cubic Boron Nitride (cBN) can sustain loads up to 10 and 15 GPa respectively. To reach pressures above 15 GPa sintered diamond (SD) anvils must be used. The choice of anvil material also depends on the scattering geometry of the experiment and whether contaminant

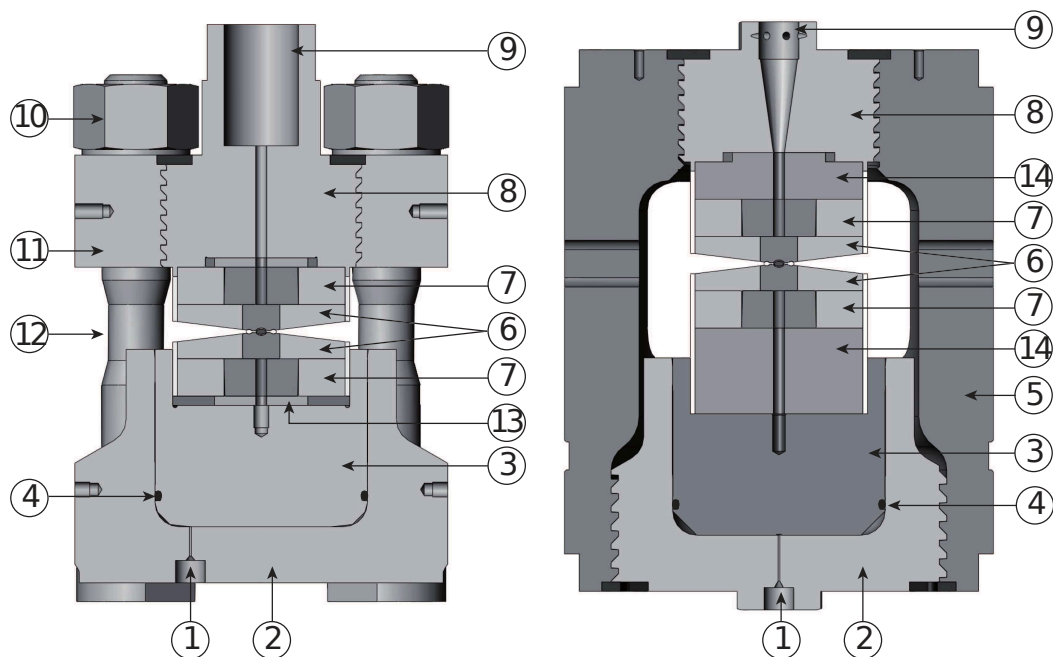


Figure 2.8: Schematic of Paris-Edinburgh cells. Left: V type. Right: VX type. Reproduced from Klotz (2012). 1: Hydraulic fluid inlet, 2: cylinder, 3: piston, 4: O-ring seal, 5: loa-frame, 6: anvils, 7: TC backing plates (seats), 8: breech, 9: front collimator, 10: nut, 11: top platen, 12: tie rod, 13: backing disk, 14: steel spacer.

Bragg peaks can be tolerated. TC and SD are preferable for transverse scattering, with cBN and SD for longitudinal.

**Gaskets:** Gaskets are used to prevent direct contact between anvils and to contain the sample. Care has to be taken as they should not react with the sample material. Two materials are commonly used for gaskets. The first is a null-scattering titanium-zirconium alloy (Marshall and Francis, 2002). The bound coherent scattering lengths are  $-3.44$  fm for Ti and  $+7.16$  fm for Zr, hence the alloy  $\text{Ti}_{0.677}\text{Zr}_{0.323}$  has zero coherent scattering length and does not produce diffraction peaks. This composition lies in the range of miscibility of the two elements. Thus the material is transparent to neutrons and has excellent mechanical properties. Its yield and tensile strength are 600 MPa at 300 K, higher at lower T. (Klotz, 2012).

The second is an alloy of copper and beryllium (CuBe) commonly used for high pressure applications. It contains about 2 mass% of beryllium. However, the solubility of Be in Cu at 300 K is only 0.2 mass%. Thermal treatment allows to dissolve Be at higher temperatures, subsequent quenching and annealing lead to formation of grains of Be. This is an example of precipitation hardening. By adjusting the annealing time the strength can be adjusted in the range of 0.5 to 1.4 GPa. The alloy used for gaskets is alloy 25, which has good mechanical properties, but attenuation of neutrons can be as high as 50% (Klotz, 2012, Table 2.2, p.24).

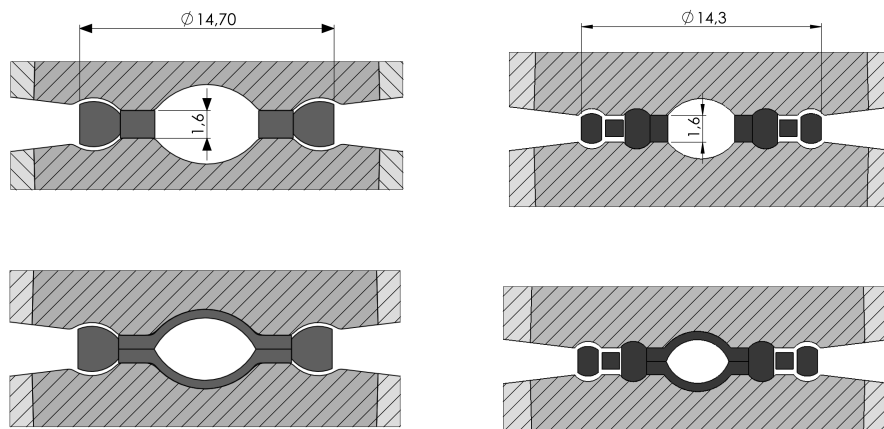


Figure 2.9: Schematic of anvils and gasket assembly for the Paris-Edinburgh cell. Showing washer geometry at the top and encapsulating gasket at the bottom. Left: single toroidal. Right: double toroidal. Reproduced from Klotz (2012).

Three possible gasket geometries are shown in Figure 2.9: simple, toroidal and double-toroidal. Toroidal gaskets were invented by Khvostantsev et al. (1977, 2004), who used them for physical property measurements. They are composed of an inner gasket and a thicker outer ring (shown in Figure 2.9). Above a threshold load of approximately 10 tons for plastic deformation of the inner gasket ( $\sigma_Y \times A$ ), the sample pressure starts to increase. The outer ring is not deformed in the initial stage of compression. Then the sample pressure is roughly linear in load up to 80 tonnes. The inner gasket, 1.6 mm thickness and  $\approx 10$  mm outer diameter, may be a simple washer or opposing cups (encapsulating gasket). The choice depends mainly on the kind of sample. As the sample chamber is about 1.6 mm thick Anvil failure (blow out) typically occurs at 3 to 4 GPa if the anvils are in direct contact with a liquid sample. For experiments on liquids and samples undergoing a phase transition under pressure encapsulating gaskets are preferable, even though the sample volume, and hence the signal, is reduced slightly.

To reach the highest pressures, up to 25 GPa, one has to use double toroidal anvils (linear characteristic). Here a second set of washer and rings enclose the first. The thickness of the second set is chosen smaller so that initial contact is only on the inner set. The pressure load relation is roughly linear up to 200 tonnes and 25 to 30 GPa. Only sintered diamond anvils sustain such high pressures. Nevertheless violent blow out events happen, manifesting by a loud bang and drop in sample pressure of 10-30%. These may damage the anvils. Proper shielding of the vicinity is required.

Moreover reducing the load on the sample carries a high risk of material failure and damage to the anvils, due to a strong hysteresis between upstroke and downstroke (decompression) as for diamond anvil cells (section 2.2.3).

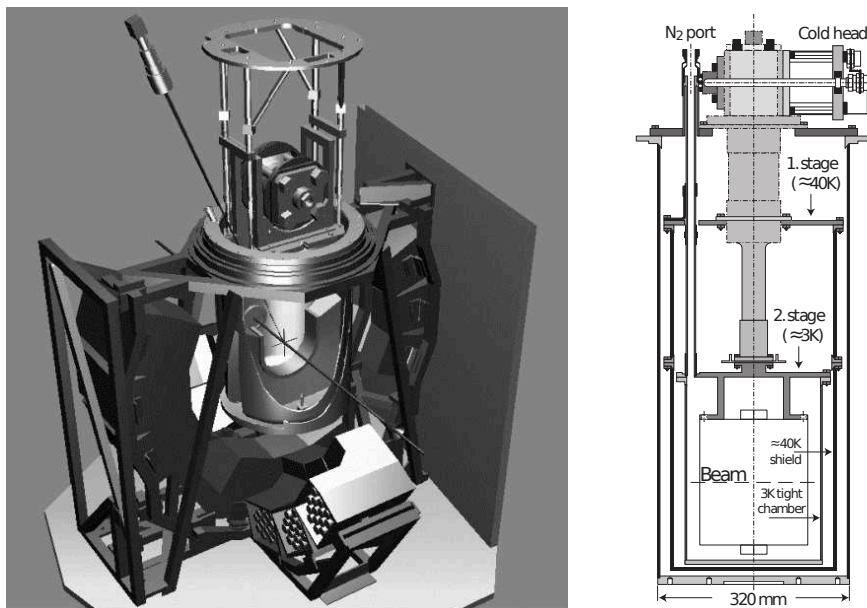


Figure 2.10: Schematic of two cryostat setups. Left: liquid nitrogen cryostat for the Paris-Edinburgh cell used on PEARL at ISIS. Right: helium flow cryostat used on D20 at ILL. Reproduced from Klotz (2012) ch. 11.

**Sample environments:** Temperature control is essential for many experiments. The temperature range accessible with with PECs spans 3.5 to 1000 K. In our experiments on ices a cryostat is required, since amorphous NaCl solution undergoes a transition near 140 K at ambient pressure. A few techniques for heating are mentioned at the end of this paragraph. Both cooling and heating are required in order to control the temperature of the sample in a stable manner.

In cryogenic set up the hydraulic fluid in the ram has to remain liquid. Standard hydraulic oils solidify below 240 K. A 5 : 1 mixture of iso- and n-pentane may be used down to 110K. At low temperatures and high loads only helium can be used, however it is prone to leak. In order to cope with these constraints two kinds cryogenic setups have been elaborated.

In the first approach the cell and sample are cooled together. This allows to reach temperatures down to 77 K in a straightforward way by suspending the press over a liquid nitrogen bath. Cooling the press takes a few hours depending on its mass. The main inconvenience is that helium has to be used as hydraulic fluid. On PEARL cryo-loading of the sample into the anvils is possible in this setup and was used for our experiment (5.2.2). The setup, shown in Figure 2.10, is available on D20 and on PEARL.

In the second approach only the sample and its immediate vicinity are cooled. The load frame of the cell remains is kept at higher temperatures. This can be done for instance by circulating a flow of liquid nitrogen through cooling rings in contact

with the anvils as done on PEARL and PLANET. Such a system allows reactive temperature changes and sealing of the hydraulic system is a lesser problem.

In both cases resistive heating coils are used to warm the body press in the first approach or the anvils directly in the second one. The temperature is measured using thermocouples attached to the anvils as close as possible to the sample while keeping them out of the beam.

The PEC can also be used with helium flow cryostats down to 3.5 K. Cooling takes 6 hours starting with liquid N<sub>2</sub> and subsequent closed cycle refrigeration (CCR). At high pressure the operation is however limited by the freezing of the helium in the hydraulics which can happen at up to 20 K at the highest hydraulic pressures (2 kbar). A more detailed description of cryogenic setups can be found in (Klotz, 2012, ch. 11 pp. 141 to 145). Experiments at these temperatures are of interest for the study of magnetism Bourgeat-Lami et al. (2006).

High temperatures can be reached on the sample by internal or external heating. Up to 500 K the anvils can be heated together with the sample. Zirconia (ZrO<sub>2</sub>) seats are used for thermal insulation between the anvils and the cell. For temperatures up to 200 K internal heating using a resistive graphite tube (furnace) placed inside the pressure chamber may be used to heat only the sample. At these temperatures the sample must be enclosed in a thermally insulating material (such as zirconia) to avoid permanent damage.

**Variants:** The Mito cell is a press that is similar to the PEC. The loading pressure is up to 100 tons and the sample pressure can go up to 10 GPa. The temperature of the sample and anvils can be controlled via a flow of liquid nitrogen below them. This assembly is isolated from the load frame by zirconia and glass-fiber-reinforced plastic. This press was used for an experiment on LiBr solutions at J-Parc. (Komatsu et al., 2013)

### 2.2.3 Diamond anvil cells

Diamond anvil cells (DACs) are the devices achieving the highest static pressures up to 4 Megabar (Bassett, 2009, Dubrovinsky et al., 2012). They were invented in the 1950s by Lawson and Tang (1950). Today they are the cutting edge tool in high-pressure and geophysics. They are used in multiple set-ups such as X-ray and neutron diffraction, Raman and laser heating.

Figure 2.11 shows a schematic representation of a DAC. The sample and gasket are held between two opposing diamonds which are enclosed in the load frame. A detailed discussion of different designs of the load frames of DACs can be found in Eremets (1996). Load frames are typically made of metals and transmit the

external force (load) onto the anvils. Two common set ups use either screws or hydraulic pressure exerted on membranes. Neutron experiments often use larger anvils, requiring loads up to 10 tonnes. Hence larger more massive load frames ( $\approx 5$  kg) are used than for X-ray experiments. Klotz (2012) Different gem-stones can be set into such pressure cells. Currently pressures above 20 GPa can be reached only using diamonds and moissanite (SiC-6H). Sapphire anvils of diameter up to 5 to 15 mm have been used for experiments with large sample volumes up to several GPa. The culet diameter can be up to 3 mm. Furuno et al. (1986) report that 14 GPa were reached with anvils of outer diameter 5 mm. Sapphire is transparent from the ultraviolet to the infrared (144 nm to 6  $\mu\text{m}$ ).

Small diamonds of diameter  $d \leq 2$  mm (0.5 carat) and brilliant cut are used in experiments. Their flat tips (culet) have a diameter a few hundred  $\mu\text{m}$ ,  $\approx 500$   $\mu\text{m}$  for 25 GPa to 150  $\mu\text{m}$  for 120 GPa. (Weck, 2001)

Mechanical and optical properties are decisive parameters when choosing the gem for an experiment. Defects and flaws of the diamond can lead to failure. The density of defects appears to be the main reason why large diamonds are not able to sustain as large loads as expected from scaling. Diamond is transparent to X-rays in the range of 3.5 eV to 8 keV. For neutrons the transmission of diamond is good in the region of 0.4 to 4 Å. For Raman a vibration band at 2450  $\text{cm}^{-1}$  overlaps with a broad peak of heavy water. (Brooker et al., 1989, Solin and Ramdas, 1970)

Natural diamonds of type II are transparent to light from 1 to 15  $\mu\text{m}$  except for a strong absorption band near 5  $\mu\text{m}$ . Synthetic diamonds are used when absorption lines due to impurities are an issue. (Weir et al., 1959)

The sample is enclosed in a metallic gasket in which a hole has been drilled (diameter  $\approx$  tens of  $\mu\text{m}$ ). Rhenium is often used at high temperatures, aluminium and TiZr are used for neutrons. Initial sample volumes of tens of microliters are typical. The hole may shrink during compression. (Eremets, 1996) The highest pressure that can be reached depends on the sample volume, for 0.2  $\text{mm}^3$  the limit appears to be around 5 GPa with currently available gems. To reach pressures above 50 GPa sample volumes smaller than  $10^{-2}$   $\text{mm}^3$  are required. (Klotz, 2012)

Since they are lighter than PECs temperature control is easier. For instance the sample in a DAC for Raman can be quenched quickly by submerging the cell in liquid nitrogen and the experiment can be performed under nitrogen vapour Bove et al. (2015). Temperatures up to several 1000 K can be reached on samples in DACs using laser heating. In such experiments graphitisation may occur, since diamond is metastable below 1100 K at ambient pressure. (Bundy et al., 1961, Ming and Bassett, 1974)

Diamond anvil cells are used to investigate the phase diagram of materials at the highest pressures. The transition at  $\approx 60$  GPa from ice VII to Ice X, the phase

where hydrogen atoms are on average located in the middle of adjacent oxygen atoms, was discovered in Raman experiments using diamond anvil cells (Goncharov et al., 1996). Another example is the search for metallic hydrogen at high pressures (Bassett, 2009, Loubeyre et al., 2004, 2002).

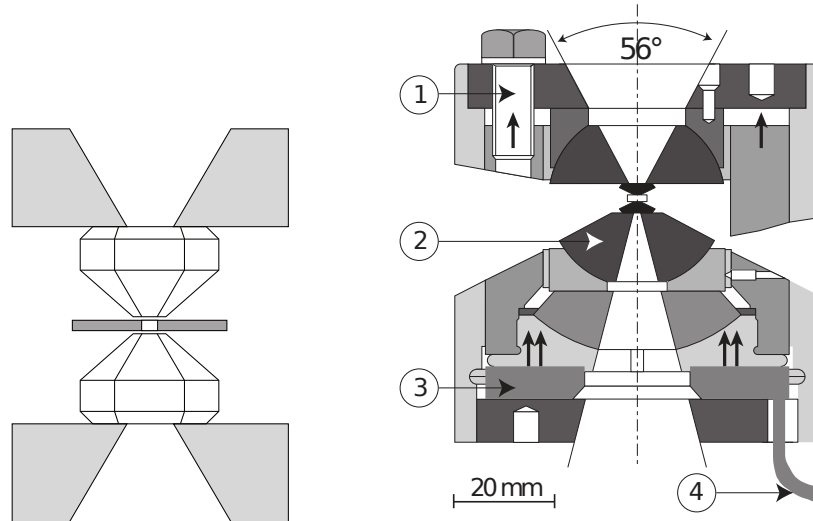


Figure 2.11: Schematic of a conventional diamond anvil cell (left) (Klotz, 2011) and hybrid type 1 for neutron experiments (right) (Goncharenko, 2007).

#### 2.2.4 Pressure gauges

Any material whose equation of state (EoS) or the fluorescence spectrum is known may be used as a pressure marker. The material should have a low bulk modulus for high sensitivity in the GPa range. It should be inert to avoid reaction with the sample or pressure transmitting medium, have a simple structure so that as few peaks as possible overlap with those of the sample. In addition it is preferable to use low absorption and strong scattering. Commonly used pressure markers in X-ray and neutron diffraction are NaCl, lead, MgO, ice VII and ice VIII. For experiments using Raman spectroscopy and on XRD beamlines the fluorescence of ruby is commonly used. With the PEC this fluorescence technique cannot be used because the anvils are opaque. If the sample is crystalline and its EoS is well known it is most convenient to use it as gauge. That is in principle the most accurate method, since the pressure of the marker might be different from that of the sample due to pressure inhomogeneities and the Lamé effect. (Klotz, 2012)

An equation of state is the pressure volume relation  $P(V)$ . It can be determined from experimental compression data and from atomistic calculations. It contains

three parameters: the volume at ambient pressure  $V_0$ , the bulk modulus at ambient pressure  $B_0$  (in GPa) and its pressure derivative  $B'_0$  which is dimensionless.

$$B_0 = -V_0 \left( \frac{\partial p}{\partial V} \right)_0 \quad (2.13)$$

$$B'_0 = \left( \frac{\partial B}{\partial p} \right)_0 \quad (2.14)$$

Three equations of state are commonly used.

The first is the Murnaghan equation of state (M 1):

$$P = \frac{B_0}{B'_0} \left[ \left( \frac{V_0}{V} \right)^{B'_0} - 1 \right] \quad (2.15)$$

The second is the Birch equation of state (B 2):

$$P = \frac{3}{2} B_0 \left[ \left( \frac{V_0}{V} \right)^{7/3} - \left( \frac{V_0}{V} \right)^{5/3} \right] \quad (2.16)$$

The third is the Birch-Murnaghan equation of state (BM 3):

$$P = \frac{3}{2} B_0 \left[ \left( \frac{V_0}{V} \right)^{7/3} - \left( \frac{V_0}{V} \right)^{5/3} \right] \left[ 1 - \frac{3}{4} (4 - B'_0) \left( \left( \frac{V_0}{V} \right)^{2/3} - 1 \right) \right] \quad (2.17)$$

Thus the pressure can be determined by fitting lattice constants of the pressure marker, and calculating the volume  $V$ . (Klotz, 2012)

We use the EoS parametrisations by Fortes et al. (2012) for ice VII, Besson et al. (1994) for ice VIII, and Strässle et al. (2014) for lead. The parameter values are given table 2.2. For NaCl we use the tabulated data by Decker (1971). For the experimental data on the crystallisation behaviour of  $\text{NaCl} \cdot 10.2\text{D}_2\text{O}$  under pressure we use peaks of solid nitrogen ( $\text{N}_2$ ) phases and their transitions to calibrate pressure. (Mills et al., 1975, 1986, Schiferl et al., 1983)

The EOS for  $\text{N}_2$  was fitted to the data of Olinger (1984) for the  $\delta$  phase at higher pressure. According to Olinger the density is continuous at the transition between  $\beta$  and  $\delta$  at 296 K. We have compared the specific volume from this fit to the data available for the  $\beta$  at 2.94 GPa and 300 K ( $V = 65.42 \text{Å}^3$  by Schiferl et al. (1983)), we find 2.91 GPa. The difference of 0.03 GPa is less than the precision of our pressure determination. We also use the volume-temperature phase diagram of  $\text{N}_2$  shown in Figure 2.12, taken from Mills et al. (1986), to determine pressures for the  $\beta$  phase.

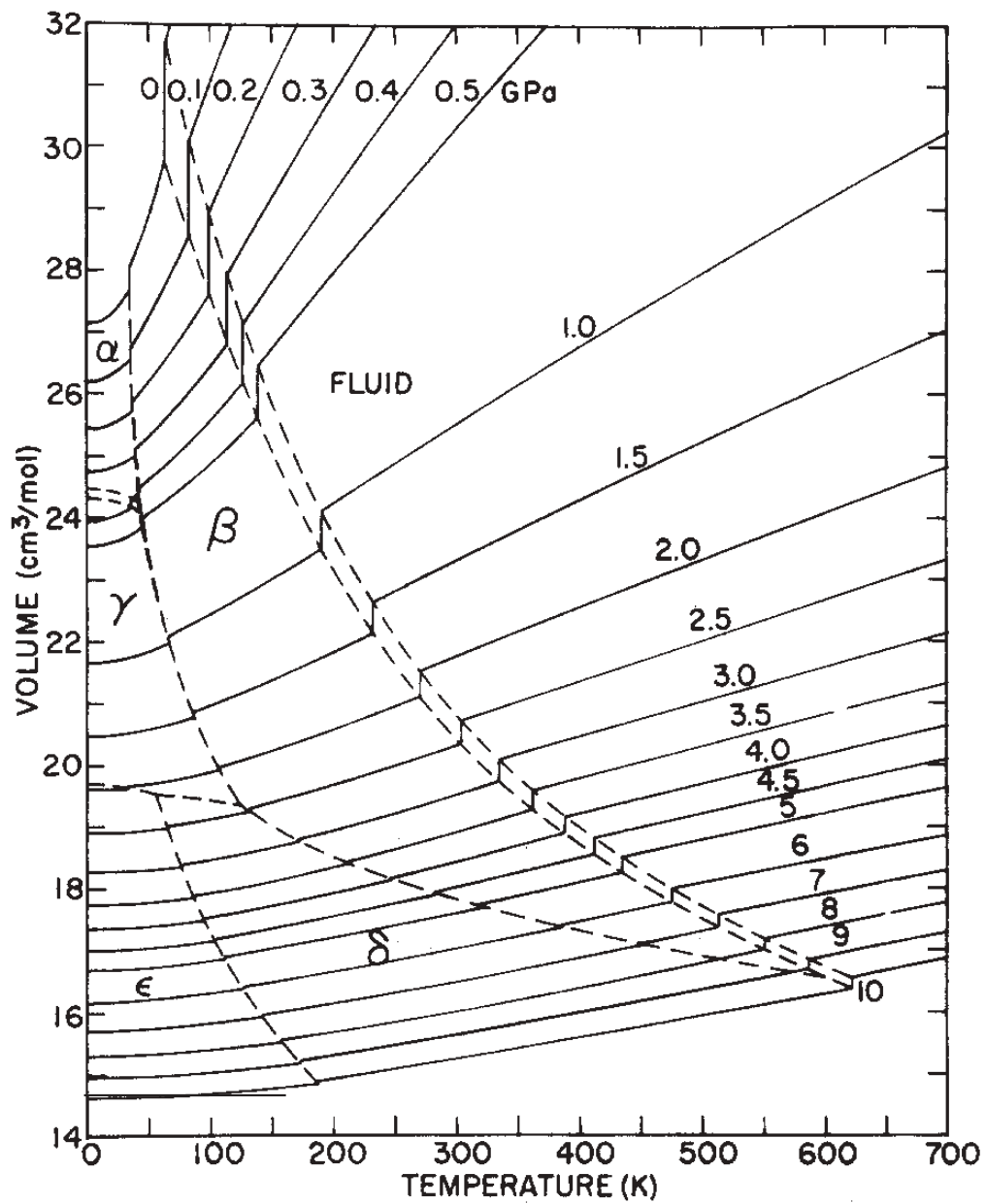


**FIG. 5. Volume-temperature diagram of N<sub>2</sub> incorporating extensive literature data, present results, and unpublished work at high temperature, Ref. 52. Dashed line, phase boundary; solid line, isobar, showing volume discontinuity at transition.**

Figure 2.12: Phase diagram of N<sub>2</sub> with isobars as solid lines and phase boundaries as dashed lines. Taken from Mills et al. (1986)

material (ref.)	EoS	$T$ K	$V_0$ $\text{\AA}^3$	$B_0$ GPa	$B'_0$ –
Pb (Strässle et al., 2014)	BM 3	298	121.2447	41.01(20)	5.72
	BM 3	80	119.1057	46.67(50)	5.50
ice VII (Fortes et al., 2012)	M	300	42.5	13	5.5
$\delta$ N <sub>2</sub> (Olinger, 1984)	BM 3	296	345.29	5.75	4.3
		K	cm <sup>3</sup> /mol	GPa	–
ice VIII (Besson et al., 1994)	BM 3	300	12.45	20.4	4.70
	BM 3	100	12.06	23.6	4.48

Table 2.2: Parameters of the equation of state for lead, ice VII and ice VIII. M stands for the Murnaghan (1944) integrated linear EoS.

# Chapter 3

## Atomistic calculations

We have used atomistic simulations to complement our experimental study of the phases of the NaCl-water system. First, the Density Functional Theory (DFT) and classical potential models for atomic interactions are presented. Second, we discuss the random structure searching and geometry optimisation, which we have used on crystalline salty ice. Third, we present Molecular Dynamics (MD) which allowed us to study systems at finite temperature. For the amorphous solutions we have used classical MD. For the crystalline ices we have used *ab initio* MD. The structural properties of the simulated system are compared to the measured structure factors from diffraction (neutron and X-ray, see chapters 4 and 5). This allowed us to obtain additional information on our system such as correlation functions, and details which cannot be measured directly in experiments, such as angular distribution functions. The methods for the evaluation of these properties are discussed in the last section (3.4) of this chapter.

### 3.1 Atomic interaction models

In this section we present the two paradigms of evaluating the interactions between particles which were used for the simulations performed in this work. Density Functional Theory is presented first. It is the method of choice to obtain highly accurate numerical electronic structure of condensed matter. The draw back of this accuracy is computational complexity, which lead us to use classical interaction models when the computational cost was not warranted for the problem considered. Systems of up to 54 water molecules were studied with DFT methods, while classical interactions were used for systems up to one order of magnitude larger and samples of more than one hundred thousand configurations.

### 3.1.1 Density Functional Theory

Here we briefly present the theory of electronic ground state structure known as Density Functional Theory (DFT). It is an increasingly useful tool for the study of molecules, clusters and solids. We have applied it in our study of the structure of crystalline salty ices.

The electronic ground state of a material is fully determined by the time independent Schrödinger equation for a multiparticle system

$$\mathcal{H}\Psi(\mathbf{r}_1, \dots, \mathbf{r}_N) = E\Psi(\mathbf{r}_1, \dots, \mathbf{r}_N) \quad (3.1)$$

where  $\Psi(\mathbf{r}_1, \dots, \mathbf{r}_N)$  is the many particle wave function. This is an eigenvalue equation for the Hamiltonian operator  $\mathcal{H}$  of a system of  $N \geq 2$  electrons.  $\mathcal{H}$  is the sum of the kinetic energy  $\mathcal{T}$  the external potential  $\mathcal{V}$ , and the Coulombian interaction between electrons  $\mathcal{U}$ .

$$\mathcal{H} = \mathcal{T} + \mathcal{V} + \mathcal{U}, \quad \text{where} \quad \mathcal{T} = \sum_{j=1}^N -\frac{\hbar^2 \nabla_j^2}{2m}, \quad (3.2)$$

$$\mathcal{V} = \sum_{j=1}^N V_{\text{ext}}(\mathbf{r}_j) \quad \text{and} \quad \mathcal{U} = \frac{1}{4\pi\epsilon_0} \sum_{j=1}^N \sum_{k>j}^N \frac{e^2}{\|\mathbf{r}_k - \mathbf{r}_j\|}$$

No analytic solutions of equation (3.1) are known for  $N \geq 2$ . Therefore approximations and methods have been developed to solve the problem numerically.

Hohenberg and Kohn (1964) showed that the electron density

$$n(\mathbf{r}) = \int d\mathbf{r}_2 \cdots \int d\mathbf{r}_N |\Psi(\mathbf{r}, \mathbf{r}_2, \dots, \mathbf{r}_N)|^2 \quad (3.3)$$

uniquely determines the external potential up to an additive constant. Hence it also determines the Hamiltonian and all properties of the system controlled by this operator, including the full  $N$ -particle ground state wave function  $\Psi$ . Considering the energy as a functional of the electron density  $E_v[n]$ , this energy is found to be minimal for the ground state density  $n_0(\mathbf{r})$ . Single particle orbitals  $\phi_j(\mathbf{r})$  obey the Kohn-Sham equation:

$$\left( -\frac{\nabla^2}{2} + V_{\text{ext}}(\mathbf{r}) + \int \frac{n(\mathbf{r}')}{\|\mathbf{r} - \mathbf{r}'\|} d^3r' + V_{XC}[n(\mathbf{r})] \right) \phi_j(\mathbf{r}) = \epsilon_j \phi_j(\mathbf{r}) \quad (3.4)$$

here expressed in atomic units (Kohn and Sham, 1965). The first term is the kinetic energy of a single particle, the second is the external potential, usually the Coulomb potential for the interaction between electrons and nuclei, the third is the mean field electrostatic interaction between electrons. The exchange-correlation poten-

tial  $V_{XC}[n]$  is the functional derivative of exchange-correlation energy  $E_{XC}[n]$  with respect to  $n$ . The exchange-correlation energy is defined by

$$E_{v(\mathbf{r})}[n(\mathbf{r})] = \int n(\mathbf{r}) V(\mathbf{r}) d^3r + T_s[n(\mathbf{r})] + \frac{1}{2} \int \frac{n(\mathbf{r}) n(\mathbf{r}')}{\|\mathbf{r} - \mathbf{r}'\|} d^3r d^3r' + E_{XC}[n(\mathbf{r})] \quad (3.5)$$

with  $T_s[n(\mathbf{r})]$  being the kinetic energy of a noninteracting system with density  $n(\mathbf{r})$ . Thus  $E_{XC}[n]$  accounts for all effects that the other terms miss.

In going from equation (3.1) to (3.4) the dimensionality of the problem reduces from  $3N$  to 3, which is the reason why DFT requires less computational effort than methods such as Hartree-Fock. Even so, this equation must be solved self-consistently like the Hartree equation. Nevertheless, it should be noted that (Kohn et al., 1996)

“Both Thomas-Fermi and Hartree-Fock-Slater methods can be regarded as ancestors of modern DFT. But whereas those theories are intrinsically approximate, modern DFT is in principle exact.”

However the difficulty lies in choosing the functional  $V_{XC}[n]$  to use. We mention two progressive approximations of this functional in common usage: LDA and GGA. The local density approximation (LDA) makes the assumption that the energy  $E_{XC}$  is locally that of a uniform interacting electron gas of density  $n$ . This is valid if the length scale of variations of  $n$  is much larger than the mean particle spacing. It also gives reasonable results for many systems where this assumption is not justified. (Kohn et al., 1996) To go beyond LDA generalised gradient approximations (GGA) take into account the dependence of  $E_{XC}$  on the gradient of the density. (Kohn et al., 1996)

For practical calculations of solutions to equation 3.4 a basis of Hilbert space has to be chosen. For systems with a periodic lattice, a plane-wave basis in reciprocal space is typically chosen, because it permits efficient calculation of the electronic density and energy.

In many cases it is sufficient to calculate only the orbitals for valence electrons. This can be achieved by using an effective static potential (so-called pseudo-potential) which approximates the potential due to the core electrons and can be added to the potential of the nuclei. This approximation allows to increase the computational efficiency significantly. (Goedecker et al., 1996)

If systems of many atoms and long time scales are to be studied DFT becomes cumbersome. Although DFT methods have become much more efficient over the years, the numerical complexity of solving (3.4) self-consistently is still much higher, than coarser methods in which the detail of electronic degrees of freedom is neglected.

### 3.1.2 Classical interaction potentials

For the study of large systems and large sets of systems, we have used classical models of interaction. The evaluation of forces using this method demands less computational time, because it neglects the details of electronic degrees of freedom. This allows to cut the computational cost at the expense of accuracy at the single atom level. For the amorphous solutions we studied, the dynamics of a box containing hundreds of water molecules were simulated for 400 ps at each thermodynamic point along the trajectory. For random structure searching we evaluated the energy of over 100 thousand configurations with classical potentials. Trading accuracy for computational time allowed us to obtain better statistical sampling of the systems that were studied.

In classical MD the forces between the constituents of the system (atoms, molecules, ions or larger objects) are derived from potential functions (also called force fields). These potentials can be tabulated or analytical and may be derived either empirically by fitting experimental observables of the system or from more accurate calculations such as *ab initio* (DFT), coupled cluster or path integral calculations.

#### Water models

Bernal and Fowler presented the first fully atomistic model of water (BF model) in 1933. The atomic structure of H<sub>2</sub>O had been published one year earlier by Mecke and Baumann (1932). The model comprises 4 sites (O, H<sub>1</sub>, H<sub>2</sub> and M) with 3 charges, their positions (total 3 parameters: 2 distances and 1 angle, planar geometry), and the Lennard-Jones parameters  $\sigma$  and  $\varepsilon$ . This is a rigid model where the relative positions of all sites are fixed. This model is the ancestor of a whole class of models (including TIP4P) that treat the water molecule as a collection of electrostatic elements: point charges and dipoles. The interaction energy between two molecules (indexed by  $i$  and  $j$ ) is a combination of a Lennard–Jones dispersion–repulsion interaction between the M sites and Coulomb interaction between the point charges.

$$V_{ij} = 4\varepsilon \left[ \left( \frac{\sigma}{r_{ij}} \right)^{12} - \left( \frac{\sigma}{r_{ij}} \right)^6 \right] + \frac{1}{4\pi\varepsilon_0} \sum_{a \in i} \sum_{b \in j} \frac{q_a q_b}{r_{ab}} \quad (3.6)$$

where  $r_{ab} = \|\mathbf{r}_a - \mathbf{r}_b\|$  is the distance between the sites  $a$  and  $b$  (among O, H<sub>1</sub>, H<sub>2</sub> and M) of two molecules,  $\varepsilon$  is the depth of the potential well, and  $\sigma$  the size of the repulsive core of the Lennard-Jones potential (Jones, 1924). In most water models the cores overlap for hydrogen bonded molecules (Remsing et al., 2011). As the formula is given in SI units, the electrostatic part contains the vacuum permittivity  $\varepsilon_0 \approx 8.854 \times 10^{-12} \text{ F m}^{-1}$ .

Pair potentials account for the interaction between two molecules. Effective pair potentials incorporate the average many-body interactions. In the latter case the self energy of polarisation ought to be included to account for cooperative strengthening of intermolecular bonds such as H-bonds in water (Berendsen et al., 1987). SPC/E is a simple rigid model with point charges and Lennard-Jones term. It is a reparametrisation of the simple point charge (SPC) model which takes into account the self-energy of polarisation, “the energy it *costs* to distort a molecule into its polarized state”, thus improving the agreement with experimental data in the condensed phase (Berendsen et al., 1987). This model was used to generate hydrogen disordered configurations of ice VII.

Figure 3.1 shows the geometry of the SPC/E model and that of the polarisable model by Dang and Chang (1997). We chose the latter because it accurately reproduces the experimental density and diffraction patterns at ambient conditions (300 K,  $\approx 1$  atm). It is a rigid model resembling the BF model. The main differences between the DC and BF models are the position of the negative charge, which sits on the oxygen site (in DC), and of the Lennard-Jones interaction centered on the M site, which is also further away from the oxygen atom in DC compared to BF. The polarisability  $\alpha$  of the water molecule is accounted for by an induced dipole placed at the M site, whose magnitude is proportional to the total electric field at the M site  $\boldsymbol{\mu}_i = \alpha_i \mathbf{E}_i$ . The total interaction energy  $V_{\text{tot}}$  for the Dang and Chang (1997) model is

$$V_{\text{tot}} = V_{ij} + V_{\text{pol}}, \quad (3.7)$$

where  $V_{ij}$  is the pair interaction of the same analytical form as in the Bernal and Fowler model, and  $V_{\text{pol}}$  is the nonadditive polarisation energy

$$V_{\text{pol}} = -\frac{1}{2} \sum_i \boldsymbol{\mu}_i \cdot \mathbf{E}_i^0. \quad (3.8)$$

In the above  $\mathbf{E}_i^0$  is the electric field produced by the fixed charges of the molecule at the atomic site  $i$

$$\mathbf{E}_i^0 = \frac{1}{4\pi\epsilon_0} \sum_{j \neq i} \frac{q_j \mathbf{r}_{ij}}{r_{ij}^3}. \quad (3.9)$$

$$\mathbf{E}_i = \mathbf{E}_i^0 + \sum_{j \neq i} \mathbf{T}_{ij} \cdot \boldsymbol{\mu}_j, \quad (3.10)$$

The total electric field at atom  $i$  is  $\mathbf{E}_i$  and  $\mathbf{T}_{ij}$  is the dipole tensor given in appendix A.4. Induced dipoles are evaluated using a standard iterative self-consistent field procedure with a tolerance of  $10^{-5}$  Debye.



Figure 3.1: Geometries of the Dang and Chang (1997) models (DC, left) and of the SPC/E (Berendsen et al., 1987) water model (right). The size of the repulsive Lennard-Jones core is given by  $\sigma$ . The angle  $\theta \approx 105^\circ$  is close in value to the ideal tetrahedral angle. The OH distance is close to 1 Å. The M site is fictitious and may host the molecular dipole.

The parameters of the models are compared in table 3.1. This model was developed to describe the properties of water at the interface between liquid and gas. It also reproduces the polarisation of water molecules due to ions quite well. For the case of doubly charged cations this has been shown by Masia et al. (2004, 2005).

These models capture the essential features of the structure of water, even though their parametrisations are quite different. The hydrogen bonding network for instance is determined by the short range part of the interaction. The dipolar interactions matter at large scales for many-body effects (Remsing et al., 2011). The experimental value of the dipole for an isolated molecule is 1.84 Debye (Sanger et al., 1932). A calculation by Coulson and Eisenberg (1966) gave 2.6 Debye in ice  $I_h$ . DFT gives 3.0 D for the liquid (Silvestrelli and Parrinello, 1999). Dang and Chang obtain a total dipole moment  $\mu_{\text{tot}} = 2.75 \pm 0.05$  Debye for liquid water at 298 K.

We expect the polarisability of the potential to improve the accuracy of calculations at non ambient conditions. During compression the density of our system increases substantially. For pure water ice at  $\approx -8^\circ\text{C} = 265\text{ K}$  the density doubles from  $0.916\text{ g cm}^3$  at 1 bar (Melinder, 2010) to  $1.86\text{ g cm}^3$  at 4 GPa (Besson et al., 1994). Given that polarization effects were shown to be sizeable in concentrated solutions already at ambient pressure by Tribello et al. (2009), it is to be expected that taking them into account, will improve the accuracy of simulations of the dense solutions under pressure, which we study. To this end we used polarizable potentials for water and ions.

model	OH (Å)	$\widehat{\text{HOH}}$ (°)	OM (Å)	$\sigma$ (Å)	$\varepsilon$ ( kcal/mol )	$q_1$ ( $e$ )	$q_2$ ( $e$ )	$\alpha$ (Å <sup>3</sup> )
DC	0.9572	104.52	0.215	3.2340	0.1825	-1.0380	0.5190	1.444
BF	0.96	105.7	0.15	2.9578	0.3125	-0.98	0.49	0.0
SPC/E	1.0	109.47	0.0	3.166	0.1554	-0.8476	0.4238	0.0

Table 3.1: Parameters of the Dang and Chang (1997) (DC), Bernal and Fowler (1933) (BF) and SPC/E (Berendsen et al., 1987) water models. The formal charges are given in units of elementary charge ( $e = 1.602177 \times 10^{-19}$ ),  $q_1$  is the charge on the oxygen or M site, and  $q_2$  that on the hydrogen sites. Although the parametrisations are different these models capture essential features of the structure of water.

### The Polarizable Ion Model

We used a polarizable ion model (PIM) recently developed by Aguado et al. (2003). This model accounts for many-body electrostatic effects via induced dipoles. It has been shown to work well for ionic solids and melts and high pressure glassy phases of GeO<sub>2</sub> (Marrocchelli et al., 2010, Salanne and Madden, 2011). The interaction energy is the sum of four terms

$$V_{\text{tot}} = V_{\text{charge}} + V_{\text{disp}} + V_{\text{rep}} + V_{\text{pol}}. \quad (3.11)$$

For the electrostatic term the Coulombic potential for point charges, here of formal charges  $-1$  or  $+1$ , is used

$$V_{\text{charge}} = \frac{1}{4\pi\epsilon_0} \sum_i \sum_{j>i} \frac{q_i q_j}{r_{ij}}. \quad (3.12)$$

The dispersion term accounts for dipole-dipole and dipole-quadrupole interaction

$$V_{\text{disp}} = - \sum_i \sum_{j>i} f_6^{ij}(r_{ij}) \frac{C_6^{ij}}{r_{ij}^6} + f_8^{ij}(r_{ij}) \frac{C_8^{ij}}{r_{ij}^8}, \quad (3.13)$$

with short-range corrections described by the Tang and Toennies (1984) damping functions

$$f_n^{ij}(r_{ij}) = 1 - e^{b_D^{ij} r_{ij}} \sum_{k=0}^n \frac{(b_D^{ij} r_{ij})^k}{k!}. \quad (3.14)$$

A decaying exponential is used to model repulsion

$$V_{\text{rep}} = \sum_i \sum_{j>i} A_{ij} e^{-B^{ij} r_{ij}}. \quad (3.15)$$

Many-body electrostatic effects are described by induced dipoles, which are obtained at each MD step by minimizing the polarization energy  $V_{\text{pol}}$  with a tolerance of  $10^{-7}$ .

$$V_{\text{pol}} = \sum_i \left( \frac{1}{2\alpha_i} \|\boldsymbol{\mu}_i\|^2 + \sum_{j>i} \left[ (q^i \mu_\alpha^j g^{ij}(r_{ij}) - q^j \mu_\alpha^i g^{ji}(r_{ij})) T_{ij}^\alpha - \mu_\alpha^i \mu_\beta^j T_{ij}^{\alpha\beta} \right] \right) \quad (3.16)$$

where  $\alpha_i$  is the atomic polarisability, and  $T_{ij}^\alpha, T_{ij}^{\alpha\beta}$  are respectively the dipole and the quadrupole interaction tensors. Latin indices refer to the labels of molecules and the Einstein summation convention is assumed for greek indices which refer to coordinates. The damping function  $g^{ij}(r_{ij})$  is of the Tang-Toennies form

$$g^{ij}(r_{ij}) = 1 - c_{ij} e^{-b_{ij} r_{ij}} \sum_{k=0}^4 \frac{(b_{ij} r_{ij})^k}{k!}. \quad (3.17)$$

The long-range charge-charge, charge-dipole and dipole-dipole terms are computed using a dipolar Ewald sum (Aguado and Madden, 2003, Laino and Hutter, 2008).

The polarisabilities for  $\text{Na}^+$  and  $\text{Cl}^-$  ions are given in Table 3.2. They were obtained from DFT calculations by direct calculation (for polarisabilities and dispersion coefficients) and via force and dipole matching for the remaining parameters. We use the values obtained by Tazi et al. (2012). They are reported in Tables 3.3, 3.4 and 3.5 Good agreement between the calculations and experimental data on first neighbour distances, coordination numbers, hydration free energy differences and diffusion coefficients on aqueous solutions and ionic crystals at ambient pressure and temperature was obtained. (Tazi et al., 2012)

particle	$\text{Li}^+$	$\text{Na}^+$	$\text{Cl}^-$	DC water
$\alpha$ ( $\text{\AA}^3$ )	0.03	0.18	3.50	1.444

Table 3.2: Polarisabilities for ions (Tazi et al., 2012) and the DC water model (Dang and Chang, 1997).

System	$A^{\text{ion-O}}$ (Ha)	$B^{\text{ion-O}}$ ( $\text{\AA}^{-1}$ )	$C_6^{\text{ion-O}}$ (Ha. $\text{\AA}^6$ )	$C_8^{\text{ion-O}}$ (Ha. $\text{\AA}^8$ )	$b_D^{ij}$ ( $\text{\AA}^{-1}$ )	$b^{\text{ion-M}}$ ( $\text{\AA}^{-1}$ )	$c^{\text{ion-M}}$ –
Li <sup>+</sup> -water	24.75	4.094	$1.103 \times 10^{-2}$	$1.037 \times 10^{-2}$	3.000	4.011	2.950
Na <sup>+</sup> -water	711.1	5.061	$1.335 \times 10^{-1}$	$1.572 \times 10^{-1}$	3.000	1.562	$6.839 \times 10^{-1}$

Table 3.3: Parameters for the cation-water interactions. As for water-water interactions, repulsion and dispersion involve the oxygen atom, while electrostatic interactions involve the additional M site. The damping parameter  $b_D$  for the dispersion interaction for the monovalent ions is chosen equal to that of the corresponding cation-chloride interaction (see table 3.5). The electrostatic damping is between the water dipole and cation charge. (Tazi et al., 2012)

System	$A^{\text{ion-O}}$ (Ha)	$B^{\text{ion-O}}$ ( $\text{\AA}^{-1}$ )	$C_6^{\text{ion-O}}$ (Ha. $\text{\AA}^6$ )	$C_8^{\text{ion-O}}$ (Ha. $\text{\AA}^8$ )	$b^{\text{ion-H}}$ ( $\text{\AA}^{-1}$ )	$c^{\text{ion-H}}$ –	$b^{\text{ion-M}}$ ( $\text{\AA}^{-1}$ )	$c^{\text{ion-M}}$ –
Cl-water	499.63	3.560	2.039	4.296	4.794	1.093	2.444	–1.901

Table 3.4: Parameters for the chloride-water interactions. The dipole damping is between the Cl<sup>–</sup> and the water charges. There is no damping of the dispersion. (Tazi et al., 2012)

System	pair $ij$	$A^{ij}$ (Ha)	$B^{ij}$ ( $\text{\AA}^{-1}$ )	$C_6^{ij}$ (Ha. $\text{\AA}^6$ )	$C_8^{ij}$ (Ha. $\text{\AA}^8$ )	$b_D^{ij}$ ( $\text{\AA}^{-1}$ )	$b^{ij}$ ( $\text{\AA}^{-1}$ )	$c^{ij}$ –
LiCl	Li <sup>+</sup> -Li <sup>+</sup>	481.9	6.958	$2.727 \times 10^{-4}$	$5.570 \times 10^{-10}$	6.958	-	-
	Li <sup>+</sup> -Cl <sup>–</sup>	15.56	3.000	$2.369 \times 10^{-2}$	$2.511 \times 10^{-2}$	3.000	3.128	1.433
	Cl <sup>–</sup> -Cl <sup>–</sup>	698.4	3.777	5.951	12.85	1.650	-	-
NaCl	Na <sup>+</sup> -Na <sup>+</sup>	$1.701 \times 10^{-2}$	4.965	$2.914 \times 10^{-2}$	$1.394 \times 10^{-2}$	4.965	-	-
	Na <sup>+</sup> -Cl <sup>–</sup>	44.43	3.000	$2.971 \times 10^{-1}$	$3.785 \times 10^{-1}$	3.000	2.775	2.040
	Cl <sup>–</sup> -Cl <sup>–</sup>	698.4	3.777	5.951	12.85	1.650	-	-

Table 3.5: Parameters for the ion-ion interactions. (Tazi et al., 2012)

## 3.2 Structure searching

For a given model of interatomic interactions, DFT or classical potentials, simulations allow us to study the stability of a system. Minimisation algorithms can be used to find the equilibrium configuration at 0 K. Sampling techniques allow us to study an ensemble of configurations. In our case of ice VII, which exhibits disorder in positions of the hydrogen atoms, we have sampled configurations where ions are randomly substituted for water molecules in a small system containing three unit cells in each direction, to find the configurations of lowest energy. The structure factors and equations of state of configurations thus generated can be compared to our experimental diffraction data.

### 3.2.1 Random search

The oxygen atoms occupy sites in the body centered cubic lattice of ice VII. Hydrogen atoms are distributed randomly, roughly along the direction to the closest O<sup>-</sup>O neighbours, while respecting the ice rules (Jorgensen and Worlton, 1985). The experimental lattice parameter of pure ice VII at  $4.00 \pm 0.01$  GPa is  $3.28646 \pm 0.0003$  Å (Fortes et al., 2012).

We apply a screening method based on Corradini et al. (2014), Coudert (2013), Wilmer et al. (2011) to a  $3 \times 3 \times 3$  supercell of ice VII containing 54 water molecules to obtain a set of candidate structures for salty ice VII. The hydrogen disordered configuration was obtained by performing classical MD using the SPC/E potential in CP2K at 1000 K for 10 ps (timestep 1 fs) on a hydrogen ordered box while keeping the oxygen atoms fixed. Thereafter the box was quenched to 300 K in 40 ps. The ice rules were checked, and the disorder of hydrogens appears clearly in the distribution of projections of the dipoles along the coordinate axes ( $x, y, z$ ) shown in Figure 3.3.

Given that the sizes of sodium and chlorine ions are of the same order as that of water, we expect both of them to substitute water molecules on sites of the ice VII lattice. We proceeded in five steps:

1. First we generated sets of structures by randomly substituting 2 ions ( $R = 52$ ) and 8 ions ( $R = 46/4 = 11.5$ ) for water molecules and evaluating their energies with the PIM in CP2K. This was done for 2000 structures containing 2 ions and about 109 thousand with 8 ions.
2. Then we evaluated the DFT energies of the 1000 configurations of lowest energy using CP2K.
3. We did geometry optimisation on 200 configurations chosen randomly among the set of step 2, keeping the cell vectors fixed. This was done in Quantum Espresso (see section 3.2.2).

4. We performed cell optimisation on 13 cells at 4 GPa.
5. We performed *ab initio* MD on one configuration of pure ice VII, one with 2 ions and one with 8 ions.

A box of pure ice VII and a box with 8 ions substituted are shown in figure Figure 3.2. When choosing 8 sites from 54, ions will have another ion at least in their second neighbour shell.

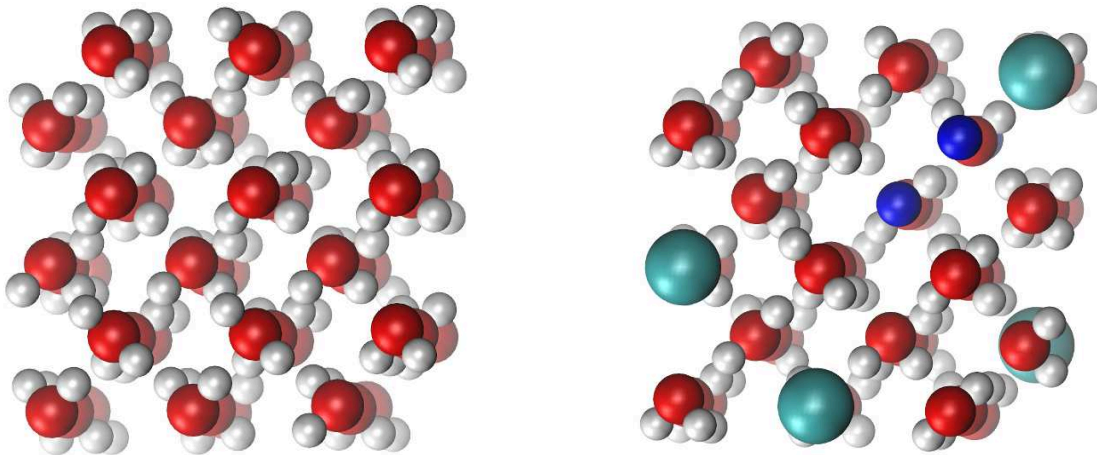


Figure 3.2: Representation of the simulation box of pure ice VII (left) and ice VII with eight ions substituted for water molecules using our screening procedure.

### 3.2.2 Structure optimisation

We have performed steps 3 and 4 using PWscf program which is part of the Quantum Espresso suite (QE) (Giannozzi et al., 2009). The calculations were run on the Occigen cluster at CINES (Montpellier, France). We use the PBE GGA functional Perdew et al. (1996), a plane wave basis set and ultra-soft pseudo-potentials of type RRKJ3 (Rappe et al., 1990). The electronic configurations are O  $2s^2 2p^4$ , H  $1s^1$ , Na<sup>+</sup>  $2s^2 2p^6 3s^1$ , Cl<sup>-</sup>  $2s^2 2p^6 3s^2 3p^6$ .

During geometry optimisation (step 3) internal degrees of freedom, including atomic positions, are moved by the BFGS algorithm until a minimum of the energy is found (Billeter et al., 2003, Fletcher, 1987). The energy convergence threshold was  $10^{-6}$  for most boxes, for some which did not converge it was relaxed to  $10^{-4}$ . A few configurations did not converge at all and were discarded. Step 3 was performed for approximately 200 boxes of ice VII with 8 ions and cell parameters of 9.9485 and 10.0544 Å. For these values the pressure averages over the set of boxes are 4 and 5 GPa respectively. The enthalpies and enthalpies of formation were calculated.

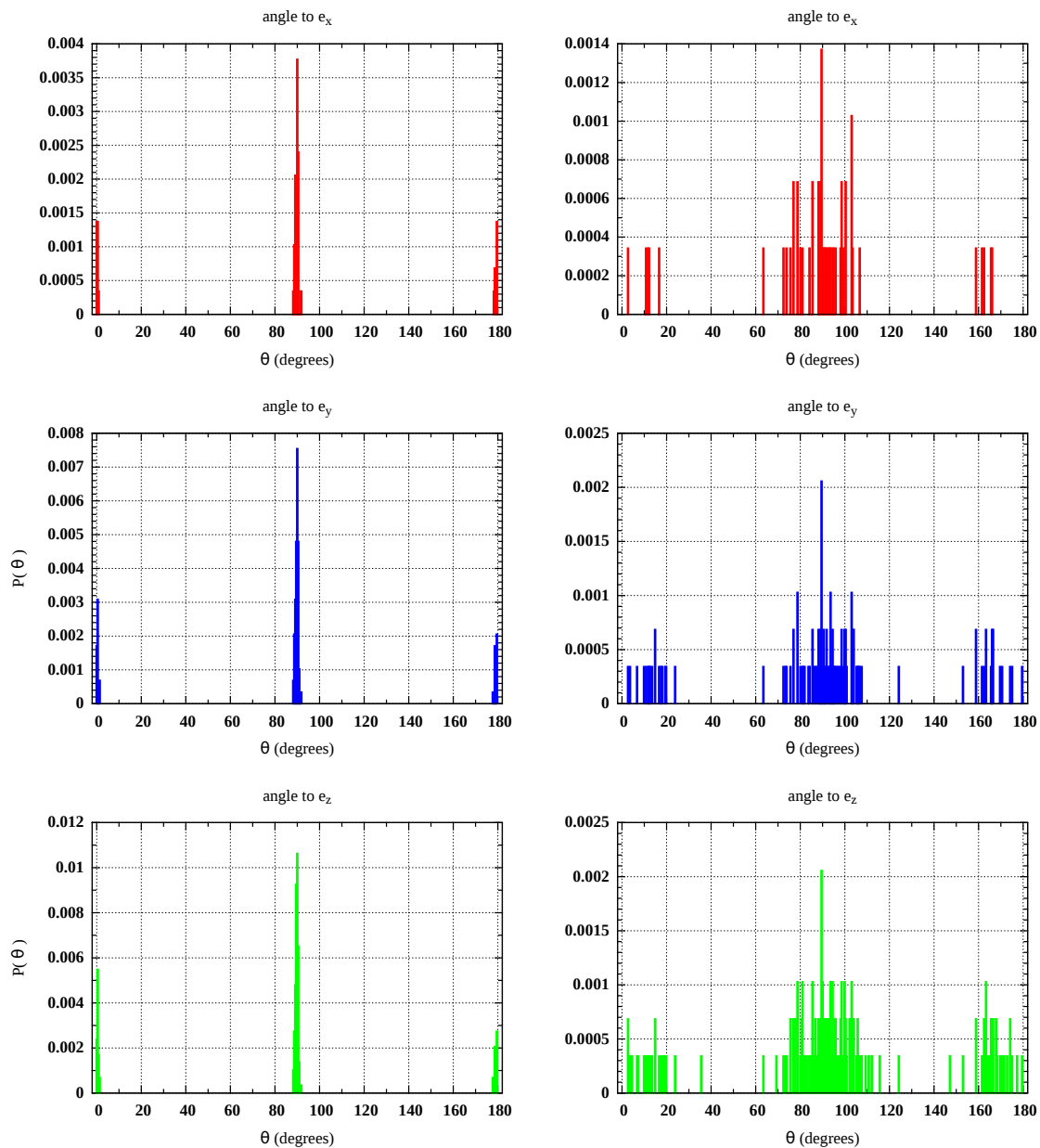


Figure 3.3: Distributions of the projections of the water molecules' dipoles along the coordinate axes ( $x, y, z$ ) for a hydrogen ordered box and a hydrogen disordered box of ice VII. Left: In the ordered box the distribution is very narrow in the directions orthogonal and parallel to the axes ( $\approx \pm 4^\circ$ ). Right: In the hydrogen disordered box the distribution is broader ( $\approx \pm 20^\circ$ ). The hydrogen disordered configuration was obtained by annealing the ordered box to 1000 K and quenching it back to 300 K, while fixing the oxygens.

During cell optimisation (step 4) the cell parameters are allowed to change in addition to the internal degrees of freedom. The structures were optimised at 4 GPa. The program was instructed to keep the cell cubic, however small distortions occurred (of the order of 1%). Therefore another geometry optimisation using the cubic root of the obtained volume as cell parameter was performed subsequently, in order to obtain a cubic structure. Step 4 was performed for 13 boxes and on pure ice VII.

An equation of state at 0 K was obtained using geometry optimisation with lattice parameters in the range of 3.0 to 3.7 Å ( $3a$  ranging from 17.0 to 21.0 Bohr) for one pure ice and one salty ice VII box. A step of 0.2 Bohr was chosen between 17.0 and 19.0 Bohr above which a value of 0.5 Bohr was used. The pressure retained is that of the last optimisation cycle.

### 3.3 Molecular Dynamics

Molecular Dynamics (MD) programs calculate numerical solutions for the motion of a system containing  $N$  particles (many body problem) and thereby enable us to sample the properties of our system at finite temperature. Since pure ice VII is the stable polymorph only at temperatures above 270 K, we use MD to probe the structures obtained at 0 K from the structure searching. We also used MD to probe the glassy state of our solution.

The dynamics of each particle ( $1 \leq i \leq N$ ) is supposed to follow Newton's equations of motion

$$\mathbf{F}_i = m_i \ddot{\mathbf{r}}_i, \quad (3.18)$$

where  $m_i$  is the mass and  $\mathbf{r}_i$  are the spatial coordinates of the particle, the double dots stand for the second time derivative. The usual approach is to integrate these differential equations using the Verlet (1967) algorithm with a fixed timestep  $\delta t$ . It requires a set of initial positions and masses of the particles, as well as a model for the interaction between particles. Forces are evaluated once per iteration, and this is the most computationally intensive step. At each step the (local) error is of order  $\delta t^2$  in the velocities and  $\delta t^4$  in the positions, this is sufficient for the conservation of the global energy given by the Hamiltonian of the system

$$H(\mathbf{r}, \mathbf{p}) = \sum_{k=1}^N \frac{\|\mathbf{p}_k\|^2}{2m_k} + V(\mathbf{r}_k). \quad (3.19)$$

The first term is the kinetic energy of the nuclei. The second term is the potential energy of the system, which can include many body terms, such as three-body interactions in our polarisable models, but it is often truncated at the level of two

body interactions  $v(\mathbf{r}_k, \mathbf{r}_l)$ . The  $\mathbf{r}_k$  are the coordinates of the system, and the  $\mathbf{p}_k$  are the momenta ;  $\mathbf{r}$  stands for the collection of all  $(\mathbf{r}_k)_{1 \leq k \leq N}$  (Allen and Tildesley, 1987). When the dynamics given above are ergodic, they sample the micro-canonical ensemble ( $NVE$ ), in which the number of particles  $N$ , the system volume  $V$  and the energy  $E$  are conserved.

The temperature  $T$  of the system can be controlled using a thermostat to sample the canonical ensemble ( $NVT$ ). We used a chain of Nosé-Hoover thermostats, which improves the techniques of Nosé (1984) and Hoover (1985), that are not ergodic for small and stiff systems (Martyna et al., 1992). Along the same line it is possible to use a barostat to control the pressure, and sample the  $NPT$  ensemble directly (Martyna et al., 1994). However, we chose to work in  $NVT$  and to control the pressure by changing the volume of the simulation box manually.

Classical MD is a means of studying the motion of the nuclei. Given that nuclei have a mass over thousand times larger than the electrons, the dynamics of the latter are much faster. Hence the electronic structure is very well approximated by the ground state and follows the motion of the nuclei adiabatically. This is known as the adiabatic or Born-Oppenheimer approximation (Born and Oppenheimer, 1927), and may be applied at different levels of the description of electronic degrees of freedom. For the polarisable potentials, which we use for ions and water molecules, the multipoles associated with each particle represent fluctuating electronic properties. These multipoles are relaxed at each time step in accordance with the assumption of adiabaticity (Aguado et al., 2003, Dang and Chang, 1997). This approximation is also applied in *ab initio* MD which is based on Density Functional Theory (section 3.1.1).

### 3.3.1 Simulation of the NaCl-water system

The simulations were performed on a cubic box containing 510 water molecules and 51 ion pairs ( $\text{Na}^+$  and  $\text{Cl}^-$ ). Hence  $R = 10$ . We used the CP2K simulation package (version 2.2.141) (developers group, 2012). For this system size simulating 200 thousand time steps with polarisable potentials, took  $\approx 24$  hours on 32 cores of the Gnome cluster at UPMC. Tests with SPC/E showed that with simpler potentials the simulation time can be reduced by a factor 40. Systems of larger sizes give more reliable data for the disordered structure of vitreous materials. Considering the accuracy versus time cost trade off, we chose to limit the system size.

To sample the canonical ensemble we used a chain of three Nosé-Hoover thermostats, with a time constant of 1 ps. The simulation cell was initially equilibrated in the liquid phase at a temperature of 300 K and experimental density. It was subsequently quenched to 80 K by successive steps of 20 K. A compression was then

made, by reducing the box size from 25.725 to 22.7 Å in steps of 0.2 Å. The final pressure was 7.2 GPa. We annealed the system to 140 K at 4 GPa, by increasing the temperature in a single step. The thermodynamic trajectories correspond to those of the experiment shown in Figure 1.8 (chapter 5). At each point the system was simulated for 400 ps, where a 1 fs time step was used in the liquid (above 160 K) and 2 fs in the amorphous domain.

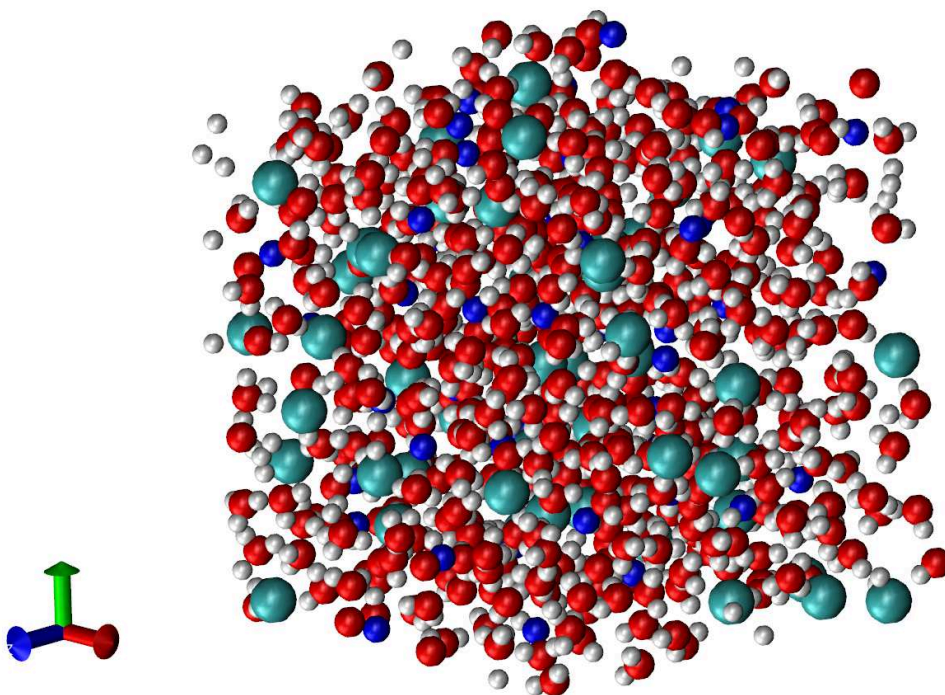


Figure 3.4: Representation of the simulation box of  $\text{NaCl} \cdot 10.2\text{D}_2\text{O}$  at 0 GPa. It contains 510 water molecules and 51 ion pairs. The figure was produced using VMD Humphrey et al. (1996). Oxygen atoms are in red, hydrogen in white, sodium ions in blue and chloride in turquoise.

### 3.3.2 *Ab initio* Molecular Dynamics

Car and Parrinello (1985) proposed a method of *ab initio* molecular dynamics (AIMD). The wave function is propagated simultaneously to the motion of the nuclei along the trajectory. While both dynamics are classical, DFT is used to evaluate electronic structure, and forces can be obtained by applying the Hellmann-Feynman theorem (Feynman, 1939, Hellman, 1939). This method is efficient and provides access to the dynamics of systems containing hundreds of atoms with reasonable computational effort on modern machines.

Three boxes of pure and salty ice VII were run with this method on the Gnome cluster. The supercell contains 162 atoms for pure ice VII, 158 when two ions

are substituted and 146 when 8 ions are substituted. The calculations have been performed using the Quickstep algorithm in CP2K (VandeVondele et al., 2005). We used GGA-BLYP exchange-correlation functional (Becke, 1988, Lee et al., 1988) with DZVP-MOLOPT-SR-GTH basis set (VandeVondele and Hutter, 2007) and GTH-BLYP pseudo potentials (Goedecker et al., 1996). The electronic configurations are the same as given above. Dispersive interactions were added through the use of the DFT-D3 correction with a cutoff radius of 30 Å (Grimme et al., 2010). The simulations were conducted in the  $NVT$  ensemble with a chain of three Nosé-Hoover thermostats for a target temperature of 300 K. Simulations took 24 hours for  $\approx 7000$  time steps of 0.1 fs on 32 cores of the Gnome cluster. The trajectory for each system is 10 ps long.

## 3.4 Evaluating structural properties

### 3.4.1 Thermodynamic sampling

The sets of configurations obtained from random structure searching and the trajectories obtained from finite temperature MD can be used to compute structural properties of the system. For equilibrium systems, all macroscopic structural quantities (density, enthalpy, chemical potential, . . .), as well as the radial distribution functions, structure factors, diffusion coefficient and shear viscosity are state functions; their values depend on the thermodynamic state, not the instantaneous microscopic state of the system (Allen and Tildesley, 1987). Here we suppose that our vitreous and crystalline systems are sufficiently well equilibrated that we can use this approach to sample phase space. We evaluate the average value of an observable  $\mathcal{A}$  as

$$\mathcal{A}_{\text{obs}} = \langle \mathcal{A} \rangle = \frac{1}{M} \sum_{\tau=1}^M \mathcal{A}(\Gamma(\tau)) \quad (3.20)$$

where  $\Gamma(\tau)$  is the point in phase space,  $\tau$  is the index of the step along the trajectory or its index in the case of random sampling of configurations,  $M$  being the number of configurations. Fluctuations are related to thermodynamic derivatives, such as the isothermal compressibility. They can be estimated as the root mean square deviation  $\sigma(\mathcal{A})$  given by

$$\sigma^2(\mathcal{A}) = \langle \mathcal{A}^2 \rangle - \langle \mathcal{A} \rangle^2 \quad (3.21)$$

We have evaluated them to check that they have converged to the expected small values, this guarantees that the average quantities obtained are meaningful.

We calculated time averages and fluctuations of the energy, pressure, temperature along the trajectories, for ergodic systems these tend towards the ensemble averages for long sampling times. The instantaneous enthalpy of a configuration is

$$H = U + pV = E_{\text{kin}} + E_{\text{pot}} + pV \quad (3.22)$$

where  $E_{\text{pot}}$  is the potential energy,  $E_{\text{kin}}$  is the kinetic energy of the particles in the box,  $p$  is the pressure and  $V$  is the volume of the box.

We computed the mixing enthalpies of our system of substitutional ice VII. Let us consider a box of finite volume  $V$  which contains  $N$  particles on the sites of a regular lattice. This is the usual representation of a unit cell of a crystal. The enthalpy  $h$  per site of the lattice is  $h = H/N$ . For a binary system which can decompose into two distinct phases  $A$  and  $B$ , the enthalpy of mixing is

$$\Delta h = h - h_{\text{sep}} \quad (3.23)$$

$$h_{\text{sep}} = \frac{\alpha}{N} h_A + \frac{\beta}{N} h_B \quad (3.24)$$

where  $\alpha$  is the number of particles that would form phase  $A$  and  $h_A$  is the enthalpy per site in the pure phase (respectively  $\beta$  and  $h_B$  pertaining to phase  $B$ ).

### 3.4.2 Microscopic structure

The radial distribution functions (RDFs), noted  $g_{AB}(r)$ , where  $A$  and  $B$  are two (possibly identical) chemical species, provide the probability of finding one specimen of species  $B$  at a distance  $r$  from a specimen of species  $A$  (Marshall and Lovesey, 1971).

$$g_{AB}(r) = \frac{1}{N_A \rho_B} \left\langle \sum_{i \in A} \sum_{j \in B} \frac{\delta(r_{ij} - r)}{4\pi r^2} \right\rangle \quad (3.25)$$

where  $N_A$  is the total number of atoms of kind  $A$  in the box,  $\rho_B = N_B/V$  is the density of kind  $B$ , and the average is taken over the set of configuration in the trajectory. The distances between atoms  $i$  and  $j$  are calculated by an algorithm which finds the shortest distance  $d_{ij}$  in the minimum image convention for given periodic boundary conditions. In our system, which contains 4 species, 10 different RDFs can be calculated. The most relevant ones are  $g_{\text{OO}}$ ,  $g_{\text{ONa}}$ ,  $g_{\text{NaCl}}$ . Changes in the water structure can be seen in  $g_{\text{OO}}$ . The hydration of sodium ions is probed by  $g_{\text{ONa}}$  and  $g_{\text{NaCl}}$  characterizes ion pairing.

Coordination numbers of atoms of species  $B$  in a given shell of neighbours around species  $A$  are calculated by integrating  $g_{AB}$  over the  $r$  range of the corresponding

O–O		Cl–H	
pressure (GPa)	$r_2$ (Å)	pressure (GPa)	$r_2$ (Å)
0.0	3.075	0.0	2.9
0.4 to 1.0	3.025	0.4	2.8
2.0 to 2.4	2.975	1.0 to 2.0	2.75
3.0 to 4.5	2.925	2.4 to 5.0	2.65
5.0 to 7.2	2.875	5.4 to 7.2	2.6

Table 3.6: The cut-off radii  $r_2$  for O–O and Cl–H pairs used to calculate coordination numbers, decrease as pressure increases.

shell:

$$N_{AB}(r) = 4\pi\rho_B \int_{r_1}^{r_2} dr r^2 g_{AB}(r). \quad (3.26)$$

A shell is therefore defined by two cut-off distances  $r_1$  and  $r_2$ . For the first neighbour shell,  $r_1$  is set to 0 and  $r_2$  is usually taken as the first minimum of the corresponding RDF. For Na–O pairs the choice, 3.1 Å, was straightforward as the position of the minimum does not change with pressure. For Na–Cl pairs 3.3 Å was chosen for the whole range of pressures as the best compromise since the minimum is affected non monotonically by pressure for  $p > 3$  GPa. For O–O and Cl–H pairs this minimum shifts to smaller distances when pressure increases and the values chosen for  $r_2$  are given in Table 3.6. The average coordination numbers  $N_{\text{OO}}$ , ( $N_{\text{NaO}} + N_{\text{NaCl}}$ ), ( $N_{\text{ClNa}} + N_{\text{ClH}}$ ), as well as the coordination distributions have been calculated for the compression at 80 K.

The distributions of the ten nearest neighbours of Na are obtained by sorting the neighbours list by distance and then binning their distance to the central ion.

The angular distribution function  $P(\theta)$  of O–O–O in the first shell was computed as

$$P(\theta) = \frac{1}{N_{\text{angles}}} \times \left\langle \sum_{\substack{i \in A \\ j \in A \setminus \{i\} \\ k \in A \setminus \{i, j\}}} \delta(r_{ij} \leq r_2) \delta(r_{ik} \leq r_2) \delta(\theta_{jik} - \theta) \right\rangle \quad (3.27)$$

where  $r_{ij}$  is the distance between two oxygen atoms and  $\theta_{jik}$  is the angle at atom  $i$  between atoms  $j$  and  $k$ . The distribution of the angles of octahedra centered on  $\text{Na}^+$  is calculated in a similar way, by selecting the  $\text{Na}^+$  ions which are exactly six fold coordinated and their first six neighbours (O or Cl).

The Ashcroft-Langreth partial structure factors  $S_{ij}^{AL}(q)$  and the total structure

factor  $S(q)$  are given by

$$S_{ij}^{AL}(q) = 1 + 4\pi(c_i c_j)^{\frac{1}{2}} \int_0^\infty dr r^2 \frac{\sin(qr)}{qr} (g_{ij}(r) - 1) \quad (3.28)$$

$$S(q) = \sum_{i,j} b_i b_j (c_i c_j)^{\frac{1}{2}} S_{ij}^{AL}(q), \quad (3.29)$$

where  $c_i$  is the concentration of species  $i$  and  $b_i$  its scattering length. The total structure factors were computed using the ISAACS program following equations (3.28) and (3.29). (Le Roux and Petkov, 2010)

The total dipole of water in the system is

$$\boldsymbol{\mu} = \sum_{i=1}^{N_w} \boldsymbol{\mu}_i. \quad (3.30)$$

where  $N_w$  is the number of water molecules in the box.

The average distance for an unlike pair X, Y of nuclei, such as NaCl, is given by

$$d_{XY} = \frac{1}{N_X N_Y} \sum_{i \in X} \sum_{j \in Y} \|\mathbf{r}_i - \mathbf{r}_j\| \quad (3.31)$$

where  $N_X$  and  $N_Y$  are the number of ions of each species in the box. Our systems respect charge neutrality, hence  $N_{\text{Na}} = N_{\text{Cl}}$ . We have studied boxes for which  $N_{\text{Na}} = 0, 1, 4$ . For like ions and the average ion distance is calculated by taking only the terms for which  $i \neq j$ , thus

$$d_{\text{ions}} = \frac{1}{N(N-1)} \sum_{1 \leq i \neq j \leq N} \|\mathbf{r}_i - \mathbf{r}_j\| \quad (3.32)$$

where  $N$  is either  $N_X$ , or  $N_Y$ , or the total number of ions  $N_{\text{Na}} + N_{\text{Cl}}$ .

We have calculated the distribution of dipoles and distances for the set of boxes generated by the random structure search and compared it to the energy and enthalpy trends (see section 5.2.3).



# Chapter 4

## Producing aqueous glasses

Water crystallizes into ice  $I_h$  when cooled below the freezing point at ambient pressure. Freezing involves formation of a critical crystal nucleus (nucleation) and its growth. The nucleus may be formed by homogeneous or heterogeneous nucleation. Homogeneous nucleation is the formation of nuclei without preferential nucleation sites. It occurs spontaneously at  $T_{\text{hom}} = 235 \text{ K} = -38 \text{ }^\circ\text{C}$  at 1 atm. If minor impurities are present, heterogeneous nucleation occurs on their surface and water freezes at higher temperatures (Koop, 2015). Since water cannot be supercooled below the homogeneous nucleation temperature, rapid cooling is necessary to prevent ice nucleation and obtain amorphous material. A number of (hyper-)quenching techniques have been employed to produce amorphous water.

For binary solutions the situation is rather different. The composition/temperature phase diagram of solutions (Figures 4.1 and 4.2), be they of metals\* or of salts in water, usually exhibits a eutectic point (E), which is the point of lowest temperature at which the liquid is stable. If nucleation is slow, it is possible to supercool the liquid below this point. For aqueous LiCl solutions this can be achieved by cooling bulk quantities at moderate rates of 20 K per hour. By cooling the system down to 80 K a glassy state can be obtained. For other systems higher cooling rates are typically required. The glass transition of a number of aqueous electrolytic solutions has been studied in detail by Angell and Sore (1970, 1980), Prével et al. (1995). For NaCl such slow cooling leads to crystallisation and phase separation on short time scales even at the eutectic composition.<sup>†</sup> However the cooling rate required to amorphise the solution is lowest near the eutectic concentration.

---

\*Crystalline metallic alloys are called solid solutions. (Inczedy et al., 1998)

<sup>†</sup>There is a claim by Warkentin et al. (2013) that concentrated aqueous solutions, including those of sodium chloride, can be amorphised by cooling rates as low as  $60 \text{ K s}^{-1}$ . However amorphisation was not determined by diffraction, but by visual inspection of the clarity of the droplet (Berejnov et al., 2006)

In this chapter, the techniques used to amorphise liquids and aqueous solutions are presented first. Then the preparation and the properties of the solutions, which we have studied, are described. Finally, their ambient pressure structure and its transformation upon annealing are discussed.

## 4.1 Quenching techniques

### 4.1.1 Quenching and amorphising solutions

Several techniques for vitrifying pure water and solutions have been developed. The first one was vapour deposition which leads to the formation of a low density amorphous form called amorphous solid water (ASW) (Burton and Oliver, 1935). This process is expected to occur in the mesosphere ( $\approx 50$  to 100 km), the coldest layer of the atmosphere, where temperatures can drop below 130 K (Koop, 2015, Nič et al., 2009). It is also common in outer space, where water is often observed in an amorphous form (Jenniskens and Blake, 1996).

Pure water can also be amorphised by compression (to  $\approx 1$  GPa) of ice  $I_h$  at low temperature (Mishima et al., 1984, Tse et al., 1999). The unannealed phase thus obtained is a strained and unrelaxed high density amorphous (uHDA) form of solid water (Loerting et al., 2011). This can be relaxed by annealing to  $\approx 125$  K under pressure yielding the expanded HDA (eHDA) form. Whereas uHDA transforms to LDA upon annealing at ambient pressure to about 115 K (Nelmes et al., 2006, Winkel et al., 2011b).

For solutions the two aforementioned techniques encounter difficulties. The first one, vapour deposition or epitaxy, is a rather slow technique and it cannot be used easily to form highly concentrated amorphous solutions. Once phase separation of a solution reaches macroscopic scales, for instance by crystallisation of ice  $I_h$  from the solution, mixing times become very long compared to the time scale of most experiments, because the diffusion of ions in the glass is very slow at low temperatures. Since ice  $I_h$  expels salts upon crystallisation, a homogeneous crystalline precursor at ambient pressure cannot be produced (Ruiz et al., 2014).

Two techniques which are suitable to amorphise solutions are jet freezing of emulsions and splat-cooling. Brüggeller and Mayer (1980) have shown that pure water and dilute solutions can be amorphised by jet freezing droplet in emulsion. For the emulsion a liquid cryomedium such as n-heptane has to be used. This method has been used for solutions of LiCl (Mishima, 2011). The main inconvenience is the difficulty to separate the sample from the cryomedium and to avoid crystallisation of the sample droplets in the process.

The technique used in this work is similar to the splat-cooling technique, which

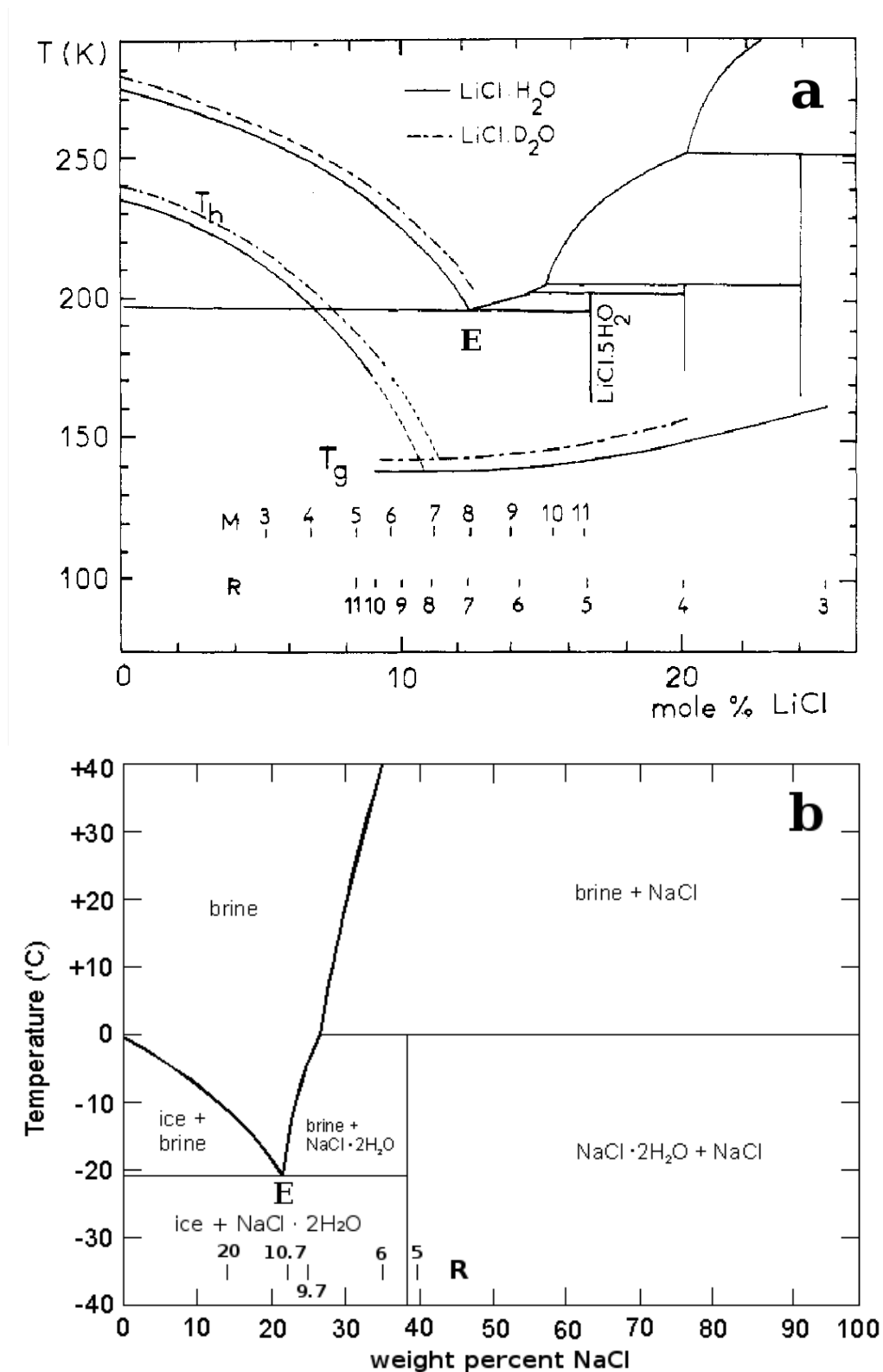


Figure 4.1: Temperature composition binary phase diagrams of LiCl and NaCl solutions in water at ambient pressure. (a) LiCl-H<sub>2</sub>O and LiCl-D<sub>2</sub>O from Elarby-Aouizerat et al. (1983),  $T_h$  indicates the line along which homogeneous nucleation occurs  $T_g$  the glass transition. The other lines are phase boundaries. (b) Diagram of NaCl-H<sub>2</sub>O from Muldrew and McGann (1997) after Landolt et al. (1964), with an added scale for the molar ratio  $R$ . The stable eutectic point for NaCl-H<sub>2</sub>O is at -21°C and 23.3 weight percent ( $R = 10.7$ ). For LiCl-H<sub>2</sub>O it is at  $R = 7$  and -75°C.

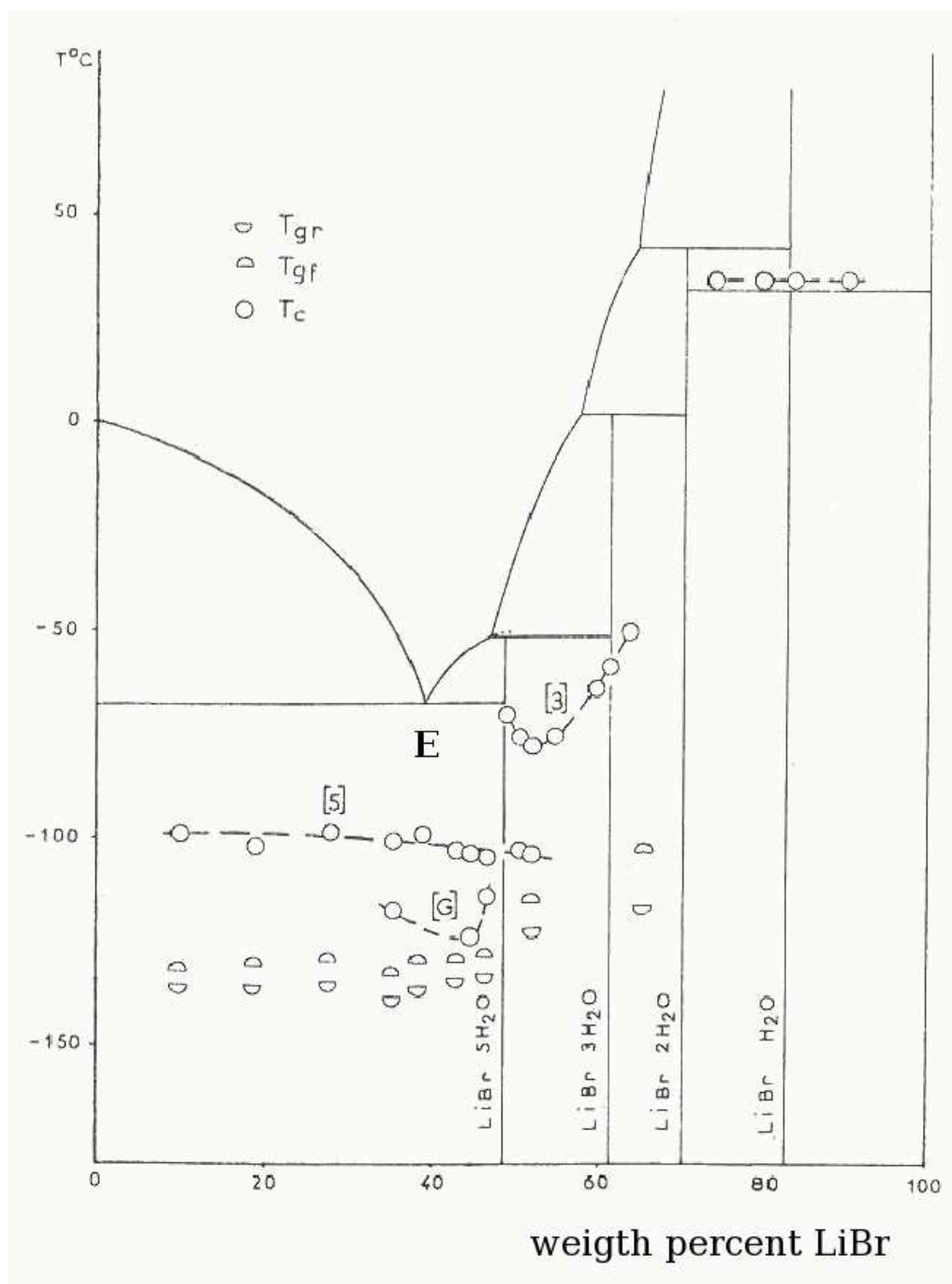


Figure 4.2: Temperature composition binary phase diagram of LiBr-H<sub>2</sub>O, from Kessis (1965). The LiBr-H<sub>2</sub>O system forms the same hydrates as the LiCl-H<sub>2</sub>O system and their phase boundaries are very similar. The stable eutectic point for LiBr-H<sub>2</sub>O is at -67°C and 39.07 weight percent (molar ratio  $R = 7.5$ ).

was originally developed for metals in the 1960s (Jones, 1973). The group of Mayer at the University of Innsbruck (Austria) were the first to apply this approach to pure water and aqueous solutions (Mayer, 1985). This technique is based on the rapid cooling of droplets (called splat) on a solid substrate. The three possible regimes of cooling are ideal cooling, intermediate cooling and Newtonian cooling. The boundaries between these regimes are expressed in terms of dimensionless Nusselt number, which is

$$\text{Nu} = \frac{h s}{K}, \quad (4.1)$$

where  $h$  is the heat transfer coefficient for the interface between splat and substrate,  $s$  is the thickness of the splat layer and  $K$  is the thermal conductivity of the splat. Their values for iron, water and sodium chloride solution are given in Table 4.1.

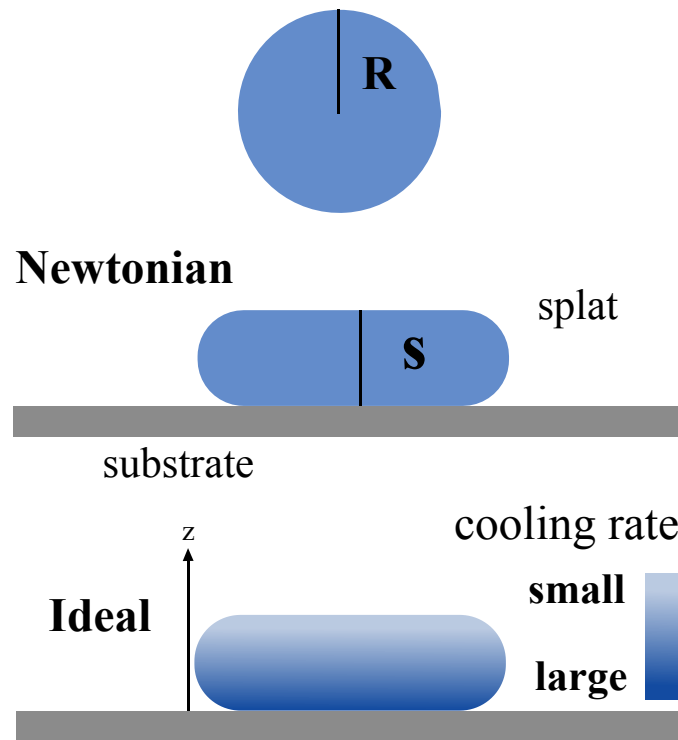


Figure 4.3: The Newtonian and ideal cooling regimes of a droplet (splat) on a substrate during splat cooling.

In the first case, known as ideal cooling ( $\text{Nu} \rightarrow +\infty$ ), the cooling rate is determined completely by the droplet's size and its thermal properties. Jones (1973) presents a simplified model of first order linear differential equations for the temperature and freezing velocity of the splat. He showed that for perfect contact ( $h = +\infty$ ) between splat and a semi-infinite substrate, whose density, specific heat and thermal conductivity are temperature independent, the cooling rate, apart from constants

material (ref.)	$K$ $\text{W m}^{-1} \text{K}^{-1}$	Nu	$s$ $\mu\text{m}$
Fe (Ruhl, 1967)	71.4	0.014	10
pure H <sub>2</sub> O	$\approx 0.6$	0.83	5
NaCl · 10.2D <sub>2</sub> O	$\approx 1$	$\approx 1$	10 to 30

Table 4.1: The thermal conductivity  $K$  and the Nusselt number Nu of iron, water and sodium chloride solution for reported values of the thickness  $s$  of the splat layer. For the heat transfer coefficient of the interface between splat and substrate we assumed  $h \approx 10^5 \text{ W m}^{-2} \text{ K}^{-1}$  given by Jones (1973) as a large value for contact between a liquid metal and substrate.

for material properties, goes as

$$\dot{T} \propto \frac{1}{z^2}, \quad (4.2)$$

$z$  being the distance from the interface. Hence larger cooling rates are achievable closer to the interface, this means that in smaller droplets and thinner splat the minimum cooling rate will be larger.

Newtonian cooling is the opposite limiting case  $\text{Nu} \ll 1$ , where the temperature gradient in the droplet is negligible and the cooling rate is determined entirely by the interface. Jones refers to the region in between as intermediate cooling. The Newtonian and ideal regime are illustrated in Figure 4.3. According to finite difference calculations by (Ruhl, 1967) for iron freezing on copper, Newtonian cooling prevails for  $\text{Nu} < 0.015$ , and ideal cooling for  $\text{Nu} > 30$ . These calculations also show that for Newtonian cooling  $\dot{T} \propto z^{-\alpha}$ , where  $\alpha \geq 1$  is a constant.

Nowadays, the group headed by Thomas Loerting at the University of Innsbruck has honed this technique and routinely use it to produce hyperquenched glassy water with less than 5 % crystalline ice impurity. They produce droplets of diameter less than  $\approx 5 \mu\text{m}$  with ultrasonic nebulizers (Kohl et al., 2005). From these experiments the cooling rate required to amorphise pure water (critical cooling rate, CCR for short) is estimated to be  $\approx 10^6$  to  $10^7 \text{ K s}^{-1}$  (Bachmann and Mayer, 1987, Kohl et al., 2005). From the available data, we estimate that the Nusselt number in their experiment is about  $\text{Nu} \approx 1$ .

Mayer (1985) pointed out that the heat transfer coefficient for contact may be dependent on the base pressure during deposition of the droplet. We think that dissolution of the carrier gas in the droplet may also have an effect on the cooling regime.

### 4.1.2 Experimental set-up

Our device for fast quenching, shown in Figure 4.4, reaches more moderate cooling rates (estimate given below). It exploits the rapid cooling of micrometer sized droplets on a solid substrate. The surface, on which droplets are projected, is a circular plate of an aluminium-copper alloy ( $K_{\text{Du}} \approx 100 \text{ W/m/K}$  at 80K) chosen for its high thermal conductivity to which  $\dot{T}$  is proportional. It is placed inside a vacuum chamber (cylindre of diamter 330 mm, height 200 mm), where the pressure is of the order of 1 mbar ( $\approx 0$  torr). The chamber is cooled by immersing its lower part in a bath of liquid nitrogen. Cooling the device to 80 K takes about 1.5 hours.

The sample may be pre-cooled to  $0^\circ\text{C}$ . This lowers the vapour pressure of the solution, thereby reducing evaporation in the vacuum and variations of the final concentration in the droplets.

Once the pneumatic valve is activated, the sample solution is injected through a nozzle (commercial models of Scheer and Fluidics) onto the cooled aluminium plate. The opening angle of the cone of injection is  $80^\circ$ . The drop size decreases with the pressure applied as shown in Figure 4.5. In our setup a pressure of up to 200 bar of helium gas was applied to the solution in the tube. Test checking the droplet size and amorphisation were performed at different pressures. The diameter of the droplets produced at 80 bar was  $\approx 10$  to  $30 \mu\text{m}$  (Figure 4.5) with an average droplet size of about  $20 \mu\text{m}$  as measured under an optical microscope. The injection time  $t$  can be varied. Times from 0.5 to 3.0 s were tested. Since the amount of material injected is roughly proportional to the injection time, the latter controls also the thickness of the layer of splat.

Then the vacuum in the chamber is broken by leaking liquid nitrogen into it through a pipe connected to a funnel. This leads at first to a turbulent flow of solid nitrogen in the chamber (nitrogen storm). In small patches sample is torn off the plate and forms a plaque, whose temperature may rise higher than that of the powder sticking to the plate. This part was discarded. The rest of the sample is slowly immersed and remains at liquid nitrogen temperature.

From our tests varying the injection pressure, time, pre-cooling temperature and surface roughness of the plate at a given concentration of the solution, the largest fraction of amorphous material of  $\text{NaCl} \cdot 10.2\text{D}_2\text{O}$  were obtained in conditions of 80 bar, 0.6 s injection, on a surface roughened up with sand paper (grade P400, average particle diameter of  $35 \mu\text{m}$ ). For droplet diameter of about  $10 \mu\text{m}$ , the Nusselt number is  $\approx 1$  hence we are in the intermediate regime of cooling. Using the data of Ruhl (1967) and Jones (1973), we estimate our cooling rate to be approximately  $10^4$  to  $10^5 \text{ K s}^{-1}$ . (Details of the quenching device are to be published in Ludl et al. (in preparation).)

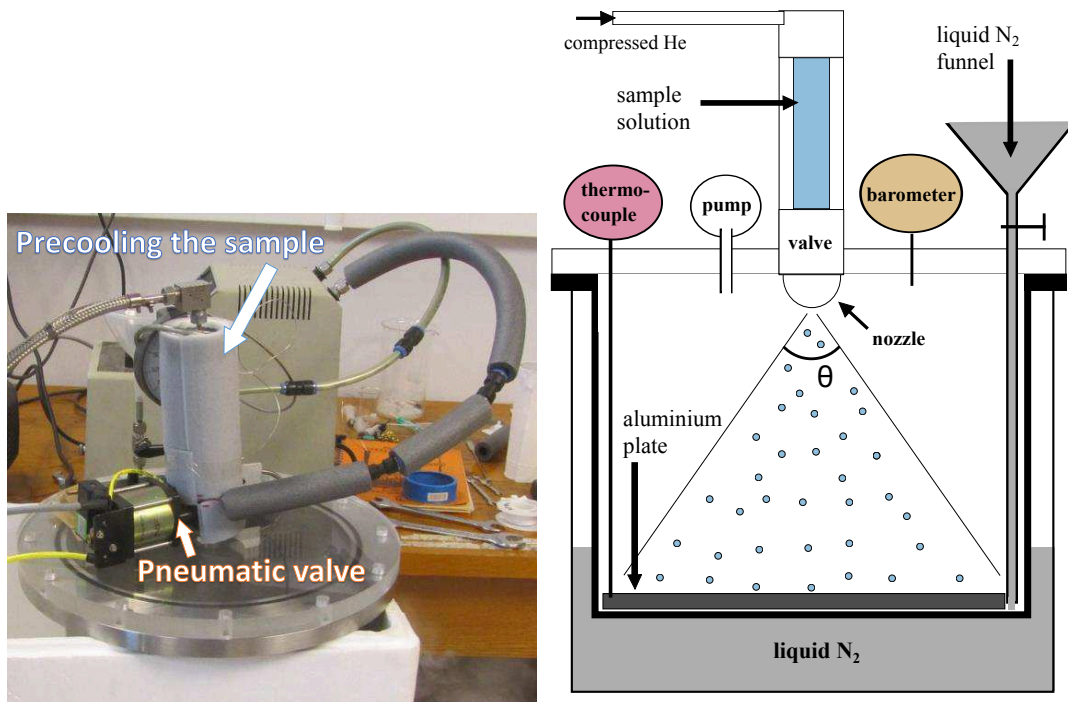


Figure 4.4: Hyper-quenching device. Left: photograph. Right: schematic. The sample in the tube above the nozzle is pre-cooled to about  $0^{\circ}\text{C}$ . The nozzle sprays fine droplets of diameter  $\approx 10$  to  $30\ \mu\text{m}$  onto the aluminum plate at  $80\ \text{K}$ , with a spraying angle  $\theta \approx 90^{\circ}$ . (Ludl et al., in preparation).

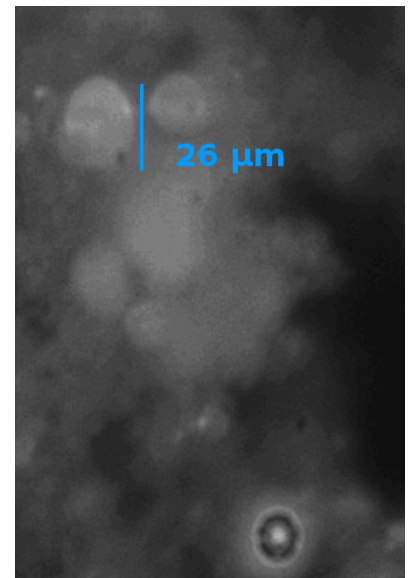
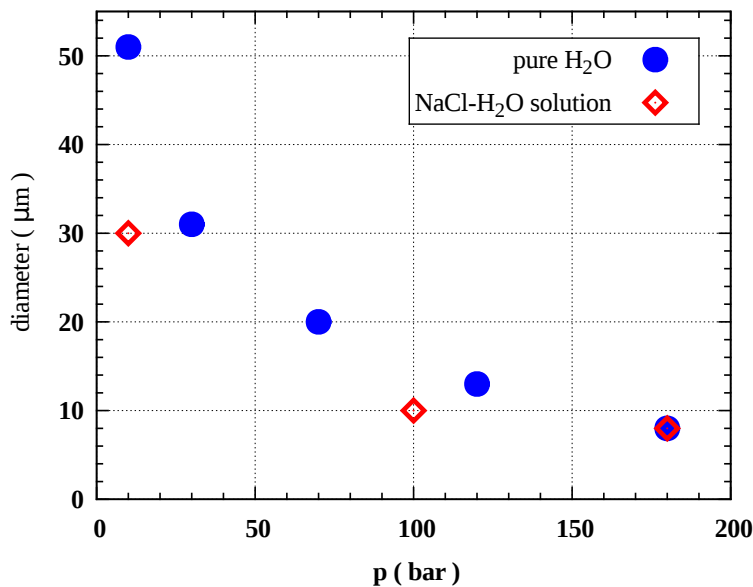


Figure 4.5: Left: Droplet size as a function of injection pressure for pure water (blue) and NaCl solution with  $R = 10.5$  (red). This Figure was produced using data from the internal report by Li (2012). Right: Photograph of the droplets produced at about 40 bar seen through the optical microscope, from Li (2012).

## 4.2 Sample preparation

### 4.2.1 Solutions

We have investigated the amorphisation of NaCl, LiCl, LiBr, MgCl<sub>2</sub> solutions. The binary composition-temperature diagrams of the stable and metastable phases at ambient pressure are shown in Figure 4.1 and Figure 4.2. It is remarkable that the phase diagrams of LiCl and LiBr are highly similar, with both phases forming mono-, tri- and pentahydrates. However, NaCl-H<sub>2</sub>O only forms a dihydrate (Klewe and Pedersen, 1974). These differences in the phase diagrams are thought to be related to the radius of the cation and its charge density, which are given in Table 4.2. Small ions have a large charge density, hence the neighbouring water molecules are strongly bound to the ion. Apart from the proton H<sup>+</sup>, Li<sup>+</sup> is the smallest monovalent cation (22.4 % smaller than Na<sup>+</sup>), which is thermodynamically stable, hence the binding between Li<sup>+</sup> and its shell of first neighbours is rather strong. Mg<sub>2</sub><sup>+</sup> is even smaller, and its salts also form a large number of hydrates. Angell and Sare (1970) discuss the correlation of glass transition temperature  $T_g$  with cationic charge density.

ion	$r$ [ Å ]	$q$ [ e Å <sup>-3</sup> ]	electrolyte	$M$ [ g mol <sup>-1</sup> ]	solubility [ g/100g ]	$\Delta H_{\text{sol}}$ [ kJ mol <sup>-1</sup> ]
Li <sup>+</sup>	0.90	0.39	LiBr	86.84	160	-48.83
Na <sup>+</sup>	1.16	0.24	LiCl	42.39	83.5	-37.03
Mg <sup>2+</sup>	0.86	0.43	MgCl <sub>2</sub>	95.21	54.6	15.67
Cl <sup>-</sup>	1.67	-0.36	NaCl	58.44	35.89	3.88
Br <sup>-</sup>	1.82	-0.10				

Table 4.2: Left: Radii of the ions constituting the salts in our solutions. (Shannon, 1976) Right: Enthalpies of solution at 25°C, solubilities at 20°C (in g per 100g of water) and molar mass for the four electrolytes investigated here. Haynes (2013), Jahn and Wolf (1993), Parker (1965) The values for MgCl<sub>2</sub> are given for comparison. (IUPAC-NIST Solubility Database, Version 1.1 NIST Standard Reference Database 106 )

Solutions of these electrolytes were prepared by dissolving salts in light or heavy water. For most X-ray diffraction experiments we used solutions in H<sub>2</sub>O. D<sub>2</sub>O solutions were used for neutron scattering because D is a coherent neutron scatterer. The D<sub>2</sub>O was at least 99.75 % pure and H<sub>2</sub>O was filtered by a Millipore DirectQ. Its resistivity is greater than 18.2 MΩ·cm at 23°C (Grade 1 of the ISO 3696 standard). Oxygen is in natural isotopic proportions: <sup>16</sup>O: 99.76%, <sup>17</sup>O: 0.039%, <sup>18</sup>O: 0.201%. Below details specific to each salt are given. The isotopic compositions are given, be-

cause the neutron scattering cross-sections (see Table 2.1) vary for different isotopes of each element. The compositions are used for the calculation of cross sections, when we compare structure factors calculated from simulations to those obtained in our experiments. The concentrations are discussed in terms of the molar ratio

$$R = \frac{n(\text{water})}{n(\text{salt})}. \quad (4.3)$$

The LiCl-H<sub>2</sub>O system can be undercooled easily and is a good glass former. The molar ratio at the stable eutectic concentration is 7 in H<sub>2</sub>O. In D<sub>2</sub>O there is a shift in the melting line to higher temperatures which shifts the eutectic to about 6.5. Slow amorphisation can be achieved for  $R \approx 6$ . (Elarby-Aouizerat et al., 1983, Prével et al., 1995) The salt LiCl has to be handled with care, because it is highly hygroscopic and its dissolution is strongly exothermic. Its enthalpy of solvation is  $\Delta H_{\text{sol}} = -37.03 \text{ kJ mol}^{-1}$  (Table 4.2) The natural isotopic composition of the salt is <sup>6</sup>Li: 7.5%, <sup>7</sup>Li: 92.5%, and <sup>35</sup>Cl: 75.77%, <sup>37</sup>Cl: 24.23%.

Solutions were prepared by weighing first the required amount of water solvent. Then the vial of salt, containing an inert atmosphere, was opened, emptied into the bottle containing the liquid which was immediately hermetically closed, so that contact with wet air was minimized. Where possible this was done under an argon atmosphere. After the salt had completely dissolved and the solution cooled to ambient temperature, the bottle was weighed again and solvent added as required.

LiBr behaves similarly to LiCl and is also highly hygroscopic. The isotopic composition of the salts is <sup>6</sup>Li: 7.5%, <sup>7</sup>Li: 92.5%, and <sup>79</sup>Br: 50.69%, <sup>81</sup>Br: 49.31%. The eutectic concentration is about  $R \approx 7.5$  in H<sub>2</sub>O (Kessis, 1965). Amorphisation by slow cooling is possible for concentrations in the vicinity of  $R = 6$  (Bove et al., 2011a). For the preparation of the solution the same procedure as for LiCl solutions was followed.

Common NaCl salt is easier to handle. The stable eutectic concentration in H<sub>2</sub>O is  $R = 10.7$  close to the maximum solubility at ambient temperature and atmospheric pressure of  $R = 9.05$ . In D<sub>2</sub>O the solubility limit is 9.7, our experiments indicate that the meta-stable eutectic is at 10.2. We used salt of natural isotopic composition: <sup>23</sup>Na: 100%, and <sup>35</sup>Cl: 75.77%, <sup>37</sup>Cl: 24.23%.

First the salt was baked for 2 hours in a furnace at 110°C to remove residual hydration water. The dried salt was weighed and water added as required for the desired concentration, after which the bottle was closed. Solutions with  $R$  in the range of 9.05 to 11 were produced to determine for which concentration the best amorphisation could be achieved.

To ensure complete and homogeneous dissolution, all solutions were plunged for about ten minutes in an ultrasonic bath.

### 4.2.2 Amorphous powder

LiCl and NaCl solutions were amorphised in our device by fast quenching of the solution to liquid nitrogen temperature (77 K) with an estimated cooling rate of  $\approx 10^4 \text{ K s}^{-1}$ . After injection the thin film of quenched solution was reduced to fine powder, recovered under  $\text{N}_2$  vapour, collected in plastic containers filled with liquid nitrogen, and stored in dewars. Roughly 1 g of powder was produced in each quenching procedure. The left panel of Figure 4.6 shows a powder sample loaded in the cryochamber at 80 K.

For high pressure experiments in the Paris-Edinburgh cell, the sample powder was compacted into spherical pellets using a dedicated press, operating in liquid nitrogen up to 2 kbar. This press was designed so that the pellets produced are of the same size as the sample volume in the gaskets used with the Paris-Edinburgh cell. We estimate the packing density of these pellets to be  $\approx 90\%$ . The right panel of Figure 4.6 shows a pellet, of diameter  $\approx 1.8 \text{ mm}$ , on the gasket and anvil of the Paris-Edinburgh cell at 80 K. To preserve the amorphous material the pellet must be stored below 140 K and loaded directly into pre-cooled gaskets and anvils.

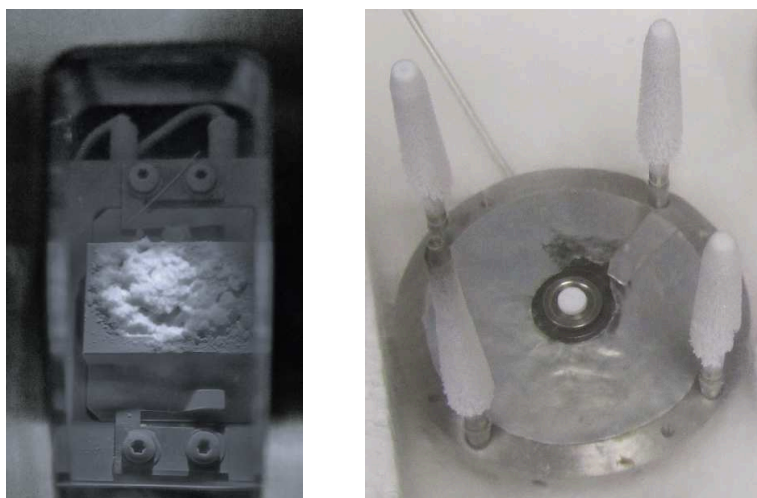


Figure 4.6: Left: powder sample of quenched  $\text{NaCl} \cdot 10.2\text{D}_2\text{O}$  solution inside the cryochamber in the XRD at IMPMC. Right: pellet ( $\varnothing \approx 1.8 \text{ mm}$ ) of amorphous powder loaded in a gasket on an anvil of the Paris-Edinburgh cell. (Ludl et al., in preparation)

## 4.3 Structure characterisation at ambient pressure

The aim of this work is the characterisation of the high pressure phases of the NaCl-water system. The starting point of our experiments are amorphous solutions at ambient pressure. Their structure was studied first by X-ray diffraction and later by neutron diffraction at low pressure ( $p < 1$  atm), before performing high-pressure experiments. First, we give an estimation of the fraction of amorphous material. Second, its structure at ambient pressure and its transformation upon annealing are compared to that of pure water and LiCl solutions.

### 4.3.1 Fraction of amorphous material

The first samples produced were NaCl-H<sub>2</sub>O. Solutions of compositions  $R$  between 9 and 11 were quenched and their structure measured in XRD. This range concentrations was chosen to bracket the stable eutectic concentration ( $R = 10.7$ ). The spectra of the known crystalline phases of the system at ambient pressure were calculated with FullProf (Rodríguez-Carvajal, 1993, Roisnel and Rodríguez-Carvajal, 2001). They are shown in the top panel of Figure 4.7. The ice I<sub>h</sub> structure (hexagonal, space group  $P6_3/mmc$ ) was taken using data given in Kuhs and Lehmann (1986). The NaCl structure (face-centered cubic, space group  $Fm\bar{3}m$ ) of Decker (1971) was used. The sodium chloride dihydrate structure (monoclinic, “probable” space group  $P2_1/c$ ) of Klewe and Pedersen (1974) was used. The experimental XRD spectrum of ice I<sub>h</sub> and the background spectrum are shown in the bottom panel of Figure 4.7.

In order to check the quality of amorphization, the samples were studied *ex situ* at ambient pressure by X-ray diffraction with a commercial X-PERT powder X-ray diffractometer at IMPMC, equipped with a low-temperature Anton Paar chamber. For samples destined to be measured by neutron diffraction, a small amount of quenched solution was systematically recovered and measured as above by XRD at IMPMC. The sample holder made of nickel plated copper was cooled to  $\approx 80$  K with liquid nitrogen and the temperature of the sample during the transfer did not exceed 95 K. This has been tested using a mixture of iso-pentane and n-pentane which undergoes a glass transition for  $T \approx 100$  K. The diffractometer has an incident wavelength of  $\lambda = 1.5418$  Å (Cu  $K\alpha$ ). During the measurement the X-ray source and the detector were set up in  $\theta/2\theta$  geometry.

The data of quenched solutions are given in subsequent figures. The quality of these data depends on the amount of sample available. In situations where there is little sample in the chamber, either due to limited availability or to difficulties upon loading, the distribution of the sample in the beam can be non uniform. In these cases the alignment of the height of the sample is difficult, this can lead to a small

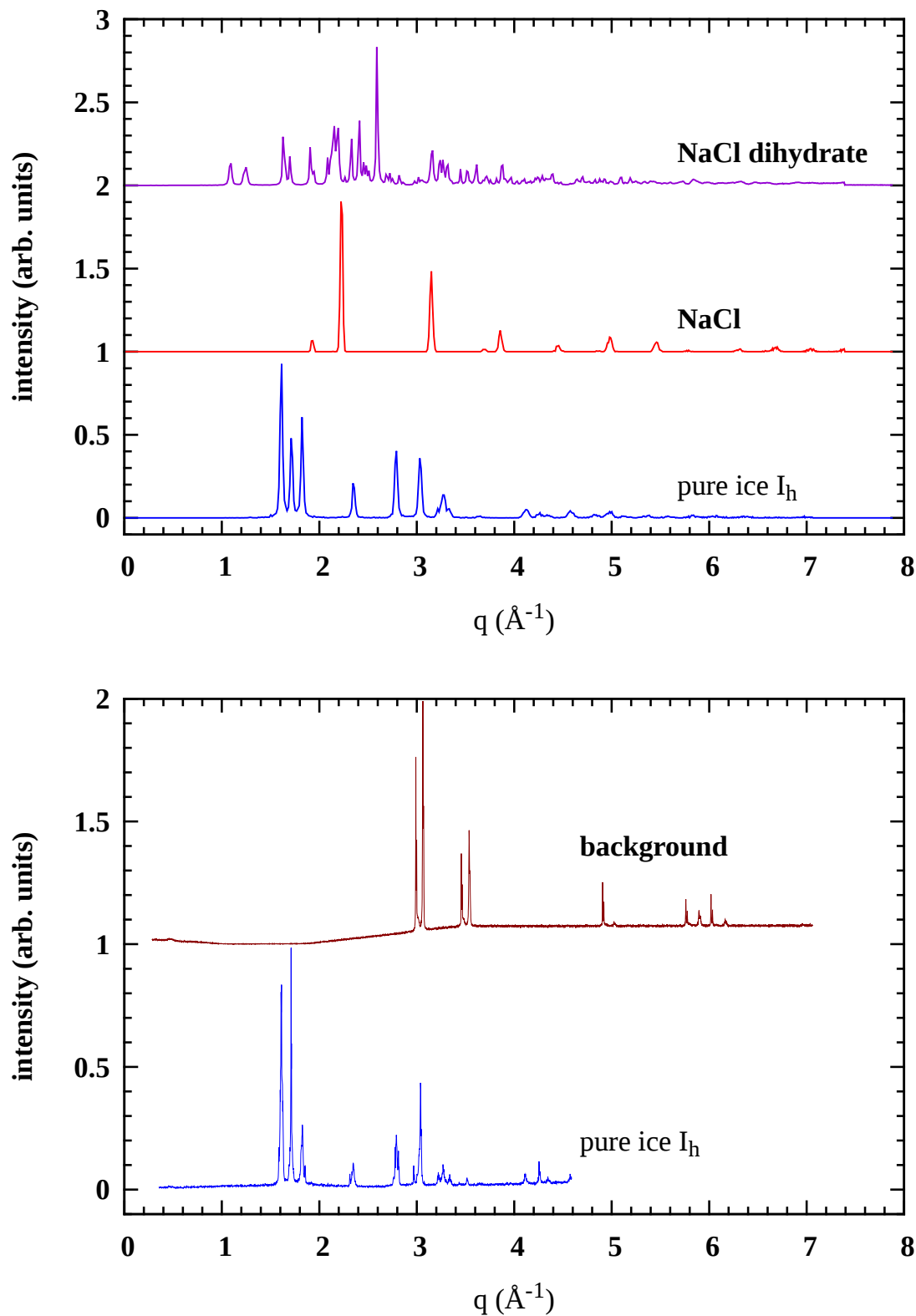


Figure 4.7: Top: X-ray structure factors of ice I<sub>h</sub>, NaCl, and NaCl · 2H<sub>2</sub>O at ambient pressure calculated with FullProf. Details and references for the structures used are given in the text. Bottom: Measured X-ray diffraction patterns of pure hexagonal ice I<sub>h</sub> at 80 K in the cryochamber and background at ambient temperature. (Although truncated at 4.6 Å<sup>-1</sup>, this ice I<sub>h</sub> spectrum was the best one available.) The peaks in the background spectrum are those of the nickel and copper in the sample holder.

shift of the spectrum in  $q$ . In some cases this causes the intensity to rise at high values of  $q$ , as seen in the data for  $R = 9.5, 10.0, 10.5$  in Figure 4.9, and the D<sub>2</sub>O solution (green data) in Figure 4.11. The data of best quality available are shown and discussed here.

Tests of quenching NaCl · 9.5H<sub>2</sub>O, while varying the injection pressure from 15 to 80 bar as shown in Figure 4.8, show that a larger amount of amorphous material is produced at higher injection pressures (50 and 80 bar). Higher injection pressure corresponds to smaller droplets, as shown in Figure 4.5, thus we expect larger cooling rates, implying better amorphisation, for smaller droplets.

Figure 4.9 shows the XRD data obtained from the tests of our quenching device with NaCl ·  $R$ H<sub>2</sub>O samples of different concentrations,  $R$  ranging from 9.05 to 11.0. The injection pressure was 80 bar. All samples contain ice I<sub>h</sub> as can be seen by comparing the peaks, notably the triplet at  $1.6 \leq q \leq 1.85 \text{ \AA}^{-1}$ , to the ice I<sub>h</sub> spectrum shown in Figure 4.7. For  $9 \leq R \leq 10$  a small amorphous contribution can be seen. Among these, the solutions with  $R = 9.5$  and  $9.8$  appear to contain a larger fraction of amorphous material. Subsequent experiments, after improvements to the quenching procedure, showed that indeed this solution is easiest to vitrify.

For D<sub>2</sub>O the solubility limit of NaCl is  $R = 9.7$  at room temperature and ambient pressure. Further screening at different concentrations showed that for  $R = 10.2$  a larger amorphous fraction could be obtained. This was confirmed in our experiment on D20 at ILL. Figure 4.10 shows the neutron diffraction patterns obtained for a sample of pure hexagonal ice of D<sub>2</sub>O, NaCl · 9.7D<sub>2</sub>O and NaCl · 10.2D<sub>2</sub>O. Although both salty samples contain amorphous material, a larger fraction is present in the sample with  $R = 10.2$ . The sample with  $R = 9.7$  shows larger ice I<sub>h</sub> peaks and also dihydrate peaks. The latter observation is coherent with the phase diagram of NaCl-H<sub>2</sub>O (Figure 4.1, panel b), since 9.7 is to the right of the eutectic point at 10.7. The fact that  $R = 10.2$  solutions amorphise without forming dihydrate indicates that the rate of formation of the dihydrate at this concentration is slower than the quenching rate of our device.

As  $R = 10.2$  had not been tested in our H<sub>2</sub>O samples previously, another test was done on this solution. Both samples were produced in the same conditions (injection at 80 bar and 0.7 s) using the improved quenching with precooling of the sample before injection. Figure 4.11 shows the X-ray diffraction patterns. The D<sub>2</sub>O solution indeed shows a larger amorphous contribution relative to the ice I<sub>h</sub> peaks.

Figure 4.12 shows the X-ray diffraction patterns of samples of which show the highest fraction of amorphous versus crystalline material.

From the above observations we conclude that the isotopic effect of substituting D for H in these solutions shifts the composition of best amorphisation from  $R = 9.5$  in H<sub>2</sub>O to  $R = 10.2$  in D<sub>2</sub>O.

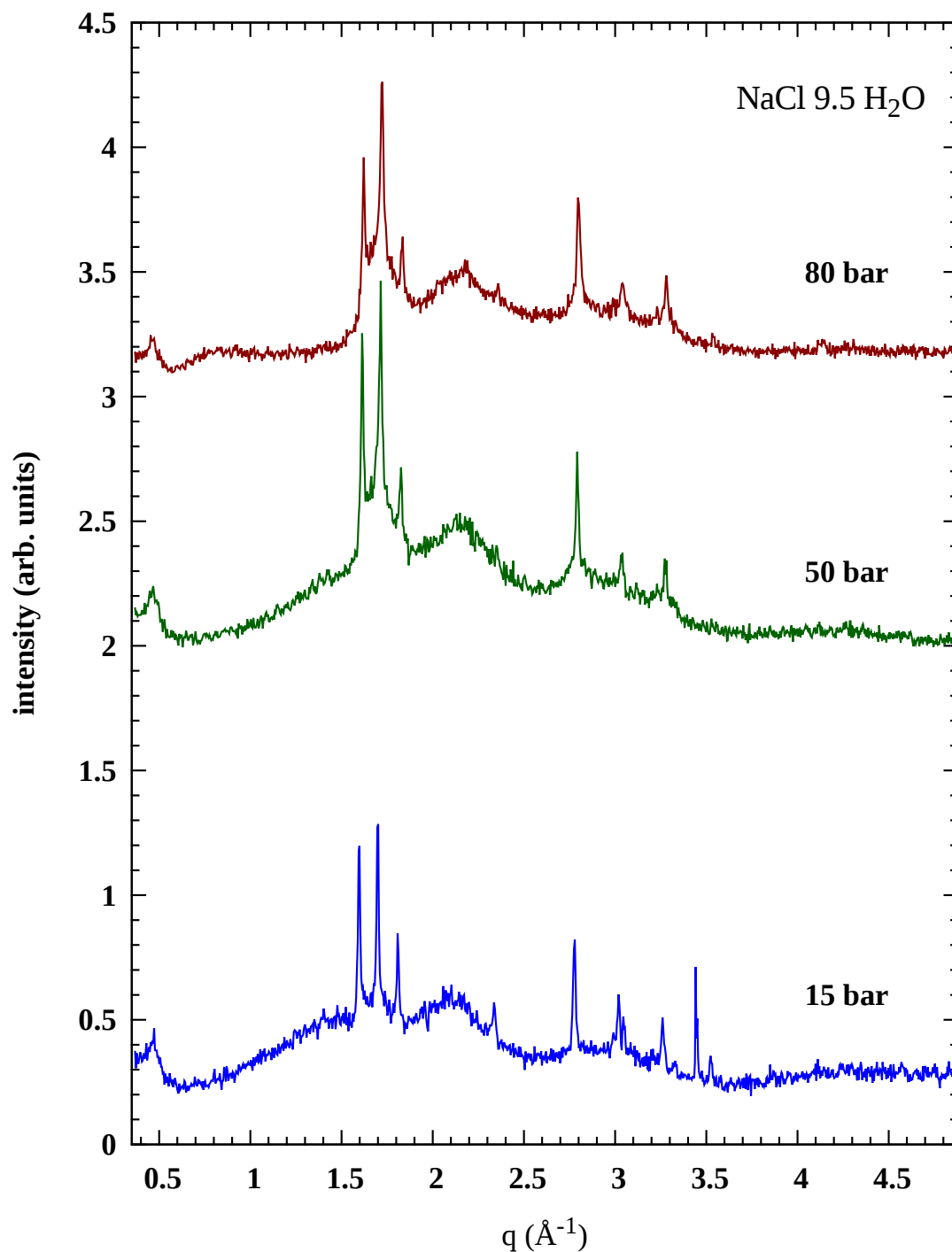


Figure 4.8: Measured X-ray diffraction patterns of quenched  $\text{NaCl} \cdot 9.5\text{H}_2\text{O}$  at 80 K in the cryochamber. Precooling was used on these samples. The injection pressure is indicated on the right. The samples injected with 50 and 80 bar contain larger fraction of amorphous over crystalline material than those produced at lower pressures. The peak at  $0.4 \text{ \AA}^{-1}$  is due to the Kapton windows.

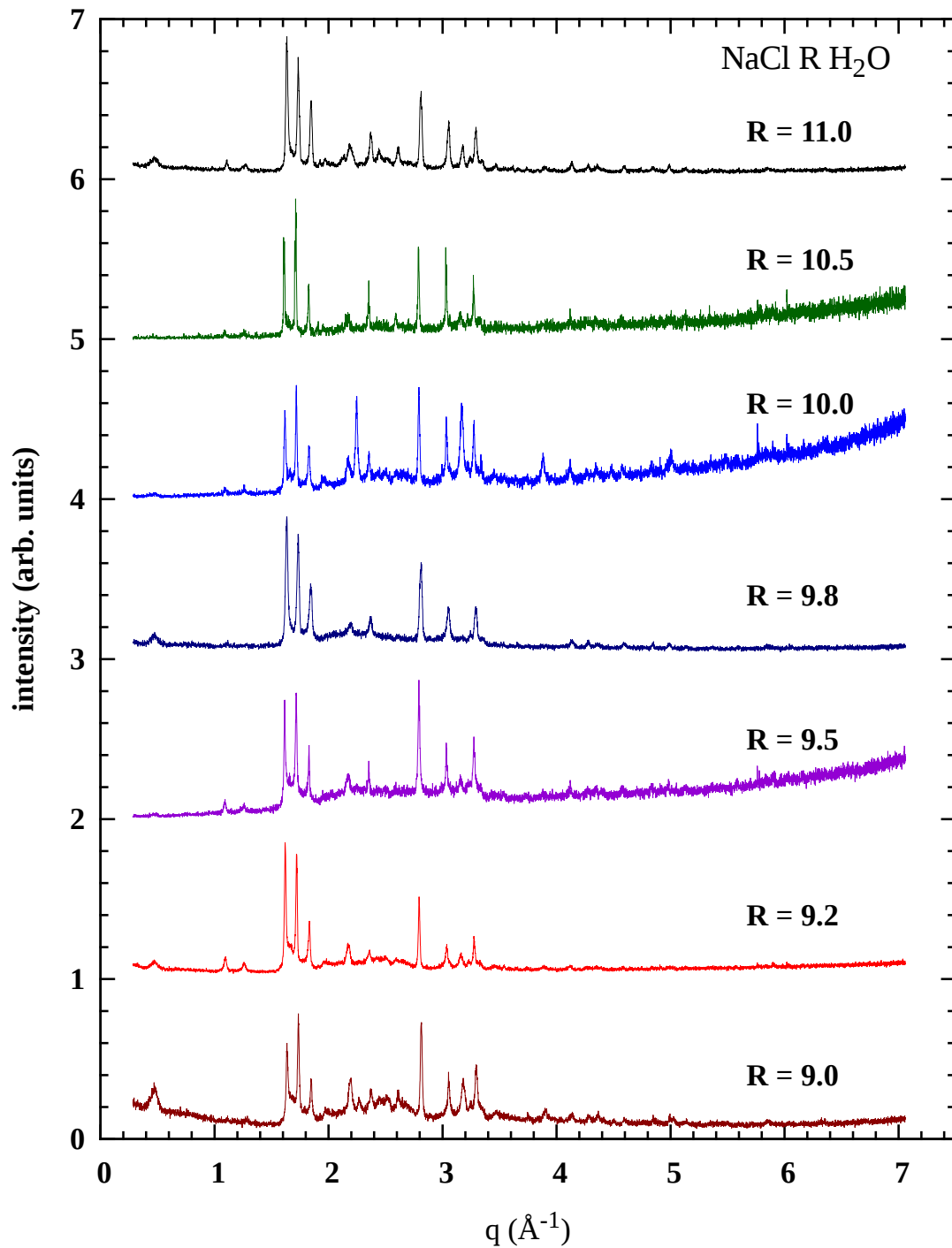


Figure 4.9: Measured X-ray diffraction patterns of quenched  $\text{NaCl} \cdot R\text{H}_2\text{O}$  at 80 K in the cryochamber, where the pressure is about  $10^{-3}$  mbar during the measurement. The molar fraction  $R$  increases from bottom to top as indicated on the right. All samples contain a large part of crystalline material. The strongest peaks, including the triplet at  $1.6 \leq q \leq 1.85 \text{ \AA}^{-1}$ , belong to ice  $I_h$ . The peak at  $0.4 \text{ \AA}^{-1}$  is due to the Kapton windows. The other peaks, including the two at  $1.05$  and  $1.15 \text{ \AA}^{-1}$ , belong to sodium chloride dihydrate. Amorphous material is visible in samples with  $9 \leq R \leq 10$ .

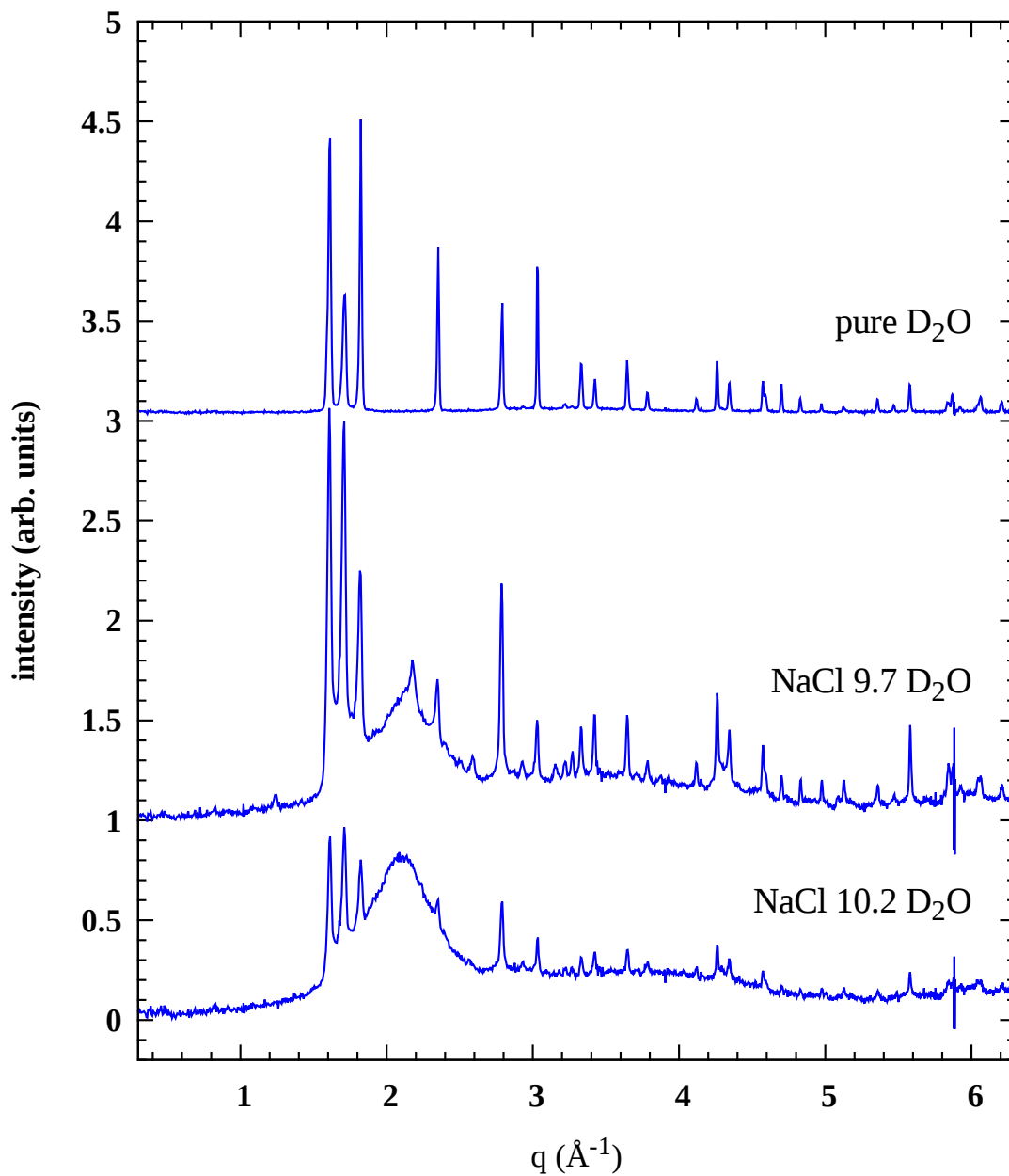


Figure 4.10: Measured neutron diffraction patterns of quenched  $\text{NaCl} \cdot R\text{D}_2\text{O}$  and pure ice  $I_h$  (top) at 80 K measured on D<sub>2</sub>O at ILL. The composition is indicated on the right. During the measurement the pressure is that of the helium exchange gas ( $\approx 100$  mbar). The sample with  $R = 10.2$  contains more amorphous material with respect to the crystalline  $I_h$ . Hydrate peaks appear in the spectrum of the sample with  $R = 9.7$  but not in that with  $R = 10.2$ .

Figure 4.13 shows a comparison of the neutron and X-ray data for the same sample. The diffraction pattern shows the peaks of crystalline material and the amorphous structure of the solution. By comparison with FullProf simulations of ice  $I_h$  peaks, we conclude that all these peaks correspond to ice  $I_h$ , although with significant texture. Therefore thirteen of the ice peaks in the neutron data at 90 K were fitted individually with pseudo-Voigt profile functions using the least squares algorithm of GNUPLLOT 4.6 (Williams et al., 2014), as shown in Figure 4.14. The fit was integrated to obtain the intensities of ice peaks and the structure factor of amorphous material, from which the fraction of the latter in the sample was calculated. Details of the fit and peak indexes are reported in Appendix A.1.1. The results of the fit are shown in the bottom panel of Figure 4.13.

By integrating the intensities from these fits the sample is found to be 92% amorphous, *i.e.* the crystalline component is 8% of the total volume (Table 4.3). The neutron experiment provides evidence that the crystalline part forms during the hyperquenching process since the measured ice peaks correspond to deuterated

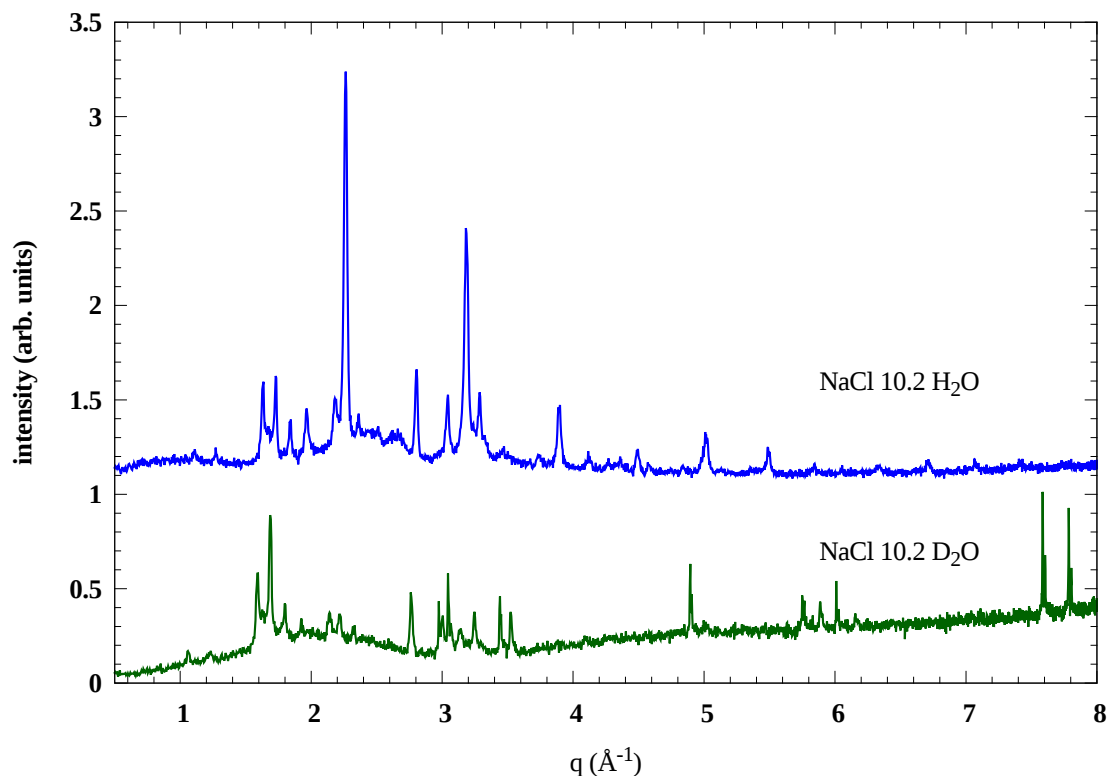


Figure 4.11: Measured X-ray diffraction patterns of quenched  $\text{NaCl} \cdot 10.2\text{D}_2\text{O}$  and  $\text{NaCl} \cdot 10.2\text{H}_2\text{O}$  at 80 K in the cryochamber. Precooling was used on these samples. Precooling was used on these samples, they were injected at 80 bar and 0.7 s. During the measurement the pressure is about  $10^{-3}$  mbar. Both samples contain a fraction of crystalline and amorphous material. The  $\text{D}_2\text{O}$  sample contains more amorphous material. The  $\text{H}_2\text{O}$  sample has formed more hydrate.

ice  $I_h$ . This cannot be formed by condensation of water from a humid ambient atmosphere during loading of the sample, which would be  $H_2O$  ice.

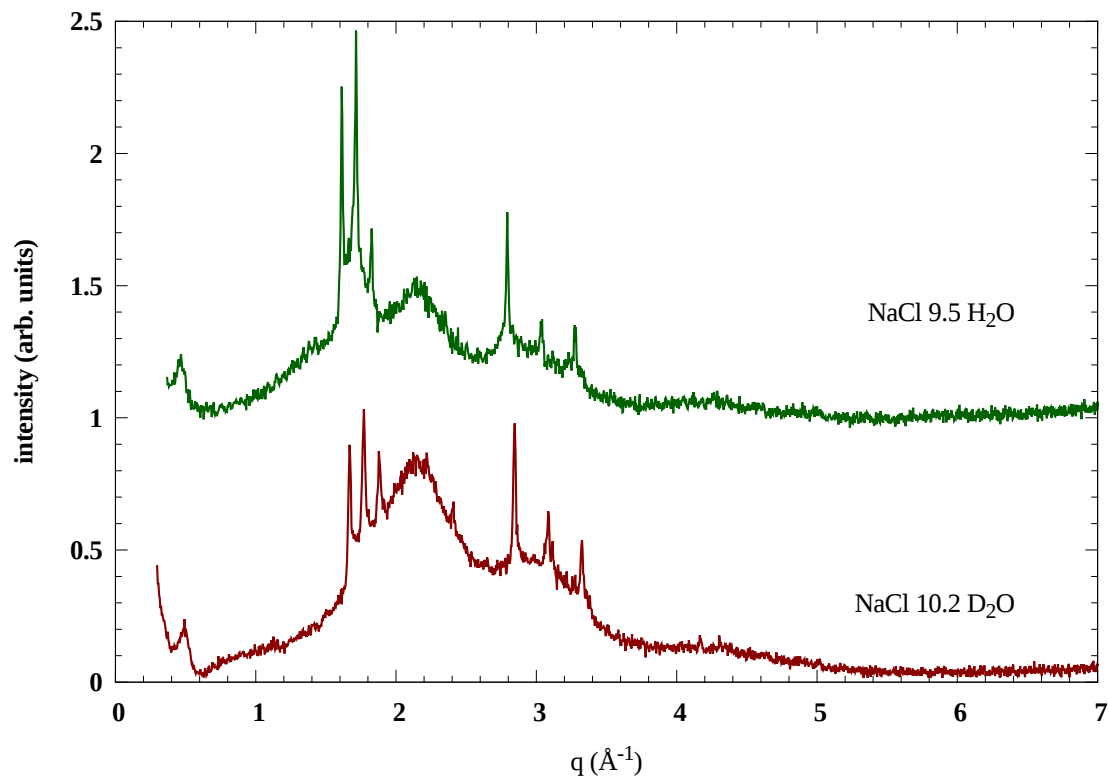


Figure 4.12: Measured X-ray diffraction patterns of quenched  $NaCl \cdot 10.2D_2O$  and  $NaCl \cdot 9.5H_2O$  at 80 K in the cryochamber. Precooling was used on these samples. These are the samples of NaCl-water, which show the largest fractions of amorphous material obtained in our experiments.

phase	intensity integral arb. unit
$I$ amorphous	89500
$I$ ice	7430
$I$ ice/ $I$ amorphous	0.083

Table 4.3: Integrated intensities of the amorphous part and 13 crystalline peaks fitted to the neutron data measured on D20 at ILL (Figure 4.14).

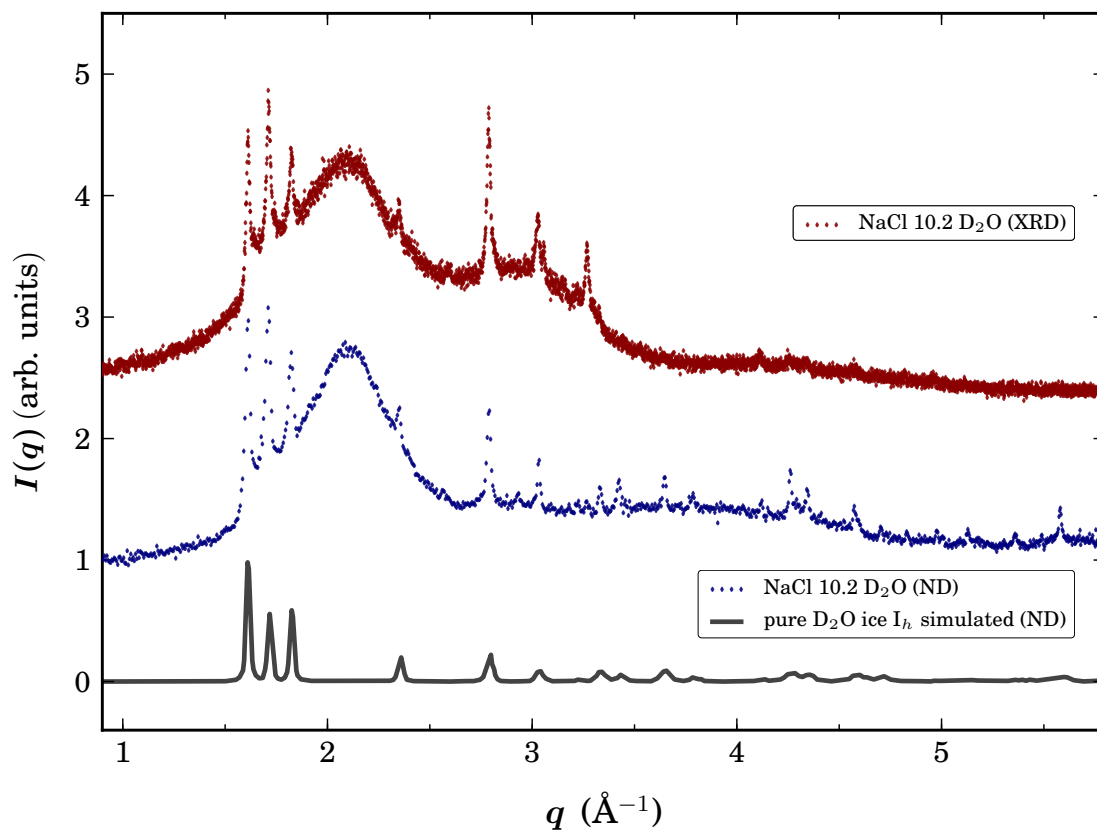


Figure 4.13: Measured diffraction patterns and simulated structure factors  $S(q)$  at low pressure. From bottom to top: in black the simulation of ice  $I_h$  neutron pattern with FullProf, in blue the  $\text{NaCl} \cdot 10.2\text{D}_2\text{O}$  neutron pattern measured at 100 mbar on D20 at ILL and in red the X-ray pattern of the same solution measured at  $10^{-3}$  mbar on the X-Pert diffractometer at IMPMC (Ludl et al., 2015).

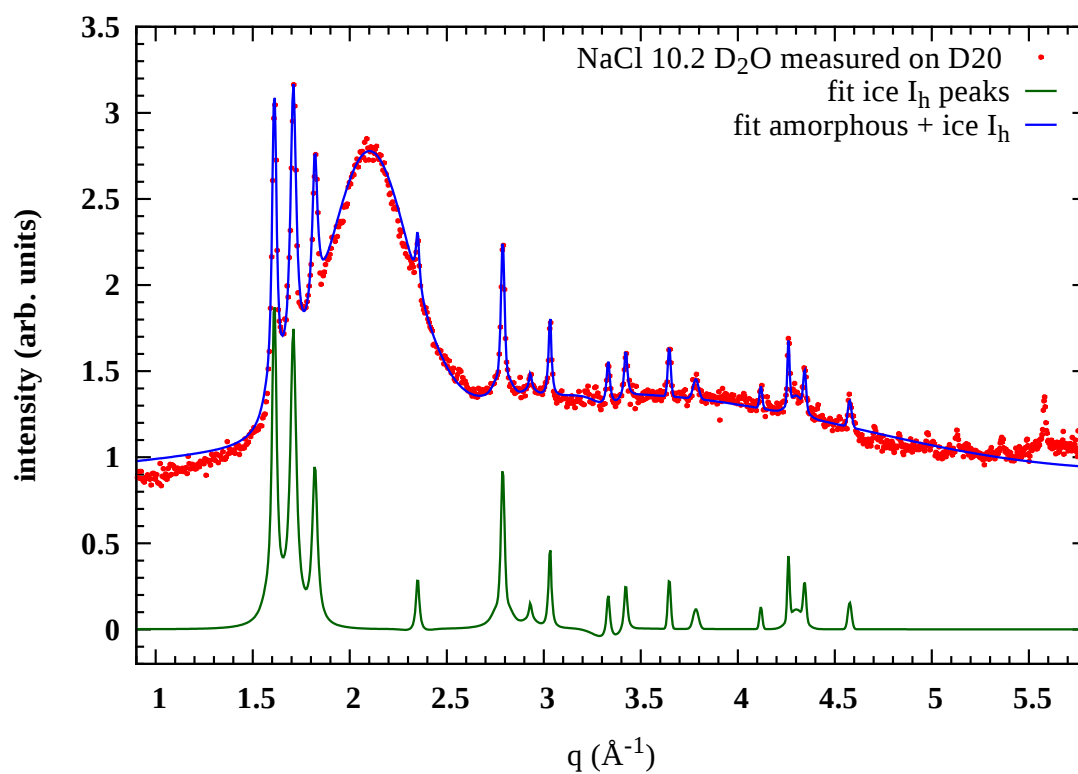


Figure 4.14: The neutron diffraction pattern of  $\text{NaCl} \cdot 10.2\text{D}_2\text{O}$  measured on  $\text{D}_2\text{O}$  at ILL (Ludl et al., 2015) at 100 mbar is shown in red. The sum of the fits of amorphous and crystalline contributions is shown in blue. The crystalline part is estimated to be about 8% of the sample material according to the fit of thirteen ice peaks with pseudo-Voigt profile functions, shown in in green.

Finally, LiCl-D<sub>2</sub>O solutions were also quenched with our device. Figure 4.15 shows the XRD spectra obtained for LiCl · 6D<sub>2</sub>O and LiCl · 20D<sub>2</sub>O. The former is almost entirely amorphous. There are weak ice peaks at the location of the triplet of ice I<sub>h</sub> at  $1.6 \leq q \leq 1.85 \text{ \AA}^{-1}$ . They are most likely due to condensation during the loading of the sample into the cryochamber. The doublets at  $\approx 3 \text{ \AA}^{-1}$ ,  $\approx 3.5 \text{ \AA}^{-1}$ , 7.6 and 7.8  $\text{\AA}^{-1}$  are from the sample holder. The LiCl · 20D<sub>2</sub>O sample contains also amorphous material, although a relatively small fraction compared to the crystalline part. This shows that our quenching procedure allows good amorphisation of solutions which are good glass formers, without spurious formation of crystalline material. Given that the cooling rate of our device is limited, the quantity of crystalline material depends on how far the concentration of the solution is from the best amorphisable concentration.

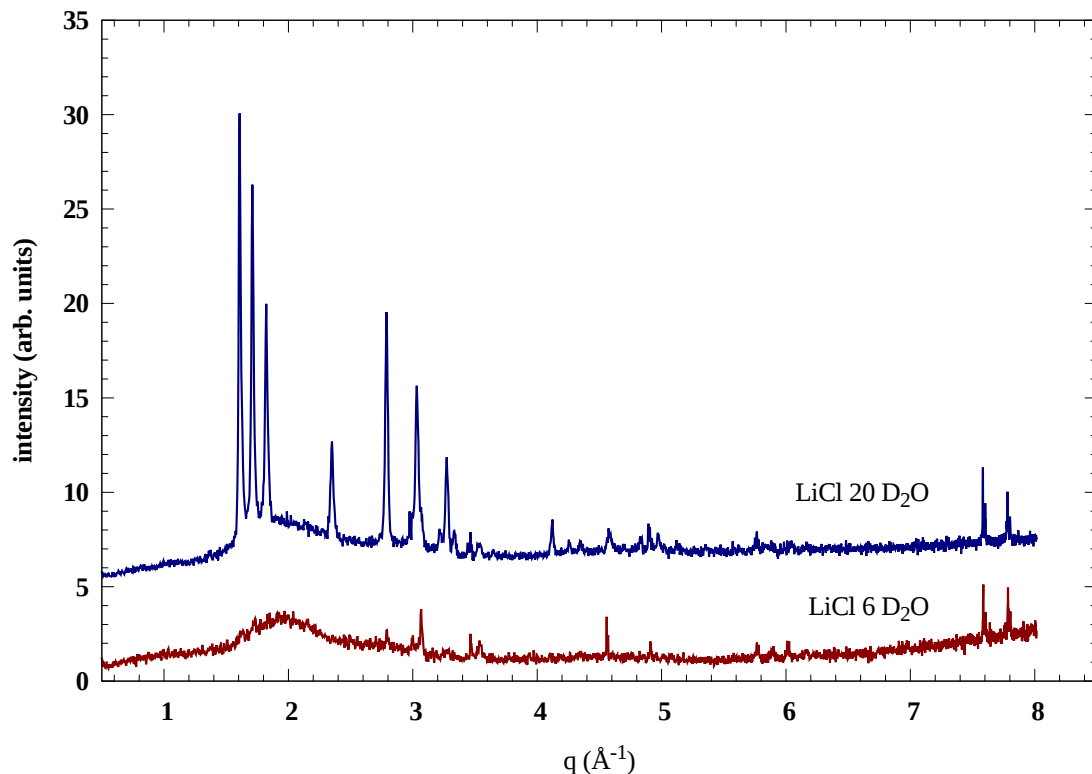


Figure 4.15: Measured X-ray diffraction patterns of quenched LiCl ·  $R$ D<sub>2</sub>O at 80 K in the cryochamber. The molar fraction  $R$  is indicated on the right. Precooling was used on these samples, they were injected at 80 bar and 0.7 s. The LiCl · 6D<sub>2</sub>O sample shows traces of crystalline material, which are due to the transfer to the cryochamber. The LiCl · 20D<sub>2</sub>O sample contains both crystalline and amorphous material.

### 4.3.2 Transformation upon annealing at ambient pressure

The ambient pressure study was carried out on the high-intensity two-axis neutron diffractometer D20 (Hansen et al., 2008c) at the high-flux reactor of the Institut Laue-Langevin (ILL, Grenoble, France). The monochromator was set to a wavelength of 1.87 Å with average resolution of  $\delta d/d = 3 \cdot 10^{-3}$ . The sample environment was a helium flow cryostat pre-cooled at 80 K, with a pressure of approximately 100 mbar of helium exchange gas. The powder sample was loaded into a cylindrical vanadium cell of 6 mm diameter kept under liquid nitrogen. During this experiment three solutions of different concentrations close to the eutectic one were measured. The one with the highest proportion of amorphous material was chosen for detailed analysis. Diffraction patterns were collected during warming from liquid nitrogen to room temperature in steps of approximately 20 K. Once the temperature was stabilized, data were collected for 40 minutes below 160 K and 20 minutes above 165 K. Empty vanadium cell, empty cryostat, and vanadium standard measurements were performed to normalize the spectra.

In order to remove the background contribution from the cryostat and correct for detector efficiency, the data were reduced using the formula

$$I_{\text{corr}}(q) = \frac{I_{\text{meas}}(q) - I_{\text{bg}}(q) - t(q) (I_{\text{ec}}(q) - I_{\text{bg}}(q))}{I_{\text{van}}(q) - I_{\text{bg}}(q) - t_{\text{van}} (I_{\text{ec}}(q) - I_{\text{bg}}(q))} \quad (4.4)$$

where  $I_{\text{meas}}$  is the intensity scattered by the sample,  $I_{\text{bg}}$  is the intensity scattered by the empty cryostat,  $I_{\text{ec}}$  the intensity scattered by the empty can,  $I_{\text{van}}$  is the intensity scattered by the can filled with vanadium standard,  $t_{\text{van}} = 0.96$  is the transmission of vanadium and  $t$  is the  $q$  dependent transmission of the sample ( $0.77 \leq t(q) \leq 0.78$ ). The data were normalised to a vanadium standard, measured in the same setup as our sample, in order to correct for the variations of detector efficiency at different angles. An example of collected data after background correction is shown in Figure 4.13, alongside the X-ray diffractogram and the neutron structure factor of pure D<sub>2</sub>O ice  $I_h$  simulated with Fullprof.

Figure 4.16 shows neutron diffraction patterns recorded during the annealing of our sample at ambient pressure. The spectrum at 90 K corresponds also to the dark blue data points in Figure 4.17. At low temperature the sample produced by quenching is largely amorphous. As mentioned above, the reflections of the remaining crystalline component (see Figure 4.13) correspond all to ice  $I_h$ . They were subtracted from the data collected during annealing to give the patterns in Figure 4.16. For the subtraction we took into account the  $q$  and temperature dependence of the Debye-Waller factor.

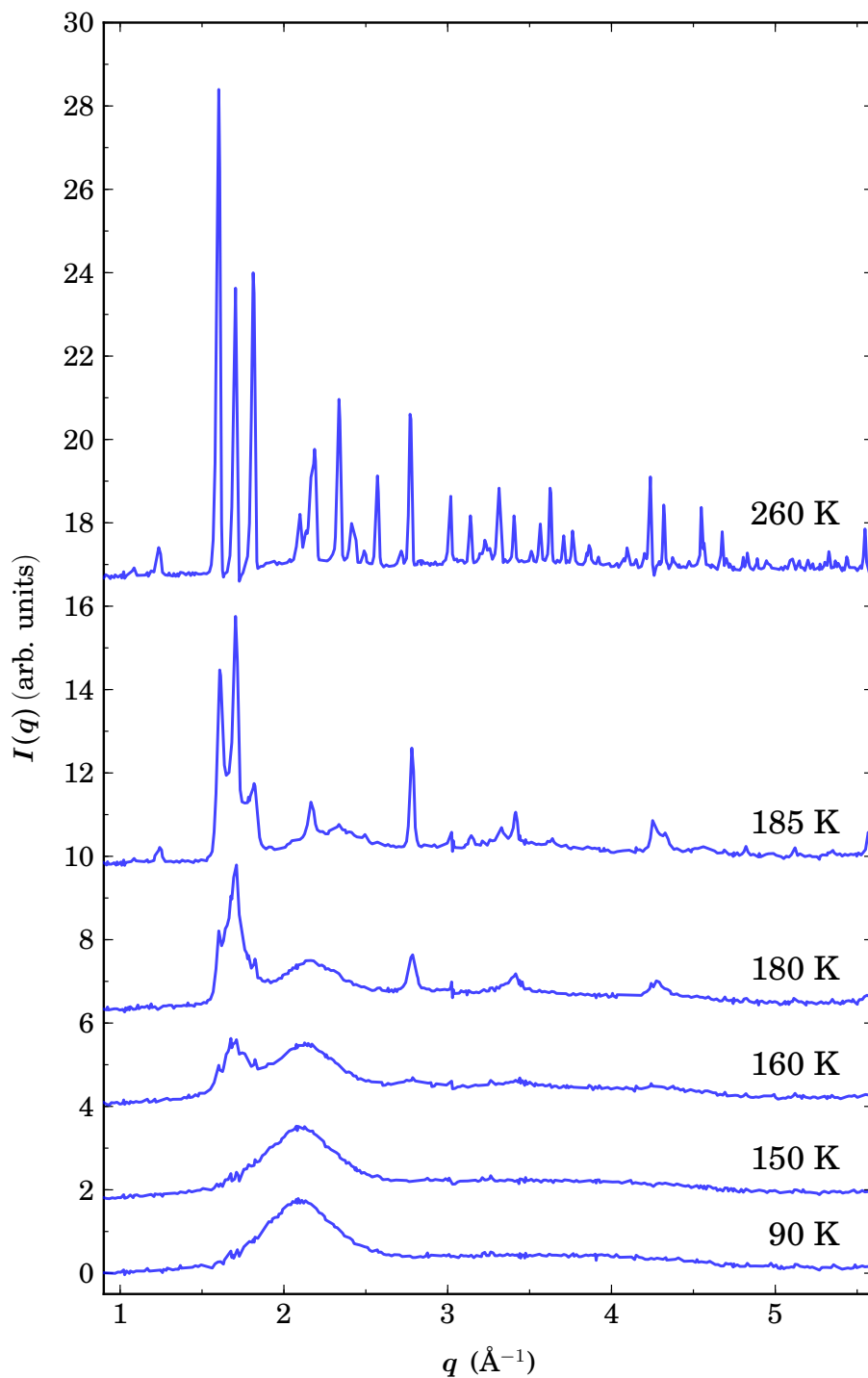


Figure 4.16: Neutron diffraction pattern of amorphous  $\text{NaCl} \cdot 10.2 \text{D}_2\text{O}$  measured at D20 (ILL) while heating at  $p = 100$  mbar. First “cubic ice” starts growing at 160 K, which then transforms into hexagonal ice at 185 K. Sodium chloride dideuterate appears at 185 K. At 260 K the spectrum shows a mixture of ice  $I_h$  and sodium chloride dideuterate. (Ludl et al., 2015)

$$I_{\text{am}}(q, T) = I_{\text{corr}}(q, T) - \frac{DW(q, T)}{DW(q, T_0)} \cdot I_{I_h, \text{fit}}(q, T_0) \quad (4.5)$$

where  $I_{\text{am}}$  is the structure factor of the amorphous part,  $I_{I_h, \text{fit}}$  is a fit of the peaks of ice  $I_h$  in the data, and  $T_0 = 80$  K. The Debye-Waller factor is given by  $DW(q, T) = D_0 \exp\left(-\frac{2}{3}q^2\langle u^2(T)\rangle\right)$  for ice  $I_h$ , with  $D_0$  being a constant and a linear estimate for the average mean square displacement  $\langle u^2(T)\rangle$  was interpolated from the experimental data quoted in (Petrenko and Whitworth, 1999, p. 24).

The data in Figure 4.16 show that the amorphous phase is stable up to 150 K. Upon warming “cubic ice” nucleates at 160 K and it transforms into hexagonal ice at 185 K. At about 185 K the amorphous  $\text{NaCl} \cdot 10.2\text{D}_2\text{O}$  solution dissociates into pure hexagonal ice and sodium chloride dideuterate.

The behaviour of our  $\text{NaCl} \cdot 10.2\text{D}_2\text{O}$  solution upon annealing at ambient pressure is analogous to that of LiCl solutions Elarby-Aouizerat et al. (1983). For these solutions of concentration in the vicinity of the metastable eutectic concentration (Prével et al., 1995), it has been observed that the water in excess is segregated in small clusters of most likely pure water, or lower concentration solution. These clusters are dispersed in a vitreous matrix of eutectic composition or higher concentration (Bove et al., 2013, Ruiz et al., 2014). These clusters are smaller than the critical ice nucleation cluster ( $\approx 100$  molecules according to simulations of Moore and Molinero (2011)). Upon annealing they amorphize as LDA which in turn transforms to a cubic ice phase at 160 K (Johari, 2005, Winkel et al., 2011b). At about 185 K the cubic ice phase transforms to hexagonal ice. The absence of peaks associated with hydrates or salts below 185 K, indicates that the vitrified solution remains metastable until the concentrated metastable liquid segregates into pure hexagonal ice and a salt hydrate (Elarby-Aouizerat et al., 1983, Ruiz et al., 2014).

The present set of experiments shows that amorphous  $\text{NaCl} \cdot 10.2\text{D}_2\text{O}$  can be produced by a fast quenching method. The structure of the quenched solution, shown in Figure 4.17, is in a dense form much more similar to the relaxed high density phase of pure water (e-HDA), than to its low density phase (LDA) produced by other quenching techniques. This is also the case for concentrated LiCl solutions (Bove et al., 2011b) and LiBr solutions as seen in the data from the experiment on the PLANET beamline at J-Parc, as shown in Figure 4.17. It is a consequence of the electrostrictive effect of sodium and lithium cations on water molecules. The usual tetrahedral coordination of water molecules, which is characteristic of the low density phases such as LDA and ice I, is highly distorted by the presence of ions in a way which is similar to the effect of pressure (Leberman and Soper, 1995, Mancinelli et al., 2007, Winkel et al., 2011b). It has been previously shown that salt inclusion

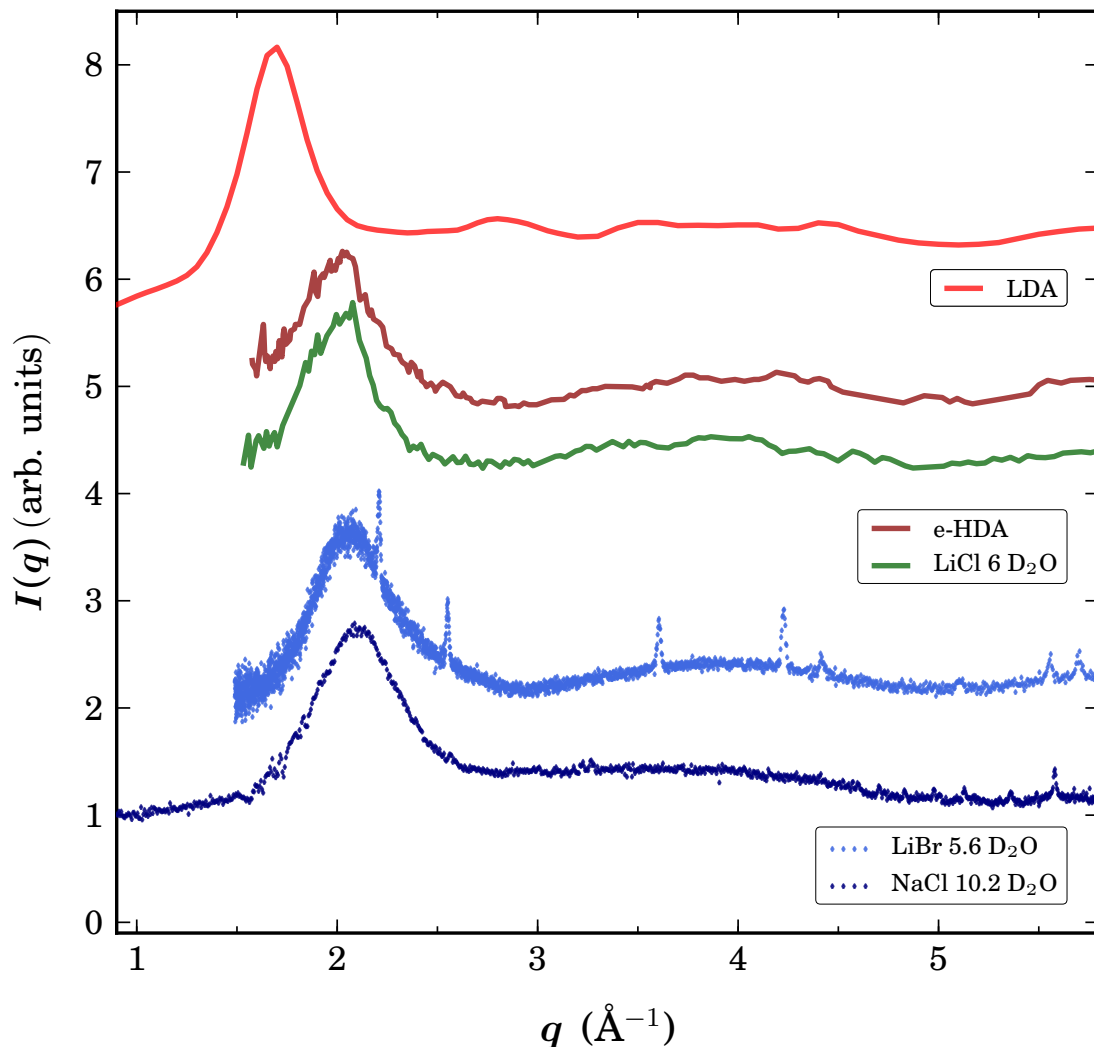


Figure 4.17: Neutron diffraction patterns of amorphous aqueous phases at low pressure. From bottom up: NaCl · 10.2D<sub>2</sub>O pattern measured on D20 at ILL (100 mbar), LiBr · 5.6D<sub>2</sub>O pattern measured on PLANET at J-Parc ( $p \leq 0.1$  GPa) LiCl · 6 D<sub>2</sub>O solution data at 1 bar (Bove et al., 2011b), pure water eHDA at 0.18 GPa (Nelmes et al., 2006) and LDA at 0.1 GPa (Bellissent-Funel et al., 1987). The position of the maximum of the first diffraction peak of NaCl · 10.2D<sub>2</sub>O is at  $2.1 \text{ \AA}^{-1}$  and for LiCl · 6D<sub>2</sub>O it is at  $2.015 \text{ \AA}^{-1}$ . The data show that NaCl, LiCl and LiBr solutions at ambient pressure closely resemble the high pressure amorphous phase of pure water (eHDA), rather than the low density amorphous phase (LDA).

in solid water, both in the amorphous water network or in the crystalline ice lattice, is possible in dense phases only (Bove et al., 2013, Le and Molinero, 2010, Ruiz et al., 2014). In the next chapter, the behaviour of the system at high pressures will be discussed, in particular the possibility of polyamorphism under high pressure and that of forming dense ice crystalline phases including ions in their lattice.

## 4.4 Summary

The quenching technique described in section 4.1.2 allows to amorphise solutions of NaCl and LiCl in water with an estimated quench rate of  $10^4$  to  $10^5$  K s<sup>-1</sup>. The best amorphous samples of NaCl solutions were obtained for  $R = 9.5$  in H<sub>2</sub>O and 10.2 in D<sub>2</sub>O. With solutions of NaCl in D<sub>2</sub>O a larger ratio of amorphous material to crystalline material than those in H<sub>2</sub>O. We have found that concentrated NaCl solutions amorphize at ambient pressure in a high density structure similar to HDA, as do LiBr and LiCl solutions. The behaviour upon annealing are common to both LiCl and NaCl solutions.



# Chapter 5

## High pressure Phases of $\text{NaCl} \cdot 10.2\text{D}_2\text{O}$

In our experiments we have followed paths 3, 4, 5, 6, 7, 8 in Figure 1.8. Here we discuss the results obtained along paths 3, 4, 5 and 6. Our simulations have explored these paths and also path 5. We present our results regarding the densification behaviour and structure of amorphous  $\text{NaCl} \cdot 10.2\text{D}_2\text{O}$  upon compression and the structure of the crystalline phases obtained upon annealing at 4 GPa.

### 5.1 Compression of amorphous $\text{NaCl} \cdot 10.2\text{D}_2\text{O}$

The amorphous states of pure water and  $\text{LiCl} \cdot 6\text{D}_2\text{O}$  show a polyamorphic transition between a high density amorphous (HDA) and a very high density amorphous form (VHDA). This is observed when they are annealed under pressure or when recovered samples, which have experience warming under pressure, are annealed at ambient pressure (Bove et al., 2011b, Klotz et al., 2005, Loerting et al., 2006).

Using the Paris-Edinburgh cell and neutron diffraction, we have studied the behaviour of amorphous  $\text{NaCl} \cdot 10.2\text{D}_2\text{O}$  upon compression to 4 GPa at 80 K and upon annealing under pressure, along the lines of the path followed by Bove et al. (2011b). The discussion below follows that given in Ludl et al. (2015).

#### 5.1.1 High-pressure neutron diffraction experiments

The high-pressure diffraction experiment was carried out at the time-of-flight PEARL beamline of the ISIS Facility pulsed neutron source in Didcot (United Kingdom) (PEARL, 2015). The pellets of pre-compressed powder (see chapter 4, section 4.2 for details) were split into two hemispheres and a small piece of lead was placed in between them to serve as a pressure calibrant. The reassembled pellet was subsequently loaded into a null-scattering titanium-zirconium encapsulating gasket (Mar-

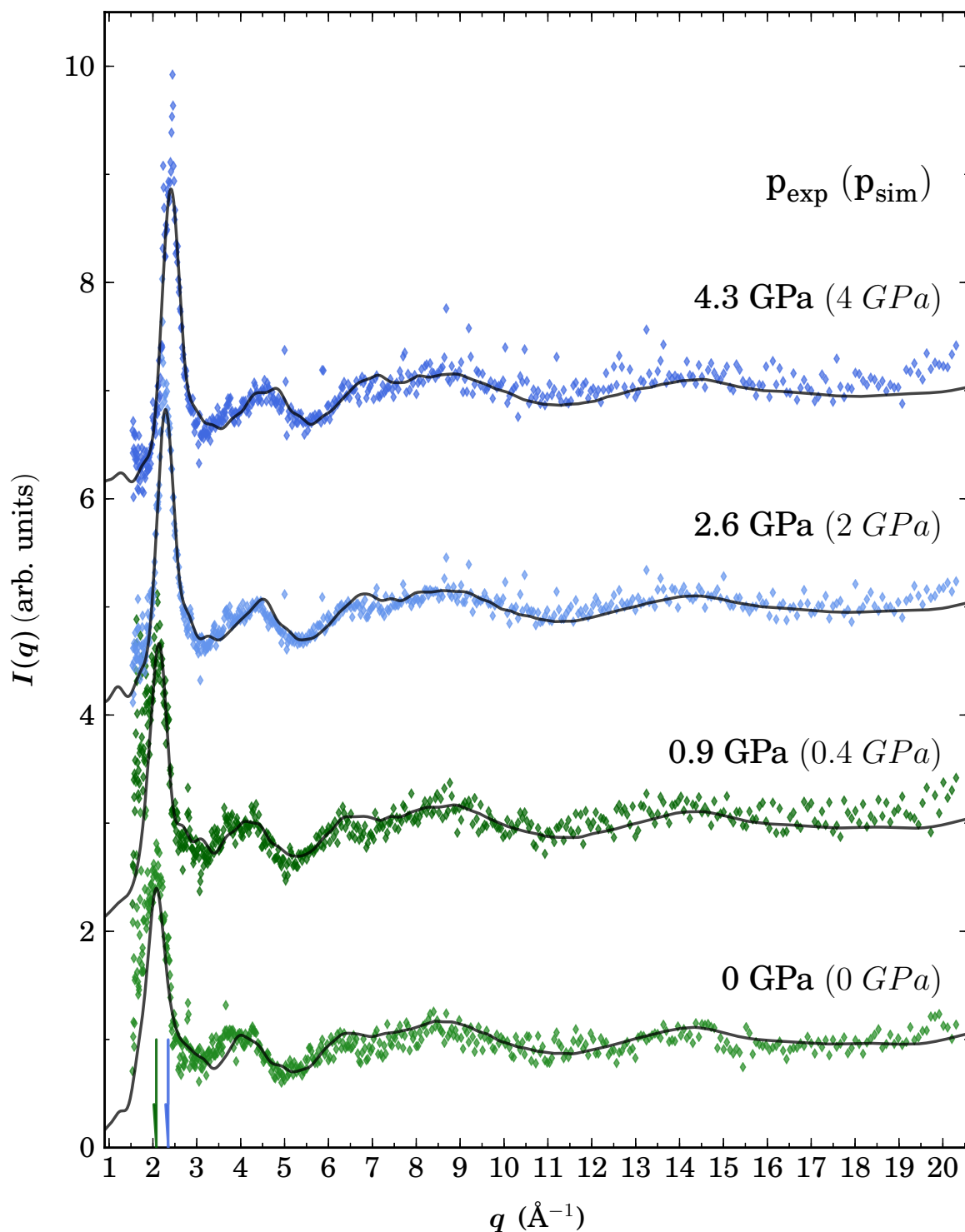


Figure 5.1: Neutron diffraction pattern upon compression of amorphous  $\text{NaCl} \cdot 10.2\text{D}_2\text{O}$  at 80K. Points are experimental data collected on PEARL (ISIS, UK) and lines are structure factors from MD simulations. The pressure in experiments and simulations are indicated on the right. During compression the structure factor of this amorphous phase changes smoothly.

shall and Francis, 2002), which had been pre-cooled to 80 K. The sample-gasket assembly was placed in pre-cooled sintered diamond anvils under liquid nitrogen, which were clamped before insertion into a pre-cooled V3 PEC. The initial sample volume was approximately 40 mm<sup>3</sup>. A liquid nitrogen cryostat was used in this experiment to cool the whole PEC. The cryogenic setup is that described in section 2.2 (chapter 2, page 46). The vanadium standard for this experiment was a sphere of vanadium of the same size as the sample. It was loaded into the gasket and the PEC in the same setup as the sample at ambient pressure and ambient temperature ( $I_{\text{van}}$  in equation (4.4)).

The gasket was sealed by applying a load of 80 kN on the anvils. The first scan was recorded at the initial load, corresponding to 0.5 GPa on the sample. Then pressure was increased in steps of about 0.5 GPa up to 4 GPa. Thereafter the sample was annealed up to 150 K at 4 GPa with a warming rate of  $\approx 20$  K hr<sup>-1</sup>. Subsequently, the load was reduced at 185 K in order to maintain the pressure close to 4 GPa on the sample. Data were collected continuously, with time slices of 1 hour being summed for the points along the thermodynamic paths 3 and 4 followed during the experiment as shown in Figure 1.8.

The diamond anvils scatter neutrons strongly and their contribution to the pattern needs to be subtracted, as described by equation (4.4) (chapter 4, page 95). The detector efficiency is corrected by calibrating with the vanadium standard. Subtracting the background is not a trivial task in measurements involving the PEC since the background depends on the anvils' separation and position in the beam. During compression the diamond peaks shift, mainly because the anvils move closer together. The intensity  $I_{\text{ec}}$  measured with an empty gasket mounted between the PE anvils at ambient pressure in the cryostat has to be shifted, to take into account the angular shift due to this displacement. We shifted  $I_{\text{ec}}$  by the median shift between the diamond peaks positions fitted for each pressure and the fitted positions at ambient pressure. The term  $I_{\text{bg}}$  in equation (4.4), which corresponds to the scattering by the sample environment, was negligible here compared to the other terms. The quality of the subtracted data can be appreciated in Figures 5.1 and 5.2 where the corrected spectra for representative pressure points are reported.

This sample also contains a fraction ( $\approx 10\%$ ) of hexagonal ice visible in the spectra as sharp peaks at ambient pressure. This part transforms during compression and its peaks shift, therefore the crystalline contribution has not been subtracted, unlike the ambient pressure data. In fact compression induces amorphization of the crystalline part into an HDA phase, which recrystallizes around 2 GPa in the ice VIII phase (Klotz et al., 2003).

Four samples were loaded into the cell. The first sample showed lead peaks. The 111, 200, 220, 311 and 222 peaks were fitted with PDIndexer (SETO et al.,

2010) to obtain the sample pressure, using the equation of state given by Strässle et al. (2014). Figure 5.3 shows the relation of pressure in the sample chamber to the gas pressure load on the piston for sample 1. The second sample suffered from bad loading and could not be measured. The third sample did not show lead peaks, the scans revealed solid nitrogen peaks during compression. The sample pressure was estimated using the calibration curve of pressure versus load (Figure 5.3) and checked using the nitrogen peaks ( $\delta$  and  $\beta$  phases) (Mills et al., 1986). The fourth sample showed both lead and nitrogen peaks.

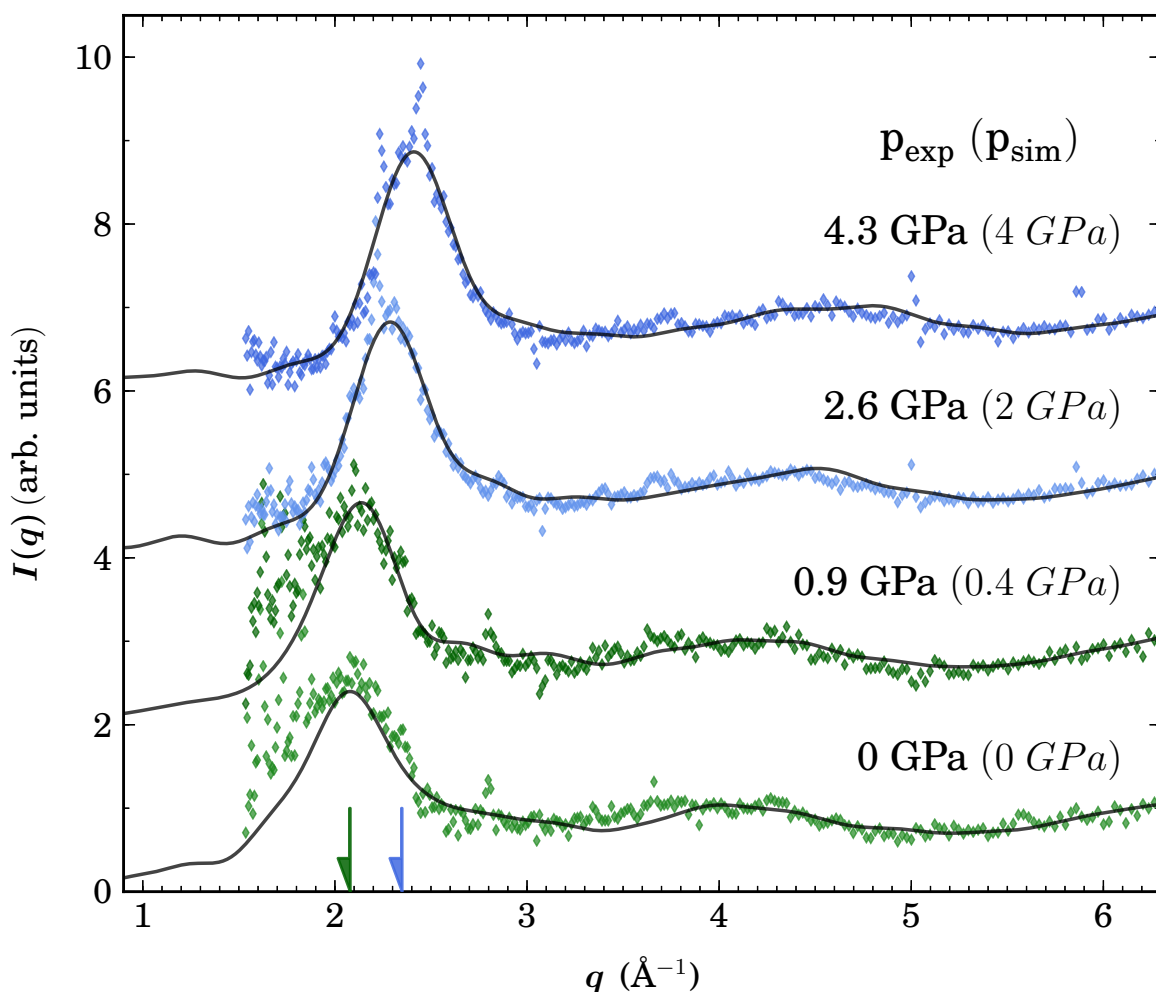


Figure 5.2: This is a zoom of the low  $q$  region of the neutron diffraction pattern upon compression of amorphous  $\text{NaCl} \cdot 10.2\text{D}_2\text{O}$  at 80K shown in Figure 5.1. Points are experimental data collected on PEARL (ISIS, UK) and lines are structure factors from MD simulations. The pressure in experiments and simulations are indicated on the right. The positions of the maxima of the first diffraction peak at 0 GPa ( $2.1 \text{\AA}^{-1}$  in green) and at 4 GPa ( $2.35 \text{\AA}^{-1}$  in blue) are indicated by arrows along the  $q$  axis in the inset.

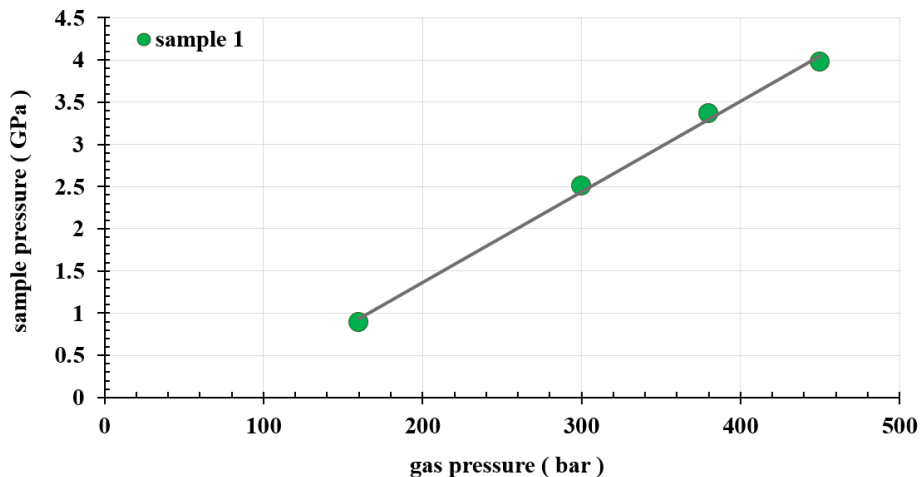


Figure 5.3: Sample pressure versus gas pressure applied on the piston for sample 1 measured on PEARL (ISIS, UK). The temperature was 80 K during compression to 450 bar. Sample pressure was obtained from fitting lead peaks (Miller indices 111, 200, 220, 311, 222). The line is a guide to the eye.

### 5.1.2 Densification under compression

The data collected during compression at 80 K (Figure 5.1 and 5.2), where the first feature of the amorphous sample shifts gradually to higher  $q$ , give a first indication that the sample shows no structural changes, a part from a continuous densification. The position of the first diffraction peak shifts continuously from  $2.08 \text{ \AA}^{-1}$  at low pressure to  $2.35 \text{ \AA}^{-1}$  at 4 GPa (Figure 5.4), and no other modification of the static structure factor is observed. This observation is confirmed by structure analysis obtained from our MD simulations (chapter 3, section 3.3.1). The first diffraction peak of the amorphous spectrum is an indication of density. Its shift with pressure in experiments and simulations increases smoothly with pressure (Figure 5.4).

This gradual densification of the structure during compression at 80 K (Figure 5.1) and annealing under high pressure (Figure 5.5) is in contrast to the stepwise change in the density found in pure water, where the transformation of LDA into HDA happens at 0.55 GPa (Mishima, 1994, Whalley et al., 1989). This stepwise change has also been observed in  $\text{LiCl} \cdot 6\text{D}_2\text{O}$ , where the transition from salty HDA to salty VHDA occurs at 140 K when annealing at 4 GPa.

In our simulations the density varies smoothly from  $\rho = 1.35 \text{ g.cm}^{-3}$  at ambient pressure and  $1.74 \text{ g.cm}^{-3}$  at 4 GPa. The structure factor changes gradually upon isothermal compression at 80 K and 140 K. It is almost unaffected upon annealing from 80 K to 140 K under high pressure (Figure 5.6). The change of slope in the enthalpy, which was calculated from our MD simulations along isothermal compression at both 80 K and 140 K (Figure 5.7), is also smooth. This further confirms the

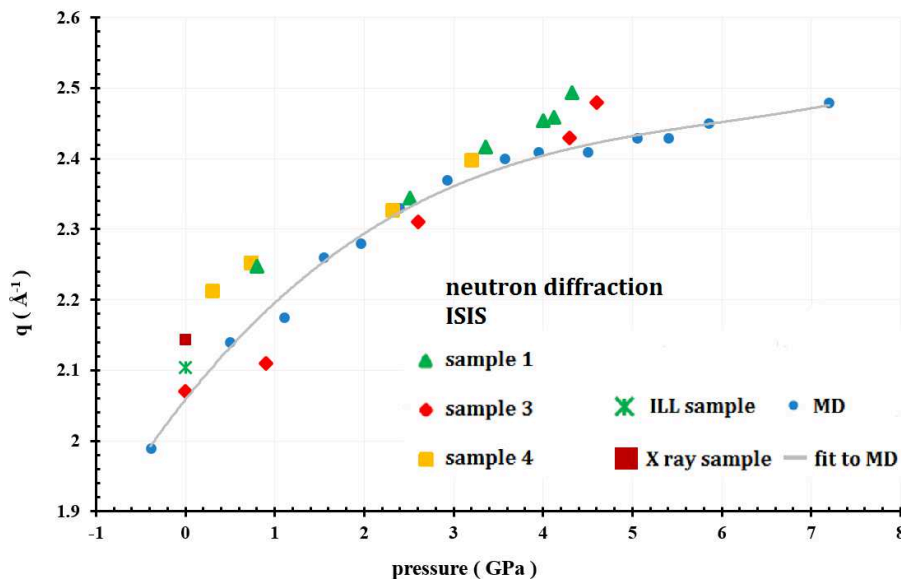


Figure 5.4: The position  $q$  of the first diffraction peak of the amorphous spectrum of  $\text{NaCl} \cdot 10.2\text{D}_2\text{O}$ . Green triangles, red diamonds and yellow squares are from our experiments on PEARL (ISIS, UK), the green x shaped symbol is from the measurement at ILL, the dark red square is from an X-ray measurement at IMPMC, blue circles from simulations. The line through the experimental points is a guide to the eye.

absence of a transition in the amorphous system.

Furthermore, the distribution of first neighbours around the cation (Figure 5.8), which was used to identify the observed transition from 4-fold to 6-fold coordination in amorphous  $\text{LiCl}$  solutions, is changing gradually with pressure here as well. This is discussed in the following section. Thus we find no evidence for polymorphism in our sodium chloride samples.

It is noteworthy that the total structure factors extracted from simulations match the experimental ones very well, as shown in Figures 5.1 and 5.2. The force fields of references (Dang and Chang, 1997, Tazi et al., 2012) had only been tested under ambient pressure previously, the agreement observed here for both the structure factor and the density shows that they are remarkably transferable to high-pressure conditions. The ability to reproduce the diffraction patterns allows us to extract additional information on the structure of the compound from our simulations.

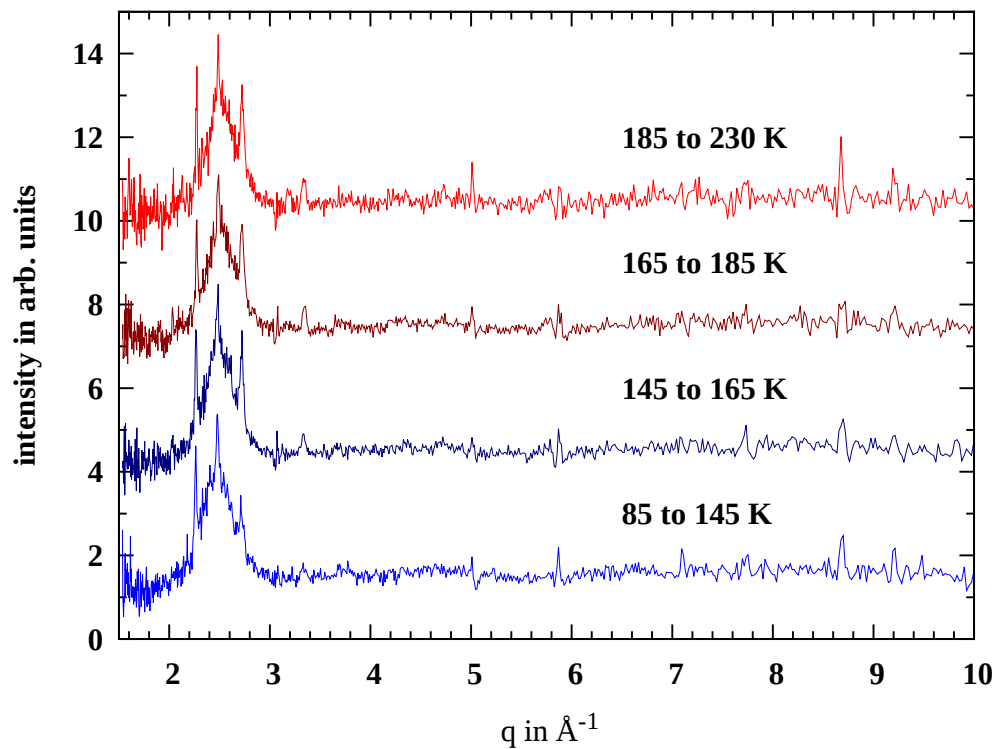


Figure 5.5: Experimental neutron diffraction pattern upon annealing of amorphous  $\text{NaCl} \cdot 10.2\text{D}_2\text{O}$  at 4 GPa. The data were collected on PEARL. The temperature is indicated on the right. The structure factor of this amorphous phase changes smoothly.

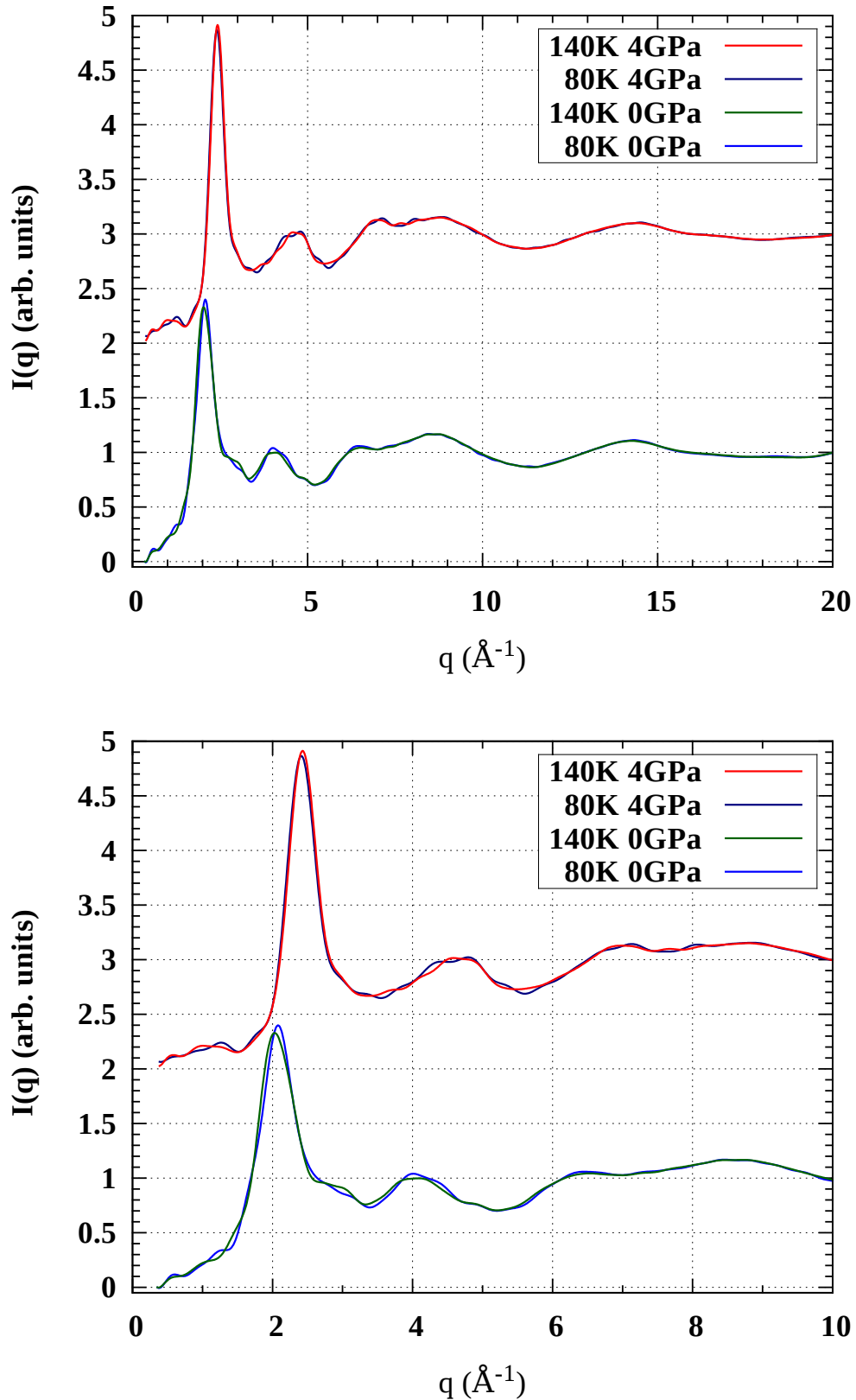


Figure 5.6: Structure factors of  $\text{NaCl} \cdot 10.2\text{D}_2\text{O}$  at 0 and 4 GPa from our MD simulations. At both pressures the data for 80 and 140 K are superposed to show that they barely change with temperature. The top panel shows the full  $q$  range and the bottom panel a zoom on the 0 to  $10 \text{ \AA}^{-1}$  region.

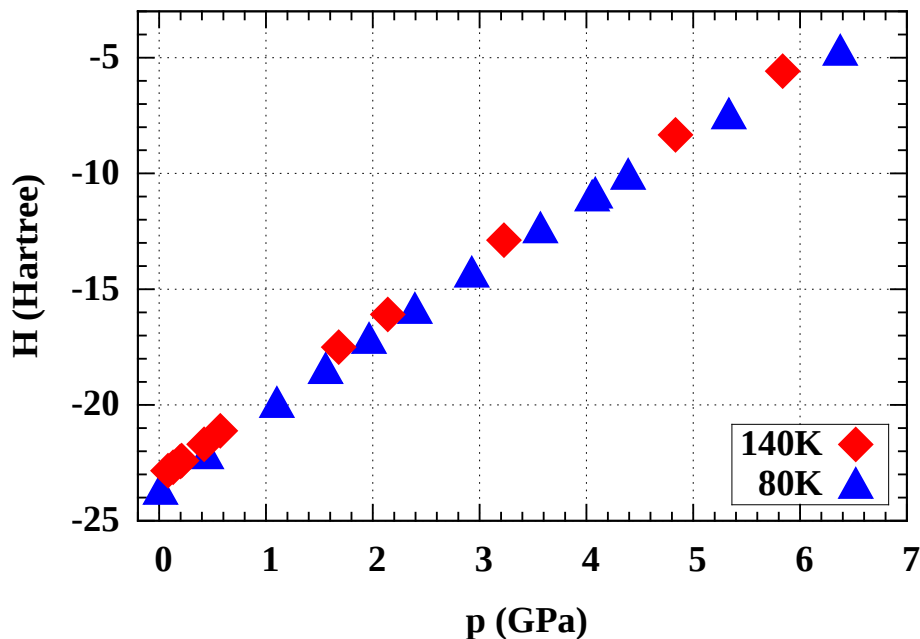


Figure 5.7: Pressure dependence of the enthalpy at 80 K (blue triangles) and 140 K (red diamonds) of the  $\text{NaCl} \cdot 10.2\text{D}_2\text{O}$  solution in our MD simulations. The lack of a variation in trend of the enthalpy confirms the absence of a transition in the amorphous system.

### 5.1.3 The role of $\text{Na}^+$ ions

In the highly concentrated solution that we study, almost all water molecules participate in the hydration of the ions. This can be seen in the oxygen-oxygen coordination number  $N_{\text{OO}}$ , which is close to 3 (Figure 5.8) over the whole pressure range, while  $N_{\text{OO}} \approx 4.3$  in pure water and dilute solutions (Mancinelli et al., 2007). More detailed analysis shows that  $N_{\text{ONa}}$  and  $N_{\text{OCl}}$  are both in the range of 0.5 to 0.6. This means that the number of oxygens having a  $\text{Na}^+$  neighbour is approximately equal to those with a  $\text{Cl}^-$  neighbour. Since water has four closest neighbours and is missing one neighbouring water molecule here, the missing neighbour is either  $\text{Na}^+$  or  $\text{Cl}^-$ . Hence half of the oxygen atoms hydrate  $\text{Na}^+$  and half of them hydrate  $\text{Cl}^-$ . The coordination numbers and radial distribution functions for  $\text{Na}^+$  (Figure 5.9) show a stronger pressure dependence, than those of  $\text{Cl}^-$  (Figure 5.10). Here we analyse the local environment of  $\text{Na}^+$  using the MD trajectories, and propose a scenario for the densification of the amorphous phase under compression.

The calculated  $g_{\text{OO}}$  (Figure 5.9) shows that, similarly to what is observed for the transformation of HDA into VHDA in pure water, the first neighbour shell of oxygen remains almost unchanged upon compression. Nevertheless in the present case the depth of the minimum at  $\approx 2.9 \text{ \AA}$  decreases less markedly than for pure water VHDA,

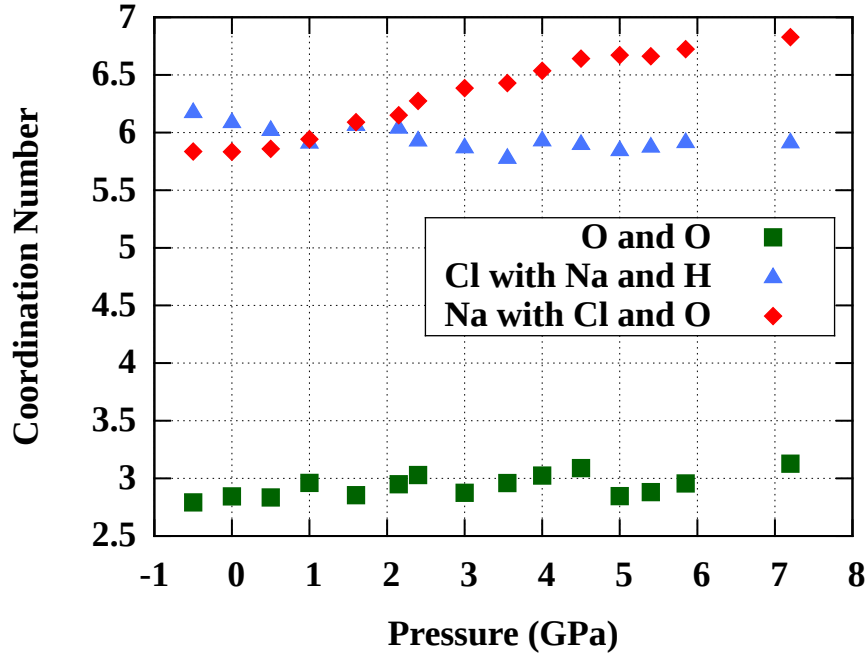


Figure 5.8: Average coordination numbers of oxygen with oxygen (dark green squares), chlorine with sodium and hydrogen (blue triangles), sodium with chlorine and oxygen (red diamonds) under isothermal compression at 80 K. The horizontal axis indicates MD pressure.

where the second peak becomes a shoulder of the first (Finney et al., 2002). The second neighbour shell changes more notably. The position of its maximum moves inwards, from 3.47 Å at ambient pressure to 3.07 Å at 4 GPa. The distribution of O-O-O angles (bottom right panel in Figure 5.9) between first neighbours of the central O, shows that the tetrahedral geometry (single peak at  $\approx 100^\circ$ ), which is still present in the HDA-like phase, is progressively distorted during compression. Above 2 GPa two peaks at  $70^\circ$  and  $120^\circ$  dominate and another peak appears at  $180^\circ$ . This has also been observed in pure water VHDA (Saitta et al., 2004). The changes in the shell of second neighbours are similar to those observed for VHDA of pure water formed at 3 GPa, where the second neighbours of O are compressed onto the first shell and distorted toward a nearly close-packed structure (Saitta et al., 2004).

Concerning the hydration of Na<sup>+</sup> ions it can be seen that the second peak in  $g_{\text{ONa}}$  at  $\approx 4.5$  Å flattens as pressure increases (relative to the first minimum the peak height drops by 25 %), while at the same time the first peak broadens in the 2.5 to 3 Å range. The inward shift of the second peak indicates that the second neighbours have moved closer to the cation. As for the  $g_{\text{OO}}$  discussed above, this means that the shell of second neighbours is progressively compressed onto the first one and distorted. Accordingly the distribution of the second peak broadens and

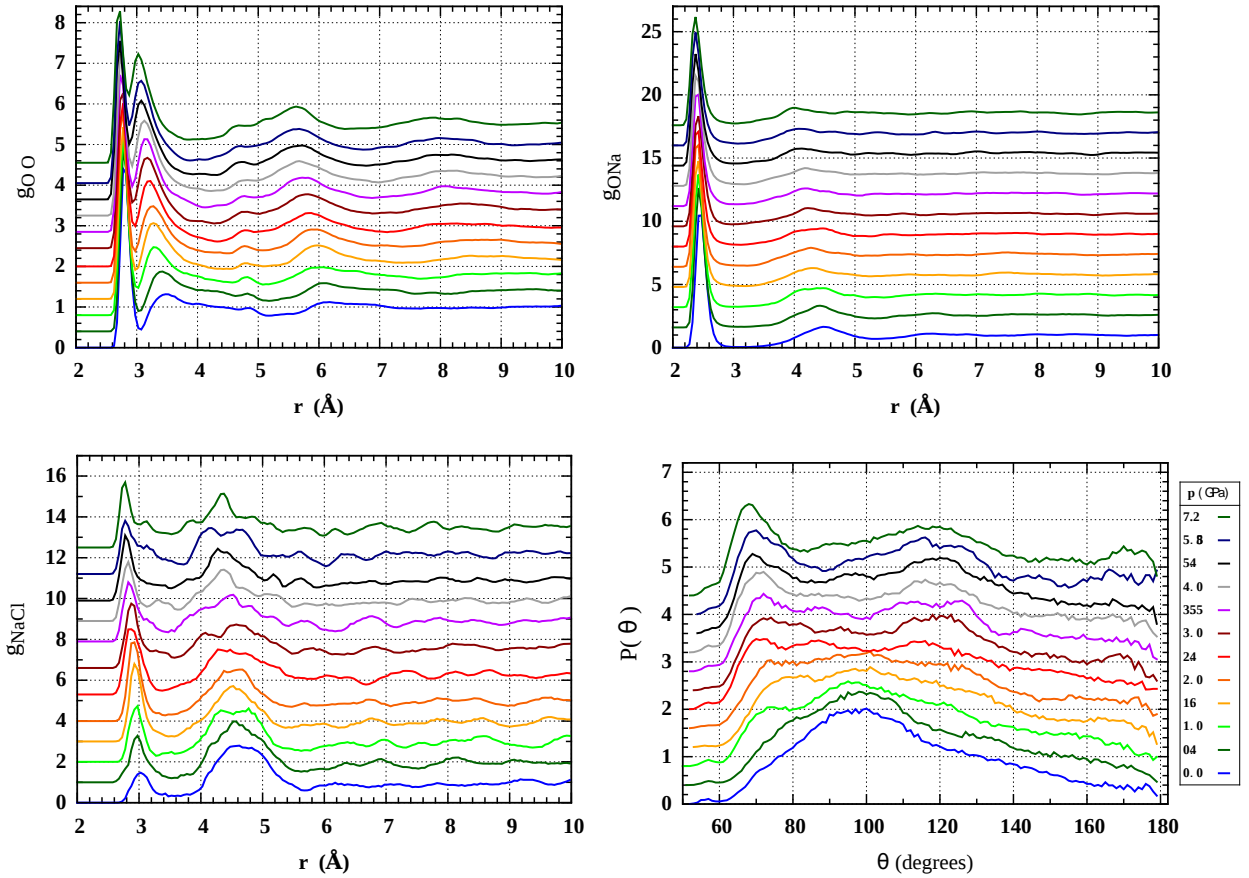


Figure 5.9: Pressure dependence of the RDFs  $g_{\text{OO}}$ ,  $g_{\text{ONa}}$ ,  $g_{\text{NaCl}}$  and the angular correlation function  $P(\theta)$  of O-O-O for amorphous  $\text{NaCl} \cdot 10.2\text{D}_2\text{O}$  solution during compression at 80K. These quantities were obtained from our MD simulations. In  $g_{\text{OO}}$  the second peak shifts toward the first, although the minimum remains more pronounced than during the transition of HDA to VHDA in pure water. In  $g_{\text{ONa}}$  the second peak flattens with increasing pressure. In  $g_{\text{NaCl}}$  the first peak increases indicating that ions tend to have counterions in their shell of first neighbours at higher pressures. The evolution of  $P(\theta)$  shows that the tetrahedral geometry of the water network is progressively distorted during compression.

flattens.

Figure 5.10 shows the RDFs  $g_{\text{OCl}}$ ,  $g_{\text{HCl}}$  which probe the hydration of  $\text{Cl}^-$  ions. It can be seen that the minimum of  $g_{\text{OCl}}$  separating the shells of first and second neighbours of  $\text{Cl}^-$  disappears during compression. This similar to the changes of  $g_{\text{OO}}$  upon compression of pure water HDA (Finney et al., 2002). The second peaks becomes a shoulder of the first one. The  $g_{\text{HCl}}$  displays a broadening of the second peak with pressure.

The evolution of average coordination numbers for isothermal compression at 80 K reported in Figure 5.8 shows that upon densification the shell of first neighbours of sodium ions is more strongly affected than those of oxygen and chlorine.

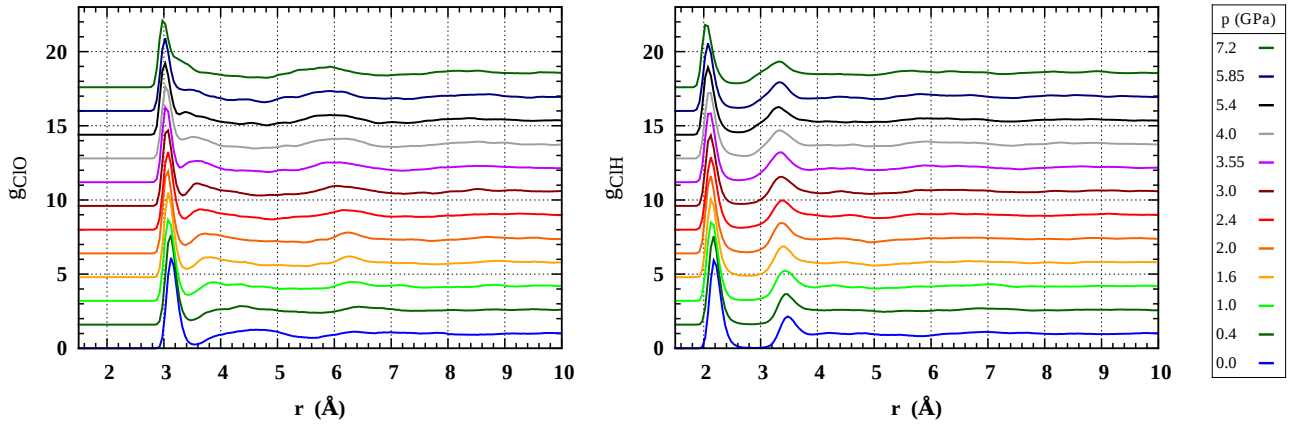


Figure 5.10: Pressure dependence of RDFs  $g_{\text{OCl}}$ ,  $g_{\text{HCl}}$  of amorphous  $\text{NaCl} \cdot 10.2\text{D}_2\text{O}$  solution during compression at 80K in our MD simulations. In  $g_{\text{OCl}}$  the second peak progressively becomes a shoulder of the first peak with increasing pressure. In  $g_{\text{HCl}}$  the second peak broadens with increasing pressure.

The coordination number of sodium with either chlorine or oxygen (*i.e.*  $N_{\text{NaO}} + N_{\text{NaCl}}$  using the notation of equation 3.26) is stable at about 6 up to 2 GPa, which corresponds to octahedral coordination shells. Then it increases nearly linearly with pressure, reaching a value of 6.8 at 7.2 GPa. This is again in contrast to the  $\text{LiCl}$  case, where the coordination number of lithium with oxygen and chlorine increased step-wise from 4.25 at ambient pressure to 5.1 above 2 GPa (Bove et al., 2011b). Since  $\text{Li}^+$  ions are small ( $r_{\text{Li}^+} = 0.9 \text{ \AA}$ , Shannon (1976)) they can be fully hydrated by 4 water molecules at ambient pressure. Larger  $\text{Na}^+$  ions ( $r_{\text{Na}^+} = 1.16 \text{ \AA}$ , Shannon (1976)) have octahedral hydration shells at ambient pressure, which are more resilient under compression. The lack of a sudden transition in coordination of the  $\text{Na}^+$  cation is consistent with the absence of a polyamorphic transition. The analysis of the distribution of coordination populations (Figure 5.11) shows that at pressures below 2 GPa almost all sodium ions remain 6-fold coordinated. Above 5 GPa the dominant population (50 %) is 7-fold coordination, with about 30 % of ions being 6-fold coordinated, and 10 to 15 % being 8-fold coordinated. The typical local environment of  $\text{Na}^+$  and the distributions of  $N_{\text{NaO}}$  and  $N_{\text{NaCl}}$  at 0 and 5.4 GPa are shown in Figure 5.12. Finally, the coordination numbers of oxygen with oxygen ( $N_{\text{OO}}$ ) and of chlorine with sodium and hydrogen ( $N_{\text{ClNa}} + N_{\text{ClH}}$ ) are only weakly affected by pressure and remain nearly constant up to 6.5 GPa.

The distribution functions for the first eight neighbours of  $\text{Na}^+$  (Figure 5.13) show two regimes of compression. In the first one up to 2 GPa, the octahedra are compacted as seen in the distribution of the six nearest neighbours of  $\text{Na}^+$  which move closer toward the center of the octahedron. The first four neighbours, which

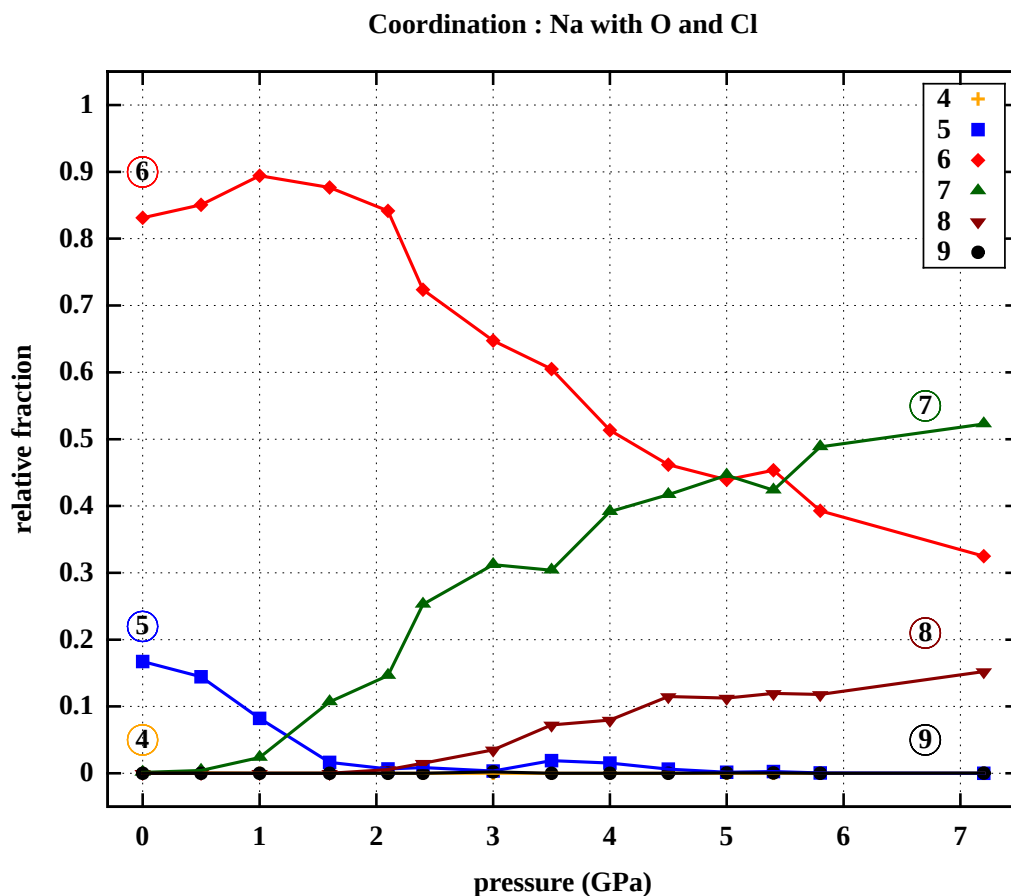


Figure 5.11: Evolution of the distribution of coordination of sodium with oxygen and chlorine for isothermal compression simulated at 80 K (the value of the pressure is that of the simulation). Six distinct populations are shown, the numbers in circles indicate the coordination number of each population. The fraction of 6 fold coordinated atoms decreases, while the fractions of 7 and 8 fold coordinated atoms increase with pressure.

occupy the region between 2.2 and 2.6 Å from the central ion, move inwards by 0.05 Å, the fifth by 0.07 Å and the sixth by 0.09 Å. In the second regime above 2 GPa the first five neighbour peaks broaden but do not shift, the sixth one broadens markedly and shifts outwards slightly. This is consistent with the seventh neighbour moving inward from a distance of 3.9 Å at low pressure to 2.6 Å above 2 GPa, thereby distorting the octahedron and eventually breaking it up. The eighth neighbour moves inward from 4.1 to 3.4 Å and the corresponding peak broadens markedly, but remains largely in the second neighbours shell region. Above 4 GPa the distributions of the first six neighbours do not show appreciable changes; the increase in the 2.6 Å peak of the seventh neighbour distribution confirms the increase in coordination.

The changes in the angular distribution functions are consistent with this sce-

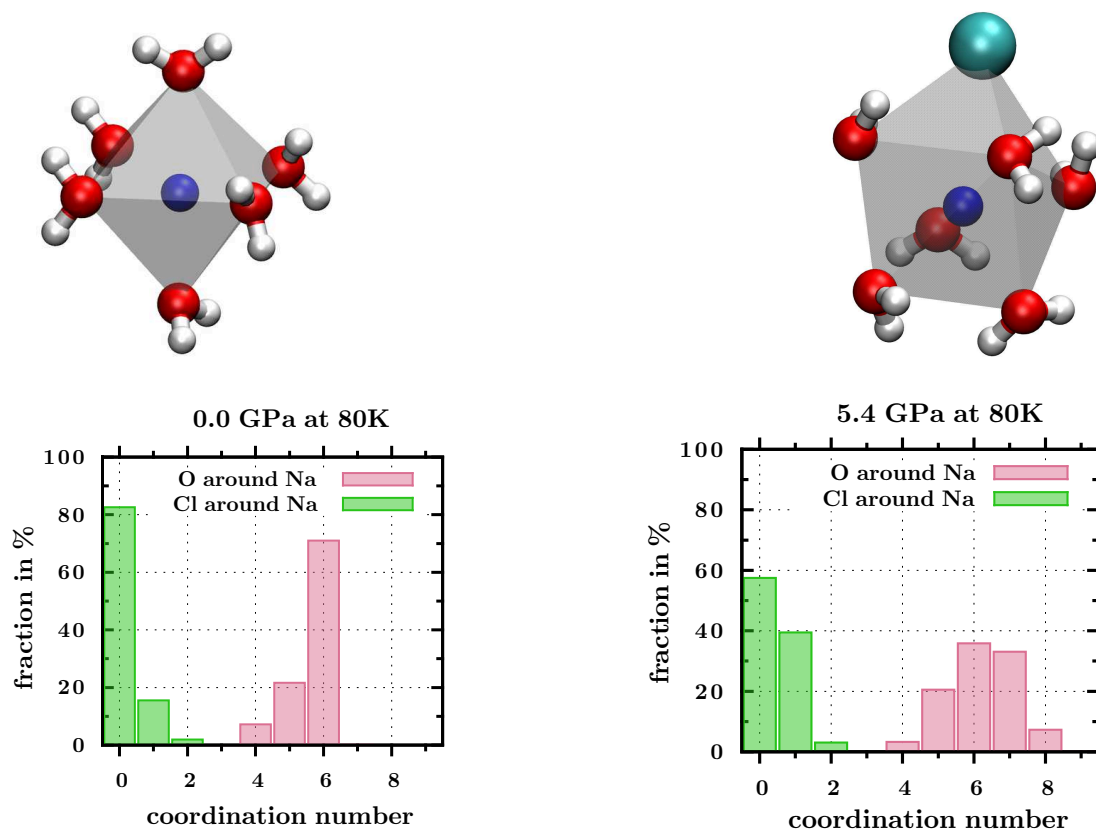


Figure 5.12: Above: Representations of the local environment of  $\text{Na}^+$  which is octahedral at low pressure and forms an irregular distorted polyhedron at pressures above 4.5 GPa in our simulations. Below: The distribution of  $N_{\text{NaO}}$  and  $N_{\text{NaCl}}$  for the sodium ions at 0.0 GPa (left) and 5.4 GPa (right).

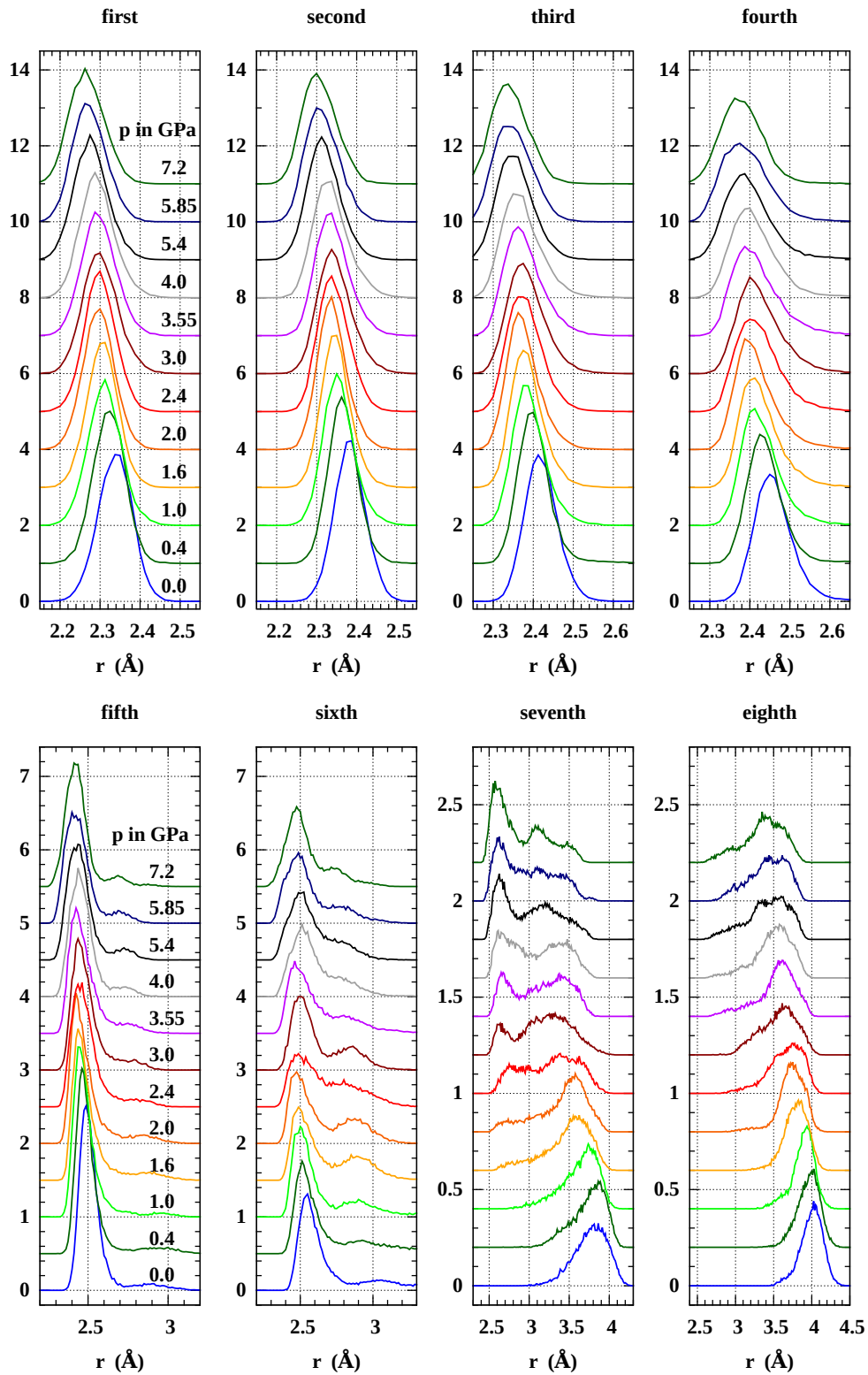


Figure 5.13: Evolution with pressure of distance distribution of eight closest neighbours (O and  $\text{Cl}^-$ ) to  $\text{Na}^+$  ions, where  $r$  is the distance to the sodium ion. The seventh and eighth neighbour move into the shell of first neighbours above 2 GPa.

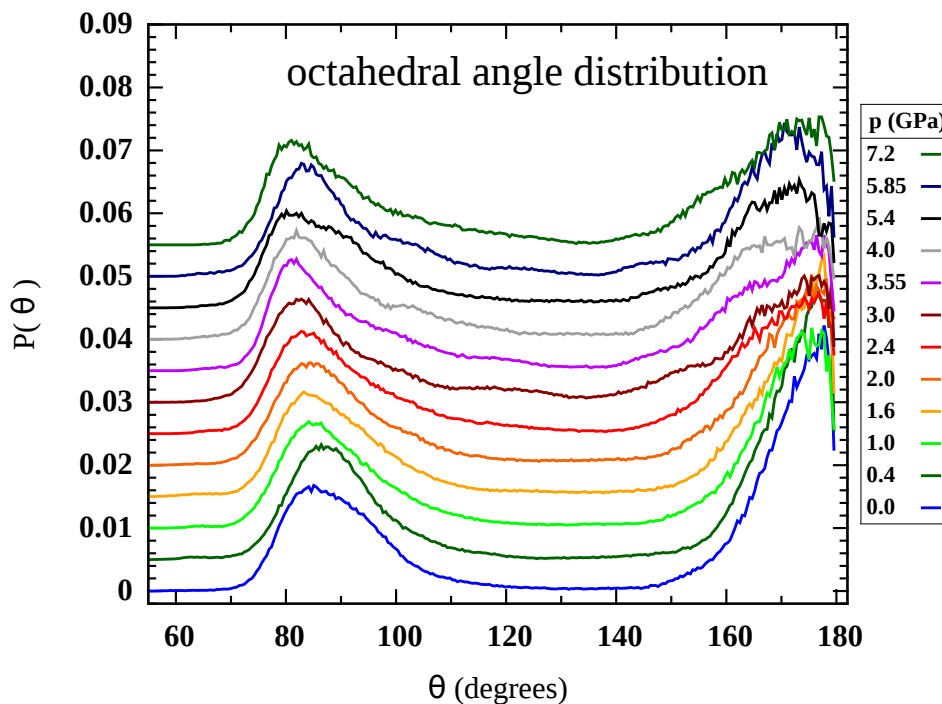


Figure 5.14: Evolution with pressure of the distribution of octahedral angles, which are the angles at the central  $\text{Na}^+$  ion between atoms at the corners of the octahedron formed by the six nearest neighbours.

nario. Figure 5.14 shows the distribution of octahedral angles (the angles at the central ion between atoms at the corners of the octahedron), it has one peak near  $90^\circ$  and one near  $180^\circ$ . In the first regime, up to 2 GPa, where the octahedra are compressed, the first peak shifts to smaller angles, from  $87^\circ$  to  $82^\circ$ . Above 2 GPa the first peak does neither shift nor broaden, the second peak broadens noticeably and shifts toward smaller angles ( $\approx 170^\circ$ ), which indicates that the octahedral geometry of the  $\text{Na}^+$  hydration shell is perturbed when the seventh neighbour starts to move inwards. The angles between  $100^\circ$  and  $140^\circ$  are populated above 3 GPa.

### 5.1.4 Conclusion

We have found that concentrated  $\text{NaCl}$  solutions transform continuously from an HDA structure to a more dense one upon compression and annealing under high pressure. The agreement between the structure factors obtained in high pressure neutron diffraction experiments and classical MD simulations using polarizable potentials is remarkably good. No evidence for polyamorphism was found, neither under compression nor under annealing at high pressure. This suggests that the polyamorphic phenomenon observed in pure water and aqueous  $\text{LiCl}$  solutions is not a general feature of electrolytic aqueous solutions. The absence of such a polyamorphic transition is ascribable to the six-fold coordination of  $\text{Na}^+$  ions already at ambient pressure.

Densification occurs first by compression of the octahedral coordination shells of  $\text{Na}^+$  ions, followed by a progressive distortion of the octahedra at pressures above 2 GPa. This is in contrast to what is observed in  $\text{LiCl}$  solutions where  $\text{Li}^+$  shows tetrahedral coordination which abruptly breaks up near 2 GPa, giving rise to a transition to a 6-fold coordinated structure (Bove et al., 2011b). The structure of ice VII is made of a body centered cubic oxygen lattice. Therefore the increase in the fraction of 8-fold coordinated ions with pressure, observed in simulations, suggests that,  $\text{Na}^+$  ions would most likely occupy a substitutional site of the body centered cubic ice VII lattice formed by the oxygen atoms. Whereas  $\text{Li}^+$  ions filled an interstitial site in the ice lattice (Klotz et al., 2009).

## 5.2 Crystalline phases

First, we present the crystallisation behaviour of amorphous  $\text{NaCl} \cdot 10.2\text{D}_2\text{O}$  solution during annealing at high pressure. We discuss the transformations of the sample and the possibility of salt inclusion in the ice lattice. Second, the experimental data are compared to a structural model of ice VII with salt ions substituted for water molecules, which was studied by atomistic simulations.

### 5.2.1 Crystallisation upon annealing

During our high-pressure neutron diffraction experiment on PEARL three samples of  $\text{NaCl} \cdot 10.2\text{D}_2\text{O}$ , which will be called sample 1, 3 and 4 in the following, were annealed at pressures in the range of 2 to 4 GPa. The pressure at 260 K was 3.9 GPa in sample 1, 3.5 GPa in sample 3 and 2.25 GPa in sample 4.

All spectra shown below contain the peaks of the sintered diamond anvils, which were fitted together with the other phases. The Rietveld fits of crystalline phases in these spectra were done in GSAS and its graphical interface EXPGUI, using time-of-flight profile function 1 (Larson and Von Dreele, 1994, Toby, 2001). The structures of ices VII and VIII were taken from the work of Kuhs et al. (1984) and Jorgensen and Worlton (1985). The phase diagram of Mills et al. (1986) was used to determine the pressure in the sample chamber by fitting the  $\beta$  and  $\delta$  phases of  $\text{N}_2$ , whose structures were taken from Streib et al. (1962) and Stinton et al. (2009) respectively. Where lead peaks were visible, these were fitted and the EOS of Strässle et al. (2014) was used. A GSAS figure showing the ticks for all phases is shown in Figure A.2 in appendix A.1.2.

The sample pellets were loaded into the assembly of gasket and anvils bathing in liquid nitrogen. Some nitrogen is likely to have been introduced into the sample chamber during loading, when the gaskets were doused with liquid  $\text{N}_2$  just before placing the pellets in the anvils.

The annealing of sample 1 is shown in Figure 5.15. The pressure was determined from the lead peaks which are present all along the low temperature compression and annealing (first peak at  $2.25 \text{ \AA}^{-1}$ ). Ice VII crystallized at 260 K during annealing at  $\approx 4$  GPa. Ice VIII forms from the pure VHDA at 120 K and grows slightly until 260 K when the salty amorphous matrix crystallizes. Figure 5.16 shows the fit and the data at 295 K and 3.9 GPa. The fit shown accounts for ice VII, the diamond,  $\beta \text{ N}_2$  and lead have also been fitted but are not shown here. The fit for lead gives a lattice parameter of  $4.824 \pm 0.0012 \text{ \AA}$ , which using the EOS of lead by Strässle et al. (2014) corresponds to a pressure of  $3.94 \pm 0.06$  GPa. This is confirmed by the

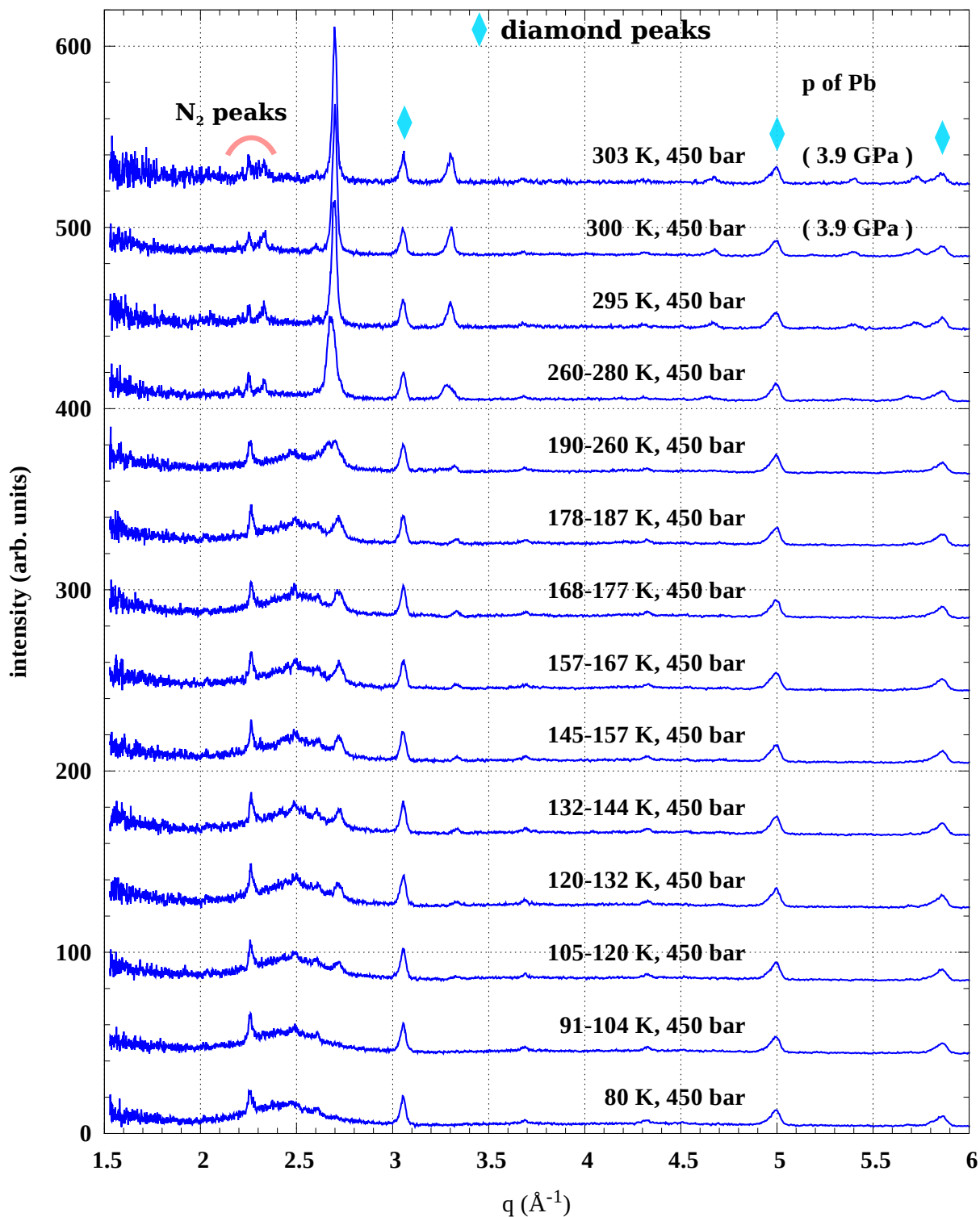


Figure 5.15: Experimental diffraction patterns of the annealing of sample 1 at  $\approx 3.9$  GPa. In this sample ice VII crystallizes at 260 K. The temperature and gas pressure are indicated for each scan. The sample pressure determined from the fit of lead peaks is indicated on the top two scans. Diamond and nitrogen peaks are indicated. The data are offset in increments of 50 along the ordinate axis for clarity.

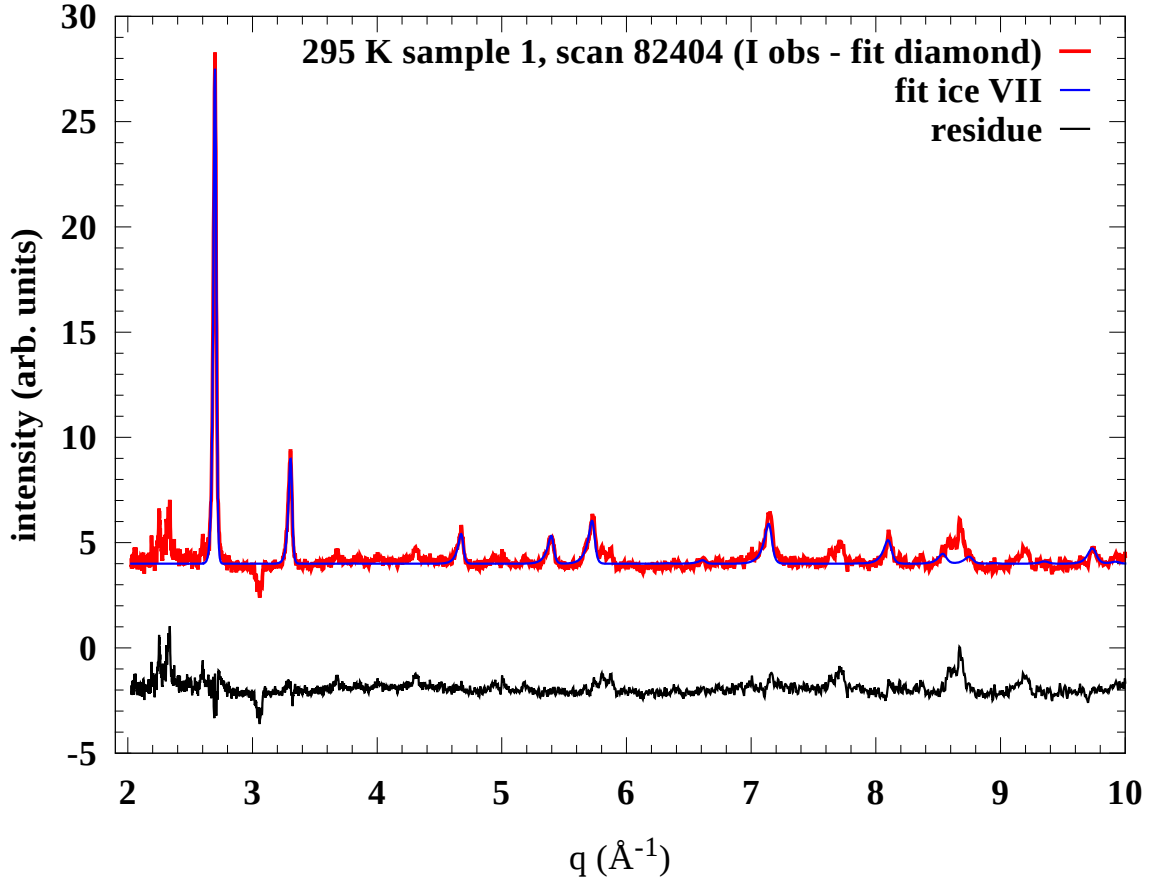


Figure 5.16: Data and fit and residue for sample 1 at 295 K and 3.9 GPa. The fit of diamond peaks has been subtracted from the data. The fit shown contains ice VII.

fit for the  $\beta$  phase of  $\text{N}_2$ , ( $a = 5.826 \text{ \AA}$ ,  $c = 3.525 \text{ \AA}$ ,  $V = 62.70 \text{ \AA}^3$ ) corresponding to a pressure of 3.8 GPa. The fit of ice VII ( $\chi^2 = 1.130$ ) gives a lattice parameter  $a = 3.28912 \pm 0.00014 \text{ \AA}$  for the cubic unit cell of the oxygen lattice. According to the EOS of Fortes et al. (2012) for ice VII, this corresponds to a pressure of 3.9 GPa. The EOS gives a lattice parameter of  $a = 3.2928 \text{ \AA}$  at 3.8 GPa. The relative variation is  $\Delta a/a = 0.0011$  and  $\Delta V/V = 0.0033$ . The full width at half maximum (FWHM) of the first ice VII peak at  $2.7 \text{ \AA}^{-1}$ , was determined by a fit to be 0.0278 at 295 K and 3.9 GPa. Whether or not this sample is pure ice VII or ice VII including  $\text{Na}^+$  and  $\text{Cl}^-$  ions cannot be established unequivocally with the available data. The ice VIII formed from the VHDA at 120 K, which is expected not to contain ions, has transformed to pure ice VII. Its peaks would overlap with those of the ice crystallised at 260 K, which could explain why the peak is large. Small NaCl peaks may be visible (at  $\approx 3.9$ , 4.1 and  $5.2 \text{ \AA}^{-1}$ ) in the scan at 295 K, but they are weak and are difficult to resolve.

The annealing of sample 3 is shown in Figure 5.17. Details of the crystallisation of sample 3, are shown in Figure 5.18, for the scans from 185 to 290 K. At temperatures below 260 K the spectra show peaks of the  $\delta$  phase of  $N_2$  (peaks at 2.2, 2.5 and 2.7  $\text{\AA}^{-1}$ ) on top of the amorphous features of  $\text{NaCl} \cdot 10.2\text{D}_2\text{O}$ . In this sample the pressure, determined from  $N_2$  peaks, varies from 2.8 to 4.2 GPa upon annealing. This is due to the fact that the annealing is isochoric, the specific volume increases with temperature and decreases with pressure, so pressure will increase when temperature increases at constant volume. The peak at 2.7  $\text{\AA}^{-1}$  appearing at 140 K shows that Ice VIII forms from the pure VHDA contained in the sample. Before crystallisation the pressure from the  $\delta$  phase of  $N_2$  is 4.2 GPa. At 260 K the  $\delta$  phase transforms into the  $\beta$  phase (new peaks at 2.0, 2.2 and 2.3  $\text{\AA}^{-1}$ ) and the amorphous  $\text{NaCl} \cdot 10.2\text{D}_2\text{O}$  nucleates ice (peaks at 2.65 and 3.25  $\text{\AA}^{-1}$ ). Upon crystallisation of ice VII the pressure, now determined from the peaks of the  $\beta$  phase, drops to 3.5 GPa. The peaks of ice grow from 260 to 290 K. The first ice VII peak at 2.65  $\text{\AA}^{-1}$  is broader here than what is normally observed in pure ice VII, its FWHM is 0.0297  $\text{\AA}^{-1}$ . Weak salt or hydrate peaks might have appeared at 3.8, 4.0 and 5.17  $\text{\AA}^{-1}$  at 290 K and 3.5 GPa.

In both samples 1 and 3 the crystallisation of the amorphous solution sets in at about 260 K (Figure 5.17), close to the phase boundary of ice VIII and VII (270 K). This is very close also to the nucleation temperature of salty ice VII (265 K) from the amorphous  $\text{LiCl} \cdot 6\text{D}_2\text{O}$  at 4 GPa (Klotz et al., 2009).

The fit of sample 3 at 260 K and 3.65 GPa is shown in Figure 5.19. The fit shown accounts for ice VII, the diamond and  $\beta$   $N_2$  have also been fitted but are not shown here. No peaks of lead are visible. The fit of ice VII with GSAS ( $\chi^2 = 2.775$ ) gives a lattice parameter  $a = 3.298572 \pm 0.00008 \text{\AA}$ , which corresponds to a pressure of 3.625 GPa in pure ice (Fortes et al., 2012). The pressure of the nitrogen phase (3.68 GPa) and ice VII phase agree to less than 0.1 GPa. Although the lattice parameter agrees with that of pure ice VII at this pressure, the ice phase may contain a (small) fraction of salt. If the ions substitute water molecules and occupy oxygen sites, this might explain the lack of expansion of the lattice parameter. Another fit of scans 82430-33 of sample 3 was done in GSAS. It used a model of ice VII in which  $\text{Na}^+$  and  $\text{Cl}^-$  ions substitute water molecules with a probability of 1/12.2 each. Since this fit yielded a roughly equal but slightly larger  $\chi^2$  value, it is not reported here. It can be found in the appendix A.1.3.

Next, the sample was cooled down from 290 to 230 K to see whether it would transform to ice VIII, as shown in the top panel of Figure 5.20. Ice VIII is a hydrogen ordered phase, hence we expect that the transition does not occur if the salt is included in the ice structure, as is the case in ice VII that contains LiCl salt (Klotz et al., 2009). In sample 3 the splitting of the 110 and 211 peaks is not clear-

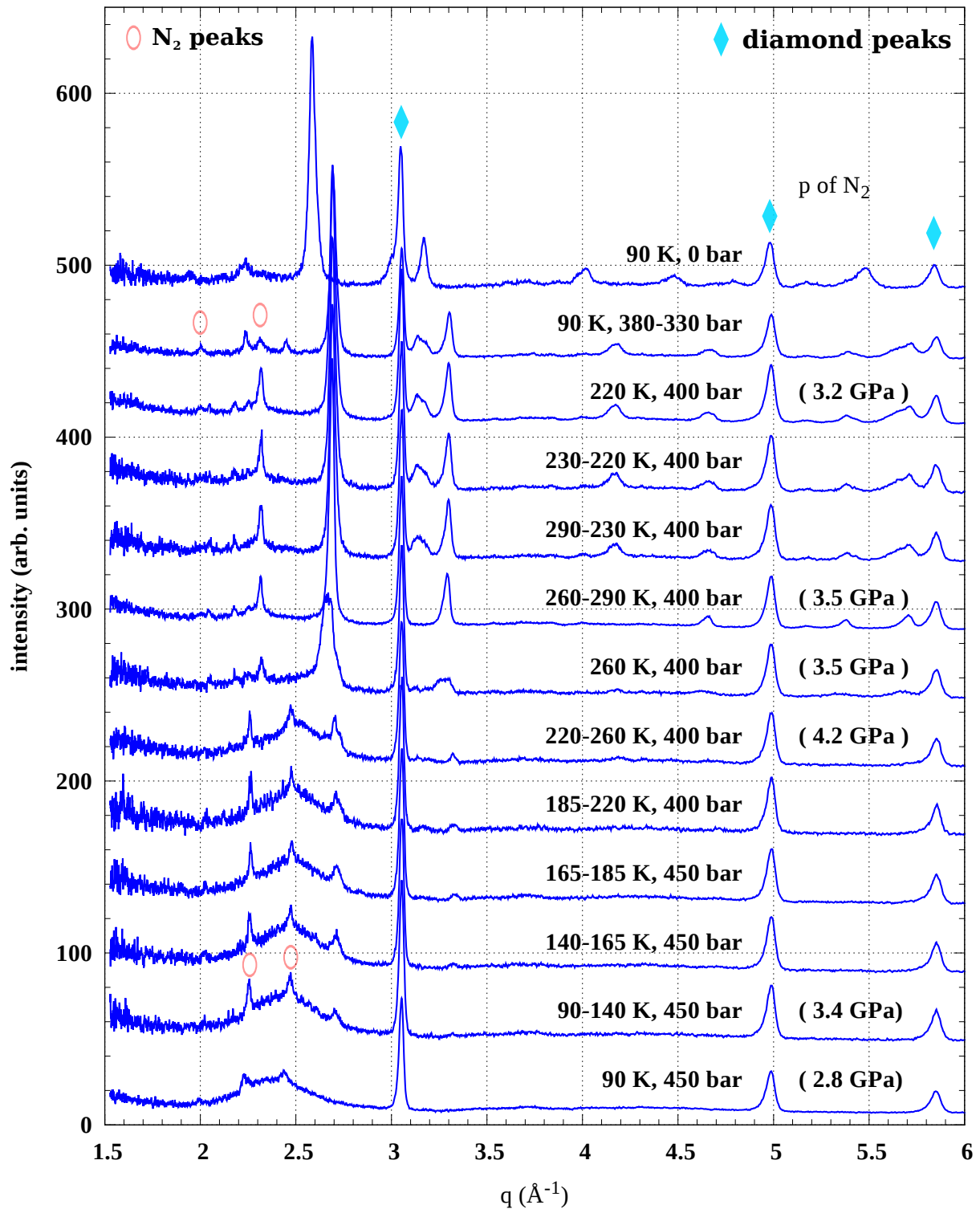


Figure 5.17: Experimental diffraction patterns of the annealing of sample 3 at  $\approx 3.5$  GPa. In this sample ice VII crystallizes at 260 K. Upon cooling below 270 K it transforms into a disordered form of ice VIII. The temperature and gas pressure are indicated for each scan. The sample pressure obtained from nitrogen peaks is indicated on some scans. Diamond and nitrogen peaks are indicated. The data are offset in increments of 50 along the ordinate axis for clarity.

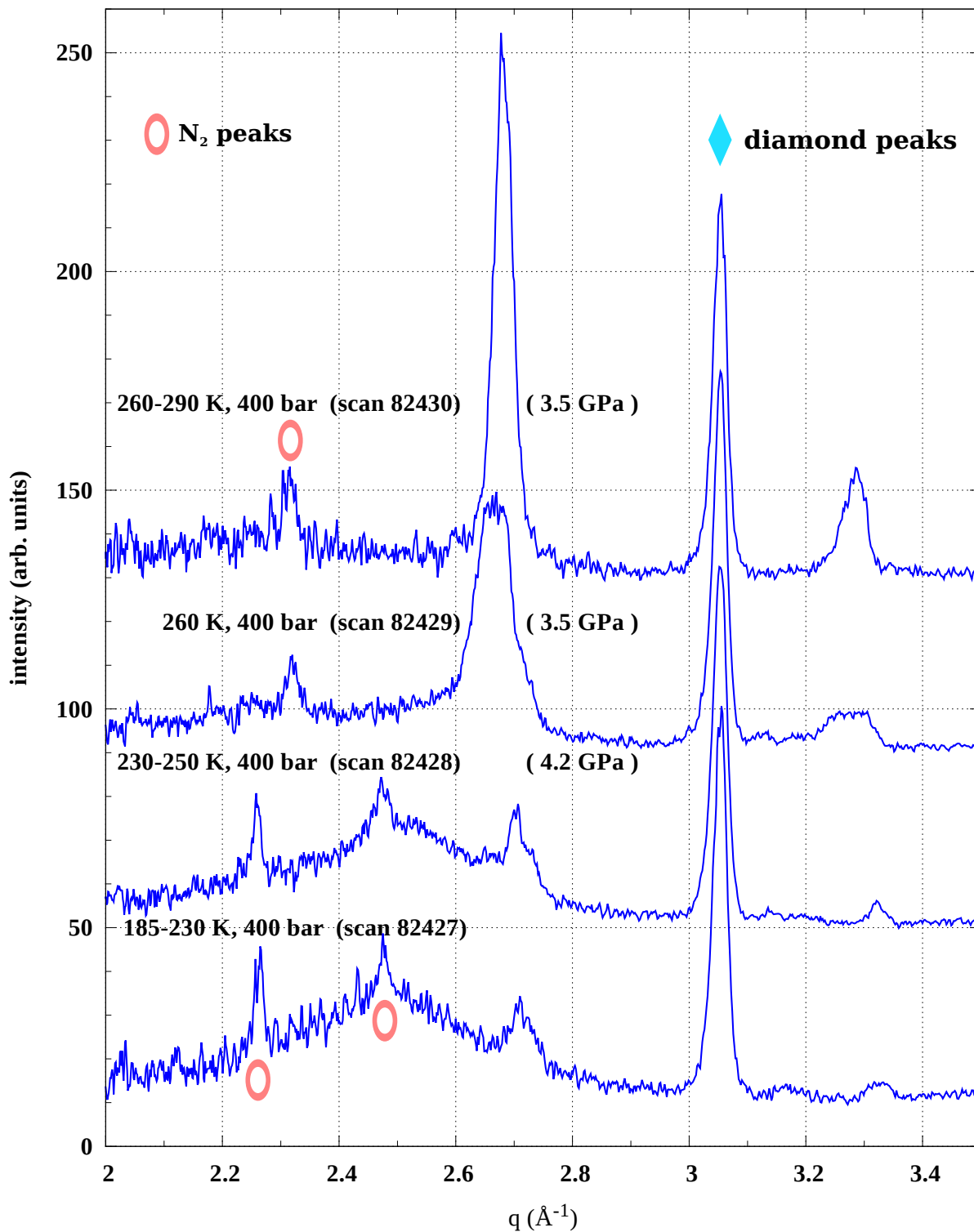


Figure 5.18: Experimental diffraction patterns of the annealing of sample 3 at  $\approx 3.5$  GPa. This plot shows the details of the previous for the scans between 185 and 290 K. In this sample ice VII crystallizes at 260 K. The temperature and gas pressure are indicated for each scan. The sample pressure obtained from nitrogen peaks is indicated on the scans. Diamond and nitrogen peaks are indicated. The data are offset in increments of 50 along the ordinate axis for clarity.

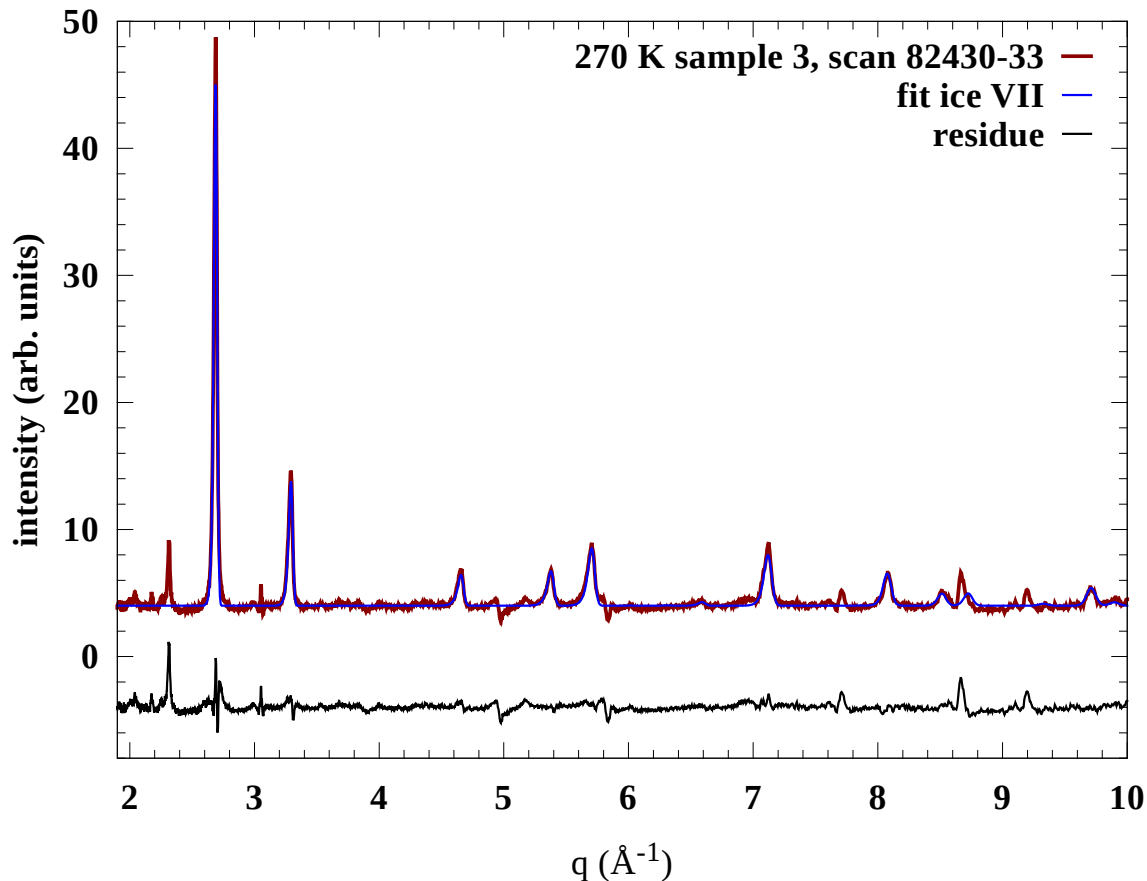


Figure 5.19: Data and fit and residue for sample 3 at 260 K and 3.65 GPa. The fit shown contains ice VII. The fit of diamond peaks has been subtracted from the data. The pressure of the nitrogen phase and ice phase agree to less than 0.1 GPa. No peaks of either lead or sodium chloride are visible in this spectrum. Although the lattice parameter corresponds to pure ice VII, the sample may contain a (small) fraction of salt.

cut, however the broad feature at  $q \approx 2 \text{ \AA}^{-1}$  with  $\text{FWHM} = 0.0372 \text{ \AA}^{-1}$  corresponds to two ice VIII peaks (103 and 211). Another peak appears at  $q \approx 1.5 \text{ \AA}^{-1}$  (213 and 301). These broad features may be an indication that this could be a disordered form of ice VIII, which might have incorporated ions. It might also be due to the superposition of peaks of ice VIII and peaks of salty ice VII. We try to quantify the amount of ions included with the help of our simulations (see section 5.2.2).

The annealing of sample 4 is shown in Figure 5.21. At temperatures below 165 K the spectra show peaks of the  $\delta$  phase of  $\text{N}_2$  on top of the amorphous features of  $\text{NaCl} \cdot 10.2\text{D}_2\text{O}$ . At 165 K the  $\delta$  phase transforms into the  $\beta$  phase and ice VIII forms from the pure VHDA in the sample. From the  $\beta$  phase a pressure of 2.5 GPa can be determined. At 220 K a strong peak appears at  $2.65 \text{ \AA}^{-1}$  and a smaller one

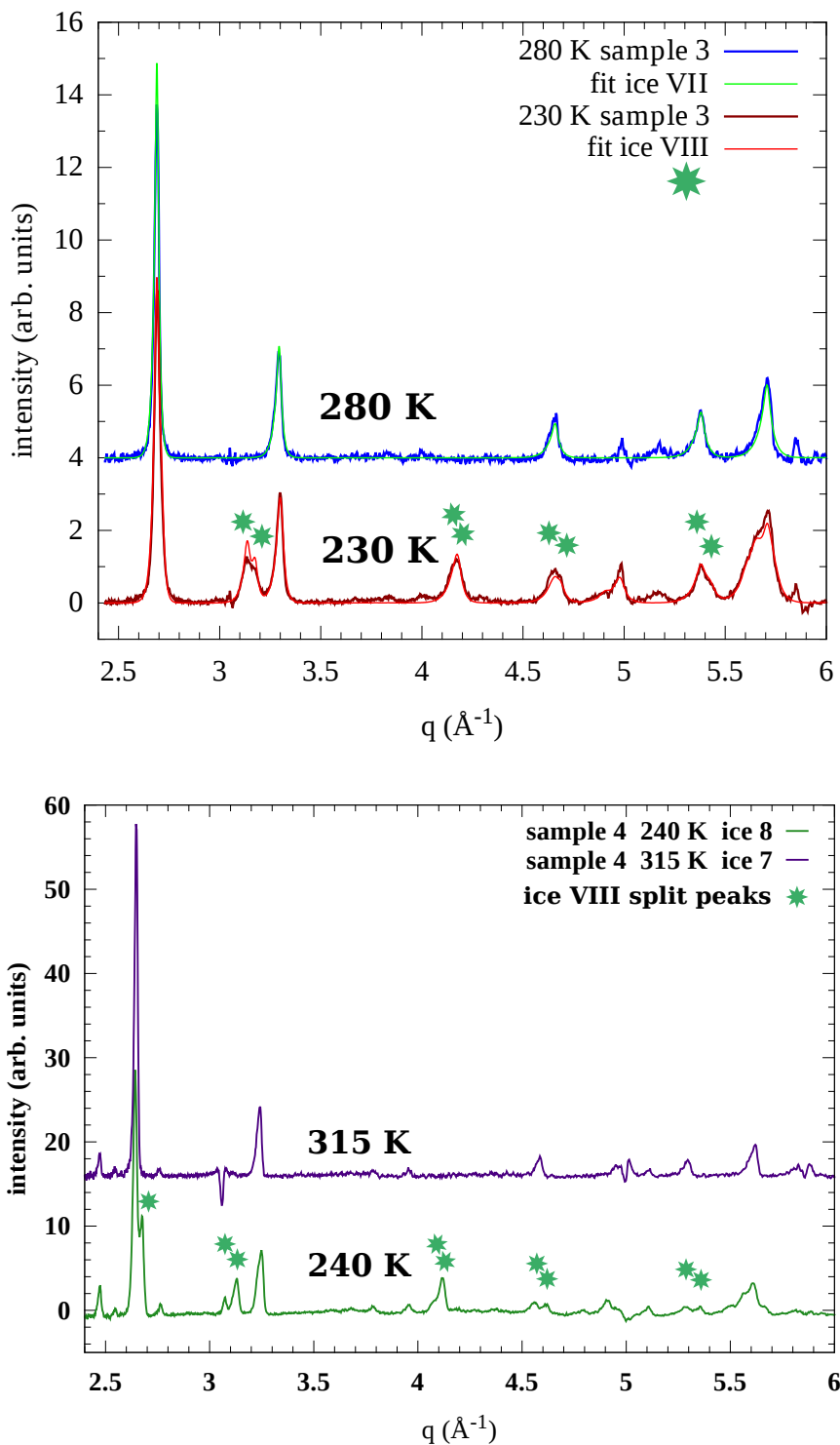


Figure 5.20: Top: Cooling of sample 3 from 300 K to 230 K. Bottom: Cooling of sample 4 from 315 K to 240 K. The doublets of ice VIII are indicated by green stars. The data shown were measured on PEARL in December 2013 using a V3 PEC. The temperatures are indicated on the plot. The diffraction patterns are offset along the ordinate axis for clarity. A fit of the diamond peaks was subtracted from the experimental data.

at  $3.25 \text{ \AA}^{-1}$ . These peaks grow from 240 to 255 K. This phase is ice VIII, which can be seen from the shoulder at  $\approx 2.7 \text{ \AA}^{-1}$  and peak at  $3.15 \text{ \AA}^{-1}$ . At 270 K both the shoulder and the next peak disappear, indicating that the sample has transformed into ice VII. This peak is narrower here than in samples 1 and 3, its FWHM is  $0.0186 \text{ \AA}^{-1}$ , which is a clear indication that this sample is pure ice VII. This is confirmed by the presence of salt peaks which can be seen at 1.98, 2.29, 3.80, 3.96 and  $5.11 \text{ \AA}^{-1}$ . Fitting the salt peaks (and lead) gives a pressure of  $2.25 \pm 0.03 \text{ GPa}$ . The same pressure is obtained by using the EOS of Fortes et al. (2012) and the lattice parameter obtained from the fit of ice VII ( $3.35 \text{ \AA}$ ).

At 240 K the peaks of the  $\beta$  phase start to weaken, probably due to melting. This would indicate a slight loss of pressure, in agreement with the pressure obtained from the salt peaks.

Starting at 240 K, several peaks appear in the region from 2 to  $2.5 \text{ \AA}^{-1}$ . They grow upon annealing to 300 K. Two of these are the salt peaks mentioned above. The phase, to which the other peaks at 2.20, 2.23, 2.47 and a weaker one at  $2.76 \text{ \AA}^{-1}$  belong, has not been identified. They may belong to a mixed phase of water and nitrogen.

The fit of sample 4 at 300 K and 2.25 GPa is shown in Figure 5.22. Salt peaks are visible here. A fit for lead peaks has been attempted, but they are weak. A fit including ice VII, diamond, sodium chloride and lead has been performed, only the ice VII contribution is shown in the figure. The fit of ice VII with GSAS ( $\chi^2 = 1.910$ ) gives a lattice parameter  $a = 3.3507 \pm 0.0001 \text{ \AA}$ , which corresponds to a pressure of 2.25 GPa in pure ice (Fortes et al., 2012). The pressure of the lead (2.23 GPa), NaCl (2.28 GPa) and ice VII phase agree to less than 0.1 GPa. Hence this sample contains pure ice VII.

Sample 4 clearly showed the transition to ice VIII. Upon cooling the splitting characteristic of ice VIII appears on the 110 and 211 peaks as shown in Figure 5.20. Also the pairs at  $q \approx 2 \text{ \AA}^{-1}$  (103 and 211) and  $q \approx 1.5 \text{ \AA}^{-1}$  (213 and 301) appear clearly split.

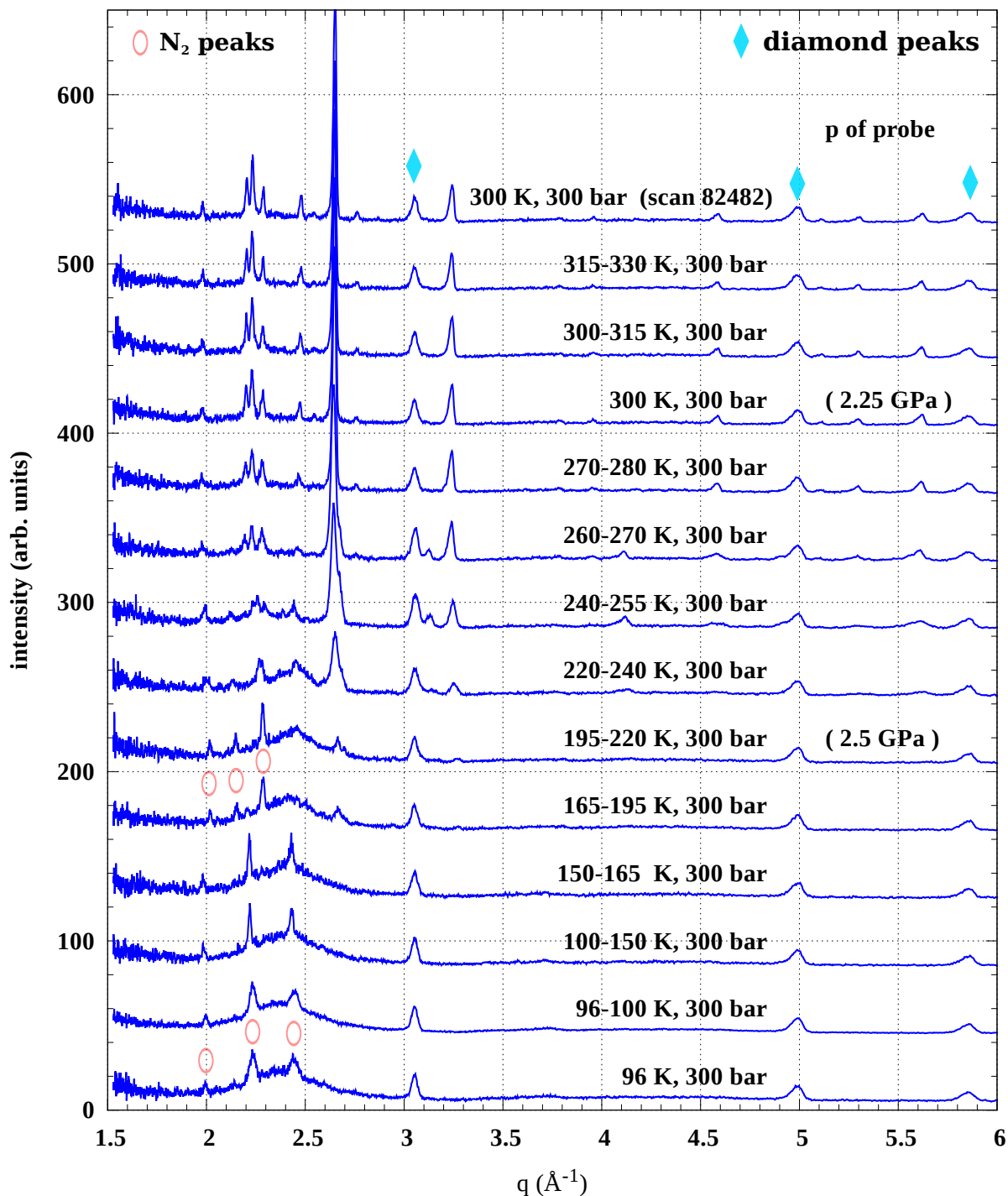


Figure 5.21: Experimental diffraction patterns of the annealing of sample 4 at  $\approx 2.4$  GPa. In this sample ice VIII crystallizes at 220 K and transforms into pure ice VII at 270 K. The temperature and gas pressure are indicated for each scan. The sample pressure determined from the fit of nitrogen peaks is indicated on the top two scans. Diamond and nitrogen peaks are indicated. The data are offset in increments of 50 along the ordinate axis for clarity.

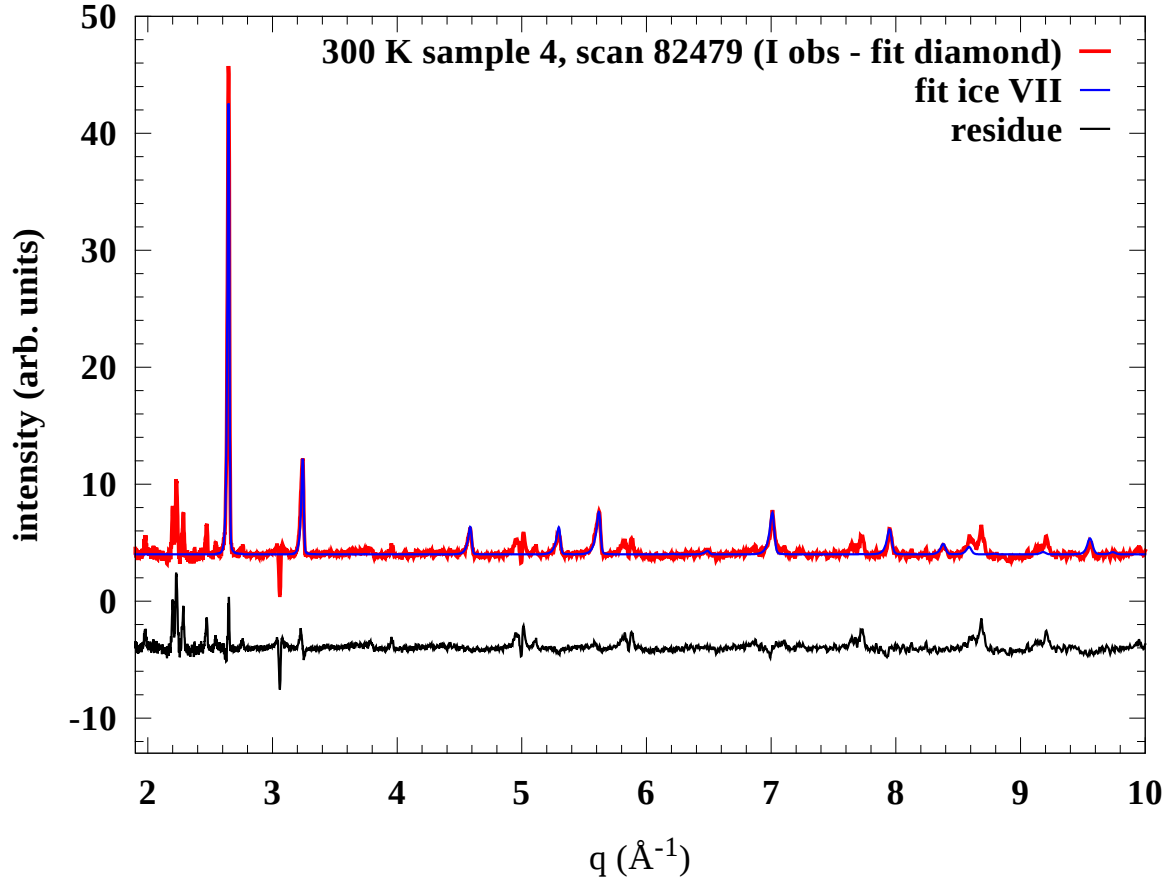


Figure 5.22: Data and fit and residue for sample 4 at 300 K and 2.25 GPa. The fit of diamond peaks has been subtracted from the data. The fit shown includes ice VII. The pressure of ice VII, sodium chloride and lead agree to less than 0.1 GPa, hence this sample contains pure ice VII. There are unidentified peaks in the range of 2 to 3  $\text{\AA}^{-1}$ , which are expected to belong to a mixed phase of nitrogen and water.

The results for the fits of ice VII in samples 1, 3 and 4 are summed up in Table 5.1, Table 5.2 and Table 5.4. The Debye-Waller factors quantify the average displacement of atoms from the crystallographic sites. This can be due to either thermal motion or static disorder. The values of  $U_{\text{iso}}$  obtained from the fits of samples 1, 3 and 4 are given in Table 5.4. For sample 1 and 3 they are in good agreement with those of pure ice (Nelmes et al., 1998). The values obtained for sample 4 are larger than those of Nelmes. This may be linked to the fact that the pressure is less than half of that in Nelmes et al. (1998) experiment.

The width of the peaks can be due to several factors. Particle size, strain and inclusion of salt ions are possible explanations. The particle size  $s$  was obtained from the fits using the Scherrer formula as given in Larson and Von Dreele

$$s = \frac{CK}{\sqrt{8 \ln(2) \sigma_2^2}} \quad (5.1)$$

where  $C = 4834.55 \mu\text{s}$  is the diffractometer constant,  $K \approx 0.9$  is the Scherrer constant and  $\sigma_2$  is a profile parameter. The particle sizes for ice VII fits of samples 1, 3 and 4 are given in Table 5.3. In sample 3 the fit gives the smallest particle size of only  $360 \text{ \AA}$  (36 nanometres). In sample 4 it is largest at about  $610 \text{ \AA}$ . This estimation of the particle size gives the average size of the grains of ice crystals in the sample.

sample, scan	$\chi^2$	ice VII $a$ ( $\text{\AA}$ )	$p$ (GPa)	pressure (GPa), probe
1 82404	1.130	3.28912	3.91	3.94 (Pb)
3 82430-33	2.775	3.29857	3.62	3.68 ( $\beta$ N <sub>2</sub> )
4 82480	1.910	3.3507	2.25	2.25 (NaCl+Pb)

Table 5.1: Results of the Rietveld fits with GSAS for samples 1, 3 and 4. The lattice parameter and pressure (by EOS of Fortes et al. (2012)) for ice VII are given. These pressure agree well with those obtained by fitting the pressure probes (Pb, N<sub>2</sub>, NaCl). The precision of the pressure estimate is  $\approx \pm 0.1$  GPa.

sample	scan	$T$ (K)	$p$ (GPa)	$q$ ( $\text{\AA}^{-1}$ )	FWHM ( $\text{\AA}^{-1}$ )
1	82404	300	3.9	2.7016	0.0278
3	82430 to 33	290	3.5	2.6909	0.0297
3	82436 to 39	220	3.2	2.6896	0.0372
4	82479	300	2.25	2.6494	0.0186

Table 5.2: Peak position and full width at half maximum (FWHM) for the first ice peak in samples 1, 3 and 4. The fits were done using Fityk with split pseudo-Voigt profiles (Wojdyr, 2010). The scan number, pressure and temperature are given.

sample	scan	$T$ (K)	$p$ (GPa)	$\sigma_2^2$ ( $\mu\text{s}^2 \text{\AA}^{-2}$ )	$s$ ( $\text{\AA}$ )
1	82404	300	3.9	17.0	450
3	82430 to 33	290	3.5	27.0	360
4	82479	300	2.25	9.3	610

Table 5.3: Ice particle size obtained from the GSAS fits of samples 1, 3 and 4.

ice VII				$U_{\text{iso}}$	$U_{\text{iso}}$
sample & scan	$T$	$p$	O	D	
	(K)	(GPa)	( $\text{\AA}^2$ )	( $\text{\AA}^2$ )	
1	82404	300	3.9	0.0150	0.0260
3	82430-33	260-290	3.5	0.0171	0.0222
4	82480	300	2.25	0.0215	0.0299

Reference	$T$	$p$	$U_{\text{iso}}$ (O)	$U_{\perp}$ (D)	$U_{\parallel}$ (D)
	(K)	(GPa)	( $\text{\AA}^2$ )	( $\text{\AA}^2$ )	( $\text{\AA}^2$ )
Nelmes et al. (1998)	290	5.0	0.018	0.027	0.017

Table 5.4: Isotropic Debye-Waller factors for O and D for the ice phases crystallised from the samples of NaCl · 10.2D<sub>2</sub>O discussed here. The scan number, pressure and temperature are given. The Debye-Waller factors obtained by Nelmes et al. (1998) on pure deuterated ice VII are given for comparison.

In a nutshell, the data clearly suggest that sample 4 forms pure ice VII. For samples 1 and 3 the data and fits alone are not sufficient to establish, whether a part of the crystalline sample has included salt into the ice VII lattice, since salt peaks are weak in all scans. To complement our study we present a model of salty ice VII in which ions are substituted for water molecules.

### 5.2.2 Proposed structures of salty ice VII

It has been found by neutron diffraction experiments combined with classical and *ab initio* simulation methods, that ice VII can incorporate LiCl into its lattice by substitution of Cl<sup>-</sup> for water molecules, and inclusion of Li<sup>+</sup> in the octahedral interstices of the body centered cubic (*bcc*) oxygen lattice of ice VII. This structure shows a significant expansion of the unit cell of 8% by volume at 4 GPa and five times larger displacement factors than those measured in pure ice VII. This leads to diffraction patterns with strong attenuation of peaks with increasing  $q$ . (Klotz et al., 2009)

This structure agrees remarkably well with the data on LiCl. Since the Li<sup>+</sup> ions are small they fit into the octahedral interstices of the *bcc* structure. However, the Na<sup>+</sup> cations are larger. Therefore the expansion and the distortion would be greater than in the case of LiCl, if ice VII would contain a comparable amount interstitial Na<sup>+</sup> ions. Since there is no evidence for either unit cell expansion or larger displacement factors in the NaCl samples, we propose another structural

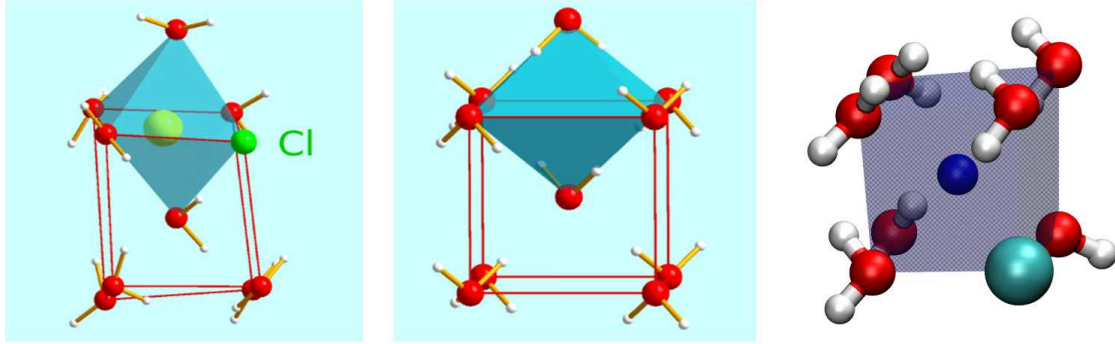


Figure 5.23: Representation of the atoms in the unit cells of pure and salty ice. Pure ice VII is shown in the center. Left: the structure of salty ice VII including  $\text{Li}^+$  (bright green) in an octahedral interstice and  $\text{Cl}^-$  (darker green) substituted for a water molecule. Right: the structure of salty ice VII including  $\text{Na}^+$  (dark blue) and  $\text{Cl}^-$  (turquoise) both substituted for water molecules, which we have investigated in this work.

model. In this model the ions are all included by substituting water molecules. The two structures are shown side by side with the structure of pure ice VII in Figure 5.23. We will first describe the equation of state obtained for this structure and the structure factors calculated from it.

Figure 5.24 shows the equations of state  $p(a)$  obtained for a box of pure ice VII, ice VII with one NaCl pair and ice VII with 4 pairs. In the box of pure ice VII disorder of deuterium has been introduced, while checking that the ice rules are respected. Then the box geometry was optimised at 0 K for a set of box sizes, which gives the  $p(a)$  relation at 0 K. The method of calculation is given in section 3.2.2. The  $p(a)$  relation was fitted to a Birch-Murnaghan EOS for the three boxes, in the range of 3.2 to 3.5 Å. Figures for each fit are given in the appendix (A.2.2).

The parameters  $a_0$ ,  $V_0$ ,  $B_0$ ,  $B'_0$  are given in Table 5.5 and compared to the values from the literature on ice VII. The salty ices have a smaller bulk modulus  $B_0$  and are therefore softer. The  $B_0$  of the ice with 8 ions is even smaller than that of the  $\delta$  phase of  $\text{N}_2$  (5.75 GPa after Mills et al. (1986)). Figure 5.25 shows the equations of state  $p(a/a_0)$ . The deviation of the data from the simulation with 8 ions (blue triangles), is a consequence of the smaller bulk modulus of the salty ice.

From the *ab initio* calculations on the ice VII with NaCl, we find an expansion of the unit cell, when comparing boxes where ions are included to the box of pure ice VII. For salty ice with 2 ions at 4 GPa the expansion is  $da/a = 1.1\%$  in the box size and  $dv/v = 3.2\%$  in volume for the single box used for the EOS. For the box of more ordered salty ice with 8 ions at 4 GPa the expansion is  $da/a = 4.2\%$  in the box size of our simulation and  $dv/v = 13\%$  in volume for the box which was used for the EOS. For the set of 200 boxes of more disordered boxes for which geometry

optimisation was done, the optimisation of a box chosen close to the average pressure of the set gives an expansion of  $da/a = 3.2\%$  in the box size and  $dv/v = 10\%$  in volume. Given these values for the expansion of salty ice VII, it would be expected that the samples measured, which show much smaller expansion compared to pure ice VII, would only include a small fraction of ions in their lattice. It should be noted that the boxes sampled in our *ab initio* calculations are small, and that moreover the equation of state was obtained for single boxes only. The spread in pressure at fixed box size for the boxes generated by random searching is of  $\pm 0.4$  GPa. Thus the two boxes chosen may not be representative for the behaviour of all boxes. To improve on this, it will be necessary to sample the EOS of several more boxes. Nevertheless the fact that the boxes expand more when they contain more ions, is consistent with what would be expected by analogy with the case of LiCl solution.

Using the Murnaghan EOS the following relation between the bulk modulus  $B$  and  $V$  can be derived (Klotz, 2012, footnote p. 168)

$$\frac{B}{B_0} = \left( \frac{V_0}{V} \right)^{B'_0}. \quad (5.2)$$

Hence the bulk modulus of a material should decrease when the volume increases. With our values for expanded salty ice with 8 ions, the left hand side gives  $B/B_0 = 0.23$  and the right hand side  $(V_0/V)^{B'_0} = 0.48$ , which is off by a factor  $\approx 2$ . For 2 ions we have  $B/B_0 = 0.66$  and  $(V_0/V)^{B'_0} = 0.81$ , which is off by a factor  $\approx 1.2$ . The agreement is approximate, but this relation is only approximately verified by most material. Still, it does show that the decrease in bulk modulus  $B_0$  is consistent with the increase in volume  $V_0$ .

system	$a_0$ Å	$V_0$ Å <sup>3</sup>	$B_0$ GPa	$B'_0$
BM ice VII $R = 11.5$	3.822	55.83	4.26	6.0
BM ice VII $R = 52$	3.4875	42.41	11.98	6.56
BM pure ice VII	3.4095	39.63	18.17	5.68
M pure ice VII (Fortes, 2012)	3.4898	42.5	13.0	5.5
BM ice VIII (Besson, 1994)		12.45 cm <sup>3</sup> /mol	20.4	4.7
BM ice VII (adapted from Besson)	3.4898	42.5	20.4	4.7

Table 5.5: Parameters of the fits of Birch-Murnaghan equation of state (EOS) to data from simulations, compared to two EOS of ice VII fitted to experiments given in literature (Besson et al., 1994, Fortes et al., 2012). M stands for the Murnaghan EOS, BM for the Birch-Murnaghan EOS.

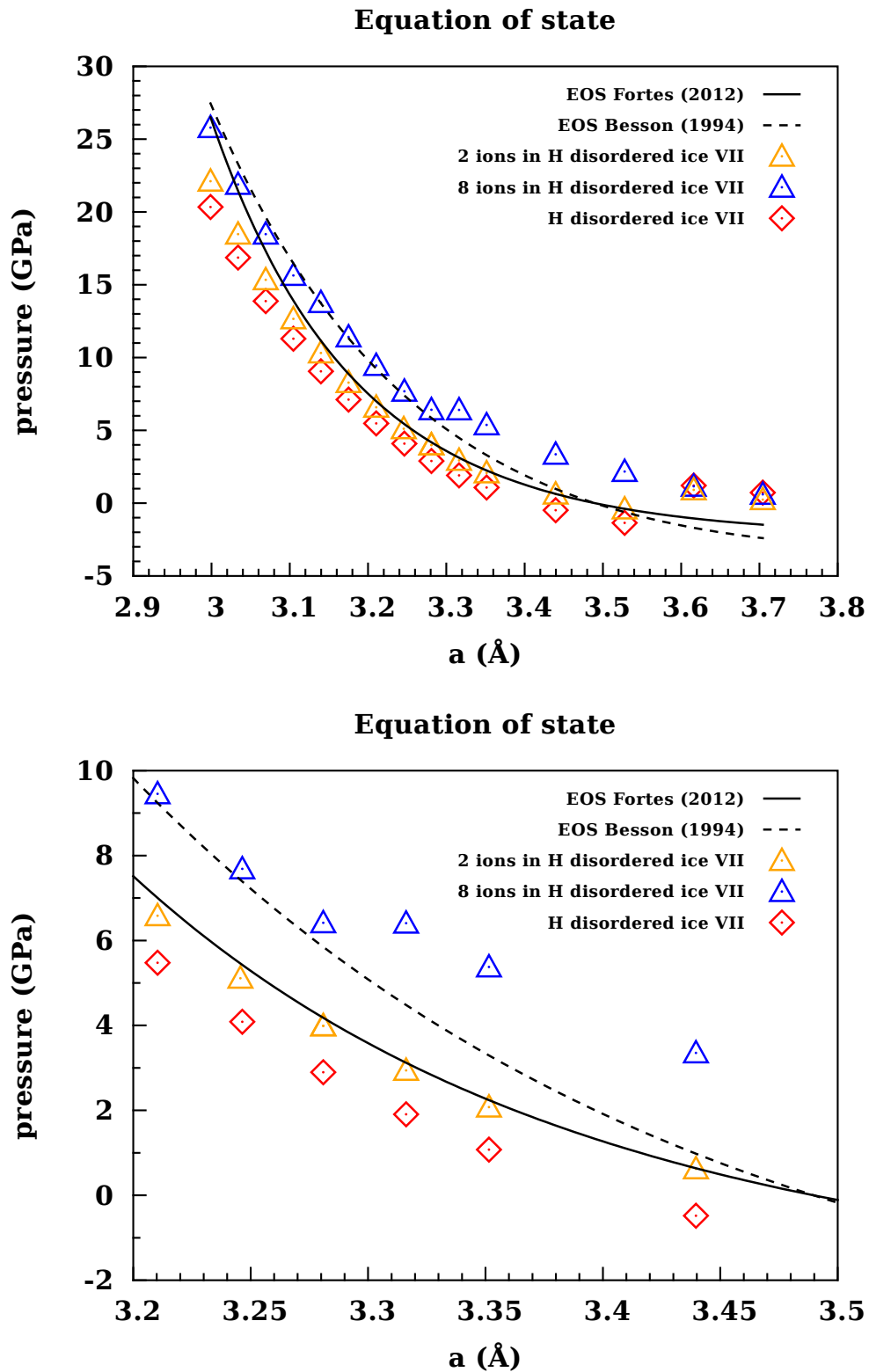


Figure 5.24: Equations of state  $p$  versus  $a$  for pure and salty ice VII from our calculation at 0 K, compared to two EOS of ice VII given in literature (Besson et al., 1994, Fortes et al., 2012).

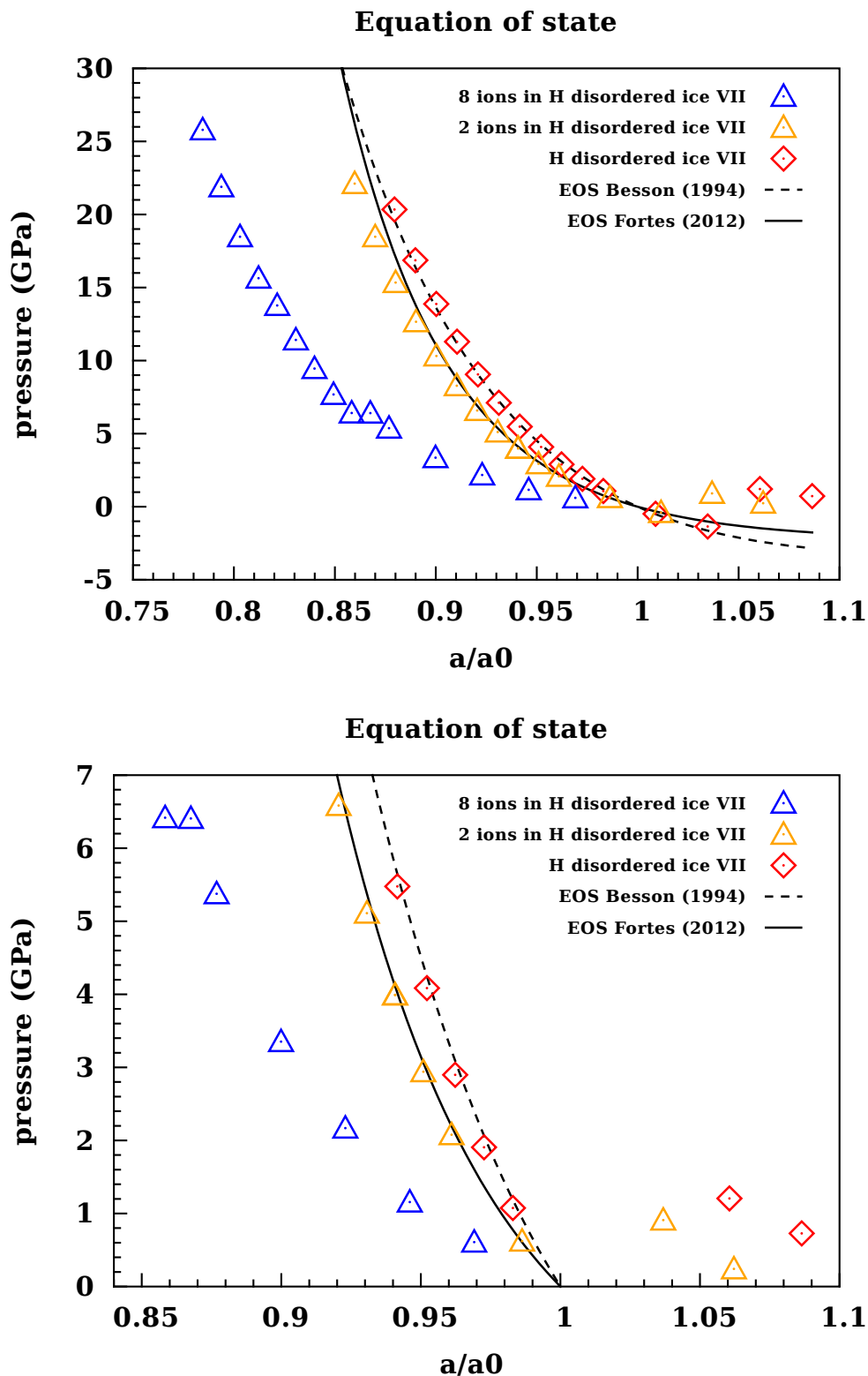


Figure 5.25: Equations of state  $p$  versus  $a/a_0$  for pure and salty ice VII from calculations at 0 K, compared to two EOS of ice VII given in literature (Besson et al., 1994, Fortes et al., 2012).

The experimental diffraction pattern of sample 3 at 260 K and 3.5 GPa is compared to different models of ice VII in Figure 5.26. Only the background fit, obtained from fitting the pattern with GSAS, was subtracted from experimental data (blue). The diamond,  $\beta$  nitrogen (peak at  $2.4 \text{ \AA}^{-1}$ ) and ice VII, which were also fitted, have not been removed in this spectrum. The FullProf model 1 (dark blue) is the same *bcc* structure as was used in the GSAS fit ( $a = 3.29857 \text{ \AA}^{-1}$ ). The relative intensities differ from those in the experimental spectrum, because this model is not a fit. Here the program assumes that all possible sites for deuterium have an occupation of  $1/2$ . The Miller indexes of twelve visible ice VII peaks are indicated on the figure.

The other three spectra were produced by FullProf by using the boxes from our simulations as unit cells with space group *P1*, all isotropic displacement factors were taken as  $B = 1 \text{ \AA}^2$ . The spectrum labelled pure ice (dark red, model 2) was produced by using the supercell containing only water molecules, in which the deuterium atoms are disordered. This spectrum shows all peaks of ice VII which appear in the Fullprof fit with reasonable intensities. The 110 peak shows at shoulder at the right side (towards larger  $q$ ). This spectrum also shows small spurious peaks at  $\approx 2.4, 3.4, 4.0$  and  $4.1 \text{ \AA}^{-1}$  due to periodic boundary conditions. The pattern of the box containing 2 ions (dark green, model 3) is highly similar that of pure ice VII. Both patterns show 7 recognisable peaks for  $2 \leq q \leq 8.5 \text{ \AA}^{-1}$  (110, 111, 200, 211, 221, 400, 330). The box sizes at 4 GPa was used to produce these spectra, this is why the peaks are slightly shifted with respect to model 1 and the experimental data.

In the pattern for the box containing 8 ions (red, model 4), the 110 peak is broader than in other models and the spectrum of sample 3, and only one other peak (111) is well defined. This 111 peak is only half as strong as that in model 2. The other 5 peaks are weak and start to merge into the background. This pattern shows less resemblance to the experimental spectrum than the other models. However these features described above are similar to those of salty ice VII crystallized from  $\text{LiCl} \cdot 6\text{D}_2\text{O}$  (Klotz et al., 2009).

From these structure factors the most plausible models for the measured spectrum are pure ice (models 1 and 2) and ice with few ions (model 3). This means that the molar ratio  $R$  may be 52 or less, but still should be significantly higher than 11.5 (model 4). Hence most of the salt would have been excluded from the ice lattice.

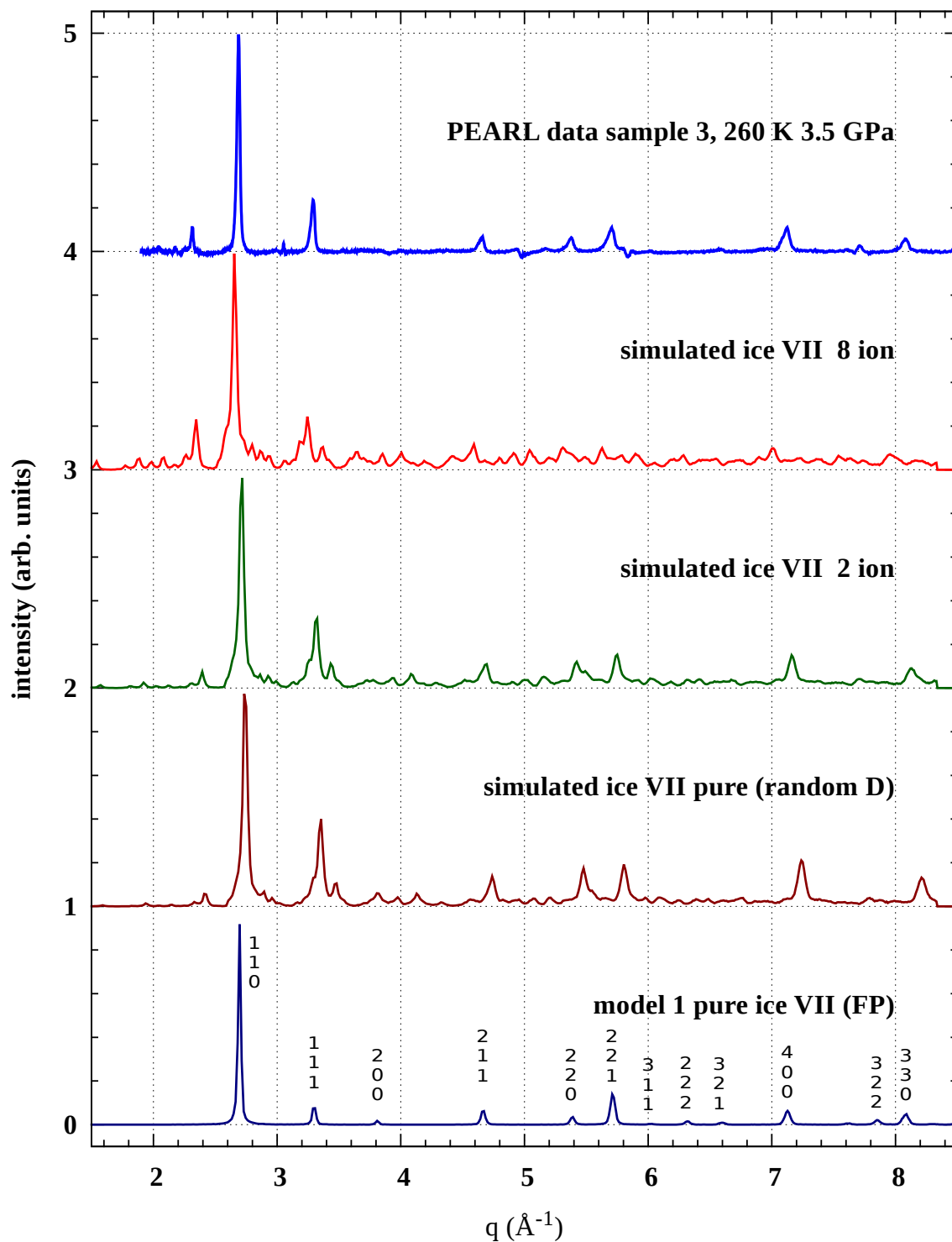


Figure 5.26: Diffraction pattern of crystallised sample 3 (blue) compared with those generated for the usual crystallographic model of ice VII (dark-blue), the hydrogen disordered supercell of ice VII (dark-red), a box with 2 ions substituted for water molecules (dark-green), and a box with 8 ions substituted for water molecules (red). All patterns for simulations were generated using Fullprof. A fit of the diamond peaks was subtracted from the experimental data of sample 3 (blue line).

### 5.2.3 Stability of salty ice VII

A set of salty ice VII with substitutional ions was generated by the random searching algorithm and then studied proceeding in the steps described in section 3.2. Here we discuss the stability ice VII including 4 ionic pairs ( $\text{Na}^+$  and  $\text{Cl}^-$ ) in the light of the results of this sampling.

The data discussed below were obtained by substituting ions into a box with partial disorder of the hydrogen atoms. Simulations were also performed on a box with a greater extent of disorder of hydrogen. This second set of simulations gives similar results, a notable difference being a shift of the energies. Their analysis is yet incomplete, therefore it is not presented here.

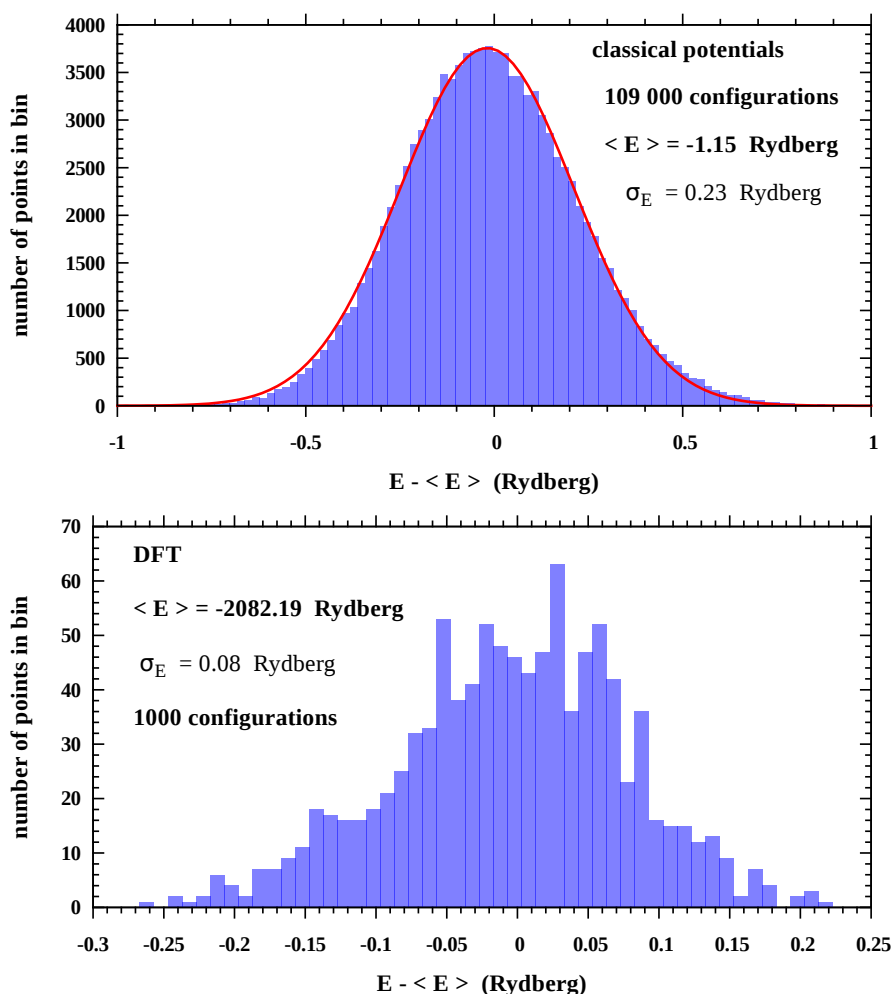


Figure 5.27: Distribution of the total energy from screening with classical potentials (top) and DFT (bottom) for the set of configurations of salty ice VII generated by random structure searching. The sample size, the average energy  $\langle E \rangle$  and the spread  $\sigma_E$  are indicated on the graphs. The red curve on in the top panel is a Gaussian fit as a guide to the eye.

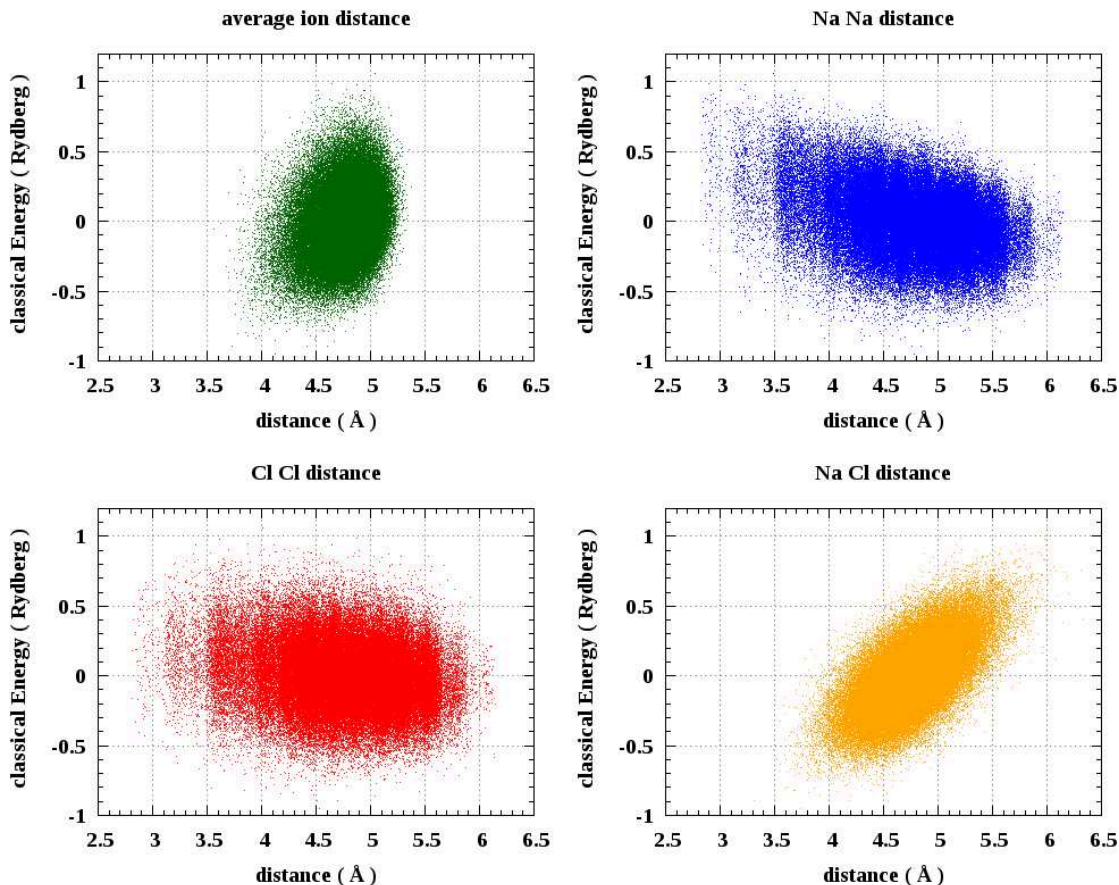


Figure 5.28: Distribution of classical energy versus ion distances for the set of 109 thousand configurations. The global average distance between all ions varies between 4 and 5.3 Å. The distributions with respect to Na Na and Cl Cl distances are broad. The highest energies correspond to Na Na distances smaller than 3.5 Å and Na Cl distances larger than 5 Å.

The distributions of the energies are shown in Figure 5.27. The total energy of approximately 109 thousand distinct configurations was computed using classical potentials. The DFT energy was computed for the subset of one thousand configurations with the lowest classical energy. Both distributions have been centered around 0 by subtracting the average energy from the values. The center averages are  $-1.15$  Ry for the classical energy and  $-2082.19$  Ry for the DFT energy. Both distributions are bell shaped. A gaussian fit to the distribution of classical energies is shown as a guide to the eye.

The distribution of the classical energies versus the average ion distances is shown in Figure 5.28. The distributions with respect to Na–Na distance and Cl–Cl distance are similar, and broader than than the global average distance between all ions, which is concentrated in the region between 4 and 5.3 Å. The highest energies correspond to Na–Na distances smaller than 3.5 Å and Na–Cl distances larger than

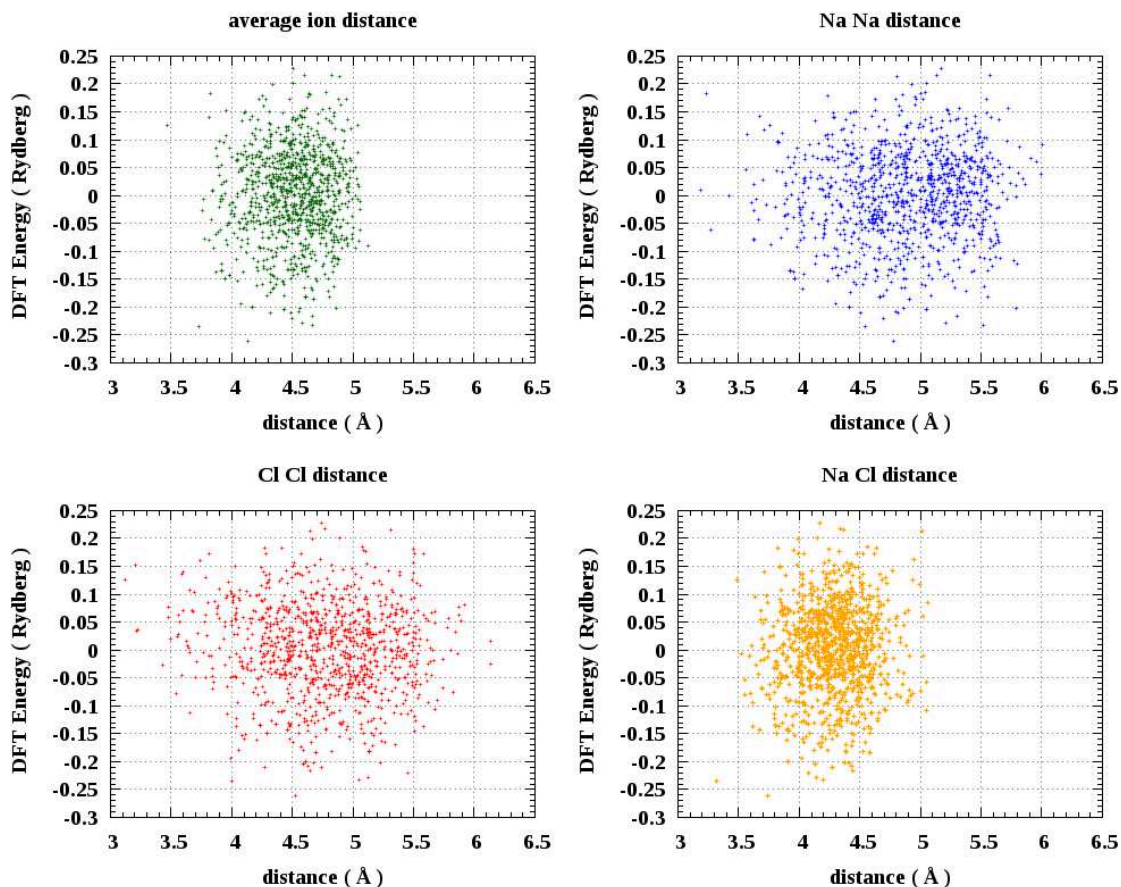


Figure 5.29: Distribution of DFT energy versus ion distances for 1000 configurations. The configurations selected were those of lowest classical energy. The average distance here is distributed as in large set in Figure 5.28. The Na Na and Cl Cl distances show almost no correlation to the DFT energy in this set. The Na Cl distance is smaller than about  $4.7 \text{ \AA}$ , in contrast to the larger set where it reached up to  $6 \text{ \AA}$ .

$5 \text{ \AA}$ . There is a trend energy decreasing when Na–Na distance increases. The average Na–Cl distance shows a marked trend of correlation with the classical energy. Lower energies correspond to smaller distances between the ions.

For DFT energies there does not appear to be a correlation of the energy with the Na–Na and Cl–Cl distances (Figure 5.29). The effect of selecting the lowest classical energies can be seen in the distribution of energy versus Na–Cl distance, which is approximately the lower half of the full distribution. This is in agreement with the correlation of classical energy with this parameter.

The distribution of energies versus dipoles showed that the value of the total dipole varies in discrete steps. The highest density of dipoles from the configurations which were sampled occurs between 4 and 7 times the dipole of an individual water molecule. No specific correlation with stability has been found. The figures are shown in appendix A.2.1.

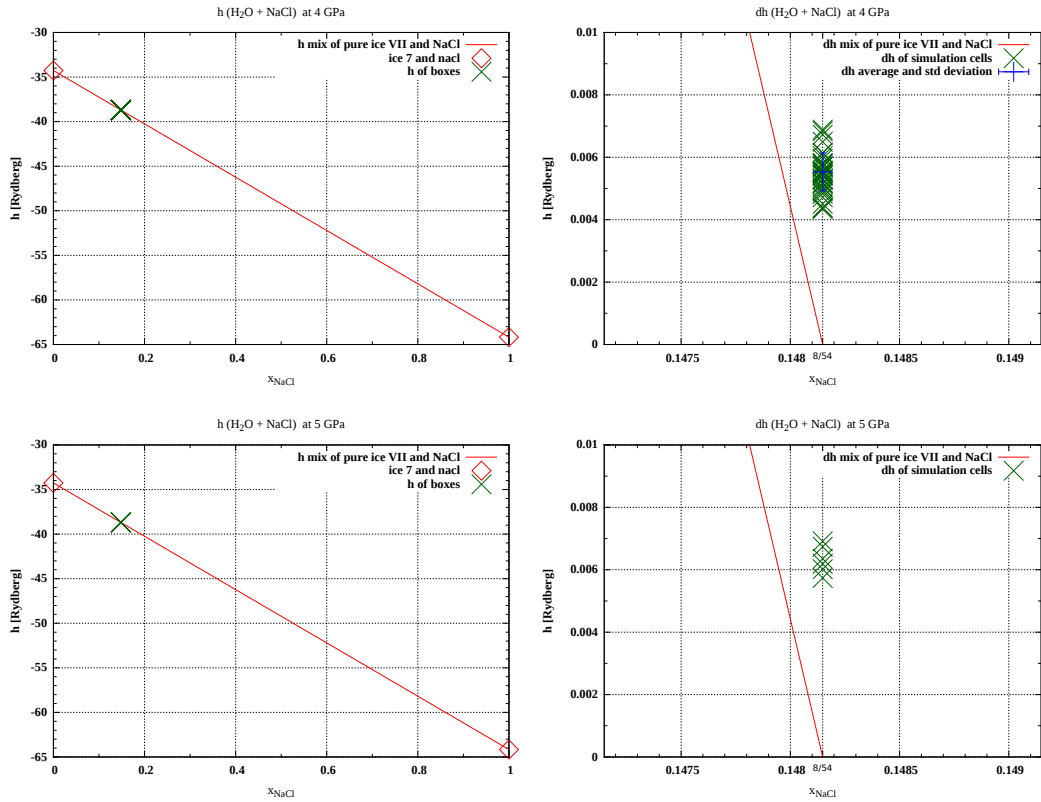


Figure 5.30: Convex hull diagram of the  $\Delta h$  enthalpy difference for configurations of salty ice with 8 ions at 4 GPa (top) and 5 GPa (bottom). The abscissa indicated the molar fraction of salt  $x_{\text{NaCl}}$ . The red line gives the energy corresponding to phase separation at a given concentration. At both pressures the energy of the salty ice lies above that of phase separation.

The stability of these ices was probed by calculating the enthalpies  $h$  and the enthalpy of mixing  $\Delta h$  per site of the oxygen lattice. The convex hull diagram of enthalpies is shown in Figure 5.30. The zoom shows that the configurations for which geometry optimisation was performed have enthalpies larger than those of the separated ice and salt. This indicates that the salty ice is unstable, but it may be metastable on the experimental time scale.

The enthalpy of mixing was computed from DFT geometry optimisation on 200 boxes of lowest DFT energy. The enthalpy of mixing  $\Delta h$  versus ion distance is shown in Figure 5.31. The configurations were filtered to lie within 0.1 GPa of 4 GPa and 5 GPa, therefore this plot contains fewer points. The spread in  $\Delta h$  is of the order of 0.002 Ry, which corresponds to  $\approx 315$  K. This suggests that the thermal energy at 300 K would be sufficient to allow the system to relax to the stable state of pure ice VII and salt.

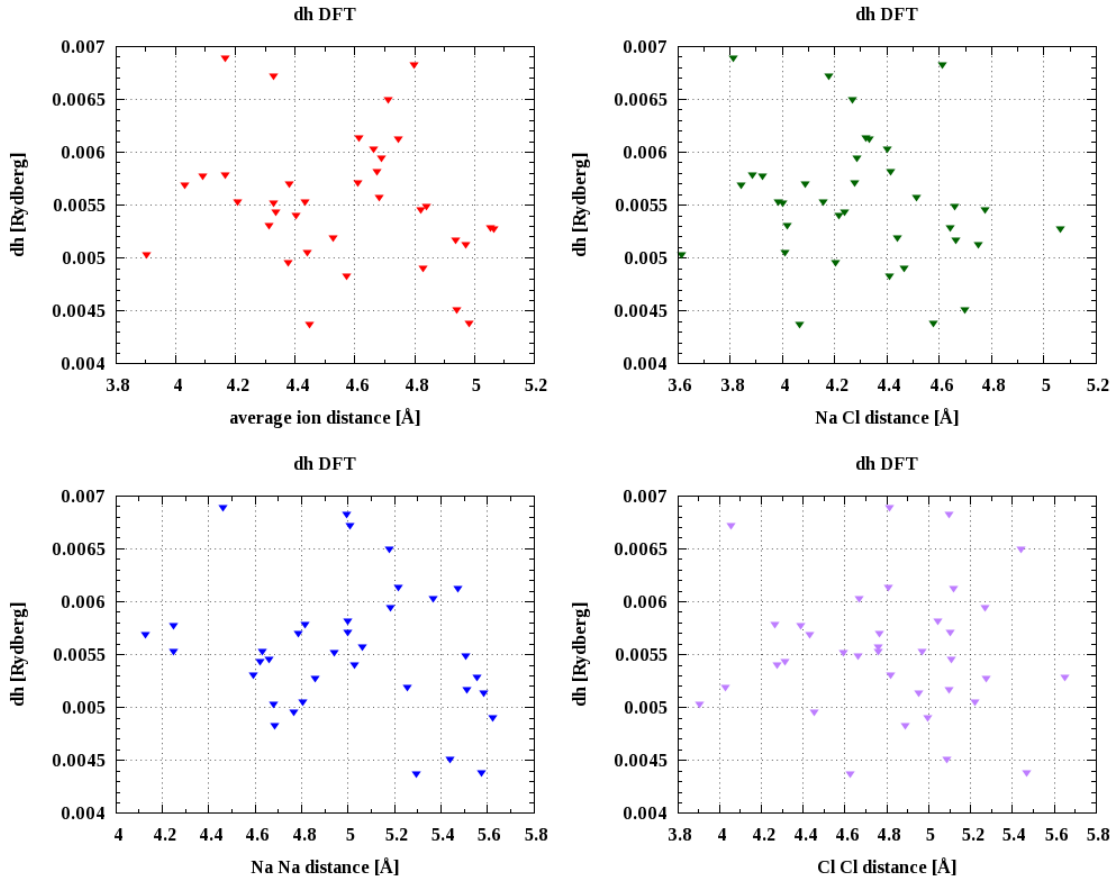


Figure 5.31: Enthalpy of mixing  $\Delta h$  versus ion distances for the 8 ion configurations at 4 GPa. The spread in  $\Delta h$  is about 0.002 Ry (*i.e.*  $\approx 315$  K).

In order to complement the results above, which were obtained from geometry optimisation at 0 K, *ab initio* MD at 300K was performed on three boxes: one with pure ice VII and one each of ice VII with 2 and with 8 ions. These MD trajectories are 10 ps long and show that the motions of water molecules and ions in the salty ice with 8 ions ( $R = 11.5$ ) are greater than in the other two cases. The pressure also oscillates more markedly in the box with 8 ions. A full analysis of the mean square displacement is needed to decide whether this box is on the verge of melting or phase separation.

### 5.2.4 Conclusion

The experimental data on the annealing of amorphous  $\text{NaCl} \cdot 10.2\text{D}_2\text{O}$  show that this amorphous phase is stable up to 220 K at 2.5 GPa, and 250 K at 4.2 GPa. This is significantly higher than pure VHDA, which in our samples crystallized between 120 and 160 K.

The ice VII forming upon crystallisation of the samples in our annealing experiments at pressures in the range of 2 to 4 GPa is likely pure or contains only few ions. The best fits for the ice VII in spectra of samples 1, 3 and 4 were obtained with models of pure ice. The lattice parameter agrees with the equation of state of Fortes et al. (2012) within the uncertainty in the pressure, which was determined using calibrants. Moreover the lattice parameter and Debye-Waller factors are in good agreement with those found for pure ice VII. In sample 4 the ice peaks are narrow which justifies this assumption. For samples 1 and 3 the broadening may be due to several factors. The first one is the average size of crystalline particles, which was extracted from the fit and is indeed smaller for these two samples than for sample 4. Another one would be the partial inclusion of ions in the structure.

The atomistic calculations, performed on the structure of ice VII including  $\text{Na}^+$  and  $\text{Cl}^-$  ions substituted for water molecules, show that these ices are either unstable or metastable. The spread in the enthalpy of mixing indicates that phase separation might occur at  $\approx 300$  K and  $\approx 4$  GPa. *Ab initio* MD simulations show that the motion of the atoms is greater in the box with 8 ions than in the boxes with 2 ions and that with pure ice.

The equation of state obtained from calculations shows that substitutional  $\text{NaCl}$ -ice VII would have a  $\approx 3.2\%$  larger lattice parameter and  $\approx 10\%$  percent larger unit cell volume. Structure factors obtained from the atomistic calculations indicate that the salty ice would have a larger Debye-Waller factor than pure ice VII. Both of these features are similar to what has been observed for  $\text{LiCl}$  solutions in the same conditions of pressure and temperature. Although these solutions are expected to adopt a structure where  $\text{Li}^+$  is interstitial.

The experimental data and simulations both suggest that the inclusion of large quantities of  $\text{Na}^+$  and  $\text{Cl}^-$  in the ice VII lattice would be unfavorable at pressures up to 4 GPa. The behaviour of the system at significantly higher pressures of 10 GPa and more may be quite different and would be worthwhile to investigate in order to provide constraints on the internal structure of massive planetary bodies such as super-earths and ice giants (Beaulieu et al., 2006).

# Chapter 6

## Conclusion

The aim of this work was to characterise the phases of salt-water systems under conditions of temperatures and pressures relevant for the interiors of icy moons and small planetary bodies. The main focus of this work was the NaCl-water system, which was studied in the range of pressures from 0 to 4 GPa and temperatures from 77 to 330 K.

The experiments were performed using a Paris-Edinburgh cell, which is a reliable tool for high-pressure neutron studies and can reach the multi giga-Pascal pressure range for temperatures from 0 to 350 K. Neutron and X-ray Diffraction techniques were employed to study the atomic structure of amorphous and crystalline phases of solutions. This experimental study went hand in hand with a computational approach based on atomistic simulations. The changes in microscopic structure of the system along the thermodynamic trajectory followed in experiments, were investigated using Molecular Dynamics simulations. Candidate structures of salty ice VII were sampled using a random structure searching algorithm.

The first step in our experimental study was to produce amorphous  $\text{NaCl} \cdot R\text{H}_2\text{O}$  with the highest ratio of amorphous to crystalline material achievable. The samples were produced using a quenching device, which was developed by S. Klotz and can achieve cooling rates of the order of  $10^4$  to  $10^5$   $\text{K}\cdot\text{s}^{-1}$  by splat quenching droplets of about 20  $\mu\text{m}$  diameter on a solid surface. The highest degree of amorphisation was achieved for  $R = 9.5$  in  $\text{H}_2\text{O}$  and 10.2 in  $\text{D}_2\text{O}$ . On average the solutions in  $\text{D}_2\text{O}$  yielded more amorphous material than those in  $\text{H}_2\text{O}$ .

The diagram in Figure 6.1 summarises our main findings regarding the highly concentrated amorphous phase and its crystallisation behaviour. At ambient pressure the amorphous phase adopts a dense structure very similar to pure water HDA and the amorphous phase of concentrated LiCl-water solutions at ambient pressure.

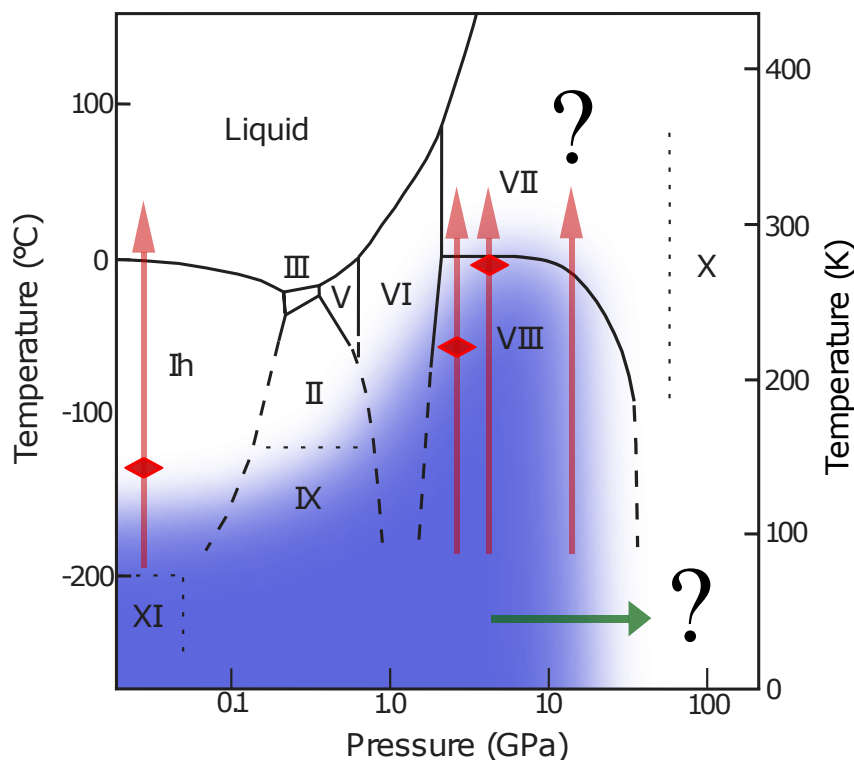


Figure 6.1: Phase diagram for NaCl-water on top of the diagram of stable phases of pure water from Finney et al. (1998). The domain in which  $\text{NaCl} \cdot 10.2\text{D}_2\text{O}$  has been observed is shown in blue. The crystallisation upon annealing is indicated by red diamonds. Red vertical arrows indicate the paths along which annealing experiments were performed in this work. The green horizontal arrow indicates the direction along which compression at low temperature ( $\approx 80$  K) was performed. Question marks indicate unexplored areas.

Upon compression to 4 GPa amorphous  $\text{NaCl} \cdot 10.2\text{D}_2\text{O}$  undergoes a smooth densification. The structure also changes gradually upon annealing to 220K at 2.5 GPa and 250 K at 4 GPa, which is in contrast to the polyamorphic transition observed in  $\text{LiCl} \cdot 6\text{D}_2\text{O}$  Bove et al. (2011b). Structural quantities were computed using Molecular Dynamics with classical polarisable potentials by Tazi et al. (2012). The structure factors from simulations agree well with the experimental ones, which showed these potentials are transferable to high pressure conditions. Thus combining the results of simulations and experiments it could be shown that the behaviour of these solutions upon compression depends on the structures of the hydration shells of  $\text{Na}^+$  and  $\text{Li}^+$ . The first neighbours' shell of  $\text{Li}^+$  has a tetrahedral structure at ambient pressure, which breaks up near 2 GPa to form an octahedral shell giving rise to a sudden change in density. In the case of  $\text{Na}^+$ , the shell is already octahedral at ambient pressure. The compression of the second neighbours onto the first neigh-

bours' shell leads to a progressive distortion of the octahedra and the formation of irregular polyhedra of 7 and 8 closest neighbours as pressure increases. This process explains the gradual change in density of  $\text{NaCl} \cdot 10.2\text{D}_2\text{O}$ . Therefore the polymorphic phenomenon observed in pure water and LiCl solutions appears not to be a general feature of electrolytic aqueous solutions.

The increase in coordination of  $\text{Na}^+$  raises the question of whether these ions could be included into the body centered cubic oxygen lattice of ice VII by substituting water molecules, because ice VII is a stable and dense phase.

The analysis of the diffraction data suggests that the ice VII which crystallised upon annealing at 2.5 and 4 GPa contains little or no salt in its lattice. This is supported by the lattice parameters and Debye-Waller factors, which are in good agreement with the literature data on pure ice VII. The broadening of peaks observed in two samples could be due to the small size of crystallites. Calculations show that substituting ions into the lattice of ice VII should lead to an expansion of the unit cell by about 10% in volume, if all of the salt in the sample were included in the ice at 0 K. The computed structure factors of salty ice show strong Debye-Waller factors at high salt concentration, which is at variance with the experimental observation. Caution should be taken when interpreting these calculations, because the equations of state (EOS) and structure factors (SF) were calculated only for a few boxes. To confirm this result, the EOS and SF of several more boxes should be evaluated. Analysis of the enthalpies of mixing obtained from the set of candidate structures shows that salty ice would be at the verge of stability at 300 K and 4 GPa. Finally, *ab initio* MD trajectories at 300 K ( $3 \leq p \leq 5$  GPa) suggests that ice VII with  $R = 11.5$  displays larger thermal motion than the pure and less salty ice ( $R = 52$ ), and may be near to melting. Both further experiments and calculations could contribute to resolve this question.

The behaviour of the system at pressures greater than 10 GPa and more may be different from the behaviour observed in this work. It would be worthwhile to investigate these higher pressures, because they occur in the interiors of massive planetary bodies such as super-earths and ice giants (Beaulieu et al., 2006). The heterogeneous environment in these celestial objects may lead to the formation of salty ices. Hence determining whether these salty ices form at high pressures, would contribute to a better understanding of the internal structure of these icy bodies.

The range of pressures in the interiors of ice giants has been probed by Raman experiments on LiCl- and NaCl-water solutions at pressures up to 145 GPa. For LiCl it was shown that the transition from ice VII to X is inhibited by the presence of

ions in the ice lattice (Bove et al., 2015). In ice X the hydrogen atoms are sitting in the middle of neighbouring oxygen atoms, this phase is non-molecular (Goncharov et al., 1996, Loubeyre et al., 1999). Bronstein et al. (2014) show that this transition is adequately described by nuclear quantum effects of the protons. A study of salty (LiCl and NaCl) ices by high-pressure experiments and MD simulations shows that inclusion of NaCl at low concentration, also inhibits the transition to ice X (Bronstein et al., 2015).

Another solution that is worthwhile to investigate is  $\text{MgCl}_2$ -water. An experiment with  $\text{MgCl}_2$ -water was attempted. The solution was cooled slowly during the experiment on PLANET, but it did not crystallise upon cooling at ambient pressure. Therefore the high-pressure annealing was not performed. Brown and Hand (2013) discuss salts and radiation products on Jupiter's moon Europa. They suggest that  $\text{MgCl}_2$  is a constituent of a Europa ocean brine, based on observational (spectroscopic) evidence for  $\text{MgSO}_4$  on the surface, which is interpreted to be a radiation product of the former salt. Thus the possibility of magnesium salts inclusion in ices ought to be investigated.

We have performed experiments on LiBr-water solution on the PLANET beamline at J-PARC. The  $R = 5.6$  solution amorphises well by slow cooling. Upon annealing at  $\approx 4$  GPa the amorphous phase crystallises at about 260 K. The diffraction pattern is very similar to that of the salty ice VII crystallised from  $\text{LiCl} \cdot 6\text{D}_2\text{O}$ . The attenuation of the peaks with increasing  $q$  is strong and suggests a large Debye-Waller factor. The analysis is in progress. The details are not reported here.

# Appendix A

## Additional data from experiments and simulations

### A.1 Fits of diffraction data

#### A.1.1 Profile functions for fitting diffraction data

Pseudo-Voigt functions were used for fitting ice  $I_h$  peaks in ambient pressure data.

A brief description of TOF functions used by GSAS for fitting ice VII peaks at several GPa.

#### A.1.2 Fit of sample 3 with peak positions

The GSAS fit of sample 3 at 260 K and 3.6 GPa with diamond,  $\beta$   $N_2$ , ice VII and NaCl is shown in Figure A.2. The background has not been subtracted from the data here. Tick marks for the peak of each phase are shown in the figure.

#### A.1.3 Fit of sample 3 with salty ice VII

The GSAS fit of sample 3 at 260 K and 3.6 GPa with diamond,  $\beta$   $N_2$ , salty ice VII and NaCl is shown in Figure A.2. The background has not been subtracted from the data here. Tick marks for the peak of each phase are shown in the figure. The ice VII structure in GSAS was modified by adding  $Na^+$  and  $Cl^-$  ions at oxygen sites and reducing the fraction of oxygen and deuterium so that the concentration corresponds to  $R = 10.2$ . The occupancy of  $Na^+$  and  $Cl^-$  was set to  $1/12.2$ , that of oxygen to  $10.2/12.2$ . This fit gave  $\chi^2 = 2.628$ , which is a little less than that for the pure ice VII fit. However there are 2 new parameters introduced *U<sub>i</sub>so* of Na and Cl and both are very large ( $0.8 \text{ \AA}^2$ ). For this reason the fit is not an improvement on the fit with pure ice VII described in chapter 5, section 5.2.1.

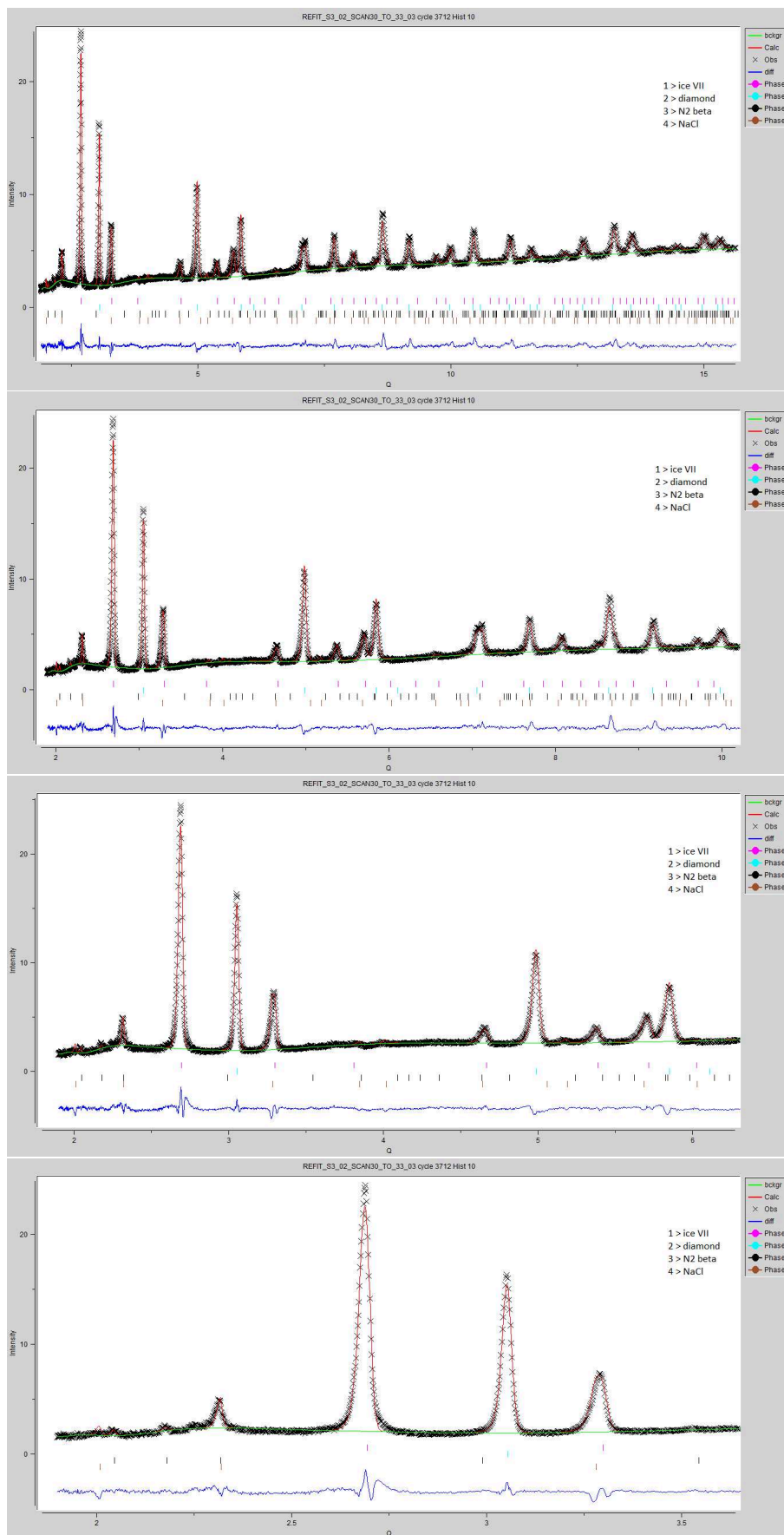


Figure A.1: GSAS fit of sample 3 at 260 K and 3.6 GPa. The fit contains the following phases, the peak positions of which are indicated by tick marks. Phase 1 is ice VII (pink), phase 2 is diamond (turquoise), phase 3 is  $\beta$  N<sub>2</sub> (black), phase 4 is NaCl (brown). for the set of salty ice VII boxes containing 8 substitutional ions.

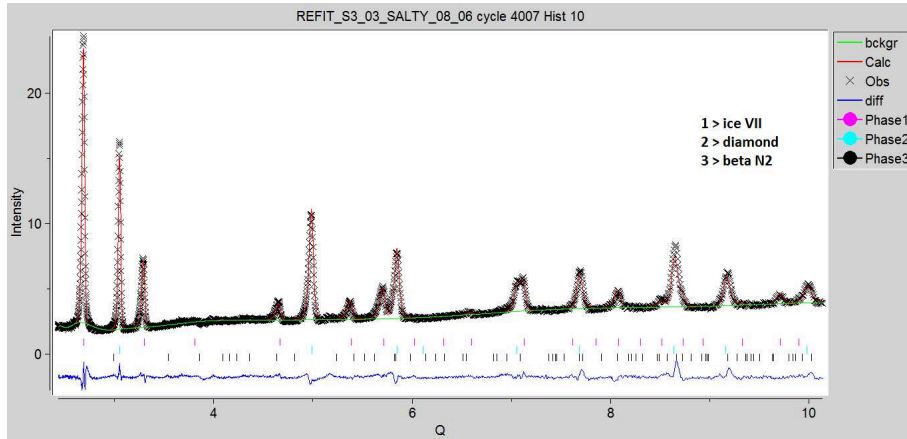


Figure A.2: GSAS fit of sample 3 at 260 K and 3.6 GPa with salty ice VII. The fit contains the following phases, the peak positions of which are indicated by tick marks. Phase 1 is salty ice VII (pink), phase 2 is diamond (turquoise), phase 3 is  $\beta$  N<sub>2</sub> (black). for the set of salty ice VII boxes containing 8 substitutional ions.

## A.2 Simulations of salty ice VII

### A.2.1 Distribution of dipoles in the set of salty ice boxes

The sum dipoles of water molecules in the boxes of ice VII containing 4 pairs of Na<sup>+</sup> and Cl<sup>-</sup> substituting water molecules were computed for a subset of 14 thousand configurations among the set of about 100 thousand hydrogen disordered configurations. The average energy of this subset is  $-1.68$  Ry with  $\sigma = 0.2$  Ry. The classical energy is shown as function of the norm of the total dipole of all water molecules in the box and its ratio to the dipole of a single water molecule are shown in A.3. The projections of dipole along the  $x$ ,  $y$ ,  $z$  directions are given in A.4. The boxes show a net dipole along the  $z$  direction.

### A.2.2 Fitted equations of state for pure and salty ice

The equations of state (EOS)  $p(a)$ , shown in Figures A.5 and A.6 were computed from geometry optimisation at 0 K. Each figure shows the EOS for a single box, which contains a  $3 \times 3 \times 3$  supercell of ice VII. The pure box contains  $2 \times 3^3 = 54$  water molecules. In the salty boxes ions were substituted for water molecules.

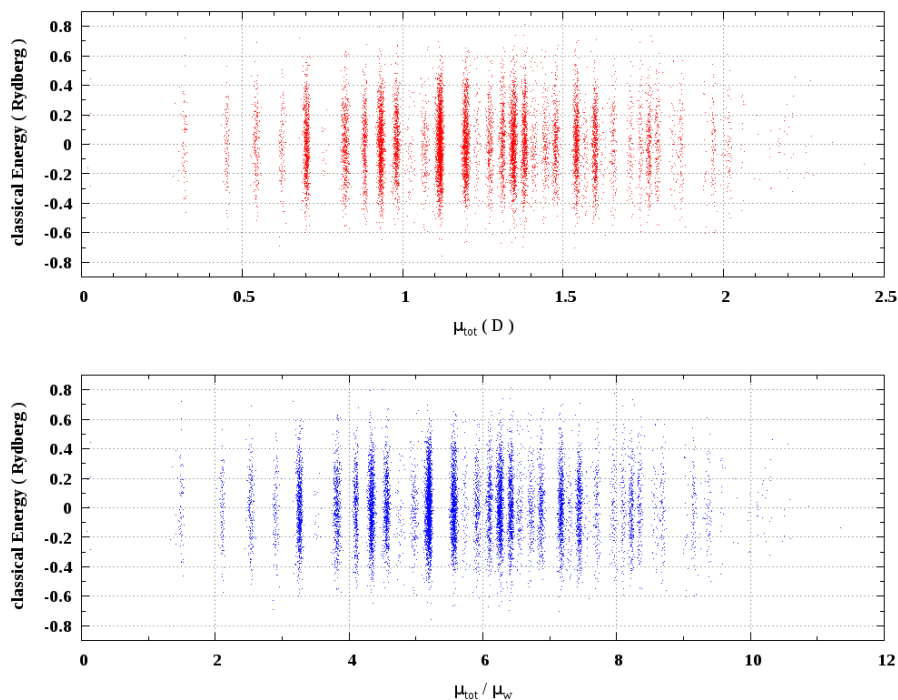


Figure A.3: The norm of the total dipole  $\mu_{\text{tot}}$  in Debye and in units of the water dipole  $\mu_w$  for the set of salty ice VII boxes containing 8 substitutional ions.

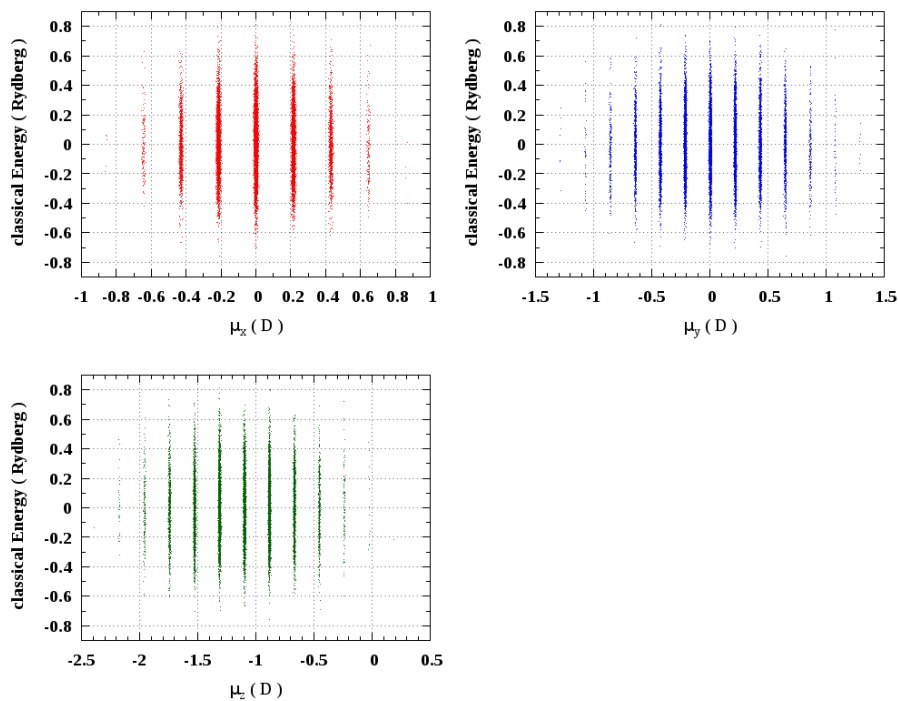


Figure A.4: Projections of the dipole  $\mu_{\text{tot}}$  along the coordinate axes. There is a net dipole along the  $z$  direction.

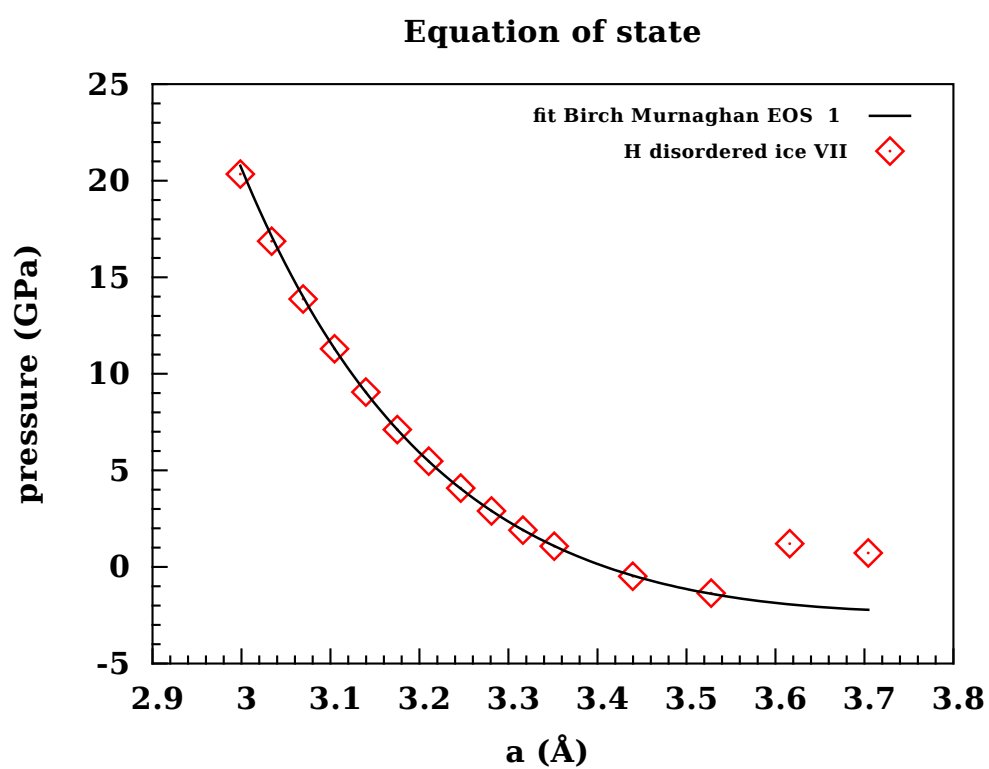


Figure A.5: BM fit of EOS  $p$  versus  $a$  for pure ice VII from simulations (54 water molecules).

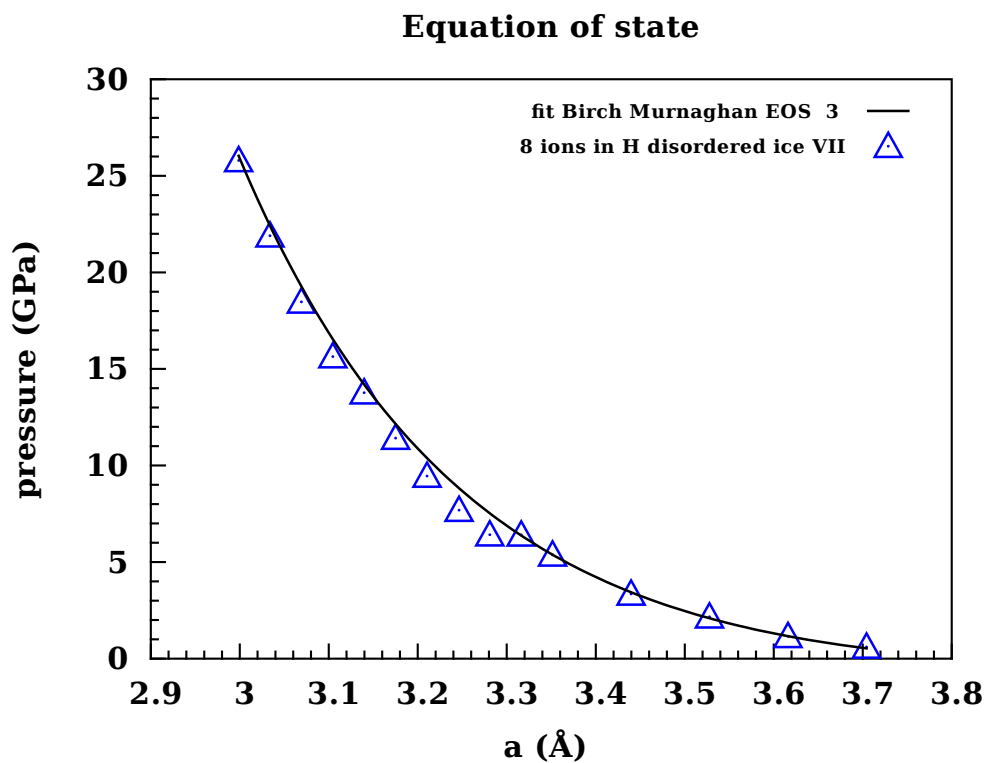
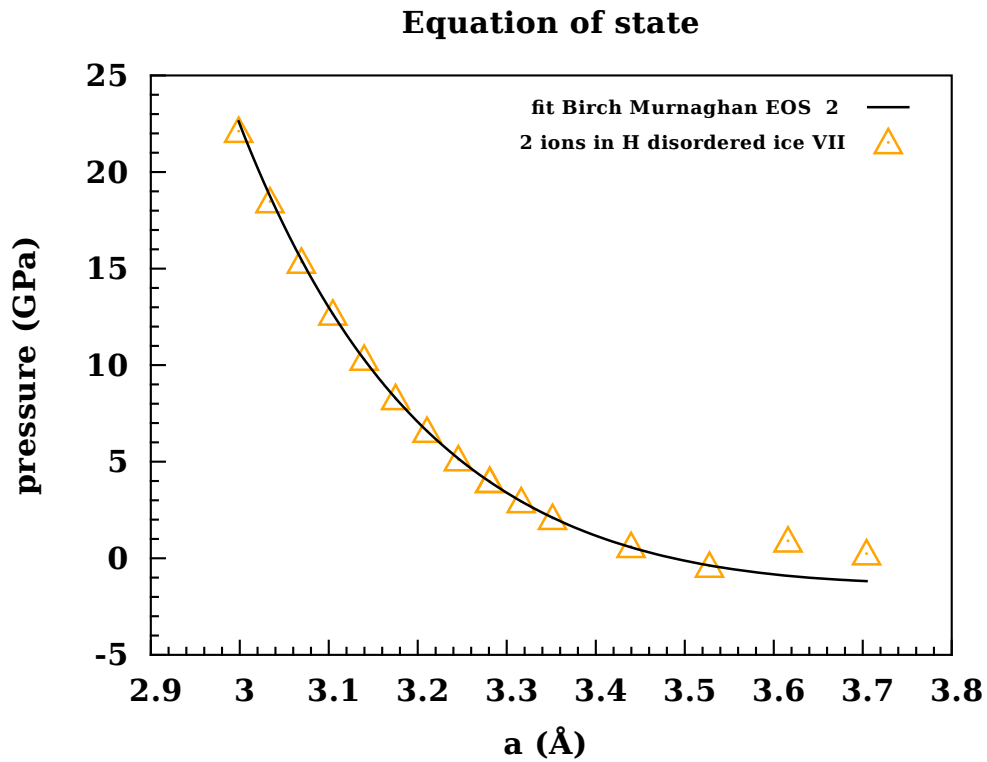


Figure A.6: Top: BM fit of EOS  $p$  versus  $a$  for salty ice VII (2 ions, 52 water molecules,  $R = 52$ ) from simulations. Bottom: BM fit of EOS  $p$  versus  $a$  for salty ice VII (8 ions, 46 water molecules,  $R = 11.5$ ) from simulations.

## Physical constants and units

$k_B$	$1.38065 \times 10^{-23}$	J/K
$N_A$	$6.02214 \times 10^{23}$	mol <sup>-1</sup>
$h$	$6.62607 \times 10^{-34}$	Js
$c$	299 792 458	m/s
$e$	$1.60219 \times 10^{-19}$	C
$m_p$	$1.67262 \times 10^{-27}$	kg
$m_n$	$1.67493 \times 10^{-27}$	kg
$R$	8.31446	kJ/mol/K

Table A.1: List of physical constants.

1 Rydberg	= 13.605 eV = $21.8 \times 10^{-19}$ Joule
1 kT	= $414.16 \times 10^{-23}$ Joule = 2105 Rydberg at $T = 300$ K
1 GPa	= $10^9$ Pa = 10 kbar
1 $a_{\text{Bohr}}$	= 0.529177249 Å

Table A.2: Unit conversions.

## A.3 Thermal average

The thermal average of an operator  $\mathbf{R}$  is given by (Squires, 2012)

$$\langle \mathbf{R} \rangle = \sum_{\mu} p_{\mu} \langle \mu | \mathbf{R} | \mu \rangle . \quad (\text{A.1})$$

He considers a quantum mechanical system at temperature  $T$  described by a single index  $\mu$ . The probability  $p_{\mu}$  to find the system in state  $\mu$  is

$$p_{\mu} = \frac{\exp(-\beta E_{\mu})}{Z} \quad (\text{A.2})$$

$$Z = \sum_{\mu} \exp(-\beta E_{\mu}) \quad (\text{A.3})$$

where  $Z$  is the canonical partition function and  $\beta = 1/(k_B T)$ .

## A.4 Multipolar expansion

The dipole and quadrupole tensors are, as defined by Stone (1996)

$$\begin{aligned}\mathbf{T}_a &= \frac{1}{4\pi\epsilon_0} \nabla_a \frac{1}{r} = -\frac{1}{4\pi\epsilon_0} \frac{r_a}{r^3} \\ \mathbf{T}_{ab} &= \frac{1}{4\pi\epsilon_0} \nabla_a \nabla_b \frac{1}{r} = \frac{1}{4\pi\epsilon_0} \frac{1}{r^3} \left( \frac{3\mathbf{r}_a\mathbf{r}_b}{r^2} - \delta_{ab} \right)\end{aligned}\tag{A.4}$$

where  $r = \|\mathbf{r}\|$ ,  $\mathbf{r}_j$  are the components of  $\mathbf{r}$ , and  $\delta_{ij}$  is the Kronecker delta symbol.

The multipolar expansion of a field is given in Landau and Lifshitz (1975).

## A.5 X-ray form factors

In chapter 2 section 2.1.2 on X-ray scattering mentions the atomic form factor  $f_n$  which replaces the neutron scattering cross-section appears in (2.8). It depends on the wavelength  $\lambda$  of the incident X-ray.

$$f_n(\lambda) = \sum_{j=1}^n f_{ej}(\lambda)\tag{A.5}$$

$$= \sum_{j=1}^n 4 \int_0^{+\infty} \pi r^2 \rho_n(r) \frac{\sin(kr)}{kr} dr\tag{A.6}$$

where  $k = 4\pi \sin(\theta)/\lambda$  and  $\rho_n$  is the charge density of each electron of the atom (Warren, 2012).

## A.6 List of abbreviations

---

AIMD	<i>ab initio</i> molecular dynamics
ASW	amorphous solid water
BLYP	a GGA exchange correlation functional (Lee et al., 1988)
BF	Bernal and Fowler fully atomistic model of water
BFGS	Billeter-Fletcher algorithm
BM	Birch-Murnaghan equation of state
CCR	critical cooling rate; closed cycle refrigeration
CINES	Centre Informatique National de l'Enseignement Supérieur
CODATA	Committee on Data for Science and Technology
CP2K	Atomistic simulation package (developers group, 2012)
D20	powder neutron diffraction beamline at ILL (France)
DAC	Diamond anvil cell
DC	Dang and Chang polarisable model of water
DFT	Density Functional Theory
eHDA	expanded HDA (High density amorphous ice)
EOS	Equation of State
ESRF	European Synchrotron Radiation Facility
ESS	European Spallation Source
EXAFS	Extended X-ray absorption spectroscopy
EXPGUI	Graphical interface EXPGUI of GSAS
FWHM	Full width at half maximum
GGA	Generalised gradient approximation in DFT (Becke, 1988)
GPa	Giga Pascal
GSAS	General Structure Analysis System
HDA	high density amorphous
ILL	Institut Laue-Langevin in Grenoble (France)
ISAACS	Interactive Structure Analysis of Amorphous and Crystalline Systems program
ISIS	Neutron source at the RAL in Oxfordshire (UK)
J-parc	Japan proton accelerator research complex
LDA	Local density approximation in DFT
LDA	Low density amorphous ice
MD	Molecular Dynamics

---

Table A.3: List of recurring abbreviations used in this thesis.

---

ND	Neutron diffraction
NIST	National Institute of Standards and Technology
NPT	isothermal–isobaric ensemble
NVE	Micro-canonical ensemble
NVT	Canonical ensemble
PBE	PBE GGA functional
PEARL	high-pressure powder neutron diffraction beamline at ISIS
PE or PEC	Paris-Edinburgh cell
PIM	Polarizable ion model
PLANET	high-pressure powder neutron diffraction beamline at J-parc (Japan)
QENS	Quasi-elastic neutron scattering
QE	Quantum Espresso program suite
RAL	Rutherford Appleton Laboratory in Oxfordshire (UK)
RDF	Radial distribution function
RRKJ3	Type of pseudo-potentials (Rappe et al., 1990)
SD	Sintered diamond
SF	Structure factor
SPC/E	Simple point charge / Extended model of water
TC	Tungsten carbide
TIP4P	planar four-site interaction potential for water
TOF	Time of flight
uHDA	unrelaxed high density amorphous
VHDA	Very high density amorphous
XRD	X-ray diffraction

---

Table A.4: List of recurring abbreviations used in this thesis. (continued)

# Appendix B

## Résumé en français

« ubi materia, ibi geometria »

Johannes Kepler (1601) \*

*De Fundamentis Astrologiae Certioribus*

Le lien entre matière et géométrie a dû s'imposer aux premiers hommes ayant tenté de décrire et représenter graphiquement ce qu'ils observaient. Les figures géométriques régulières apparaissent naturellement, comme en témoignent les flocons de neige. Kepler suggéra justement que les flocons devaient leur symétrie hexagonale à l'empilement des "plus petites unités de liquide" dans *De Nive Sexangula* (1611) (Ball, 2011). On a depuis montré par diffraction aux rayons X que la structure cristalline de la glace ordinaire (Ih) est effectivement hexagonale, bien qu'il ne s'agisse pas d'un empilement compact comme l'avait conjecturé Kepler. Les travaux présentés dans cette thèse ont pour objet la structure de solutions aqueuses d'électrolytes et les transitions de phase qui surviennent lorsque les structures locale et globale du matériau sont modifiées au gré des contraintes de température et de pression. On s'intéresse ici essentiellement aux solutions de sel (NaCl) dans l'eau (H<sub>2</sub>O ou D<sub>2</sub>O), dont la structure, à température et pression ambiantes, s'organise autour de deux entités géométriques élémentaires : le tétraèdre et l'octaèdre (Figure 1.1). Les premiers voisins d'une molécule d'eau occupent les sommets des tétraèdres ; tandis que les couches de solvation des cations sodium forment les octaèdres (Enderby et Neilson, 1981). Lorsque la pression s'accroît, ces deux éléments structurels subissent des déformations. La section suivante expose une brève discussion des propriétés physiques de l'eau et de la glace telles que l'on les rencontre dans la nature. Il s'ensuit une discussion de la structure des solutions aqueuses d'électrolytes. La dernière section donne un aperçu du travail présenté dans les chapitres suivants.

---

\*\*Qui peut être traduit ainsi : " Là où il y a de la matière, il y a de la géométrie ".

## B.1 L'eau et la glace

**L'eau** sur Terre est indissociable de la vie et de la civilisation humaine. Ses formes liquide, cristallisées ou gazeuse nous sont toutes familières. En effet les conditions de température et de pression ambiantes, 300 K et 1 atm, ne sont pas trop éloignées du point triple de l'eau, 273,16K et 611,73 Pa, où les trois phases coexistent en équilibre thermodynamique (NIST, IAPWS) (NIST, 2015, Wagner, 1999, Wikipedia, 2015). Ce point triple plutôt bas et les propriétés thermodynamiques de l'eau sont les conséquences de l'interaction entre les molécules d'eau. Cette interaction est aussi responsable du réseau de liaisons hydrogène formées par les molécules d'eau en phases liquide et solide (Debenedetti, 1996). L'eau est une substance singulière qui manifeste de nombreuses propriétés inattendues voire "anormales" comparées aux autres liquides. Les anomalies observées dans le régime de surfusion sont présentées en page 161.

**La glace**, à pression ambiante, flotte sur l'eau, car la densité de la glace cristalline hexagonale (Ih) est moindre que celle de la phase liquide. C'est là probablement la plus surprenante propriété de l'eau, qui la distingue de la plupart des autres substances, par exemple les liquides simples comme l'argon. C'est aussi l'une des raisons pour lesquelles l'eau a une telle influence sur le climat (Koop, 2015). Cependant, il ne s'agit pas d'une propriété universelle de la glace. À haute pression la glace devient en effet plus dense que la phase liquide : elle coule donc. C'est le cas des glaces VI et VII. Dans cette thèse on s'intéresse surtout aux hautes pressions ( $p > 1$  GPa). Dans ce domaine de pression et pour des températures variant de 77 à environ 350 K, le diagramme de phase de l'eau pure présente une surprenante diversité de phases solides distinctes (Figure 1.2). Seize phases cristallines de glace ont jusqu'ici été répertoriées, et sont traditionnellement identifiées par des chiffres romains, ainsi que trois phases amorphes. L'existence de tant de phases différentes est due à la structure des molécules d'eau et aux liaisons hydrogène qu'elles génèrent. Si la configuration d'équilibre d'une molécule d'eau au repos est un triangle isocèle, dans les glaces, en revanche, ce triangle se déforme. La géométrie et l'environnement d'une molécule d'eau dans la phase de glace Ih sont représentés en Figure 1.1. L'angle  $\widehat{\text{HOH}}$  mesure environ  $106^\circ$ . Cette valeur est proche de celle de l'angle au centre d'un tétraèdre régulier et il en va de même pour toutes les phases de glace moléculaire. Ainsi la molécule d'eau est encline à former quatre liaisons hydrogène avec ses voisins dans la plupart des phases, d'où les règles de Bernal-Fowler, dites "règles de la glace" :

- (i) chaque atome d'oxygène établit quatre liaisons hydrogène avec ses voisins ;
- (ii) pour chaque paire d'oxygènes voisins, exactement un atome d'hydrogène se situe entre les deux atomes d'oxygène où il occupe l'une des deux positions disponibles ;
- (iii) exactement deux atomes d'hydrogène se situent dans un rayon intramoléculaire d'environ 1 Å autour de chaque atome d'oxygène.

FIGURE 1.1

Ces règles sont valables dans les phases de glace moléculaire cristalline, sauf dans le cas des défauts de Bjerrum, qui sont rares (Bjerrum, 1952). En volume, ces défauts entraînent l'apparition de grandes lacunes dans le réseau. Soumis à la pression, ce réseau se densifie et sa structure se transforme (Bartels-Rausch et al., 2012). Ce réseau de liaisons hydrogènes subsiste aussi partiellement en phase liquide et il a été avancé que ce réseau percolateur serait à l'origine des anomalies de l'eau (voire plus loin et Geiger et al. (1979)). Quatre phases cristallines seront évoquées dans les chapitres suivants : la glace hexagonale I (glace Ih), la glace "cubique" (glace Ic), la glace cubique VII, et la glace tétragonale VIII. †

Les glaces Ih et Ic sont des polymorphes de basse pression ; la première étant la phase prédominante sur la surface de la Terre. Sa structure consiste en un réseau hexagonal d'atome d'oxygène (groupe d'espace  $P63/mmc$ ) et fut identifiée dans les années 1920 (Dennison, 1921). En 1935, Pauling suggéra d'abord que les atomes d'hydrogène dans la glace Ih seraient désordonnés de façon à expliquer l'entropie résiduelle mesurée dans les expériences à basse température (Giauque et Ashley, 1933). La structure du désordre dans la glace Ih a fait l'objet d'études approfondies par le passé (Kuhs et Lehman, 1986, 1987). La glace Ic devrait être strictement cubique (groupe d'espace  $Fd3m$ ) si elle apparaissait sous forme pure, ce qui n'a jamais pu être vérifié en pratique car tous les échantillons contenant de la glace Ic comportaient aussi une fraction de glace structure hexagonale (Hansen et al., 2015, Kuhs et al., 2012). Cela est dû au fait que ces deux phases ne se distinguent l'une de l'autre que par l'ordre d'empilement des plans du réseau le long de l'axe  $c$  du cristal. Il a été avancé que la glace cubique contiendrait toujours des défauts d'empilement et par conséquent une fraction de matière en disposition hexagonale

---

† Dans un cristal, les particules (atomes ou molécules) sont arrangées selon un réseau périodique (Kittel et McEuen, 1976). Les cristaux sont répertoriés selon sept systèmes périodiques et 14 réseaux de Bravais. Il existe 230 groupes d'isométrie distincts pour les réseaux périodiques dans l'espace euclidien à trois dimension. Ils sont appelés groupes d'espace et sont listés dans les Tables Internationales de Cristallographie (Hahn, 2006).

(Hansen et al., 2008a,b, Malkin et al., 2015). Cette phase existe à basse température et se transforme en glace Ih au delà de 190 K.

FIGURE 1.2

Les glaces VII et VIII sont des phases de haute pression (stables à partir d'environ 1.5 GPa). La glace VII est cubique et les hydrogènes y sont désordonnés. Sa structure est composée de deux réseaux de glace Ic imbriqués. Son groupe d'espace est Pn3m et le lecteur en trouvera la description exhaustive dans (Jorgensen and Worlton, 1985, Kuhs et al., 1984). La phase de basse température correspondante est la glace tétragonale VIII, dont le groupe d'espace est P42nm. Dans cette phase, les hydrogènes sont (partiellement) ordonnés (Johari, 1974, Kuhs et al., 1984). Pour les phases de glace cristalline, la règle générale régissant l'ordre parmi les hydrogènes semble être la suivante : « toute phase cristalline contiguë à la phase liquide (glaces Ih, III, V, VI et VII) a des liaisons hydrogènes désordonnées », d'après (Chaplin, 2015, Holzapfel, 1972, Johari, 1974, Kuhs et al., 1984, Pauling, 1935).

Certaines phases aux hydrogènes ordonnés sont difficiles à obtenir expérimentalement, même à basses températures. Il est possible de les rendre stables en dopant la glace avec des ions. Pour la glace XI, on dope de la glace Ih avec du KOH (à la concentration de 10 mM), à pression ambiante et basse température ( $T \approx 72$  K) (Fukazawa et al., 1998, Matsuo et al., 1986, Pamuk et al., 2015). Les glaces XIII et XIV ont été obtenues à l'aide de dopage à l'HCl (Salzmann, 2006). Remarquons au passage que cette base simple et cet acide simple sont propices à l'ordre des hydrogènes, alors que les autres sels (halogénures alcalins comme le LiCl et le NaCl) ont tendance à provoquer le désordre parmi les liaisons hydrogènes. Ceci est probablement dû à l'interaction privilégiée entre les défauts de  $\text{H}_3\text{O}^+$  et  $\text{HO}^-$  et les molécules d'eau.

FIGURE 1.3

**Glaces amorphes :** Les domaines de stabilité en pression et température des trois structures amorphes distinctes de glace pure (Loerting et al., 2011) sont représentés en figure 1.3. On peut distinguer cinq états amorphes en fonction de leur méthode de préparation. Le premier est l'eau solide amorphe (ASW), que l'on obtient via dépôt par phase vapeur sur un substrat à température d'azote liquide. Vient ensuite l'eau solide vitreuse (HGW), obtenue par hypertrempe de gouttelettes liquides. Toutes deux sont des états amorphes de basse densité, dont les structures sont très similaires à celle de la forme amorphe de basse densité (LDA) que l'on produit par recuit de la forme de haute densité à pression ambiante (Kohl et al., 2005). Par sa structure

localement tétraédrique, cette dernière s'apparente à la glace Ih. La forme de haute densité (HDA) apparaît lorsque l'on compresse les phases de basse pression (glace Ih, Ic ou LDA) au-delà de 0,2 GPa ; elle est métastable à pression ambiante et basse température. On peut en produire une forme plus relâchée, appelée forme de haute densité expansée (eHDA) par recuit de la forme de haute densité à environ 125K et à pression modérée (Winkel et al. 2008, 2011b). Le même procédé à des pressions excédant le GPa produit la forme de très haute densité (VHDA). On pourra en obtenir à pression ambiante grâce à l'hysteresis (Nelmes et al., 2006). Les facteurs de structure de ces phases amorphes sont présentés dans la figure 1.4, due à Bowron et al. (2006). Les flèches verticales y mettent en évidence le déplacement du premier pic de diffraction vers les vecteurs d'onde plus grands pour les phases plus denses. Les techniques de trempe employées pour obtenir des glaces amorphes au laboratoire seront traitées au chapitre 4.

On parle de polyamorphisme lorsque deux états amorphes, qui diffèrent par leur densité et l'arrangement local des molécules, coexistent. La transition entre deux tels états, qui correspond aux changements de structure et de densité, se fait plus ou moins rapidement selon le paramètre extérieur qui la provoque. Ainsi la transition entre les phases HDA et LDA par recuit à 0,2 GPa est réversible et soudaine (Mishima, 1991). En revanche une hystérèse nette caractérise la décompression des phases HDA et VHDA à 77 K, comme évoqué précédemment.

**La surfusion** décrit l'eau liquide en dessous du point de fusion ( $0^\circ\text{C}$  à 1 atm). Il s'agit d'un état métastable au sein duquel la formation de la glace devrait s'amorcer. La température où l'on peut observer de l'eau surfondue dépend de la pureté de celle-ci. La surfusion d'échantillons très purs est envisageable jusqu'à la température de nucléation homogène ( $T_H \approx 235\text{K} = -38^\circ\text{C}$  à 1 atm), à laquelle l'eau gèle sans site de nucléation privilégié (impuretés ou perturbations) (Koop, 2015). Dans des conditions expérimentales adaptées, l'eau subsiste dans cet état métastable (Debenedetti, 1996).

La région du diagramme température-pression située sous la courbe de température de nucléation homogène, et au-dessus des transitions vitreuses des glaces amorphes, dans laquelle ni phase liquide ni phase amorphe n'ont été observées dans les expériences, a été baptisée No man's land. On entend par là qu'il est impossible d'observer la transition vitreuse dans l'eau pure sur une large plage de températures, à l'inverse de ce que l'on observe pour d'autres systèmes vitrifiables. Selon Speedy et Angell (1976), la compressibilité isotherme semble diverger lorsque la température décroît juste en-deçà de  $T_H$ . De nombreux autres coefficients thermodynamiques (capacité thermique, viscosité, coefficients de dilatation thermique et d'auto-diffusion, conductivité thermique, divers temps de relaxation) auraient aussi

tendance à diverger d'après les extrapolations de nombreuses expériences (Angell et al., 1982, Mishima, 2000, Stanley and Mallamace, 2015). Ces divergences sont inattendues et plusieurs explications y ont été proposées (Holten et al., 2012, Speedy et Angell, 1976). Une fois les phases de glace amorphes découvertes et leurs transitions mieux caractérisées, il a été suggéré qu'une transition de phase du premier ordre entre deux liquides (LLPT) pourrait prolonger la transition entre les phases LDA et HDA pour les températures plus élevées. Il y aurait alors un liquide de basse densité (LDL) et un autre plus dense (HDL) correspondant chacun à une des phases amorphes en question. L'existence d'un second point critique à l'extrémité de la transition LLPT en-dessous de TH a été avancé comme explication des divergences apparentes (Stanley et Mallamace, 2015, Stanley et Mishima, 1998).

La dynamique et la structure de l'eau au niveau de la limite supérieure du No man's land (vers 227 K) pour des intervalles de temps réduits ont fait l'objet d'une étude récente utilisant des techniques de laser à électrons libres en rayons X (Sellberg et al., 2014). Une autre étude aborde cette région depuis le côté des basses températures (Amann-Winkel et al., 2013). Toutefois le No man's land demeure très peu exploré expérimentalement. En revanche les simulations permettent de sonder le comportement de l'eau dans cette région, ce qui donne lieu à un débat actif à son sujet (Limmer et Chandler, 2013, Palmer et al., 2014). Afin d'étudier le No man's land, il est aussi possible d'utiliser de l'eau nano-confinée (Chen et al., 2006, Mallamace et al., 2006), par exemple avec des minéraux poreux (comme les zéolithes) ou des cellules qui ne gèlent pas à la température de nucléation homogène TH dans le volume (Nigro et al., 2015), ou encore des solutions aqueuses qui peuvent être surfondues dans cette région (voir section suivante).

**Les glaces astrophysiques** . L'eau est une molécule abondante dans l'espace. Elle est produite lors de la formation des étoiles et peut être trouvée dans les atmosphères stellaires ainsi que dans les nuages interstellaires. Lorsque ceux-ci se refroidissent, la vapeur d'eau (et les autres gaz comme le CO), se condensent et de la glace se forme à la surface des grains de poussière cosmique. Cela arrive au-delà de la ligne de la glace, à environ 3 unités astronomiques du soleil dans le cas des débuts de notre système solaire. Comme les grains sont habituellement froids (moins de 200 K), cette glace est en général amorphe (ASW ou LDA) ou cubique (Ciesla, 2014, Hogerheijde, 2010). Les phases amorphes constituent donc probablement l'essentiel de la glace interstellaire (Jenniskens et Blake, 1996). Par ailleurs on estime que la masse totale de glace, toutes phases confondues, vaudrait le double de celle de la matière rocheuse (Lodders, 2003). Au sein des disques protoplanétaires entourant les jeunes étoiles, ces grains entrent en collision et s'agglomèrent en débris, comètes, planétésimaux et à long terme en planètes comme celles de notre système. La glace

joue certainement un rôle majeur dans ce processus d'accrétion. Des études expérimentales et théoriques ont montré que la coagulation des particules de poussière est entravée par les rebonds et la fragmentation (Gundlach et al., 2011a,b, Wada et al., 2008). Peu après, Ros et Johansen (2013) ont prouvé à l'aide d'un modèle numérique que la condensation de la vapeur est un mode de croissance efficace pour la formation de cailloux galets de l'ordre du décimètre.

#### FIGURE 1.4

Au cours de l'accrétion, de violentes collisions entre des planétésimaux de plus en plus grands se produisent.

La glace a aussi été envisagée comme milieu pour le développement de molécules organiques et de la chimie prébiotique (Modica et al., 2014). La glace marine sur terre pourrait elle aussi être liée aux origines de la vie (Trinks et al., 2005).

NB : Dans la suite, le mot « glace », seul, désignera exclusivement les phases cristallines. Toute allusion à la phase amorphe sera explicitement indiquée. Cette phase sera aussi désignée par « état amorphe » ou encore « glace amorphe ».

## B.2 Les solutions aqueuses

Les solutions aqueuses d'électrolytes, comme le LiCl et le NaCl en solution, apparaissent spontanément dans la nature et sont étudiées dans divers domaines de la science, de la géologie aux techniques de l'énergie. Dans ces systèmes, les espèces chimiques chargées soumettent les molécules d'eau à l'interaction coulombienne. La limite du nombre d'ions que l'on peut dissoudre dans un certain volume d'eau est appelée solubilité. Les propriétés des ions en solution et celles de leurs couches de solvatation ont été largement étudiées (Bankura et al., 2013, Mancinelli et al., 2007, Neilson et Enderby, 1979), notamment parce-que leur compréhension est cruciale à celle de nombreux mécanismes chimiques et biologiques. Les concepts de structure-breaking et de structure-making ont été largement exploités pour expliquer, au moins qualitativement, les effets des ions sur la structure de l'eau. Les ions sont censés soit briser le réseau de liaisons hydrogène soit former une structure de solvatation ionique (Gallo et al., 2011, Leberman et Soper, 1995, Mancinelli et al., 2007, Winkel et al., 2011a). Les solutions de LiCl ont fait l'objet d'études approfondies depuis le début des années 1970, afin d'aborder les propriétés thermodynamiques et structurales de l'eau dans le régime de surfusion à basse température (Angell et Sore, 1970, Kanno, 1987, Prével et al., 1995), dont la stabilité est accrue par la présence d'ions.

#### FIGURE 1.5

La plupart des solutions électrolytiques présentent la caractéristique commune de ne pas inclure les ions dans la glace formée lorsqu'elles cristallisent. Selon leur concentration, ceux-ci peuvent alors être exclus de la glace vers une solution de forte concentration (appelée saumure), ou bien former des hydrates de compositions bien définies ou des précipités ioniques purs. (Elarby-Aouizerat et al., 1983, Kessis, 1965, Klewe et Pedersen, 1974, Vrbka et Jungwirth, 2006). C'est la raison principale pour laquelle le domaine solide du diagramme de phases de telles solutions a été peu exploré à haute pression. Le comportement de solutions aqueuses de LiCl à haute pression a été étudié plus récemment via des expériences de diffraction de neutrons et des simulations atomistiques (Bove et al., 2011b, Klotz et al., 2009, Ruiz et al., 2014). Une transition polyamorphique entre des structures de haute densité et de très haute densité a été mise en évidence à haute pression (Bove et al., 2011b). Cette transition est similaire à celle que l'on observe dans l'eau pure. Par surcroît, des résultats expérimentaux appuient maintenant l'existence de phases de glace de haute pression qui comportent une quantité considérable d'ions dans leurs réseaux (Klotz et al., 2009).

FIGURE 1.6

L'état relâché de haute densité a été produit en refroidissant une solution eutectique de  $\text{LiCl} \cdot 6\text{D}_2\text{O}$  (Dupuy-Philon et al., 1992) à pression ambiante. Il est très similaire à l'état eHDA de l'eau pure, comme illustré dans le panneau de gauche de la figure 1.6. Cet état de type HDA subit une transition polyamorphique vers l'état de très haute densité lors du recuit de la solution sous haute pression (panneau de droite de la figure 1.6). Ce dernier état s'est avéré très stable jusqu'à des pressions de plusieurs GPa. Remarquons que l'ion  $\text{Li}^+$  est de coordinence octaédrique à haute pression, qu'il soit en phase amorphe ou cristalline (voir paragraphe suivant). La transition polyamorphique observée (eHDA vers HDA) est due au changement d'environnement de l'ion  $\text{Li}^+$  dont l'indice de coordination passe de 4, à pression ambiante, à 6 à haute pression (Bove et al., 2011b). On ignore encore si les transitions polyamorphiques sont une caractéristique fréquente chez les solutions électrolytiques, et leur éventuelle corrélation avec les transitions analogues observées pour l'eau pure (Klotz et al., 2005), suggérée par de récentes mesures au Raman (Suzuki and Mishima, 2009a), est à confirmer. Les travaux présentés ici contribuent à ces investigations à travers l'étude de solutions de NaCl. La phase de glace VII, qui cristallise par recuit de l'état VHDA à 4 GPa, s'est avérée incorporer le LiCl au sein de son réseau en substituant des molécules d'eau par des ions  $\text{Cl}^-$ , et en incluant des ions  $\text{Li}^+$  dans les interstices octaédriques du système cubique centré (bcc) des oxygènes dans la glace VII. Cette structure présente une expansion de la

maille élémentaire de 8% en volume à 4 GPa, et des facteurs de déplacement 5 fois supérieurs à ceux que l'on mesure pour la glace VII pure. Cela se traduit, comme montré en figure 1.7, par une forte atténuation des pics lorsque  $q$  augmente dans les diagrammes de diffraction (Klotz et al., 2009).

FIGURE 1.7

## B.3 Aperçu des travaux

Que ce soit en biologie ou en géochimie, le NaCl tient une place plus importante que le LiCl ; aussi l'existence de nouvelles phases amorphes ou cristallines de solution de NaCl pourrait se révéler primordiale, aussi bien pour la physique des organismes vivants que pour celle des corps célestes (Bezacier et al., 2014a, Frank et al., 2006). Jusqu'ici le di-hydrate de NaCl est le seul composé solide connu formé de NaCl et d'H<sub>2</sub>O. Aucune transition de phase de l'état solide n'a été découverte (Klewe and Pedersen, 1974), à l'inverse du système LiCl – H<sub>2</sub>O qui peut selon la concentration en sel et les conditions de pression former plusieurs hydrates (Elarby-Aouizerat et al., 1983).

Nous étudions ici les phases (métastables) amorphes et cristallines de solutions aqueuses de NaCl proches du mélange eutectique à haute pression. Nous avons combiné diffraction de neutrons à haute pression et simulations de dynamique moléculaire afin d'obtenir des informations précises sur la structure des solutions. Nos expériences suivent les chemins de la figure B.1, qui donne aussi le diagramme des phases métastables de la solution de LiCl. Le chemin 1 correspond à la trempe de la solution. Le chemin 2 est un recuit à température ambiante. Le chemin 3 est la compression de l'échantillon jusqu'à 4 GPa à 80 K ; le chemin 3' celle à 140 K, uniquement en simulation. Le chemin 4 est le recuit de la phase amorphe jusqu'à 140 K ; le chemin 5 celui de la solution jusqu'à 300 K à 4 GPa. Le chemin 6 est le refroidissement de la phase cristalline jusqu'à 80 K à 4 GPa. Le chemin 7 est la décompression jusqu'à pression ambiante à 80 K. Le chemin 8 est le recuit de l'échantillon récupéré à pression ambiante, qui a été effectué expérimentalement mais ne sera pas discuté ici. Des expériences avec des échantillons de NaCl · 10.2D<sub>2</sub>O ont été menées selon chacun de ces chemins à l'exception du 3', et des simulations effectuées pour les chemins 1,3,3',4 et 5. Les techniques expérimentales de diffraction de rayons X et diffraction de neutrons, ainsi que celles de hautes pressions sont présentées au chapitre 2. Les méthodes de simulations atomistiques que nous avons employées sont décrites au chapitre 3. La technique de trempe et la structure

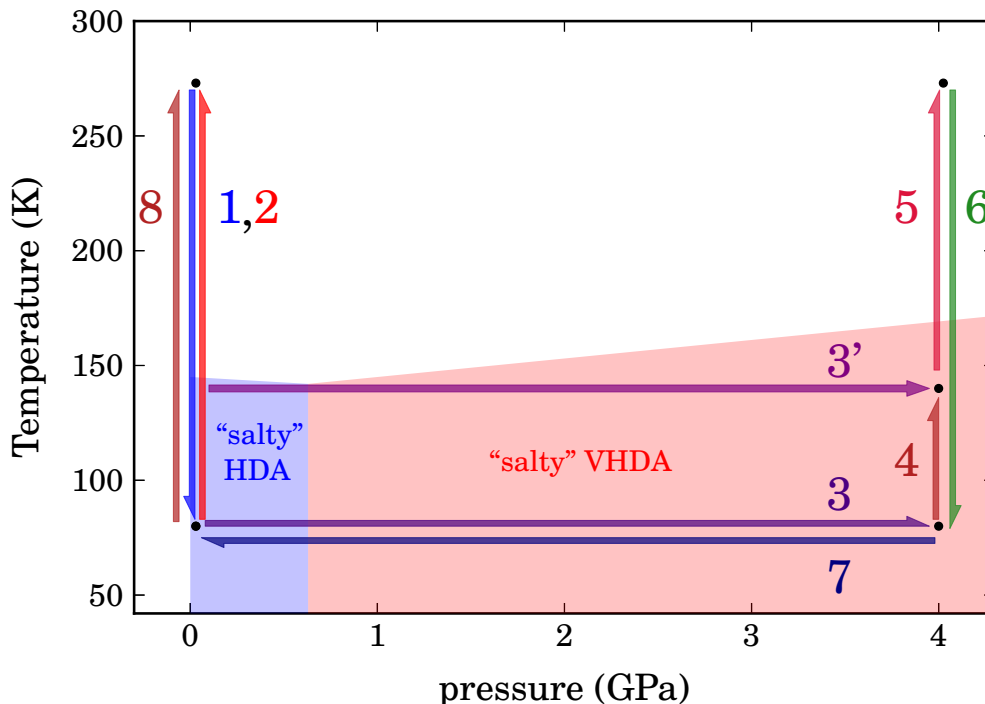


Figure B.1: Le chemin thermodynamique le long duquel la solution  $\text{NaCl} \cdot 10.2\text{D}_2\text{O}$  a été étudiée en diffraction de neutrons et simulations de DM. Les aires colorées indiquent les domaines de phases amorphes de  $\text{LiCl} \cdot 6\text{D}_2\text{O}$  étudiée préalablement (Bove et al., 2011b). Flèches: 1: hyper-trempe à pression ambiante, 2: réchauffement à pression ambiante (Figure 4.16), 3: compression à 80 K (Figure 5.1), 3': compression à 140 K (simulations de DM seules), 4: recuit à 4 GPa (DM et ND) 5: recuit à 300 K à 4 GPa, 6: trempe à 80 K à 4 GPa, 7: récupération de l'échantillon à pression ambiante (décompression), 8: recuit à pression ambiante de l'échantillon récupéré.

amorphe obtenue à pression ambiante sont exposées au chapitre 4. Les résultats concernant la compression du  $\text{NaCl} \cdot 10.2\text{D}_2\text{O}$  à basse température et son recuit à haute pression, en pratique et en simulation, sont présentés au chapitre 5. Certains détails auxquels le texte fait allusion ont été regroupés dans l'appendice qui clôt ce manuscrit.

## B.4 Conclusion

Le but de ce travail était de caractériser les phases de systèmes eau-sel en conditions de température et pression correspondant aux intérieurs des lunes glacées et de petits corps planétaires. Ces travaux se concentraient sur le système eau-NaCl qui a été étudié dans le domaine de pressions de 0 à 4 GPa et températures de 77 à 330 K.

Pour ces expériences nous avons utilisé la presse Paris-Edinburgh, qui est un outil fiable pour les études de diffusion de neutrons à haute pression. Cette presse

permet d'accéder au domaine de pressions d'une dizaine de giga Pascal pour des températures de 0 à 350 K. Les techniques de diffraction de neutrons et rayons X ont été employées pour étudier la structure atomique des phases amorphes et cristallines des solutions. Le volet expérimental de cette étude a été complété par une approche numérique s'appuyant sur des simulations atomistiques. Des simulations de dynamique moléculaire ont été employées pour suivre les transformations de la structure microscopique du système le long du chemin thermodynamique suivi dans les expériences. Un algorithme de recherche aléatoire de structures a été utilisé pour échantillonner des structures candidates pour la glace VII salée.

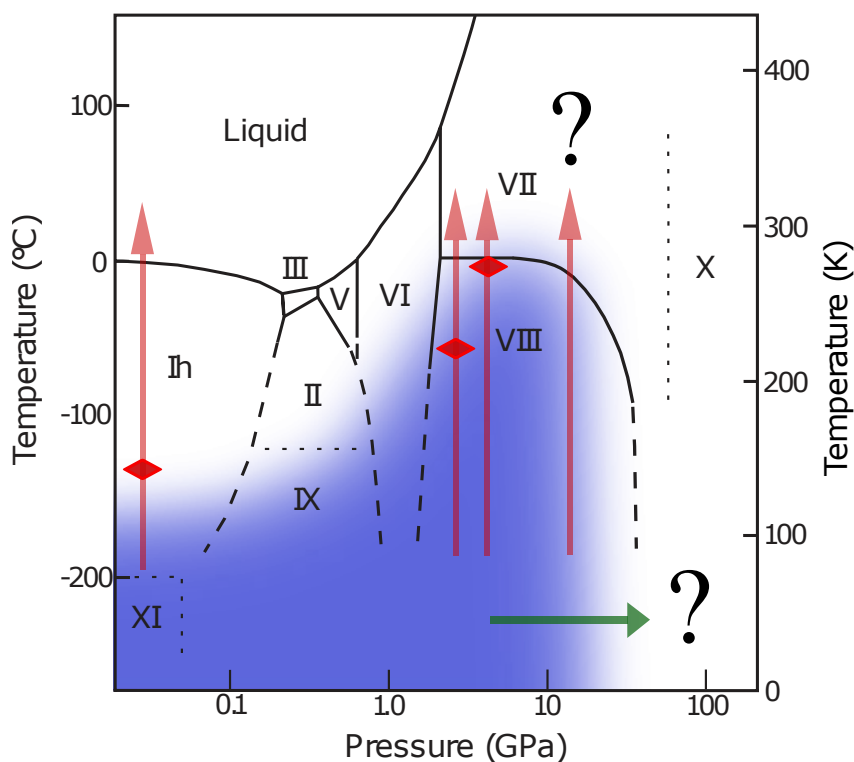


Figure B.2: Diagramme des phases des solutions d'eau-NaCl, superposé à celui des phases stables de l'eau pure de [kuhs finney et al etc nature 1998]. La région bleue indique celle dans laquelle la phase amorphe a été observée expérimentalement. Les losanges rouges indiquent la cristallisation lors du recuit. Les flèches verticales rouges indiquent les chemins selon lesquels les expériences de recuit ont été faites. La flèche verte indique la direction le long de laquelle la compression à basse température ( $\approx 80$  K) a été faite. Les points d'interrogation indiquent les régions inexplorées.

La première étape de l'étude expérimentale était de produire du  $\text{NaCl} \cdot 10.2\text{D}_2\text{O}$  amorphe avec la plus grande fraction de matière amorphe. Les échantillons ont été produits à l'aide d'un dispositif de trempe développé par S. Klotz. Ce dispositif permet d'atteindre des vitesses de trempe de l'ordre de  $10^4$  à  $10^5$  K/s par « splat

cooling » de gouttelettes d'environ 20  $\mu\text{m}$  de diamètre sur une surface solide. La plus grande amorphisation a été obtenue pour  $R = 9.5$  dans  $\text{H}_2\text{O}$  et 10.2 dans  $\text{D}_2\text{O}$ . Les amorphes de solution en  $\text{H}_2\text{O}$  que nous avons obtenues avec cette méthode, montrent un degré d'amorphisation supérieur à celles en  $\text{D}_2\text{O}$  obtenues par la même méthode.

Le diagramme de phase de la figure B.2 résume nos résultats sur la phase amorphe de la solution très concentrée et son comportement de cristallisation. A basse pression la phase amorphe adopte une structure dense très proche de celle de la phase HDA de l'eau pure et de celles des solutions de LiCl-eau à pression ambiante. En compression jusqu'à 4 GPa l'échantillon amorphe  $\text{NaCl} \cdot 10.2\text{D}_2\text{O}$  subit une densification progressive. La structure se transforme de manière progressive aussi selon les chemins de recuits jusqu'à 220 K à 2.5 GPa et 250 K à 4 GPa, contrairement aux observations de transition polyamorphique entre états amorphes de  $\text{LiCl} \cdot 6\text{D}_2\text{O}$  Bove et al. (2011b). Des grandeurs structurales ont été obtenues grâce à des calculs de dynamique Moléculaire classique utilisant les potentiels polarisables de Tazi et al. (2012). Les facteurs de structure des simulations sont en bon accord avec ceux des expériences, ce qui montre la transférabilité des potentiels à des pressions élevées. Pris ensemble, les résultats des simulations et des expériences ont permis de montrer que le comportement de ces solutions dépend de la structure des couches de solvation des cations ( $\text{Na}^+$  ou  $\text{Li}^+$ ). La couche des premiers voisins de  $\text{Li}^+$  possède une structure tétraédrique à pression ambiante, qui se brise brutalement lorsque la pression dépasse 2 GPa et la couche devient octaédrique entraînant une densification soudaine. Pour  $\text{Na}^+$  cette couche est déjà octaédrique à pression ambiante. Lorsque la pression croît, la compression des seconds voisins sur les premiers voisins entraîne une distorsion progressive des octaèdres et la formation de polyèdres irréguliers de 7 et 8 plus proches voisins.

En raison de l'augmentation de la coordination de  $\text{Na}^+$  nous nous avons étudié à la possibilité de l'inclusion de ces ions dans le réseau cubique centré de la glace VII en substituant des molécules d'eau, puisque la glace VII est une phase stable et dense.

L'analyse des données de diffraction suggère que la glace VII qui cristallise en recuit à 2.5 et 4 GPa, contient peu ou pas de sel dans sa maille. À ceci s'ajoute le fait que les paramètres de maille et les facteurs de Debye-Waller obtenus à partir du fit de ces données sont en bon accord avec les valeurs de la littérature pour la glace VII pure. L'élargissement des pics observé dans deux de nos échantillons pourrait être dû à la petite taille des cristallites. Nos calculs ont montré que l'inclusion d'ions substitutionnels dans la maille de la glace VII conduirait à une expansion de cette maille de 10% du volume, si tous le sel dans l'échantillon était inclus dans la glace à 0 K. Les facteurs de structure calculés à partir des simulations de la glace

salée montrent des facteurs de Debye-Waller élevés pour les fortes concentrations de sel, en contraste avec les observations expérimentales. L'interprétation de ces résultats nécessite quelques précautions, car l'équation d'état (EoS) et les facteurs de structure (SF) ont été calculés seulement pour quelques boîtes. Afin de confirmer ce résultat les EOS et les FS de plusieurs boîtes devraient être évalués. L'analyse des enthalpies de mélange, qui ont été obtenues à partir des ensembles de structures candidates montre que la glace salée serait en marge de stabilité à 300 K et 4 GPa. Enfin des trajectoires de dynamique moléculaire *ab-initio* à 300 K ( $3 < p < 5$  GPa) suggèrent que l'agitation thermique est de plus grande amplitude dans les glaces salées avec  $R = 11.5$  que dans les glaces pures et moins salées ( $R = 52$ ). Ainsi la glace très salée pourrait être proche du point de fusion. Afin de répondre à cette question plus de calculs et de mesures sont requises.

Le comportement du système à des pressions de 10 GPa et plus pourrait être différent de ce que nous avons constaté dans cette étude. Étant donné que ces pressions sont typiques des intérieurs des planètes plus massives tels que des super terres et les géants de glace [Beaulieu 2006], ce domaine de pression vaut la peine d'être étudié. L'environnement hétérogène dans les objets célestes pourrait être propice à la formation de glaces salées. En déterminant si ces glaces salées peuvent exister, on peut contribuer à la compréhension de la structure interne de ces objets glacés

Le domaine des pressions des intérieurs de planètes géantes glacées a été étudié par des expériences au Raman sur des solutions de LiCl et NaCl dans l'eau, jusqu'à des pressions de 145 GPa. Dans le cas de LiCl, il a été montré que la transition de la glace VII à la glace X est entravée par la présence d'ions dans la maille de la glace (Bove et al., 2015). Dans la glace X non moléculaire, les hydrogènes se trouvent au milieu entre les atomes d'oxygène voisins (??). Bronstein et al. (2014) ont montré que les effets de quantiques protons permettent de décrire cette transition correctement. Une étude combinant expériences et simulations de dynamique moléculaire sur des glaces salées (LiCl et NaCl) à haute pression montre que la présence de NaCl à faible concentration inhibe également la transition vers la glace X (Bronstein et al., 2015).

Une autre solution qui est à étudier est celle de  $\text{MgCl}_2$  dans l'eau. Nous avons tenté une expérience avec cette solution. La solution a été refroidie lentement lors de l'expérience sur la ligne PLANET, mais elle est cristallisée lors du refroidissement à pression ambiante. Brown et Hand 2013 discutent des sels et autres produits des radiations sur la lune Europe. Ils proposent que  $\text{MgCl}_2$  serait l'un des constituants de la saumure océanique sur Europe, en raison des indications spectroscopiques pour  $\text{MgSO}_4$  à la surface, ce dernier serait un produit de radiation formé à partir du premier. Ainsi il est de mise d'étudier la possibilité d'inclure des sels de magnésium

dans la glace.

Nous avons fait des expériences avec des solutions de LiBr dans l'eau sur la ligne PLANET à J-Parc. La solution à  $R = 5.6$  amorphise bien lors du refroidissement. Lors du recuit à  $\approx 4$  GPa la phase amorphe cristallise vers 260 K. Le diffractogramme est très similaire à celui de la glace VII cristallisée à partir de  $\text{LiCl} \cdot 6\text{D}_2\text{O}$ . L'atténuation des pics avec  $q$  croissant est forte et suggère un facteur de Debye-Waller élevé. L'analyse est en cours. Les détails ne sont pas présentés ici.

# List of Figures

- 1.1 Left: Geometry of the water molecule and its local tetrahedral environment in ice  $I_h$  from Casassa et al. (2005). The structural properties of  $H_2O$   $d_{OO} \approx 2.7 \text{ \AA}$ ,  $d_{OH} \approx 0.95 \text{ \AA}$ ,  $\theta \approx 106^\circ$ , the average distance to nearest neighbour is  $d_{Hbond} \approx 1.75 \text{ \AA}$ . Right: Octahedron of nearest neighbours of a  $Na^+$  ion at ambient pressure  $d_{ONa} \approx 2.5 \text{ \AA}$ , from Ludl et al. (2015). . . . . 17
- 1.2 The temperature-pressure phase diagram of water and crystalline ices. The stability domains of ices I to XI ices are shown, those of ices XII to XVI are not indicated in this figure. Dashed lines indicate phase boundaries across which metastability has been observed. (Finney et al., 1998). . . . . 18
- 1.3 The stability domains of the three metastable amorphous phases of ice (LDA, HDA, VHDA). The “no man’s land” is the region where only crystalline ices are stable. The blue circle is the proposed second critical point of pure water. The dot-dashed line emanating from it, is the line of proposed first order transitions in (inaccessible) water. (Nelmes et al., 2006) . . . . . 19
- 1.4 The structure factors of LDA, HDA, VHDA, HGW and ASW prepared from  $D_2O$ . The data were obtained by neutron diffraction experiments at 80 K and ambient pressure (Bowron et al., 2006). The grey arrows indicate the positions of the first peak in the diffraction patterns of LDA, HDA and VHDA. . . . . 22
- 1.5 Left: (i) Photograph of rocksalt ( $NaCl$ ) crystallising from an evaporatin drop a saturated brine. Right: (ii) Brine rejection of  $NaCl$  from the ice lattice in a simulation using Molecular Dynamics. The snapshots A, B, C, D were taken every 200 ns (Vrbka and Jungwirth, 2006). . . . . 24

- 1.6 Left: Comparison between the diffraction pattern of the HDA form of amorphous  $\text{LiCl} \cdot 6\text{D}_2\text{O}$  at 80 K and ambient pressure (blue dots) and that of pure ice eHDA (light green). Right: Comparison of salty HDA (blue) and salty VHDA (red) both recovered to ambient pressure. Arrows indicate the position of the first and second diffraction peaks. The inset shows the pressure under isochoric annealing, measured from the lead calibrant. (Bove et al., 2011b) . . . . . 25
- 1.7 The neutron diffraction pattern of  $\text{LiCl} \cdot 6\text{D}_2\text{O}$  at 4 GPa and 280 K is shown by blue circles. The line through the data is a Rietveld fit based on the ice VII structure with interstitial  $\text{Li}^+$  and substitutional  $\text{Cl}^-$  ions. The inset shows the structures of ice VII (hydrogen disordered, body centered cubic) and VIII (hydrogen ordered, tetragonal). (Klotz et al., 2009) . . . . . 26
- 1.8 The thermodynamic path along which  $\text{NaCl} \cdot 10.2\text{D}_2\text{O}$  has been studied, by neutron diffraction and MD simulations. The coloured regions indicate the boundaries of amorphous phases of previously studied  $\text{LiCl} \cdot 6\text{D}_2\text{O}$ . (Bove et al., 2011b) Arrows: 1: hyper-quench at ambient pressure, 2: warming at ambient pressure (Figure 4.16), 3: compression at 80 K (Figure 5.1), 3': compression at 140 K (MD simulations only), 4: annealing at 4 GPa (MD and neutron diffraction experiments), 5: annealing to 300 K at 4 GPa, 6: quench to 80K at 4 GPa, 7: recovery to ambient pressure (decompression), 8: annealing at ambient pressure of the recovered sample . . . . . 28
- 2.1 Sketch of the geometry of a diffraction experiment. The spacing between lattice planes is  $d$ , the angle between the incident and the scattered beam is  $2\theta$ ,  $\lambda$  is the wavelength of incoming radiation. . . . 30
- 2.2 Left: Structures of a two-dimensional hexagonal lattice. The unit cell and the vectors  $a_1$  and  $a_2$  are shown. The distances corresponding to the shells of first, second and third neighbours are shown by circles. The sites which are empty in graphene and ice  $\text{I}_h$  are filled grey circles (graphic made with Inkscape 0.91 [www.inkscape.org]). Right: The radial distribution function  $g(r)$  for graphene, the two dimensional hexagonal polymorph of carbon, at 300 K and 3500 K showing the peaks corresponding to the first, second and third neighbours (Fasolino et al., 2007). . . . . 32

2.3	Right: the radial distribution function $g(r)$ of an amorphous configuration of atoms. The dashed circles indicate the positions of first and second neighbour peaks of the $g(r)$ . Right: the corresponding structure factor $S(k)$ . (Reichman and Charbonneau, 2005) . . . . .	32
2.4	Measured neutron diffraction patterns and simulated structure factors $S(q)$ . From bottom to top: Simulation of ice $I_h$ pattern with FullProf, and amorphous LDA and e-HDA of pure water pure water e-HDA (dark green) (Nelmes et al., 2006) at 0.18 GPa and LDA (Bellissent-Funel et al., 1987) at 0.1 GPa, and NaCl · 10.2D <sub>2</sub> O pattern measured at ILL (Ludl et al., 2015). . . . .	34
2.5	Diffraction data for single crystals of ice $I_h$ . (a) Diffuse X-ray scattering intensity map of H <sub>2</sub> O ice $I_h$ at 175 K in the $L = 0$ (HK0 <sub>h</sub> ) plane from Wehinger et al. (2014). (b) Positions of the diffuse spots (heavy lines) and approximate positions of the diffuse streaks (dotted lines) in the layer $L = 0$ , (c) experimental recording of X-ray diffraction data along the hexagonal axis (4 hour exposure, $-5^\circ\text{C}$ ), this recording is rotated $30^\circ$ around the normal to the plane with respect to (a) and (b). (b) and (c) are taken from Owston (1949). . . . .	35
2.6	Setup of the D20 diffractometer at ILL after Hansen et al. (2008c). . . . .	40
2.7	Setup of the PEARL diffractometer at ISIS after PEARL (2015). . . . .	41
2.8	Schematic of Paris-Edinburgh cells. Left: V type. Right: VX type. Reproduced from Klotz (2012). 1: Hydraulic fluid inlet, 2: cylinder, 3: piston, 4: O-ring seal, 5: loa-frame, 6: anvils, 7: TC backing plates (seats), 8: breech, 9: front collimator, 10: nut, 11: top platen, 12: tie rod, 13: backing disk, 14: steel spacer. . . . .	43
2.9	Schematic of anvils and gasket assembly for the Paris-Edinburgh cell. Showing washer geometry at the top and encapsulating gasket at the bottom. Left: single toroidal. Right: double toroidal. Reproduced from Klotz (2012). . . . .	45
2.10	Schematic of two cryostat setups. Left: liquid nitrogen cryostat for the Paris-Edinburgh cell used on PEARL at ISIS. Right: helium flow cryostat used on D20 at ILL. Reproduced from Klotz (2012) ch. 11. . . . .	46
2.11	Schematic of a conventional diamond anvil cell (left) (Klotz, 2011) and hybrid type 1 for neutron experiments (right) (Goncharenko, 2007). . . . .	49
2.12	Phase diagram of N <sub>2</sub> with isobars as solid lines and phase boundaries as dashed lines. Taken from Mills et al. (1986) . . . . .	52

- 3.1 Geometries of the Dang and Chang (1997) models (DC, left) and of the SPC/E (Berendsen et al., 1987) water model (right). The size of the repulsive Lennard-Jones core is given by  $\sigma$ . The angle  $\theta \approx 105^\circ$  is close in value to the ideal tetrahedral angle. The OH distance is close to 1 Å. The M site is fictitious and may host the molecular dipole. . . . . 58
- 3.2 Representation of the simulation box of pure ice VII (left) and ice VII with eight ions substituted for water molecules using our screening procedure. . . . . 63
- 3.3 Distributions of the projections of the water molecules' dipoles along the coordinate axes ( $x, y, z$ ) for a hydrogen ordered box and a hydrogen disordered box of ice VII. Left: In the ordered box the distribution is very narrow in the directions orthogonal and parallel to the axes ( $\approx \pm 4^\circ$ ). Right: In the hydrogen disordered box the distribution is broader ( $\approx \pm 20^\circ$ ). The hydrogen disordered configuration was obtained by annealing the ordered box to 1000 K and quenching it back to 300 K, while fixing the oxygens. . . . . 64
- 3.4 Representation of the simulation box of  $\text{NaCl} \cdot 10.2\text{D}_2\text{O}$  at 0 GPa. It contains 510 water molecules and 51 ion pairs. The figure was produced using VMD Humphrey et al. (1996). Oxygen atoms are in red, hydrogen in white, sodium ions in blue and chloride in turquoise. 67
- 4.1 Temperature composition binary phase diagrams of LiCl and NaCl solutions in water at ambient pressure. (a) LiCl- $\text{H}_2\text{O}$  and LiCl- $\text{D}_2\text{O}$  from Elarby-Aouizerat et al. (1983),  $T_h$  indicates the line along which homogeneous nucleation occurs  $T_g$  the glass transition. The other lines are phase boundaries. (b) Diagram of NaCl- $\text{H}_2\text{O}$  from Muldrew and McGann (1997) after Landolt et al. (1964), with an added scale for the molar ratio  $R$ . The stable eutectic point for NaCl- $\text{H}_2\text{O}$  is at  $-21^\circ\text{C}$  and 23.3 weight percent ( $R = 10.7$ ). For LiCl- $\text{H}_2\text{O}$  it is at  $R = 7$  and  $-75^\circ\text{C}$ . . . . . 75
- 4.2 Temperature composition binary phase diagram of LiBr- $\text{H}_2\text{O}$ , from Kessis (1965). The LiBr- $\text{H}_2\text{O}$  system forms the same hydrates as the LiCl- $\text{H}_2\text{O}$  system and their phase boundaries are very similar. The stable eutectic point for LiBr- $\text{H}_2\text{O}$  is at  $-67^\circ\text{C}$  and 39.07 weight percent (molar ratio  $R = 7.5$ ). . . . . 76
- 4.3 The Newtonian and ideal cooling regimes of a droplet (splat) on a substrate during splat cooling. . . . . 77

- 4.4 Hyper-quenching device. Left: photograph. Right: schematic. The sample in the tube above the nozzle is pre-cooled to about 0°C. The nozzle sprays fine droplets of diameter  $\approx 10$  to  $30 \mu\text{m}$  onto the aluminum plate at 80 K, with a spraying angle  $\theta \approx 90^\circ$ . (Ludl et al., in preparation). . . . . 79
- 4.5 Left: Droplet size as a function of injection pressure for pure water (blue) and NaCl solution with  $R = 10.5$  (red). This Figure was produced using data from the internal report by Li (2012). Right: Photograph of the droplets produced at about 40 bar seen through the optical microscope, from Li (2012). . . . . 81
- 4.6 Left: powder sample of quenched  $\text{NaCl} \cdot 10.2\text{D}_2\text{O}$  solution inside the cryochamber in the XRD at IMPMC. Right: pellet ( $\varnothing \approx 1.8 \text{ mm}$ ) of amorphous powder loaded in a gasket on an anvil of the Paris-Edinburgh cell. (Ludl et al., in preparation) . . . . . 83
- 4.7 Top: X-ray structure factors of ice  $I_h$ , NaCl, and  $\text{NaCl} \cdot 2\text{H}_2\text{O}$  at ambient pressure calculated with FullProf. Details and references for the structures used are given in the text. Bottom: Measured X-ray diffraction patterns of pure hexagonal ice  $I_h$  at 80 K in the cryochamber and background at ambient temperature. (Although truncated at  $4.6 \text{ \AA}^{-1}$ , this ice  $I_h$  spectrum was the best one available.) The peaks in the background spectrum are those of the nickel and copper in the sample holder. . . . . 85
- 4.8 Measured X-ray diffraction patterns of quenched  $\text{NaCl} \cdot 9.5\text{H}_2\text{O}$  at 80 K in the cryochamber. Precooling was used on these samples. The injection pressure is indicated on the right. The samples injected with 50 and 80 bar contain larger fraction of amorphous over crystalline material than those produced at lower pressures. The peak at  $0.4 \text{ \AA}^{-1}$  is due to the Kapton windows. . . . . 87
- 4.9 Measured X-ray diffraction patterns of quenched  $\text{NaCl} \cdot R\text{H}_2\text{O}$  at 80 K in the cryochamber, where the pressure is about  $10^{-3}$  mbar during the measurement. The molar fraction  $R$  increases from bottom to top as indicated on the right. All samples contain a large part of crystalline material. The strongest peaks, including the triplet at  $1.6 \leq q \leq 1.85 \text{ \AA}^{-1}$ , belong to ice  $I_h$ . The peak at  $0.4 \text{ \AA}^{-1}$  is due to the Kapton windows. The other peaks, including the two at 1.05 and  $1.15 \text{ \AA}^{-1}$ , belong to sodium chloride dihydrate. Amorphous material is visible in samples with  $9 \leq R \leq 10$ . . . . . 88

- 4.10 Measured neutron diffraction patterns of quenched  $\text{NaCl} \cdot R\text{D}_2\text{O}$  and pure ice  $I_h$  (top) at 80 K measured on D20 at ILL. The composition is indicated on the right. During the measurement the pressure is that of the helium exchange gas ( $\approx 100$  mbar). The sample with  $R = 10.2$  contains more amorphous material with respect to the crystalline  $I_h$ . Hydrate peaks appear in the spectrum of the sample with  $R = 9.7$  but not in that with  $R = 10.2$ . . . . . 89
- 4.11 Measured X-ray diffraction patterns of quenched  $\text{NaCl} \cdot 10.2\text{D}_2\text{O}$  and  $\text{NaCl} \cdot 10.2\text{H}_2\text{O}$  at 80 K in the cryochamber. Precooling was used on these samples. Precooling was used on these samples, they were injected at 80 bar and 0.7 s. During the measurement the pressure is about  $10^{-3}$  mbar. Both samples contain a fraction of crystalline and amorphous material. The  $\text{D}_2\text{O}$  sample contains more amorphous material. The  $\text{H}_2\text{O}$  sample has formed more hydrate. . . . . 90
- 4.12 Measured X-ray diffraction patterns of quenched  $\text{NaCl} \cdot 10.2\text{D}_2\text{O}$  and  $\text{NaCl} \cdot 9.5\text{H}_2\text{O}$  at 80 K in the cryochamber. Precooling was used on these samples. These are the samples of NaCl-water, which show the largest fractions of amorphous material obtained in our experiments. 91
- 4.13 Measured diffraction patterns and simulated structure factors  $S(q)$  at low pressure. From bottom to top: in black the simulation of ice  $I_h$  neutron pattern with FullProf, in blue the  $\text{NaCl} \cdot 10.2\text{D}_2\text{O}$  neutron pattern measured at 100 mbar on D20 at ILL and in red the X-ray pattern of the same solution measured at  $10^{-3}$  mbar on the X-Pert diffractometer at IMPMC (Ludl et al., 2015). . . . . 92
- 4.14 The neutron diffraction pattern of  $\text{NaCl} \cdot 10.2\text{D}_2\text{O}$  measured on D20 at ILL (Ludl et al., 2015) at 100 mbar is shown in red. The sum of the fits of amorphous and crystalline contributions is shown in blue. The crystalline part is estimated to be about 8% of the sample material according to the fit of thirteen ice peaks with pseudo-Voigt profile functions, shown in in green. . . . . 93
- 4.15 Measured X-ray diffraction patterns of quenched  $\text{LiCl} \cdot R\text{D}_2\text{O}$  at 80 K in the cryochamber. The molar fraction  $R$  is indicated on the right. Precooling was used on these samples, they were injected at 80 bar and 0.7 s. The  $\text{LiCl} \cdot 6\text{D}_2\text{O}$  sample shows traces of crystalline material, which are due to the transfer to the cryochamber. The  $\text{LiCl} \cdot 20\text{D}_2\text{O}$  sample contains both crystalline and amorphous material. . . . . 94

- 4.16 Neutron diffraction pattern of amorphous  $\text{NaCl} \cdot 10.2 \text{D}_2\text{O}$  measured at D20 (ILL) while heating at  $p = 100$  mbar. First “cubic ice” starts growing at 160 K, which then transforms into hexagonal ice at 185 K. Sodium chloride dideuterate appears at 185 K. At 260 K the spectrum shows a mixture of ice  $\text{I}_h$  and sodium chloride dideuterate. (Ludl et al., 2015) . . . . . 96
- 4.17 Neutron diffraction patterns of amorphous aqueous phases at low pressure. From bottom up:  $\text{NaCl} \cdot 10.2\text{D}_2\text{O}$  pattern measured on D20 at ILL (100 mbar),  $\text{LiBr} \cdot 5.6\text{D}_2\text{O}$  pattern measured on PLANET at J-Parc ( $p \leq 0.1$  GPa)  $\text{LiCl} \cdot 6\text{D}_2\text{O}$  solution data at 1 bar (Bove et al., 2011b), pure water eHDA at 0.18 GPa (Nelmes et al., 2006) and LDA at 0.1 GPa (Bellissent-Funel et al., 1987). The position of the maximum of the first diffraction peak of  $\text{NaCl} \cdot 10.2\text{D}_2\text{O}$  is at  $2.1 \text{ \AA}^{-1}$  and for  $\text{LiCl} \cdot 6\text{D}_2\text{O}$  it is at  $2.015 \text{ \AA}^{-1}$ . The data show that  $\text{NaCl}$ ,  $\text{LiCl}$  and  $\text{LiBr}$  solutions at ambient pressure closely resemble the high pressure amorphous phase of pure water (eHDA), rather than the low density amorphous phase (LDA). . . . . 98
- 5.1 Neutron diffraction pattern upon compression of amorphous  $\text{NaCl} \cdot 10.2\text{D}_2\text{O}$  at 80K. Points are experimental data collected on PEARL (ISIS, UK) and lines are structure factors from MD simulations. The pressure in experiments and simulations are indicated on the right. During compression the structure factor of this amorphous phase changes smoothly. . . . . 102
- 5.2 This is a zoom of the low  $q$  region of the neutron diffraction pattern upon compression of amorphous  $\text{NaCl} \cdot 10.2\text{D}_2\text{O}$  at 80K shown in Figure 5.1. Points are experimental data collected on PEARL (ISIS, UK) and lines are structure factors from MD simulations. The pressure in experiments and simulations are indicated on the right. The positions of the maxima of the first diffraction peak at 0 GPa ( $2.1 \text{ \AA}^{-1}$  in green) and at 4 GPa ( $2.35 \text{ \AA}^{-1}$  in blue) are indicated by arrows along the  $q$  axis in the inset. . . . . 104
- 5.3 Sample pressure versus gas pressure applied on the piston for sample 1 measured on PEARL (ISIS, UK). The temperature was 80 K during compression to 450 bar. Sample pressure was obtained from fitting lead peaks (Miller indices 111, 200, 220, 311, 222). The line is a guide to the eye. . . . . 105

- 5.4 The position  $q$  of the first diffraction peak of the amorphous spectrum of  $\text{NaCl} \cdot 10.2\text{D}_2\text{O}$ . Green triangles, red diamonds and yellow squares are from our experiments on PEARL (ISIS, UK), the green x shaped symbol is from the measurement at ILL, the dark red square is from an X-ray measurement at IMPMC, blue circles from simulations. The line through the experimental points is a guide to the eye. . . . . 106
- 5.5 Experimental neutron diffraction pattern upon annealing of amorphous  $\text{NaCl} \cdot 10.2\text{D}_2\text{O}$  at 4 GPa. The data were collected on PEARL. The temperature is indicated on the right. The structure factor of this amorphous phase changes smoothly. . . . . 107
- 5.6 Structure factors of  $\text{NaCl} \cdot 10.2\text{D}_2\text{O}$  at 0 and 4 GPa from our MD simulations. At both pressures the data for 80 and 140 K are superposed to show that they barely change with temperature. The top panel shows the full  $q$  range and the bottom panel a zoom on the 0 to  $10 \text{ \AA}^{-1}$  region. . . . . 108
- 5.7 Pressure dependence of the enthalpy at 80 K (blue triangles) and 140 K (red diamonds) of the  $\text{NaCl} \cdot 10.2\text{D}_2\text{O}$  solution in our MD simulations. The lack of a variation in trend of the enthalpy confirms the absence of a transition in the amorphous system. . . . . 109
- 5.8 Average coordination numbers of oxygen with oxygen (dark green squares), chlorine with sodium and hydrogen (blue triangles), sodium with chlorine and oxygen (red diamonds) under isothermal compression at 80 K. The horizontal axis indicates MD pressure. . . . . 110
- 5.9 Pressure dependence of the RDFs  $g_{\text{OO}}, g_{\text{ONa}}, g_{\text{NaCl}}$  and the angular correlation function  $P(\theta)$  of O-O-O for amorphous  $\text{NaCl} \cdot 10.2\text{D}_2\text{O}$  solution during compression at 80K. These quantities were obtained from our MD simulations. In  $g_{\text{OO}}$  the second peak shifts toward the first, although the minimum remains more pronounced than during the transition of HDA to VHDA in pure water. In  $g_{\text{ONa}}$  the second peak flattens with increasing pressure. In  $g_{\text{NaCl}}$  the first peak increases indicating that ions tend to have counterions in their shell of first neighbours at higher pressures. The evolution of  $P(\theta)$  shows that the tetrahedral geometry of the water network is progressively distorted during compression. . . . . 111
- 5.10 Pressure dependence of RDFs  $g_{\text{OCl}}, g_{\text{HCl}}$  of amorphous  $\text{NaCl} \cdot 10.2\text{D}_2\text{O}$  solution during compression at 80K in our MD simulations. In  $g_{\text{OCl}}$  the second peak progressively becomes a shoulder of the first peak with increasing pressure. In  $g_{\text{HCl}}$  the second peak broadens with increasing pressure. . . . . 112

- 5.11 Evolution of the distribution of coordination of sodium with oxygen and chlorine for isothermal compression simulated at 80 K (the value of the pressure is that of the simulation). Six distinct populations are shown, the numbers in circles indicate the coordination number of each population. The fraction of 6 fold coordinated atoms decreases, while the fractions of 7 and 8 fold coordinated atoms increase with pressure. . . . . 113
- 5.12 Above: Representations of the local environment of  $\text{Na}^+$  which is octahedral at low pressure and forms an irregular distorted polyhedron at pressures above 4.5 GPa in our simulations. Below: The distribution of  $N_{\text{NaO}}$  and  $N_{\text{NaCl}}$  for the sodium ions at 0.0 GPa (left) and 5.4 GPa (right). . . . . 114
- 5.13 Evolution with pressure of distance distribution of eight closest neighbours (O and  $\text{Cl}^-$ ) to  $\text{Na}^+$  ions, where  $r$  is the distance to the sodium ion. The seventh and eighth neighbour move into the shell of first neighbours above 2 GPa. . . . . 115
- 5.14 Evolution with pressure of the distribution of octahedral angles, which are the angles at the central  $\text{Na}^+$  ion between atoms at the corners of the octahedron formed by the six nearest neighbours. . . . . 116
- 5.15 Experimental diffraction patterns of the annealing of sample 1 at  $\approx 3.9$  GPa. In this sample ice VII crystallizes at 260 K. The temperature and gas pressure are indicated for each scan. The sample pressure determined from the fit of lead peaks is indicated on the top two scans. Diamond and nitrogen peaks are indicated. The data are offset in increments of 50 along the ordinate axis for clarity. . . . . 119
- 5.16 Data and fit and residue for sample 1 at 295 K and 3.9 GPa. The fit of diamond peaks has been subtracted from the data. The fit shown contains ice VII. . . . . 120
- 5.17 Experimental diffraction patterns of the annealing of sample 3 at  $\approx 3.5$  GPa. In this sample ice VII crystallizes at 260 K. Upon cooling below 270 K it transforms into a disordered form of ice VIII. The temperature and gas pressure are indicated for each scan. The sample pressure obtained from nitrogen peaks is indicated on some scans. Diamond and nitrogen peaks are indicated. The data are offset in increments of 50 along the ordinate axis for clarity. . . . . 122

- 5.18 Experimental diffraction patterns of the annealing of sample 3 at  $\approx 3.5$  GPa. This plot shows the details of the previous for the scans between 185 and 290 K. In this sample ice VII crystallizes at 260 K. The temperature and gas pressure are indicated for each scan. The sample pressure obtained from nitrogen peaks is indicated on the scans. Diamond and nitrogen peaks are indicated. The data are offset in increments of 50 along the ordinate axis for clarity. . . . . 123
- 5.19 Data and fit and residue for sample 3 at 260 K and 3.65 GPa. The fit shown contains ice VII. The fit of diamond peaks has been subtracted from the data. The pressure of the nitrogen phase and ice phase agree to less than 0.1 GPa. No peaks of either lead or sodium chloride are visible in this spectrum. Although the lattice parameter corresponds to pure ice VII, the sample may contain a (small) fraction of salt. . . 124
- 5.20 Top: Cooling of sample 3 from 300 K to 230 K. Bottom: Cooling of sample 4 from 315 K to 240 K. The doublets of ice VIII are indicated by green stars. The data shown were measured on PEARL in December 2013 using a V3 PEC. The temperatures are indicated on the plot. The diffraction patterns are offset along the ordinate axis for clarity. A fit of the diamond peaks was subtracted from the experimental data. . . . . 125
- 5.21 Experimental diffraction patterns of the annealing of sample 4 at  $\approx 2.4$  GPa. In this sample ice VIII crystallizes at 220 K and transforms into pure ice VII at 270 K. The temperature and gas pressure are indicated for each scan. The sample pressure determined from the fit of nitrogen peaks is indicated on the top two scans. Diamond and nitrogen peaks are indicated. The data are offset in increments of 50 along the ordinate axis for clarity. . . . . 127
- 5.22 Data and fit and residue for sample 4 at 300 K and 2.25 GPa. The fit of diamond peaks has been subtracted from the data. The fit shown includes ice VII. The pressure of ice VII, sodium chloride and lead agree to less than 0.1 GPa, hence this sample contains pure ice VII. There are unidentified peaks in the range of 2 to 3  $\text{\AA}^{-1}$ , which are expected to belong to a mixed phase of nitrogen and water. . . . . 128

- 5.23 Representation of the atoms in the unit cells of pure and salty ice. Pure ice VII is shown in the center. Left: the structure of salty ice VII including  $\text{Li}^+$  (bright green) in an octahedral interstice and  $\text{Cl}^-$  (darker green) substituted for a water molecule. Right: the structure of salty ice VII including  $\text{Na}^+$  (dark blue) and  $\text{Cl}^-$  (turquoise) both substituted for water molecules, which we have investigated in this work. . . . . 131
- 5.24 Equations of state  $p$  versus  $a$  for pure and salty ice VII from our calculation at 0 K, compared to two EOS of ice VII given in literature (Besson et al., 1994, Fortes et al., 2012). . . . . 133
- 5.25 Equations of state  $p$  versus  $a/a_0$  for pure and salty ice VII from calculations at 0 K, compared to two EOS of ice VII given in literature (Besson et al., 1994, Fortes et al., 2012). . . . . 134
- 5.26 Diffraction pattern of crystallised sample 3 (blue) compared with those generated for the usual crystallographic model of ice VII (dark-blue), the hydrogen disordered supercell of ice VII (dark-red), a box with 2 ions substituted for water molecules (dark-green), and a box with 8 ions substituted for water molecules (red). All patterns for simulations were generated using Fullprof. A fit of the diamond peaks was subtracted from the experimental data of sample 3 (blue line). . . . . 136
- 5.27 Distribution of the total energy from screening with classical potentials (top) and DFT (bottom) for the set of configurations of salty ice VII generated by random structure searching. The sample size, the average energy  $\langle E \rangle$  and the spread  $\sigma_E$  are indicated on the graphs. The red curve on in the top panel is a Gaussian fit as a guide to the eye. . . . . 137
- 5.28 Distribution of classical energy versus ion distances for the set of 109 thousand configurations. The global average distance between all ions varies between 4 and 5.3 Å. The distributions with respect to Na Na and Cl Cl distances are broad. The highest energies correspond to Na Na distances smaller than 3.5 Å and Na Cl distances larger than 5 Å. . . . . 138
- 5.29 Distribution of DFT energy versus ion distances for 1000 configurations. The configurations selected were those of lowest classical energy. The average distance here is distributed as in large set in Figure 5.28. The Na Na and Cl Cl distances show almost no correlation to the DFT energy in this set. The Na Cl distance is smaller than about 4.7 Å, in contrast to the larger set where it reached up 6 Å. . . . . 139

5.30	Convex hull diagram of the $\Delta h$ enthalpy difference for configurations of salty ice with 8 ions at 4 GPa (top) and 5 GPa (bottom). The abscissa indicated the molar fraction of salt $x_{\text{NaCl}}$ . The red line gives the energy corresponding to phase separation at a given concentration. At both pressures the energy of the salty ice lies above that of phase separation. . . . .	140
5.31	Enthalpy of mixing $\Delta h$ versus ion distances for the 8 ion configurations at 4 GPa. The spread in $\Delta h$ is about 0.002 Ry ( <i>i.e.</i> $\approx 315$ K).	141
6.1	Phase diagram for NaCl-water on top of the diagram of stable phases of pure water from Finney et al. (1998). The domain in which NaCl $\cdot$ 10.2D <sub>2</sub> O has been observed is shown in blue. The crystallisation upon annealing is indicated by red diamonds. Red vertical arrows indicate the paths along which annealing experiments were performed in this work. The green horizontal arrow indicates the direction along which compression at low temperature ( $\approx 80$ K) was performed. Question marks indicate unexplored areas. . . . .	144
A.1	GSAS fit of sample 3 at 260 K and 3.6 GPa. The fit contains the following phases, the peak positions of which are indicated by tick marks. Phase 1 is ice VII (pink), phase 2 is diamond (turquoise), phase 3 is $\beta$ N <sub>2</sub> (black), phase 4 is NaCl (brown). for the set of salty ice VII boxes containing 8 substitutional ions. . . . .	148
A.2	GSAS fit of sample 3 at 260 K and 3.6 GPa with salty ice VII. The fit contains the following phases, the peak positions of which are indicated by tick marks. Phase 1 is salty ice VII (pink), phase 2 is diamond (turquoise), phase 3 is $\beta$ N <sub>2</sub> (black). for the set of salty ice VII boxes containing 8 substitutional ions. . . . .	149
A.3	The norm of the total dipole $\mu_{\text{tot}}$ in Debye and in units of the water dipole $\mu_{\text{w}}$ for the set of salty ice VII boxes containing 8 substitutional ions. . . . .	150
A.4	Projections of the dipole $\mu_{\text{tot}}$ along the coordinate axes. There is a net dipole along the $z$ direction. . . . .	150
A.5	BM fit of EOS $p$ versus $a$ for pure ice VII from simulations (54 water molecules). . . . .	151
A.6	Top: BM fit of EOS $p$ versus $a$ for salty ice VII (2 ions, 52 water molecules, $R = 52$ ) from simulations. Bottom: BM fit of EOS $p$ versus $a$ for salty ice VII (8 ions, 46 water molecules, $R = 11.5$ ) from simulations. . . . .	152

- B.1 Le chemin thermodynamique le long duquel la solution  $\text{NaCl} \cdot 10.2\text{D}_2\text{O}$  a été étudiée en diffraction de neutrons et simulations de DM. Les aires colorées indiquent les domaines de phases amorphes de  $\text{LiCl} \cdot 6\text{D}_2\text{O}$  étudiée préalablement (Bove et al., 2011b). Flèches: 1: hyper-trempe à pression ambiante, 2: réchauffement à pression ambiante (Figure 4.16), 3: compression à 80 K (Figure 5.1), 3': compression à 140 K (simulations de DM seules), 4: recuit à 4 GPa (DM et ND) 5: recuit à 300 K à 4 GPa, 6: trempe à 80 K à 4 GPa, 7: récupération de l'échantillon à pression ambiante (décompression), 8: recuit à pression ambiante de l'échantillon récupéré. . . . . 166
- B.2 Diagramme des phases des solutions d'eau-NaCl, superposé à celui des phases stables de l'eau pure de [kuhs finney et al etc nature 1998]. La région bleue indique celle dans laquelle la phase amorphe a été observée expérimentalement. Les losanges rouges indiquent la cristallisation lors du recuit. Les flèches verticales rouges indiquent les chemins selon lesquels les expériences de recuit ont été faites. La flèche verte indique la direction le long de laquelle la compression à basse température ( $\approx 80$  K) a été faite. Les points d'interrogation indiquent les régions inexplorées. . . . . 167



# List of Tables

2.1	Neutron scattering lengths and cross sections from NIST for thermal neutrons ( $\approx 300K$ ) NIST [NIST neutron scattering Lengths]. $c$ is the relative abundance of an isotope of the respective element. (1 barn = $10^{-28} \text{ m}^2$ ) . . . . .	38
2.2	Parameters of the equation of state for lead, ice VII and ice VIII. M stands for the Murnaghan (1944) integrated linear EoS. . . . .	50
3.1	Parameters of the Dang and Chang (1997) (DC), Bernal and Fowler (1933) (BF) and SPC/E (Berendsen et al., 1987) water models. The formal charges are given in units of elementary charge ( $e = 1.602177 \times 10^{-19}$ ), $q_1$ is the charge on the oxygen or M site, and $q_2$ that on the hydrogen sites. Although the parametrisations are different these models capture essential features of the structure of water. . . . .	58
3.2	Polarisabilities for ions (Tazi et al., 2012) and the DC water model (Dang and Chang, 1997). . . . .	60
3.3	Parameters for the cation-water interactions. As for water-water interactions, repulsion and dispersion involve the oxygen atom, while electrostatic interactions involve the additional M site. The damping parameter $b_D$ for the dispersion interaction for the monovalent ions is chosen equal to that of the corresponding cation-chloride interaction (see table 3.5). The electrostatic damping is between the water dipole and cation charge. (Tazi et al., 2012) . . . . .	61
3.4	Parameters for the chloride-water interactions. The dipole damping is between the $\text{Cl}^-$ and the water charges. There is no damping of the dispersion. (Tazi et al., 2012) . . . . .	61
3.5	Parameters for the ion-ion interactions. (Tazi et al., 2012) . . . . .	61
3.6	The cut-off radii $r_2$ for O–O and Cl–H pairs used to calculate coordination numbers, decrease as pressure increases. . . . .	70

4.1	The thermal conductivity $K$ and the Nusselt number $Nu$ of iron, water and sodium chloride solution for reported values of the thickness $s$ of the splat layer. For the heat transfer coefficient of the interface between splat and substrate we assumed $h \approx 10^5 \text{ W m}^{-2} \text{ K}^{-1}$ given by Jones (1973) as a large value for contact between a liquid metal and substrate. . . . .	78
4.2	Left: Radii of the ions constituting the salts in our solutions. (Shannon, 1976) Right: Enthalpies of solution at $25^\circ\text{C}$ , solubilities at $20^\circ\text{C}$ (in g per 100g of water) and molar mass for the four electrolytes investigated here. Haynes (2013), Jahn and Wolf (1993), Parker (1965) The values for $\text{MgCl}_2$ are given for comparison. (IUPAC-NIST Solubility Database, Version 1.1 NIST Standard Reference Database 106 ) . . . . .	81
4.3	Integrated intensities of the amorphous part and 13 crystalline peaks fitted to the neutron data measured on D20 at ILL (Figure 4.14). . . . .	91
5.1	Results of the Rietveld fits with GSAS for samples 1, 3 and 4. The lattice parameter and pressure (by EOS of Fortes et al. (2012)) for ice VII are given. These pressure agree well with those obtained by fitting the pressure probes (Pb, $\text{N}_2$ , NaCl). The precision of the pressure estimate is $\approx \pm 0.1 \text{ GPa}$ . . . . .	129
5.2	Peak position and full width at half maximum (FWHM) for the first ice peak in samples 1, 3 and 4. The fits were done using Fityk with split pseudo-Voigt profiles (Wojdyr, 2010). The scan number, pressure and temperature are given. . . . .	129
5.3	Ice particle size obtained from the GSAS fits of samples 1, 3 and 4. . . . .	129
5.4	Isotropic Debye-Waller factors for O and D for the ice phases crystallised from the samples of $\text{NaCl} \cdot 10.2\text{D}_2\text{O}$ discussed here. The scan number, pressure and temperature are given. The Debye-Waller factors obtained by Nelmes et al. (1998) on pure deuterated ice VII are given for comparison. . . . .	130
5.5	Parameters of the fits of Birch-Murnaghan equation of state (EOS) to data from simulations, compared to two EOS of ice VII fitted to experiments given in literature (Besson et al., 1994, Fortes et al., 2012). M stands for the Murnaghan EOS, BM for the Birch-Murnaghan EOS. . . . .	132
A.1	List of physical constants. . . . .	153
A.2	Unit conversions. . . . .	153
A.3	List of recurring abbreviations used in this thesis. . . . .	155

---

A.4 List of recurring abbreviations used in this thesis. (continued) . . . .	156
--	-----



# Bibliography

- Andrés Aguado and Paul A. Madden. Ewald summation of electrostatic multipole interactions up to the quadrupolar level. *The Journal of Chemical Physics*, 119(14):7471–7483, 2003. doi: <http://dx.doi.org/10.1063/1.1605941>. URL <http://scitation.aip.org/content/aip/journal/jcp/119/14/10.1063/1.1605941>.
- Andros Aguado, Leonardo Bernasconi, Sandro Jahn, and Paul A. Madden. Multipoles and interaction potentials in ionic materials from planewave-DFT calculations. *Faraday Disc.*, 124:171, 2003. doi: 10.1039/b300319c. URL <http://dx.doi.org/10.1039/B300319C>.
- J. Alberi, J. Fischer, V. Radeka, L.C. Rogers, and B. Schoenborn. A two-dimensional position-sensitive detector for thermal neutrons. *Nuclear Science, IEEE Transactions on*, 22(1):255–268, Feb 1975. ISSN 0018-9499. doi: 10.1109/TNS.1975.4327648.
- P. Allen and D.J. Tildesley. *Computer simulation of liquids*. Oxford science publications. Clarendon Press, 1987. ISBN 9780198553755. URL <http://books.google.fr/books?id=ibURAQAIAAJ>.
- K. Amann-Winkel, C. Gainaru, P. H. Handle, M. Seidl, H. Nelson, R. Bohmer, and T. Loerting. Water’s second glass transition. *Proceedings of the National Academy of Sciences*, 110(44):17720–17725, oct 2013. doi: 10.1073/pnas.1311718110. URL <http://dx.doi.org/10.1073/pnas.1311718110>.
- C. A. Angell and E. J. Sare. Glass-forming composition regions and glass transition temperatures for aqueous electrolyte solutions. *The Journal of Chemical Physics*, 52(3):1058, 1970. ISSN 0021-9606. URL <http://dx.doi.org/10.1063/1.1673099>.
- C. A. Angell, W. J. Sichina, and M. Oguni. Heat capacity of water at extremes of supercooling and superheating. *The Journal of Physical Chemistry*, 86(6):998–1002, mar 1982. doi: 10.1021/j100395a032. URL <http://dx.doi.org/10.1021/j100395a032>.

- CA Angell and EJ Sare. Glass-formation in aqueous sodium-salt solutions. *Cryoletters*, 1(8):257–260, 1980.
- H Arima, T Hattori, K Komatsu, J Abe, W Utsumi, H Kagi, A Suzuki, K Suzuya, T Kamiyama, M Arai, and T Yagi. Designing PLANET: Neutron beamline for high-pressure material science at j-PARC. *J. Phys.: Conf. Ser.*, 215:012025, mar 2010. doi: 10.1088/1742-6596/215/1/012025. URL <http://dx.doi.org/10.1088/1742-6596/215/1/012025>.
- M Atkinson, J Fent, C Fisher, P Freund, P Hughes, Jasper Kirkby, A Osthoff, and K Pretzl. Initial tests of a high resolution scintillating fibre (scifi) tracker. *Nuclear Instruments and Methods in Physics Research Section A: Accelerators, Spectrometers, Detectors and Associated Equipment*, 254(3):500–514, 1987.
- Luis Bachmann and Erwin Mayer. Physics of water and ice: implications for cryofixation. In *Cryotechniques in biological electron microscopy*, pages 3–34. Springer, 1987.
- Philip Ball. In retrospect: On the six-cornered snowflake. *Nature*, 480(7378):455–455, dec 2011. doi: 10.1038/480455a. URL <http://dx.doi.org/10.1038/480455a>.
- Arindam Bankura, Vincenzo Carnevale, and Michael L. Klein. Hydration structure of salt solutions from ab initio molecular dynamics. *The Journal of Chemical Physics*, 138(1):014501, 2013. doi: <http://dx.doi.org/10.1063/1.4772761>. URL <http://scitation.aip.org/content/aip/journal/jcp/138/1/10.1063/1.4772761>.
- Thorsten Bartels-Rausch, Vance Bergeron, Julyan HE Cartwright, Rafael Escibano, John L Finney, Hinrich Grothe, Pedro J Gutiérrez, Jari Haapala, Werner F Kuhs, Jan BC Pettersson, et al. Ice structures, patterns, and processes: A view across the icefields. *Reviews of Modern Physics*, 84(2):885, 2012.
- William A. Bassett. Diamond anvil cell, 50th birthday. *High Pressure Research*, 29(2):163–186, jun 2009. doi: 10.1080/08957950802597239. URL <http://dx.doi.org/10.1080/08957950802597239>.
- J.-P. Beaulieu, D. P. Bennett, P. Fouqué, A. Williams, M. Dominik, U. G. Jørgensen, D. Kubas, A. Cassan, C. Coutures, J. Greenhill, K. Hill, J. Menzies, P. D. Sackett, M. Albrow, S. Brillant, J. A. R. Caldwell, J. J. Calitz, K. H. Cook, E. Corrales, M. Desort, S. Dieters, D. Dominis, J. Donatowicz, M. Hoffman, S. Kane, J.-B. Marquette, R. Martin, P. Meintjes, K. Pollard, K. Sahu, C. Vinter, J. Wambsganss, K. Woller, K. Horne, I. Steele, D. M. Bramich, M. Burgdorf,

- C. Snodgrass, M. Bode, A. Udalski, M. K. Szymański, M. Kubiak, T. Wieckowski, G. Pietrzyński, I. Soszyński, O. Szewczyk, Ł. Wyrzykowski, B. Paczyński, F. Abe, I. A. Bond, T. R. Britton, A. C. Gilmore, J. B. Hearnshaw, Y. Itow, K. Kamiya, P. M. Kilmartin, A. V. Korpela, K. Masuda, Y. Matsubara, M. Moto-mura, Y. Muraki, S. Nakamura, C. Okada, K. Ohnishi, N. J. Rattenbury, T. Sako, S. Sato, M. Sasaki, T. Sekiguchi, D. J. Sullivan, P. J. Tristram, P. C. M. Yock, and T. Yoshioka. Discovery of a cool planet of 5.5 earth masses through gravitational microlensing. *Nature*, 439(7075):437–440, jan 2006. doi: 10.1038/nature04441. URL <http://dx.doi.org/10.1038/nature04441>.
- A. D. Becke. Density-functional exchange-energy approximation with correct asymptotic behavior. *Phys. Rev. A*, 38:3098–3100, Sep 1988. doi: 10.1103/PhysRevA.38.3098. URL <http://link.aps.org/doi/10.1103/PhysRevA.38.3098>.
- M.-C. Bellissent-Funel, J. Teixeira, and L. Bosio. Structure of high-density amorphous water. II. Neutron scattering study. *The Journal of Chemical Physics*, 87(4):2231–2235, 1987. doi: <http://dx.doi.org/10.1063/1.453150>. URL <http://scitation.aip.org/content/aip/journal/jcp/87/4/10.1063/1.453150>.
- Paul Ben Ishai, Eugene Mamontov, Jonathan D. Nickels, and Alexei P. Sokolov. Influence of ions on water diffusion—a neutron scattering study. *The Journal of Physical Chemistry B*, 117(25):7724–7728, 2013. doi: 10.1021/jp4030415. URL <http://dx.doi.org/10.1021/jp4030415>. PMID: 23713450.
- Viatcheslav Berejnov, Naji S Hussein, Osama A Alsaied, and Robert E Thorne. Effects of cryoprotectant concentration and cooling rate on vitrification of aqueous solutions. *Journal of Applied Crystallography*, 39(2):244–251, 2006.
- H. J. C. Berendsen, J. R. Grigera, and T. P. Straatsma. The missing term in effective pair potentials. *J. Phys. Chem.*, 91(24):6269–6271, nov 1987. doi: 10.1021/j100308a038. URL <http://dx.doi.org/10.1021/j100308a038>.
- JD Bernal and RH Fowler. A theory of water and ionic solution, with particular reference to hydrogen and hydroxyl ions. *Journal of Chemical Physics*, 1(8):515–548, 1933.
- JM Besson, RJ Nelmes, G Hamel, JS Loveday, G Weill, and S Hull. Neutron powder diffraction above 10 gpa. *Physica B: Condensed Matter*, 180:907–910, 1992.
- JM Besson, Ph Pruzan, S Klotz, G Hamel, B Silvi, RJ Nelmes, JS Loveday, RM Wilson, and S Hull. Variation of interatomic distances in ice viii to 10 gpa. *Physical Review B*, 49(18):12540, 1994.

- Lucile Bezacier, Baptiste Journaux, Jean-Philippe Perrillat, Hervé Cardon, Michael Hanfland, and Isabelle Daniel. Equations of state of ice VI and ice VII at high pressure and high temperature. *The Journal of Chemical Physics*, 141(10):104505, 2014a. doi: <http://dx.doi.org/10.1063/1.4894421>. URL <http://scitation.aip.org/content/aip/journal/jcp/141/10/10.1063/1.4894421>.
- Lucile Bezacier, Baptiste Journaux, Jean-Philippe Perrillat, Hervé Cardon, Michael Hanfland, and Isabelle Daniel. Equations of state of ice vi and ice vii at high pressure and high temperature. *The Journal of chemical physics*, 141(10):104505, 2014b.
- Salomon R Billeter, Alessandro Curioni, and Wanda Andreoni. Efficient linear scaling geometry optimization and transition-state search for direct wavefunction optimization schemes in density functional theory using a plane-wave basis. *Computational Materials Science*, 27(4):437–445, jun 2003. doi: 10.1016/S0927-0256(03)00043-0. URL [http://dx.doi.org/10.1016/S0927-0256\(03\)00043-0](http://dx.doi.org/10.1016/S0927-0256(03)00043-0).
- N. Bjerrum. Structure and properties of ice. *Science*, 115(2989):385–390, apr 1952. doi: 10.1126/science.115.2989.385. URL <http://dx.doi.org/10.1126/science.115.2989.385>.
- A. Bogdan, M. J. Molina, M. Kulmala, H. Tenhu, and T. Loerting. Solution coating around ice particles of incipient cirrus clouds. *Proceedings of the National Academy of Sciences*, 110(27):E2439–E2439, may 2013. doi: 10.1073/pnas.1304471110. URL <http://dx.doi.org/10.1073/pnas.1304471110>.
- Anatoli Bogdan, Mario J. Molina, Heikki Tenhu, Erminald Bertel, Natalia Bogdan, and Thomas Loerting. Visualization of freezing process in situ upon cooling and warming of aqueous solutions. *Sci. Rep.*, 4:7414, dec 2014. doi: 10.1038/srep07414. URL <http://dx.doi.org/10.1038/srep07414>.
- M. Born and R. Oppenheimer. Zur quantentheorie der molekeln. *Ann. Phys.*, 389(20):457–484, 1927. doi: 10.1002/andp.19273892002. URL <http://dx.doi.org/10.1002/andp.19273892002>.
- Eric Bourgeat-Lami, Jean-François Chapuis, Jérémie Chastagnier, Steffen Demas, Jean-Paul Gonzales, Morley-Patrick Keay, Jean-Luc Laborier, Eddy Lelièvre-Berna, Olivier Losserand, Paul Martin, et al. Overview of the projects recently developed by the advanced neutron environment team at the ill. *Physica B: Condensed Matter*, 385:1303–1305, 2006.
- L. Bove, C. Dreyfus, A. Polian, B. Bonello, I. Malfanti, A. Taschin, R. Torre, and R. M. Pick. The low frequency dynamics of supercooled LiBr, 6h2o. *J. Chem.*

- Phys.*, 134(3):034514, 2011a. doi: 10.1063/1.3526939. URL <http://dx.doi.org/10.1063/1.3526939>.
- L. Bove, S. Klotz, J. Philippe, and A. Saitta. Pressure-induced polyamorphism in salty water. *Physical Review Letters*, 106:125701, Mar 2011b. doi: 10.1103/PhysRevLett.106.125701. URL <http://link.aps.org/doi/10.1103/PhysRevLett.106.125701>.
- L. E. Bove, C. Dreyfus, R. Torre, and R. M. Pick. Observation of nanophase segregation in LiCl aqueous solutions from transient grating experiments. *The Journal of Chemical Physics*, 139(4):044501, 2013. doi: <http://dx.doi.org/10.1063/1.4813283>. URL <http://scitation.aip.org/content/aip/journal/jcp/139/4/10.1063/1.4813283>.
- Livia Eleonora Bove, Richard Gaal, Zamaan Raza, Adriaan-Alexander Ludl, Stefan Klotz, Antonino Marco Saitta, Alexander F. Goncharov, and Philippe Gillet. Effect of salt on the h-bond symmetrization in ice. *Proceedings of the National Academy of Sciences*, 112(27):8216–8220, jun 2015. doi: 10.1073/pnas.1502438112. URL <http://dx.doi.org/10.1073/pnas.1502438112>.
- D. T. Bowron, J. L. Finney, A. Hallbrucker, I. Kohl, T. Loerting, E. Mayer, and A. K. Soper. The local and intermediate range structures of the five amorphous ices at 80 k and ambient pressure: A faber-ziman and bhatia-thornton analysis. *The Journal of Chemical Physics*, 125(19):194502, 2006. doi: 10.1063/1.2378921. URL <http://dx.doi.org/10.1063/1.2378921>.
- W. H. Bragg and W. L. Bragg. The reflection of x-rays by crystals. *Proceedings of the Royal Society of London A: Mathematical, Physical and Engineering Sciences*, 88(605):428–438, 1913. ISSN 0950-1207. doi: 10.1098/rspa.1913.0040.
- Percy Williams Bridgman. *Physics of high pressure*. 1952.
- Yael Bronstein, Philippe Depondt, Fabio Finocchi, and Antonino Marco Saitta. Quantum-driven phase transition in ice described via an efficient langevin approach. *Phys. Rev. B*, 89:214101, Jun 2014. doi: 10.1103/PhysRevB.89.214101. URL <http://link.aps.org/doi/10.1103/PhysRevB.89.214101>.
- Yael Bronstein, Philippe Depondt, , Livia Bove, Richard Gaal, Antonino Marco Saitta, and Fabio Finocchi. Quantum versus classical protons in pure and salty ice under pressure. *submitted*, 2015.
- M. H. Brooker, G. Hancock, B. C. Rice, and J. Shapter. Raman frequency and intensity studies of liquid h<sub>2</sub>o, h<sub>2</sub>18o and d<sub>2</sub>o. *Journal of Raman Spectroscopy*,

- 20(10):683–694, 1989. ISSN 1097-4555. doi: 10.1002/jrs.1250201009. URL <http://dx.doi.org/10.1002/jrs.1250201009>.
- M. E. Brown and K. P. Hand. SALTS AND RADIATION PRODUCTS ON THE SURFACE OF EUROPA. *The Astronomical Journal*, 145(4):110, mar 2013. doi: 10.1088/0004-6256/145/4/110. URL <http://dx.doi.org/10.1088/0004-6256/145/4/110>.
- Peter Brüggeller and Erwin Mayer. Complete vitrification in pure liquid water and dilute aqueous solutions. 1980.
- Griffin Bullock and Valeria Molinero. Low-density liquid water is the mother of ice: on the relation between mesostructure, thermodynamics and ice crystallization in solutions. *Faraday Discuss.*, 167:371, 2013. doi: 10.1039/c3fd00085k. URL <http://dx.doi.org/10.1039/C3FD00085K>.
- Francis Pettit Bundy, Harold Paul Bovenkerk, Herbert Maxwell Strong, and Robert H Wentorf Jr. Diamond-graphite equilibrium line from growth and graphitization of diamond. *The Journal of Chemical Physics*, 35(2):383–391, 1961.
- EF Burton and WF Oliver. X-ray diffraction patterns of ice. *Nature*, 135:505–506, 1935.
- R. Car and M. Parrinello. Unified approach for molecular dynamics and density-functional theory. *Phys. Rev. Lett.*, 55:2471–2474, Nov 1985. doi: 10.1103/PhysRevLett.55.2471. URL <http://link.aps.org/doi/10.1103/PhysRevLett.55.2471>.
- S Casassa, M Calatayud, K Doll, C Minot, and C Pisani. Proton ordered cubic and hexagonal periodic models of ordinary ice. *Chemical physics letters*, 409(1): 110–117, 2005.
- David Chandler. Introduction to modern statistical mechanics. *Introduction to Modern Statistical Mechanics, by David Chandler, pp. 288. Foreword by David Chandler. Oxford University Press, Sep 1987. ISBN-10: 0195042778. ISBN-13: 9780195042771*, 1, 1987.
- Martin Chaplin. *Water webpage*. LSBU London, 2015. URL [http://www1.lsbu.ac.uk/water/water\\_phase\\_diagram.html](http://www1.lsbu.ac.uk/water/water_phase_diagram.html).
- S.-H. Chen, F. Mallamace, C.-Y. Mou, M. Broccio, C. Corsaro, A. Faraone, and L. Liu. The violation of the stokes-einstein relation in supercooled water. *Proceedings of the National Academy of Sciences*, 103(35):12974–12978, aug 2006. doi: 10.1073/pnas.0603253103. URL <http://dx.doi.org/10.1073/pnas.0603253103>.

- Mathieu Choukroun, SusanW. Kieffer, Xinli Lu, and Gabriel Tobie. Clathrate hydrates: Implications for exchange processes in the outer solar system. In Murthy S. Gudipati and Julie Castillo-Rogez, editors, *The Science of Solar System Ices*, volume 356 of *Astrophysics and Space Science Library*, pages 409–454. Springer New York, 2013. ISBN 978-1-4614-3075-9. doi: 10.1007/978-1-4614-3076-6\_12. URL [http://dx.doi.org/10.1007/978-1-4614-3076-6\\_12](http://dx.doi.org/10.1007/978-1-4614-3076-6_12).
- Fred J. Ciesla. THE PHASES OF WATER ICE IN THE SOLAR NEBULA. *ApJ*, 784(1):L1, mar 2014. doi: 10.1088/2041-8205/784/1/11. URL <http://dx.doi.org/10.1088/2041-8205/784/1/L1>.
- D Corradini, M Rovere, and P Gallo. A route to explain water anomalies from results on an aqueous solution of salt. *The Journal of Chemical Physics*, 132(13):134508, 2010.
- Dario Corradini, Paola Gallo, and Mauro Rovere. Effect of concentration on the thermodynamics of sodium chloride aqueous solutions in the supercooled regime. *The Journal of Chemical Physics*, 130(15):154511, 2009.
- Dario Corradini, Damien Dambournet, and Mathieu Salanne. Screening of structures in highly fluorinated anatase  $\text{TiO}_2$  by computer simulations. *arXiv preprint arXiv:1403.5525*, 2014.
- François-Xavier Coudert. Systematic investigation of the mechanical properties of pure silica zeolites: stiffness, anisotropy, and negative linear compressibility. *Phys. Chem. Chem. Phys.*, 15(38):16012, 2013. doi: 10.1039/c3cp51817e. URL <http://dx.doi.org/10.1039/C3CP51817E>.
- C. A. Coulson and D. Eisenberg. Interactions of  $\text{H}_2\text{O}$  molecules in ice. i. the dipole moment of an  $\text{H}_2\text{O}$  molecule in ice. *Proceedings of the Royal Society A: Mathematical, Physical and Engineering Sciences*, 291(1427):445–453, apr 1966. doi: 10.1098/rspa.1966.0105. URL <http://dx.doi.org/10.1098/rspa.1966.0105>.
- Liem X. Dang and Tsun-Mei Chang. Molecular dynamics study of water clusters, liquid, and liquid–vapor interface of water with many-body potentials. *The Journal of Chemical Physics*, 106(19):8149–8159, 1997. doi: 10.1063/1.473820. URL <http://scitation.aip.org/content/aip/journal/jcp/106/19/10.1063/1.473820>.
- Otten D.E. and Saykally R.J. Spectroscopy and modeling of aqueous interfaces. *Proceedings of the International School of Physics Enrico Fermi*, 187(Water: Fundamentals as the Basis for Understanding the Environment and Promoting Tech-

- nology):137–150, 2015. ISSN 0074-784X. doi: 10.3254/978-1-61499-507-4-137. URL <http://doi.org/10.3254/978-1-61499-507-4-137>.
- Pablo G Debenedetti. *Metastable liquids: concepts and principles*. Princeton University Press, 1996.
- D. L. Decker. High-Pressure Equation of State for NaCl, KCl, and CsCl. *Journal of Applied Physics*, 42(8):3239–3244, 1971. doi: <http://dx.doi.org/10.1063/1.1660714>. URL <http://scitation.aip.org/content/aip/journal/jap/42/8/10.1063/1.1660714>.
- D. M. Dennison. The crystal structure of ice. *Phys. Rev.*, 17:20–22, Jan 1921. doi: 10.1103/PhysRev.17.20. URL <http://link.aps.org/doi/10.1103/PhysRev.17.20>.
- CP2K developers group. *CP2K website*. CP2K developers group, 2012. URL <http://www.cp2k.org>.
- Leonid Dubrovinsky, Natalia Dubrovinskaia, Vitali B. Prakapenka, and Artem M. Abakumov. Implementation of micro-ball nanodiamond anvils for high-pressure studies above 6 mbar. *Nature communications*, 3:1163, 2012.
- J. Dupuy-Philon, J.F. Jal, and B. Prével. Dynamical studies of an aqueous electrolyte in the supercooled liquid and glassy states. *Journal of Non-Crystalline Solids*, 150(1–3):275 – 280, 1992. ISSN 0022-3093. doi: [http://dx.doi.org/10.1016/0022-3093\(92\)90136-8](http://dx.doi.org/10.1016/0022-3093(92)90136-8). URL <http://www.sciencedirect.com/science/article/pii/0022309392901368>. Proceedings of the Fifth International Conference on the structure of Non-Crystalline Materials (NCM 5).
- A. Elarby-Aouizerat, J. F. Jal, C. Ferradou, J. Dupuy, P. Chieux, and A. Wright. On the optimal conditions for the homogeneous nucleation of cubic ice from concentrated solutions of lithium chloride-deuterium oxide. *The Journal of Physical Chemistry*, 87(21):4170–4173, 1983. doi: 10.1021/j100244a039. URL <http://pubs.acs.org/doi/abs/10.1021/j100244a039>.
- J E Enderby and G W Neilson. The structure of electrolyte solutions. *Reports on Progress in Physics*, 44(6):593, 1981. URL <http://stacks.iop.org/0034-4885/44/i=6/a=001>.
- M. I. Eremets. *High pressure experimental methods*. Oxford university press, 1996.
- A. Fasolino, J. H. Los, and M. I. Katsnelson. Intrinsic ripples in graphene. *Nature Materials*, 6(11):858–861, sep 2007. doi: 10.1038/nmat2011. URL <http://dx.doi.org/10.1038/nmat2011>.

- R. P. Feynman. Forces in molecules. *Phys. Rev.*, 56:340–343, Aug 1939. doi: 10.1103/PhysRev.56.340. URL <http://link.aps.org/doi/10.1103/PhysRev.56.340>.
- J. L. Finney, C. Lobban, and W. F. Kuhs. *Nature*, 391(6664):268–270, jan 1998. doi: 10.1038/34622. URL <http://dx.doi.org/10.1038/34622>.
- J. L. Finney, D. T. Bowron, A. K. Soper, T. Loerting, E. Mayer, and A. Hallbrucker. Structure of a new dense amorphous ice. *Physical Review Letters*, 89:205503, Oct 2002. doi: 10.1103/PhysRevLett.89.205503. URL <http://link.aps.org/doi/10.1103/PhysRevLett.89.205503>.
- R Fletcher. Practical methods of. *Optimization*, 1:784–794, 1987.
- A. D. Fortes, I. G. Wood, M. G. Tucker, and W. G. Marshall. The  $p - v - t$  equation of state of d 2 o ice VI determined by neutron powder diffraction in the range  $0 < p < 2.6$  GPa and  $120 < t < 330$  k, and the isothermal equation of state of d 2 o ice VII from 2 to 7 GPa at room temperature. *Journal of Applied Crystallography*, 45(3):523–534, may 2012. doi: 10.1107/s0021889812014847. URL <http://dx.doi.org/10.1107/S0021889812014847>.
- A. Dominic Fortes and Mathieu Choukroun. Phase behaviour of ices and hydrates. *Space Science Reviews*, 153(1-4):185–218, 2010. ISSN 0038-6308. doi: 10.1007/s11214-010-9633-3. URL <http://dx.doi.org/10.1007/s11214-010-9633-3>.
- Mark R. Frank, Yingwei Fei, and Jingzhu Hu. Constraining the equation of state of fluid h2o to 80 GPa using the melting curve, bulk modulus, and thermal expansivity of ice VII. *Geochimica et Cosmochimica Acta*, 68(13):2781–2790, jul 2004. doi: 10.1016/j.gca.2003.12.007. URL <http://dx.doi.org/10.1016/j.gca.2003.12.007>.
- Mark R. Frank, Claire E. Runge, Henry P. Scott, Steven J. Maglio, Jessica Olson, Vitali B. Prakapenka, and Guoyin Shen. Experimental study of the NaCl-H<sub>2</sub>O system up to 28GPa: Implications for ice-rich planetary bodies. *Physics of the Earth and Planetary Interiors*, 155(1-2):152–162, 2006. ISSN 0031-9201. doi: <http://dx.doi.org/10.1016/j.pepi.2005.12.001>. URL <http://www.sciencedirect.com/science/article/pii/S0031920105002499>.
- Mark R. Frank, Henry P. Scott, Steven J. Maglio, Vitali B. Prakapenka, and Guoyin Shen. Temperature induced immiscibility in the NaCl-h<sub>2</sub>o system at high pressure. *Physics of the Earth and Planetary Interiors*, 170(1-2):107–114, sep 2008. doi: 10.1016/j.pepi.2008.07.035. URL <http://dx.doi.org/10.1016/j.pepi.2008.07.035>.

- Hiroshi Fukazawa, Susumu Ikeda, and Shinji Mae. Incoherent inelastic neutron scattering measurements on ice XI; the proton-ordered phase of ice Ih doped with KOH. *Chemical Physics Letters*, 282(2):215–218, jan 1998. doi: 10.1016/S0009-2614(97)01266-9. URL [http://dx.doi.org/10.1016/S0009-2614\(97\)01266-9](http://dx.doi.org/10.1016/S0009-2614(97)01266-9).
- Katsuhisa Furuno, Akifumi Onodera, and Shoichi Kume. Sapphire-anvil cell for high pressure research. *Japanese Journal of Applied Physics*, 25(Part 2, No. 8): L646–L647, aug 1986. doi: 10.1143/jjap.25.l646. URL <http://dx.doi.org/10.1143/JJAP.25.L646>.
- P. Gallo, D. Corradini, and M. Rovere. Ion hydration and structural properties of water in aqueous solutions at normal and supercooled conditions: a test of the structure making and breaking concept. *Phys. Chem. Chem. Phys.*, 13(44):19814, 2011. doi: 10.1039/c1cp22166c. URL <http://dx.doi.org/10.1039/C1CP22166C>.
- P. Gallo, D. Corradini, and M. Rovere. Do ions affect the structure of water? the case of potassium halides. *Journal of Molecular Liquids*, 189:52–56, jan 2014. doi: 10.1016/j.molliq.2013.05.023. URL <http://dx.doi.org/10.1016/j.molliq.2013.05.023>.
- A. Geiger, F. H. Stillinger, and A. Rahman. Aspects of the percolation process for hydrogen-bond networks in water. *The Journal of Chemical Physics*, 70(9):4185, 1979. doi: 10.1063/1.438042. URL <http://dx.doi.org/10.1063/1.438042>.
- Paolo Giannozzi, Stefano Baroni, Nicola Bonini, Matteo Calandra, Roberto Car, Carlo Cavazzoni, Davide Ceresoli, Guido L Chiarotti, Matteo Cococcioni, Ismaila Dabo, Andrea Dal Corso, Stefano de Gironcoli, Stefano Fabris, Guido Fratesi, Ralph Gebauer, Uwe Gerstmann, Christos Gougoussis, Anton Kokalj, Michele Lazzeri, Layla Martin-Samos, Nicola Marzari, Francesco Mauri, Riccardo Mazzarello, Stefano Paolini, Alfredo Pasquarello, Lorenzo Paulatto, Carlo Sbraccia, Sandro Scandolo, Gabriele Sclauzero, Ari P Seitsonen, Alexander Smogunov, Paolo Umari, and Renata M Wentzcovitch. QUANTUM ESPRESSO: a modular and open-source software project for quantum simulations of materials. *Journal of Physics: Condensed Matter*, 21(39):395502, sep 2009. doi: 10.1088/0953-8984/21/39/395502. URL <http://dx.doi.org/10.1088/0953-8984/21/39/395502>.
- W. F. Giauque and Muriel F. Ashley. Molecular rotation in ice at 10k. free energy of formation and entropy of water. *Phys. Rev.*, 43:81–82, Jan 1933. doi: 10.1103/PhysRev.43.81.2. URL <http://link.aps.org/doi/10.1103/PhysRev.43.81.2>.

- S. Goedecker, M. Teter, and J. Hutter. Separable dual-space gaussian pseudopotentials. *Physical Review B*, 54(3):1703–1710, jul 1996. doi: 10.1103/physrevb.54.1703. URL <http://dx.doi.org/10.1103/PhysRevB.54.1703>.
- IN Goncharenko. New techniques for high-pressure neutron and x-ray studies. *High Pressure Research*, 27(1):183–188, 2007.
- A. F. Goncharov, V. V. Struzhkin, M. S. Somayazulu, R. J. Hemley, and H. K. Mao. Compression of ice to 210 gigapascals: Infrared evidence for a symmetric hydrogen-bonded phase. *Science*, 273(5272):218–220, 1996. doi: 10.1126/science.273.5272.218. URL <http://www.sciencemag.org/content/273/5272/218.abstract>.
- Stefan Grimme, Jens Antony, Stephan Ehrlich, and Helge Krieg. A consistent and accurate ab initio parametrization of density functional dispersion correction (DFT-d) for the 94 elements h-pu. *J. Chem. Phys.*, 132(15):154104, 2010. doi: 10.1063/1.3382344. URL <http://dx.doi.org/10.1063/1.3382344>.
- B. Gundlach, S. Kiliyas, E. Beitz, and J. Blum. Micrometer-sized ice particles for planetary-science experiments – i. preparation, critical rolling friction force, and specific surface energy. *Icarus*, 214(2):717–723, aug 2011a. doi: 10.1016/j.icarus.2011.05.005. URL <http://dx.doi.org/10.1016/j.icarus.2011.05.005>.
- B. Gundlach, Yu.V. Skorov, and J. Blum. Outgassing of icy bodies in the solar system – i. the sublimation of hexagonal water ice through dust layers. *Icarus*, 213(2):710–719, jun 2011b. doi: 10.1016/j.icarus.2011.03.022. URL <http://dx.doi.org/10.1016/j.icarus.2011.03.022>.
- Th. Hahn, editor. *International Tables for Crystallography*. International Union of Crystallography, oct 2006. doi: 10.1107/97809553602060000100. URL <http://dx.doi.org/10.1107/97809553602060000100>.
- T. C. Hansen, M. M. Koza, and W. F. Kuhs. Formation and annealing of cubic ice: I. modelling of stacking faults. *Journal of Physics: Condensed Matter*, 20(28):285104, jun 2008a. doi: 10.1088/0953-8984/20/28/285104. URL <http://dx.doi.org/10.1088/0953-8984/20/28/285104>.
- T. C. Hansen, M. M. Koza, P. Lindner, and W. F. Kuhs. Formation and annealing of cubic ice: II. kinetic study. *Journal of Physics: Condensed Matter*, 20(28):285105, jun 2008b. doi: 10.1088/0953-8984/20/28/285105. URL <http://dx.doi.org/10.1088/0953-8984/20/28/285105>.

- Thomas C Hansen, Paul F Henry, Henry E Fischer, Jacques Torregrossa, and Pierre Convert. The D20 instrument at the ILL: a versatile high-intensity two-axis neutron diffractometer. *Measurement Science and Technology*, 19(3):034001, Jan 2008c. ISSN 1361-6501. URL <http://dx.doi.org/10.1088/0957-0233/19/3/034001>.
- Thomas C. Hansen, Christian Sippel, and Werner F. Kuhs. Approximations to the full description of stacking disorder in ice I for powder diffraction. *Zeitschrift für Kristallographie - Crystalline Materials*, 230(1), jan 2015. doi: 10.1515/zkri-2014-1780. URL <http://dx.doi.org/10.1515/zkri-2014-1780>.
- William M Haynes. *CRC handbook of chemistry and physics*. CRC press, 2013.
- H Hellman. Einführung in die quantenchemie (deuticke, leipzig, 1937); rp feynman. *Phys. Rev*, 56:340, 1939.
- Wayne A. Hendrickson and Craig M. Ogata. [28] phase determination from multiwavelength anomalous diffraction measurements. In *Methods in Enzymology*, pages 494–523. Elsevier BV, 1997. doi: 10.1016/S0076-6879(97)76074-9. URL [http://dx.doi.org/10.1016/S0076-6879\(97\)76074-9](http://dx.doi.org/10.1016/S0076-6879(97)76074-9).
- M. R. Hogerheijde, E. A. Bergin, C. Brinch, L. I. Cleaves, J. K. J. Fogel, G. A. Blake, C. Dominik, D. C. Lis, G. Melnick, D. Neufeld, O. Panic, J. C. Pearson, L. Kristensen, U. A. Yildiz, and E. F. van Dishoeck. Detection of the water reservoir in a forming planetary system. *Science*, 334(6054):338–340, oct 2011. doi: 10.1126/science.1208931. URL <http://dx.doi.org/10.1126/science.1208931>.
- P. Hohenberg and W. Kohn. Inhomogeneous electron gas. *Phys. Rev.*, 136:B864–B871, Nov 1964. doi: 10.1103/PhysRev.136.B864. URL <http://link.aps.org/doi/10.1103/PhysRev.136.B864>.
- Vincent Holten, CE Bertrand, MA Anisimov, and JV Sengers. Thermodynamics of supercooled water. *The Journal of chemical physics*, 136(9):094507, 2012.
- W. B. Holzapfel. On the symmetry of the hydrogen bonds in ice VII. *The Journal of Chemical Physics*, 56(2):712, 1972. doi: 10.1063/1.1677221. URL <http://dx.doi.org/10.1063/1.1677221>.
- William G Hoover. Canonical dynamics: equilibrium phase-space distributions. *Physical Review A*, 31(3):1695, 1985.
- Arpa Hudait and Valeria Molinero. Ice crystallization in ultrafine water–salt aerosols: Nucleation, ice–solution equilibrium, and internal structure. *J. Am.*

- Chem. Soc.*, 136(22):8081–8093, jun 2014. doi: 10.1021/ja503311r. URL <http://dx.doi.org/10.1021/ja503311r>.
- William Humphrey, Andrew Dalke, and Klaus Schulten. VMD – Visual Molecular Dynamics. *Journal of Molecular Graphics*, 14:33–38, 1996.
- Janos Inczedy, Tamas Lengyel, AM Ure, A Gelencsér, and A Hulanicki. Compendium of analytical nomenclature. *Blackwell, Oxford*, 1998.
- H. Jahn and G. Wolf. The enthalpy of solution of  $\text{mgcl}_2$  and  $\text{mgcl}_2 \cdot 6\text{h}_2\text{o}$  in water at  $25^\circ\text{c}$ . i. the integral molar enthalpy of solution. *Journal of Solution Chemistry*, 22(11):983–994, 1993. ISSN 0095-9782. doi: 10.1007/BF00647722. URL <http://dx.doi.org/10.1007/BF00647722>.
- P Jenniskens and DF Blake. Crystallization of amorphous water ice in the solar system. *The Astrophysical Journal*, 473(2):1104, 1996.
- G. P. Johari. Dielectric properties of ice VII and VIII and the phase boundary between ice VI and VII. *The Journal of Chemical Physics*, 61(10):4292, 1974. doi: 10.1063/1.1681733. URL <http://dx.doi.org/10.1063/1.1681733>.
- G. P. Johari. Water’s size-dependent freezing to cubic ice. *The Journal of Chemical Physics*, 122(19):194504, 2005. doi: <http://dx.doi.org/10.1063/1.1900723>. URL <http://scitation.aip.org/content/aip/journal/jcp/122/19/10.1063/1.1900723>.
- H. Jones. Splat cooling and metastable phases. *Reports on Progress in Physics*, 36(11):1425, 1973. URL <http://stacks.iop.org/0034-4885/36/i=11/a=002>.
- J. E. Jones. On the determination of molecular fields. II. from the equation of state of a gas. *Proceedings of the Royal Society A: Mathematical, Physical and Engineering Sciences*, 106(738):463–477, oct 1924. doi: 10.1098/rspa.1924.0082. URL <http://dx.doi.org/10.1098/rspa.1924.0082>.
- James D. Jorgensen and Thomas G. Worlton. Disordered structure of  $\text{d}_2\text{o}$  ice VII from in situ neutron powder diffraction. *J. Chem. Phys.*, 83(1):329, 1985. doi: 10.1063/1.449867. URL <http://dx.doi.org/10.1063/1.449867>.
- B Journaux, I Daniel, R Caracas, G Montagnac, and H Cardon. Influence of  $\text{nacl}$  on ice vi and ice vii melting curves up to 6gpa, implications for large icy moons. *Icarus*, 226(1):355–363, 2013.
- H. Kanno. Double glass transitions in aqueous lithium chloride solutions vitrified at high pressures: evidence for a liquid-liquid immiscibility. *The Journal of Physical*

- Chemistry*, 91(7):1967–1971, 1987. doi: 10.1021/j100291a057. URL <http://dx.doi.org/10.1021/j100291a057>.
- J.-J. Kessis. Le système eau-bromure de lithium. *Bulletin de la société chimique de France*, (1):48, 1965.
- LG Khvostantsev, LF Vereshchagin, and AP Novikov. Device of toroid type for high pressure generation. *High Temp.-High Pressures*, 9(6):637–639, 1977.
- LG Khvostantsev, VN Slesarev, and VV Brazhkin. Toroid type high-pressure device: history and prospects. *High Pressure Research*, 24(3):371–383, 2004.
- Charles Kittel and Paul McEuen. *Introduction to solid state physics*, volume 8. Wiley New York, 1976.
- B. Klewe and B. Pedersen. The crystal structure of sodium chloride dihydrate. *Acta Crystallographica Section B Structural Crystallography and Crystal Chemistry*, 30(10):2363–2371, oct 1974. doi: 10.1107/s0567740874007138. URL <http://dx.doi.org/10.1107/S0567740874007138>.
- S. Klotz. *Techniques in High Pressure Neutron Scattering*. Taylor & Francis, 2012. ISBN 9781439835623. URL [http://books.google.fr/books?id=sqDFAwJ3C\\\_oC](http://books.google.fr/books?id=sqDFAwJ3C\_oC).
- S Klotz, G Hamel, JS Loveday, RJ Nelmes, and M Guthrie. Recrystallisation of hda ice under pressure by in-situ neutron diffraction to 3.9 gpa. *Zeitschrift für Kristallographie*, 218(2/2003):117–122, 2003.
- S. Klotz, Th. Strässle, R. J. Nelmes, J. S. Loveday, G. Hamel, G. Rousse, B. Canny, J. C. Chervin, and A. M. Saitta. Nature of the polyamorphic transition in ice under pressure. *Physical Review Letters*, 94:025506, Jan 2005. doi: 10.1103/PhysRevLett.94.025506. URL <http://link.aps.org/doi/10.1103/PhysRevLett.94.025506>.
- Stefan Klotz. chapter High-Pressure Devices. 2011.
- Stefan Klotz, Livia E. Bove, Thierry Strässle, Thomas C. Hansen, and Antonino M. Saitta. The preparation and structure of salty ice VII under pressure. *Nature Materials*, 8(5):405–409, May 2009. ISSN 1476-1122. doi: 10.1038/nmat2422. URL <http://dx.doi.org/10.1038/nmat2422>.
- G.F. Knoll, T.F. Knoll, and T.M. Henderson. Light collection in scintillation detector composites for neutron detection. *Nuclear Science, IEEE Transactions on*, 35(1):872–875, Feb 1988. ISSN 0018-9499. doi: 10.1109/23.12850.

- Ingrid Kohl, Luis Bachmann, Andreas Hallbrucker, Erwin Mayer, and Thomas Loerting. Liquid-like relaxation in hyperquenched water at  $\leq 140$  K. *Phys. Chem. Chem. Phys.*, 7(17):3210, 2005. doi: 10.1039/b507651j. URL <http://dx.doi.org/10.1039/b507651j>.
- W. Kohn and L. J. Sham. Self-consistent equations including exchange and correlation effects. *Physical Review*, 140(4A):A1133–A1138, nov 1965. doi: 10.1103/physrev.140.a1133. URL <http://dx.doi.org/10.1103/PhysRev.140.A1133>.
- W. Kohn, A. D. Becke, and R. G. Parr. Density functional theory of electronic structure. *J. Phys. Chem.*, 100(31):12974–12980, jan 1996. doi: 10.1021/jp960669l. URL <http://dx.doi.org/10.1021/jp960669l>.
- Kazuki Komatsu, Masato Moriyama, Tamami Koizumi, Kazuya Nakayama, Hiroyuki Kagi, Jun Abe, and Stefanus Harjo. Development of a new p-t controlling system for neutron-scattering experiments. *High Pressure Research*, 33(1):208–213, 2013. doi: 10.1080/08957959.2012.762914. URL <http://dx.doi.org/10.1080/08957959.2012.762914>.
- T. Koop. Atmospheric water. *Proceedings of the International School of Physics Enrico Fermi*, 187(Water: Fundamentals as the Basis for Understanding the Environment and Promoting Technology):45–75, 2015. ISSN 0074-784X. doi: 10.3254/978-1-61499-507-4-45. URL <http://doi.org/10.3254/978-1-61499-507-4-45>.
- W. F. Kuhs and M. S. Lehmann. The structure of ice-ih. *Water science reviews*, 2: 1–65, 1986.
- W. F. Kuhs and M. S. Lehmann. The geometry and orientation of the water molecule in ice Ih. *J. Phys. Colloques*, 48(C1):C1-3 – C1-8, 1987. doi: 10.1051/jphyscol:1987101. URL <http://dx.doi.org/10.1051/jphyscol:1987101>.
- W. F. Kuhs, J. L. Finney, C. Vettier, and D. V. Bliss. Structure and hydrogen ordering in ices VI, VII, and VIII by neutron powder diffraction. *J. Chem. Phys.*, 81(8):3612, 1984. doi: 10.1063/1.448109. URL <http://dx.doi.org/10.1063/1.448109>.
- W. F. Kuhs, C. Sippel, A. Falenty, and T. C. Hansen. Extent and relevance of stacking disorder in "ice ic". *Proceedings of the National Academy of Sciences*, 109(52):21259–21264, dec 2012. doi: 10.1073/pnas.1210331110. URL <http://dx.doi.org/10.1073/pnas.1210331110>.

- Teodoro Laino and Jürg Hutter. Notes on “ewald summation of electrostatic multipole interactions up to quadrupolar level” [j. chem. phys.119, 7471 (2003)]. *The Journal of Chemical Physics*, 129(7):074102, 2008. doi: 10.1063/1.2970887. URL <http://scitation.aip.org/content/aip/journal/jcp/129/7/10.1063/1.2970887>.
- L. D. Landau and E. M. Lifshitz. The classical theory of fields. *Course of theoretical physics*, 2, 1975.
- Hans Landolt, Richard Bornstein, Heinz Borchers, Werner Helling, and Ernst Schmidt. *Landolt-Börnstein. Zahlenwerte und Funktionen aus Physik, Chemie, Astronomie, Geophysik und Technik: 6. Auflage... Technik. 2. Teil.[Stoffwerte und Verhalten von metallischen Werkstoffen.] Bandteil b. Sinterwerkstoffe. Schwermetalle (ohne Sonderwerkstoffe)... Herausgegeben von Heinz Borchers und Ernst Schmidt unter Mitwirkung von Werner Helling...* Springer-Verlag, 1964.
- AC Larson and RB Von Dreele. General structure analysis system (gsas); report laur 86-748; los alamos national laboratory: Los alamos, nm, 2000. *There is no corresponding record for this reference.*
- Allen C Larson and Robert B Von Dreele. Gsas. *General Structure Analysis System. LANSCE, MS-H805, Los Alamos, New Mexico*, 1994.
- M Laue. A quantitative examination of the theory for the interference appearances in X-rays. *Annalen der Physik*, 41(10):989–1002, AUG 1913. ISSN 0003-3804.
- A. W. Lawson and T.-Y. Tang. A diamond bomb for obtaining powder pictures at high pressures. *Review of Scientific Instruments*, 21(9):815–815, 1950. doi: <http://dx.doi.org/10.1063/1.1745728>. URL <http://scitation.aip.org/content/aip/journal/rsi/21/9/10.1063/1.1745728>.
- Ly Le and Valeria Molinero. Nanophase segregation in supercooled aqueous solutions and their glasses driven by the polyamorphism of water. *The Journal of Physical Chemistry A*, 115(23):5900–5907, 2010.
- Sébastien Le Roux and Valeri Petkov. ISAACS – interactive structure analysis of amorphous and crystalline systems. *Journal of Applied Crystallography*, 43(1): 181–185, Feb 2010. doi: 10.1107/S0021889809051929. URL <http://dx.doi.org/10.1107/S0021889809051929>.
- R. Leberman and A. K. Soper. Effect of high salt concentrations on water structure. *Nature*, 378(6555):364–366, November 1995. URL <http://dx.doi.org/10.1038/378364a0>.

- Chengteh Lee, Weitao Yang, and Robert G. Parr. Development of the colle-salvetti correlation-energy formula into a functional of the electron density. *Phys. Rev. B*, 37:785–789, Jan 1988. doi: 10.1103/PhysRevB.37.785. URL <http://link.aps.org/doi/10.1103/PhysRevB.37.785>.
- Jiaqi Li. Mise au point d'un système de hypertrempe pour des solutions aqueuses. 2012.
- David T. Limmer and David Chandler. The putative liquid-liquid transition is a liquid-solid transition in atomistic models of water. II. *The Journal of Chemical Physics*, 138(21):214504, jun 2013. doi: 10.1063/1.4807479. URL <http://dx.doi.org/10.1063/1.4807479>.
- Katharina Lodders. Solar system abundances and condensation temperatures of the elements. *ApJ*, 591(2):1220–1247, jul 2003. doi: 10.1086/375492. URL <http://dx.doi.org/10.1086/375492>.
- Thomas Loerting, Werner Schustereder, Katrin Winkel, Christoph G. Salzmann, Ingrid Kohl, and Erwin Mayer. Amorphous ice: Stepwise formation of very-high-density amorphous ice from low-density amorphous ice at 125 k. *Phys. Rev. Lett.*, 96:025702, Jan 2006. doi: 10.1103/PhysRevLett.96.025702. URL <http://link.aps.org/doi/10.1103/PhysRevLett.96.025702>.
- Thomas Loerting, Katrin Winkel, Markus Seidl, Marion Bauer, Christian Mitterdorfer, Philip H. Handle, Christoph G. Salzmann, Erwin Mayer, John L. Finney, and Daniel T. Bowron. How many amorphous ices are there? *Phys. Chem. Chem. Phys.*, 13(19):8783, 2011. doi: 10.1039/c0cp02600j. URL <http://dx.doi.org/10.1039/C0CP02600J>.
- P. Loubeyre, P. M. Celliers, D. G. Hicks, E. Henry, A. Dewaele, J. Pasley, J. Eggert, M. Koenig, F. Occelli, K. M. Lee, R. Jeanloz, D. Neely, A. Benuzzi-Mounaix, D. Bradley, M. Bastea, Steve Moon, and G. W. Collins. Coupling static and dynamic compressions: first measurements in dense hydrogen. *High Pressure Research*, 24(1):25–31, 2004. doi: 10.1080/08957950310001635792. URL <http://dx.doi.org/10.1080/08957950310001635792>.
- Paul Loubeyre, René LeToullec, Elodie Wolanin, Michel Hanfland, and Daniel Hausermann. *Nature*, 397(6719):503–506, feb 1999. doi: 10.1038/17300. URL <http://dx.doi.org/10.1038/17300>.
- Paul Loubeyre, Florent Occelli, and Rene LeToullec. Optical studies of solid hydrogen to 320[thinsp]gpa and evidence for black hydrogen. *Nature*, 416(6881):613–617, April 2002. ISSN 0028-0836. URL <http://dx.doi.org/10.1038/416613a>.

- A.-A. Ludl, L. E. Bove, and S. Klotz. Work in preparation. in preparation.
- Adriaan-Alexander Ludl, Livia E Bove, A. Marco Saitta, Mathieu Salanne, Thomas Hansen, Craig L. Bull, Richard Gaal, and Stefan Klotz. Structural characterization of eutectic aqueous nacl solutions under variable temperature and pressure conditions. *Phys. Chem. Chem. Phys.*, pages –, 2015. doi: 10.1039/C5CP00224A. URL <http://dx.doi.org/10.1039/C5CP00224A>.
- Tamsin L. Malkin, Benjamin J. Murray, Christoph G. Salzmann, Valeria Molinero, Steven J. Pickering, and Thomas F. Whale. Stacking disorder in ice i. *Phys. Chem. Chem. Phys.*, 17(1):60–76, 2015. doi: 10.1039/c4cp02893g. URL <http://dx.doi.org/10.1039/C4CP02893G>.
- F. Mallamace, M. Broccio, C. Corsaro, A. Faraone, U. Wanderlingh, L. Liu, C.-Y. Mou, and S. H. Chen. The fragile-to-strong dynamic crossover transition in confined water: nuclear magnetic resonance results. *The Journal of Chemical Physics*, 124(16):161102, 2006. doi: 10.1063/1.2193159. URL <http://dx.doi.org/10.1063/1.2193159>.
- R. Mancinelli, A. Botti, F. Bruni, M. A. Ricci, and A. K. Soper. Perturbation of water structure due to monovalent ions in solution. *Physical Chemistry Chemical Physics*, 9(23):2959, 2007. ISSN 1463-9084. URL <http://dx.doi.org/10.1039/b701855j>.
- Davide Mantegazzi, Carmen Sanchez-Valle, and Thomas Driesner. Thermodynamic properties of aqueous NaCl solutions to 1073K and 4.5GPa, and implications for dehydration reactions in subducting slabs. *Geochimica et Cosmochimica Acta*, 121(0):263 – 290, 2013. ISSN 0016-7037. doi: <http://dx.doi.org/10.1016/j.gca.2013.07.015>. URL <http://www.sciencedirect.com/science/article/pii/S0016703713003943>.
- Dario Marrocchelli, Mathieu Salanne, and Paul A Madden. High-pressure behaviour of GeO<sub>2</sub> : a simulation study. *Journal of Physics: Condensed Matter*, 22(15):152102, mar 2010. doi: 10.1088/0953-8984/22/15/152102. URL <http://dx.doi.org/10.1088/0953-8984/22/15/152102>.
- Walter Marshall and Stephen W Lovesey. *Theory of thermal neutron scattering: the use of neutrons for the investigation of condensed matter*. Clarendon Press Oxford, 1971.
- William G. Marshall and Duncan J. Francis. Attainment of near-hydrostatic compression conditions using the paris–edinburgh cell. *Journal of Applied Cryst-*

- tallography*, 35(1):122–125, jan 2002. doi: 10.1107/s0021889801018350. URL <http://dx.doi.org/10.1107/S0021889801018350>.
- Glenn J Martyna, Michael L Klein, and Mark Tuckerman. Nosé–hoover chains: the canonical ensemble via continuous dynamics. *The Journal of chemical physics*, 97(4):2635–2643, 1992.
- Glenn J. Martyna, Douglas J. Tobias, and Michael L. Klein. Constant pressure molecular dynamics algorithms. *J. Chem. Phys.*, 101(5):4177, 1994. doi: 10.1063/1.467468. URL <http://dx.doi.org/10.1063/1.467468>.
- Marco Masia, Michael Probst, and Rossend Rey. On the performance of molecular polarization methods. i. water and carbon tetrachloride close to a point charge. *The Journal of Chemical Physics*, 121(15):7362–7378, 2004. doi: <http://dx.doi.org/10.1063/1.1791637>. URL <http://scitation.aip.org/content/aip/journal/jcp/121/15/10.1063/1.1791637>.
- Marco Masia, Michael Probst, and Rossend Rey. On the performance of molecular polarization methods. ii. water and carbon tetrachloride close to a cation. *The Journal of Chemical Physics*, 123(16):164505, 2005. doi: <http://dx.doi.org/10.1063/1.2075107>. URL <http://scitation.aip.org/content/aip/journal/jcp/123/16/10.1063/1.2075107>.
- Takasuke Matsuo, Yoshimitsu Tajima, and Hiroshi Suga. Calorimetric study of a phase transition in d2o ice ih doped with KOD: Ice XI. *Journal of Physics and Chemistry of Solids*, 47(2):165–173, jan 1986. doi: 10.1016/0022-3697(86)90126-5. URL [http://dx.doi.org/10.1016/0022-3697\(86\)90126-5](http://dx.doi.org/10.1016/0022-3697(86)90126-5).
- Erwin Mayer. New method for vitrifying water and other liquids by rapid cooling of their aerosols. *Journal of applied physics*, 58(2):663–667, 1985.
- R Mecke and W Baumann. The rotation oscillation spectrum of water vapour. *Physikalische Zeitschrift*, 33:833–835, 1932.
- Å. Melinder. Properties and other aspects of aqueous solutions used for single phase and ice slurry applications. *International Journal of Refrigeration*, 33(8):1506–1512, dec 2010. doi: 10.1016/j.ijrefrig.2010.07.014. URL <http://dx.doi.org/10.1016/j.ijrefrig.2010.07.014>.
- Valentina Migliorati, Giordano Mancini, Simone Tatoli, Andrea Zitolo, Adriano Filippini, Simone De Panfilis, Andrea Di Cicco, and Paola D’Angelo. Hydration properties of the Zn<sup>2+</sup> ion in water at high pressure. *Inorganic Chemistry*, 52(2):1141–1150, 2013. doi: 10.1021/ic302530k. URL <http://dx.doi.org/10.1021/ic302530k>. PMID: 23276257.

- RL Mills, DH Liebenberg, and JC Bronson. Sound velocity and the equation of state of n2 to 22 kbar. *The Journal of Chemical Physics*, 63(3):1198–1204, 1975.
- RL Mills, Bart Olinger, and DT Cromer. Structures and phase diagrams of n2 and co to 13 gpa by x-ray diffraction. *The Journal of chemical physics*, 84(5): 2837–2845, 1986.
- Lichung Ming and William A. Bassett. Laser heating in the diamond anvil press up to 2000° c sustained and 3000 c pulsed at pressures up to 260 kilobars. *Review of Scientific Instruments*, 45(9):1115–1118, 1974. doi: <http://dx.doi.org/10.1063/1.1686822>. URL <http://scitation.aip.org/content/aip/journal/rsi/45/9/10.1063/1.1686822>.
- O. Mishima, L. D. Calvert, and E. Whalley. ‘melting ice’ i at 77 k and 10 kbar: a new method of making amorphous solids. *Nature*, 310(5976):393–395, aug 1984. doi: 10.1038/310393a0. URL <http://dx.doi.org/10.1038/310393a0>.
- Osamu Mishima. Reversible first-order transition between two h2o amorphs at ~0.2 GPa and ~135 k. *The Journal of Chemical Physics*, 100(8):5910, 1994. doi: 10.1063/1.467103. URL <http://dx.doi.org/10.1063/1.467103>.
- Osamu Mishima. Liquid-liquid critical point in heavy water. *Phys. Rev. Lett.*, 85: 334–336, Jul 2000. doi: 10.1103/PhysRevLett.85.334. URL <http://link.aps.org/doi/10.1103/PhysRevLett.85.334>.
- Osamu Mishima. Application of polyamorphism in water to spontaneous crystallization of emulsified licl-h2o solution. *The Journal of chemical physics*, 123(15): 154506, 2005.
- Osamu Mishima. Phase separation in dilute licl-h2o solution related to the polyamorphism of liquid water. *Journal of Chemical Physics*, 126(24):244507, 2007.
- Osamu Mishima. Melting of the precipitated ice IV in LiCl aqueous solution and polyamorphism of water. *The Journal of Physical Chemistry B*, 115(48):14064–14067, dec 2011. doi: 10.1021/jp203669p. URL <http://dx.doi.org/10.1021/jp203669p>.
- Himanshu Mishra, Robert J. Nielsen, Shinichi Enami, Michael R. Hoffmann, Agustín J. Colussi, and William A. Goddard. Quantum chemical insights into the dissociation of nitric acid on the surface of aqueous electrolytes. *Int. J. Quantum Chem.*, 113(4):413–417, may 2012. doi: 10.1002/qua.24151. URL <http://dx.doi.org/10.1002/qua.24151>.

- Paola Modica, Cornelia Meinert, Pierre de Marcellus, Laurent Nahon, Uwe J. Meierhenrich, and Louis Le Sergeant d'Hendecourt. ENANTIOMERIC EXCESSES INDUCED IN AMINO ACIDS BY ULTRAVIOLET CIRCULARLY POLARIZED LIGHT IRRADIATION OF EXTRATERRESTRIAL ICE ANALOGS: A POSSIBLE SOURCE OF ASYMMETRY FOR PREBIOTIC CHEMISTRY. *ApJ*, 788(1):79, may 2014. doi: 10.1088/0004-637x/788/1/79. URL <http://dx.doi.org/10.1088/0004-637X/788/1/79>.
- Emily B. Moore and Valeria Molinero. Structural transformation in supercooled water controls the crystallization rate of ice. *Nature*, 479(7374):506–508, November 2011. ISSN 0028-0836. URL <http://dx.doi.org/10.1038/nature10586>.
- Ken Muldrew and Locksley E. McGann. Ch. 6 phase diagrams, Oct. 1997. URL [http://people.ucalgary.ca/~kmuldrew/cryo\\_course/cryo\\_chap6\\_1.html](http://people.ucalgary.ca/~kmuldrew/cryo_course/cryo_chap6_1.html).
- K Nakamura. Review of particle physics. *Journal of Physics G: Nuclear and Particle Physics*, 37(7A):075021, jul 2010. doi: 10.1088/0954-3899/37/7a/075021. URL <http://dx.doi.org/10.1088/0954-3899/37/7A/075021>.
- GW Neilson and JE Enderby. Neutron and x-ray diffraction studies of concentrated aqueous electrolyte solutions. *Annual Reports Section "C"(Physical Chemistry)*, 76:185–220, 1979.
- W J Nellis. Dynamic compression of materials: metallization of fluid hydrogen at high pressures. *Rep. Prog. Phys.*, 69(5):1479–1580, apr 2006. doi: 10.1088/0034-4885/69/5/r05. URL <http://dx.doi.org/10.1088/0034-4885/69/5/R05>.
- R. J. Nelmes, J. S. Loveday, W. G. Marshall, G. Hamel, J. M. Besson, and S. Klotz. Multisite disordered structure of ice vii to 20 gpa. *Phys. Rev. Lett.*, 81:2719–2722, Sep 1998. doi: 10.1103/PhysRevLett.81.2719. URL <http://link.aps.org/doi/10.1103/PhysRevLett.81.2719>.
- Richard J. Nelmes, John S. Loveday, Thierry Strässle, Craig L. Bull, Malcolm Guthrie, Gerard Hamel, and Stefan Klotz. Annealed high-density amorphous ice under pressure. *Nature Physics*, 2(6):414–418, Jun 2006. ISSN 1745-2473. doi: 10.1038/nphys313. URL <http://dx.doi.org/10.1038/nphys313>.
- Miloslav Nič, Jiří Jirát, Bedřich Košata, Aubrey Jenkins, and Alan McNaught, editors. *IUPAC Compendium of Chemical Terminology*. IUPAC, jun 2009. doi: 10.1351/goldbook. URL <http://dx.doi.org/10.1351/goldbook>.
- V. Nigro, F. Bruni, and M. A. Ricci. Water in confined geometries. *Proceedings of the International School of Physics Enrico Fermi*, 187(Water: Fundamentals

- as the Basis for Understanding the Environment and Promoting Technology): 209–222, 2015. ISSN 0074-784X. doi: 10.3254/978-1-61499-507-4-209. URL <http://doi.org/10.3254/978-1-61499-507-4-209>.
- NIST. Neutron scattering lengths.
- NIST. *Thermophysical Properties of Fluid Systems*. NIST, 2015. URL <http://webbook.nist.gov/chemistry/fluid/>.
- Nobel Foundation. Nobel prize webpage, May 2015. URL [http://www.nobelprize.org/nobel\\_prizes/physics/laureates/](http://www.nobelprize.org/nobel_prizes/physics/laureates/).
- Shuichi Nosé. A unified formulation of the constant temperature molecular dynamics methods. *The Journal of chemical physics*, 81(1):511–519, 1984.
- A. Oed. Position-sensitive detector with microstrip anode for electron multiplication with gases. *Nuclear Instruments and Methods in Physics Research Section A: Accelerators, Spectrometers, Detectors and Associated Equipment*, 263(2–3):351 – 359, 1988. ISSN 0168-9002. doi: [http://dx.doi.org/10.1016/0168-9002\(88\)90970-9](http://dx.doi.org/10.1016/0168-9002(88)90970-9). URL <http://www.sciencedirect.com/science/article/pii/0168900288909709>.
- Bart Olinger. The compression of solid n<sub>2</sub> at 296 k from 5 to 10 GPa. *J. Chem. Phys.*, 80(3):1309, 1984. doi: 10.1063/1.446810. URL <http://dx.doi.org/10.1063/1.446810>.
- P. G. Owston. Diffuse scattering of x-rays by ice. *Acta Crystallogr*, 2(4):222–228, aug 1949. doi: 10.1107/s0365110x4900059x. URL <http://dx.doi.org/10.1107/S0365110X4900059X>.
- Jeremy C. Palmer, Fausto Martelli, Yang Liu, Roberto Car, Athanassios Z. Panagiotopoulos, and Pablo G. Debenedetti. Metastable liquid–liquid transition in a molecular model of water. *Nature*, 510(7505):385–388, jun 2014. doi: 10.1038/nature13405. URL <http://dx.doi.org/10.1038/nature13405>.
- Betül Pamuk, Philip B. Allen, and M.-V. Fernández-Serra. Electronic and nuclear quantum effects on the ice xi/ice ih phase transition. *Phys. Rev. B*, 92:134105, Oct 2015. doi: 10.1103/PhysRevB.92.134105. URL <http://link.aps.org/doi/10.1103/PhysRevB.92.134105>.
- Vivian Barfield Parker. *Thermal properties of aqueous uni-univalent electrolytes*, volume 2. US Government Printing Office Washington, DC, USA, 1965.

- Linus Pauling. The structure and entropy of ice and of other crystals with some randomness of atomic arrangement. *J. Am. Chem. Soc.*, 57(12):2680–2684, dec 1935. doi: 10.1021/ja01315a102. URL <http://dx.doi.org/10.1021/ja01315a102>.
- PEARL. Pearl website. 2015. URL <http://www.isis.stfc.ac.uk/instruments/pearl/pearl2122.html>.
- John P. Perdew, Kieron Burke, and Matthias Ernzerhof. Generalized gradient approximation made simple. *Phys. Rev. Lett.*, 77(18):3865–3868, oct 1996. doi: 10.1103/physrevlett.77.3865. URL <http://dx.doi.org/10.1103/PhysRevLett.77.3865>.
- Victor F Petrenko and Robert W Whitworth. *Physics of ice*. Oxford University Press, 1999.
- B. Prével, J. F. Jal, J. Dupuy Philon, and A. K. Soper. Structural characterization of an electrolytic aqueous solution,  $\text{LiCl} \cdot 6\text{H}_2\text{O}$ , in the glass, supercooled liquid, and liquid states. *The Journal of Chemical Physics*, 103(5):1886–1896, 1995. doi: <http://dx.doi.org/10.1063/1.469713>. URL <http://scitation.aip.org/content/aip/journal/jcp/103/5/10.1063/1.469713>.
- E. Prince, editor. *International Tables for Crystallography*. International Union of Crystallography, oct 2006. doi: 10.1107/97809553602060000103. URL <http://dx.doi.org/10.1107/97809553602060000103>.
- B. G. Pummer, C. Budke, S. Augustin-Bauditz, D. Niedermeier, L. Felgitsch, C. J. Kampf, R. G. Huber, K. R. Liedl, T. Loerting, T. Moschen, M. Schauerperl, M. Tollinger, C. E. Morris, H. Wex, H. Grothe, U. Pöschl, T. Koop, and J. Fröhlich-Nowoisky. Ice nucleation by water-soluble macromolecules. *Atmospheric Chemistry and Physics*, 15(8):4077–4091, 2015. doi: 10.5194/acp-15-4077-2015. URL <http://dx.doi.org/10.5194/acp-15-4077-2015>.
- Roger Pynn. *Neutron Scattering, A Primer*, volume 19. 1990.
- Andrew M. Rappe, Karin M. Rabe, Efthimios Kaxiras, and J. D. Joannopoulos. Optimized pseudopotentials. *Phys. Rev. B*, 41:1227–1230, Jan 1990. doi: 10.1103/PhysRevB.41.1227. URL <http://link.aps.org/doi/10.1103/PhysRevB.41.1227>.
- David R Reichman and Patrick Charbonneau. Mode-coupling theory. *J. Stat. Mech.*, 2005(05):P05013, may 2005. doi: 10.1088/1742-5468/2005/05/p05013. URL <http://dx.doi.org/10.1088/1742-5468/2005/05/P05013>.

- Richard C. Remsing, Jocelyn M. Rodgers, and John D. Weeks. Deconstructing classical water models at interfaces and in bulk. *Journal of Statistical Physics*, 145(2):313–334, aug 2011. doi: 10.1007/s10955-011-0299-3. URL <http://dx.doi.org/10.1007/s10955-011-0299-3>.
- Juan Rodríguez-Carvajal. Recent advances in magnetic structure determination by neutron powder diffraction. *Physica B: Condensed Matter*, 192(1-2):55–69, 1993. ISSN 0921-4526. doi: [http://dx.doi.org/10.1016/0921-4526\(93\)90108-I](http://dx.doi.org/10.1016/0921-4526(93)90108-I). URL <http://www.sciencedirect.com/science/article/pii/092145269390108I>.
- Juan Rodríguez-Carvajal. Recent advances in magnetic structure determination by neutron powder diffraction. *Physica B: Condensed Matter*, 192(1):55–69, 1993.
- Th Roisnel and Juan Rodríguez-Carvajal. Winplotr: a windows tool for powder diffraction pattern analysis. In *Materials Science Forum*, volume 378, pages 118–123. Transtec Publications; 1999, 2001.
- K. Ros and A. Johansen. Ice condensation as a planet formation mechanism. *Astronomy & Astrophysics*, 552:A137, apr 2013. doi: 10.1051/0004-6361/201220536. URL <http://dx.doi.org/10.1051/0004-6361/201220536>.
- Robert C Ruhl. Cooling rates in splat cooling. *Materials Science and Engineering*, 1(6):313–320, 1967.
- G. N. Ruiz, L. E. Bove, H. R. Corti, and T. Loerting. Pressure-induced transformations in LiCl – H<sub>2</sub>O at 77 K. *Phys. Chem. Chem. Phys.*, 16:18553–18562, 2014. doi: 10.1039/C4CP01786B. URL <http://dx.doi.org/10.1039/C4CP01786B>.
- A. Marco Saitta, Thierry Strässle, Gwenaëlle Rouse, Gérard Hamel, Stefan Klotz, Richard J. Nelmes, and John S. Loveday. High density amorphous ices: Disordered water towards close packing. *The Journal of Chemical Physics*, 121(17):8430–8434, 2004. doi: <http://dx.doi.org/10.1063/1.1804493>. URL <http://scitation.aip.org/content/aip/journal/jcp/121/17/10.1063/1.1804493>.
- Mathieu Salanne and Paul A. Madden. Polarization effects in ionic solids and melts. *Molecular Physics*, 109(19):2299–2315, oct 2011. doi: 10.1080/00268976.2011.617523. URL <http://dx.doi.org/10.1080/00268976.2011.617523>.
- C. G. Salzmann. The preparation and structures of hydrogen ordered phases of ice. *Science*, 311(5768):1758–1761, mar 2006. doi: 10.1126/science.1123896. URL <http://dx.doi.org/10.1126/science.1123896>.

- R. Sanger, O. Steiger, and K. Gachter. Temperatureffekt der molekularpolarisation einiger gase und dampfe. 1932. doi: 10.5169/seals-110168. URL <http://dx.doi.org/10.5169/seals-110168>.
- DAVID Schiferl, DT Cromer, ROBERT R Ryan, ALLEN C Larson, RICHARD LeSar, and RL Mills. Structure of n<sub>2</sub> at 2.94 gpa and 300 k. *Acta Crystallographica Section C: Crystal Structure Communications*, 39(9):1151–1153, 1983.
- J. A. Sellberg, C. Huang, T. A. McQueen, N. D. Loh, H. Laksmono, D. Schlesinger, R. G. Sierra, D. Nordlund, C. Y. Hampton, D. Starodub, D. P. DePonte, M. Beye, C. Chen, A. V. Martin, A. Barty, K. T. Wikfeldt, T. M. Weiss, C. Caronna, J. Feldkamp, L. B. Skinner, M. M. Seibert, M. Messerschmidt, G. J. Williams, S. Boutet, L. G. M. Pettersson, M. J. Bogan, and A. Nilsson. Ultrafast x-ray probing of water structure below the homogeneous ice nucleation temperature. *Nature*, 510(7505):381–384, jun 2014. doi: 10.1038/nature13266. URL <http://dx.doi.org/10.1038/nature13266>.
- Yusuke SETO, Daisuke NISHIO-HAMANE, Takaya NAGAI, and Nagayoshi SATA. Development of a software suite on x-ray diffraction experiments. *The Review of High Pressure Science and Technology*, 20(3):269–276, 2010. doi: 10.4131/jshpreview.20.269. URL <http://dx.doi.org/10.4131/jshpreview.20.269>.
- R. D. Shannon. Revised effective ionic radii and systematic studies of interatomic distances in halides and chalcogenides. *Acta Crystallographica Section A*, 32(5):751–767, Sep 1976. doi: 10.1107/S0567739476001551. URL <http://dx.doi.org/10.1107/S0567739476001551>.
- Pier Luigi Silvestrelli and Michele Parrinello. Water molecule dipole in the gas and in the liquid phase. *Phys. Rev. Lett.*, 82:3308–3311, Apr 1999. doi: 10.1103/PhysRevLett.82.3308. URL <http://link.aps.org/doi/10.1103/PhysRevLett.82.3308>.
- Frank Sohl, Mathieu Choukroun, Jeffrey Kargel, Jun Kimura, Robert Pappalardo, Steve Vance, and Mikhail Zolotov. Subsurface water oceans on icy satellites: Chemical composition and exchange processes. *Space Science Reviews*, 153(1-4):485–510, 2010. ISSN 0038-6308. doi: 10.1007/s11214-010-9646-y. URL <http://dx.doi.org/10.1007/s11214-010-9646-y>.
- S. A. Solin and A. K. Ramdas. Raman spectrum of diamond. *Phys. Rev. B*, 1:1687–1698, Feb 1970. doi: 10.1103/PhysRevB.1.1687. URL <http://link.aps.org/doi/10.1103/PhysRevB.1.1687>.

- RJ Speedy and CA Angell. Isothermal compressibility of supercooled water and evidence for a thermodynamic singularity at- 45 c. *The Journal of Chemical Physics*, 65(3):851–858, 1976.
- G.L. Squires. *Introduction to the Theory of Thermal Neutron Scattering*. Cambridge University Press, 2012. ISBN 9781107644069. URL [http://books.google.fr/books?id=KUVD8KJt7\\\_0C](http://books.google.fr/books?id=KUVD8KJt7\_0C).
- H. E. Stanley and F. Mallamace. Experimental tests of the liquid-liquid phase transition hypothesis. *Proceedings of the International School of Physics Enrico Fermi*, 187(Water: Fundamentals as the Basis for Understanding the Environment and Promoting Technology):1–17, 2015. ISSN 0074-784X. doi: 10.3254/978-1-61499-507-4-1. URL <http://doi.org/10.3254/978-1-61499-507-4-1>.
- H. Eugene Stanley and Osamu Mishima. *Nature*, 396(6709):329–335, nov 1998. doi: 10.1038/24540. URL <http://dx.doi.org/10.1038/24540>.
- G. W. Stinton, I. Loa, L. F. Lundegaard, and M. I. McMahon. The crystal structures of  $\delta$  and  $\delta^*$  nitrogen. *J. Chem. Phys.*, 131(10):104511, 2009. doi: 10.1063/1.3204074. URL <http://dx.doi.org/10.1063/1.3204074>.
- AJ Stone. *The Theory of Intermolecular Forces, International Series of Monographs on Chemistry Vol. 32*. Clarendon Press, Oxford, 1996.
- Th. Strässle, S. Klotz, K. Kunc, V. Pomjakushin, and J. S. White. Equation of state of lead from high-pressure neutron diffraction up to 8.9 gpa and its implication for the nacl pressure scale. *Physical Review B*, 90:014101, Jul 2014. doi: 10.1103/PhysRevB.90.014101. URL <http://link.aps.org/doi/10.1103/PhysRevB.90.014101>.
- William E. Streib, Truman H. Jordan, and William N. Lipscomb. Single-crystal x-ray diffraction study of  $\beta$  nitrogen. *J. Chem. Phys.*, 37(12):2962, 1962. doi: 10.1063/1.1733125. URL <http://dx.doi.org/10.1063/1.1733125>.
- Yoshiharu Suzuki and Osamu Mishima. Two distinct raman profiles of glassy dilute licl solution. *Physical review letters*, 85(6):1322, 2000.
- Yoshiharu Suzuki and Osamu Mishima. Differences between pressure-induced densification of LiCl–H<sub>2</sub>O glass and polyamorphic transition of H<sub>2</sub>O. *Journal of Physics: Condensed Matter*, 21(15):155105, 2009a. URL <http://stacks.iop.org/0953-8984/21/i=15/a=155105>.

- Yoshiharu Suzuki and Osamu Mishima. Differences between pressure-induced densification of  $\text{licl-h}_2\text{o}$  glass and polyamorphic transition of  $\text{h}_2\text{o}$ . *Journal of Physics: Condensed Matter*, 21(15):155105, 2009b.
- K. T. Tang and J. Peter Toennies. An improved simple model for the van der waals potential based on universal damping functions for the dispersion coefficients. *J. Chem. Phys.*, 80(8):3726, 1984. doi: 10.1063/1.447150. URL <http://dx.doi.org/10.1063/1.447150>.
- Sami Tazi, John J. Molina, Benjamin Rotenberg, Pierre Turq, Rodolphe Vuilleumier, and Mathieu Salanne. A transferable ab initio based force field for aqueous ions. *The Journal of Chemical Physics*, 136(11):114507, 2012. doi: 10.1063/1.3692965. URL <http://scitation.aip.org/content/aip/journal/jcp/136/11/10.1063/1.3692965>.
- G Tobie, M Choukroun, O Grasset, S Le Mouélic, J.I Lunine, C Sotin, O Bourgeois, D Gautier, M Hirtzig, S Lebonnois, and L Le Corre. Evolution of titan and implications for its hydrocarbon cycle. *Philosophical Transactions of the Royal Society of London A: Mathematical, Physical and Engineering Sciences*, 367(1889): 617–631, 2009. ISSN 1364-503X. doi: 10.1098/rsta.2008.0246.
- Brian H Toby. Expgui, a graphical user interface for gsas. *Journal of Applied Crystallography*, 34(2):210–213, 2001.
- Gareth A. Tribello, Fabien Bruneval, CheeChin Liew, and Michele Parrinello. A molecular dynamics study of the early stages of calcium carbonate growth. *J. Phys. Chem. B*, 113(34):11680–11687, aug 2009. doi: 10.1021/jp902606x. URL <http://dx.doi.org/10.1021/jp902606x>.
- H Trinks, W Schröder, and CK Bierbricher. Sea ice as a promoter of the emergence of first life. *Origins Life Evol. Biospheres*, 35:429–445, 2005.
- J. S. Tse, D. D. Klug, C. A. Tulk, I. Swainson, E. C. Svensson, C.-K. Loong, V. Shpakov, V. R. Belosludov, R. V. Belosludov, and Y. Kawazoe. *Nature*, 400(6745):647–649, aug 1999. doi: 10.1038/23216. URL <http://dx.doi.org/10.1038/23216>.
- P. Valenti, R.J. Bodnar, and C. Schmidt. Experimental determination of  $\text{h}_2\text{o-nacl}$  liquid to 25% NaCl and 1.4GPa: Application to the Jovian satellite Europa. *Geochimica et Cosmochimica Acta*, 92(0):117 – 128, 2012. ISSN 0016-7037. doi: <http://dx.doi.org/10.1016/j.gca.2012.06.007>. URL <http://www.sciencedirect.com/science/article/pii/S0016703712003596>.

- Steve Vance, Mathieu Bouffard, Mathieu Choukroun, and Christophe Sotin. Ganymede's internal structure including thermodynamics of magnesium sulfate oceans in contact with ice. *Planetary and Space Science*, 96:62–70, jun 2014. doi: 10.1016/j.pss.2014.03.011. URL <http://dx.doi.org/10.1016/j.pss.2014.03.011>.
- Joost VandeVondele and Jürg Hutter. Gaussian basis sets for accurate calculations on molecular systems in gas and condensed phases. *J. Chem. Phys.*, 127(11):114105, 2007. doi: 10.1063/1.2770708. URL <http://dx.doi.org/10.1063/1.2770708>.
- Joost VandeVondele, Matthias Krack, Fawzi Mohamed, Michele Parrinello, Thomas Chassaing, and Jürg Hutter. Quickstep: Fast and accurate density functional calculations using a mixed gaussian and plane waves approach. *Computer Physics Communications*, 167(2):103–128, apr 2005. doi: 10.1016/j.cpc.2004.12.014. URL <http://dx.doi.org/10.1016/j.cpc.2004.12.014>.
- Loup Verlet. Computer "experiments" on classical fluids. i. thermodynamical properties of lennard-jones molecules. *Phys. Rev.*, 159:98–103, Jul 1967. doi: 10.1103/PhysRev.159.98. URL <http://link.aps.org/doi/10.1103/PhysRev.159.98>.
- Luboš Vrbka and Pavel Jungwirth. Homogeneous freezing of water starts in the subsurface. *The Journal of Physical Chemistry B*, 110(37):18126–18129, sep 2006. doi: 10.1021/jp064021c. URL <http://dx.doi.org/10.1021/jp064021c>.
- Koji Wada, Hidekazu Tanaka, Toru Suyama, Hiroshi Kimura, and Tetsuo Yamamoto. Numerical simulation of dust aggregate collisions. II. compression and disruption of three-dimensional aggregates in head-on collisions. *ApJ*, 677(2):1296–1308, apr 2008. doi: 10.1086/529511. URL <http://dx.doi.org/10.1086/529511>.
- W. Wagner. The IAPWS formulation 1995 for the thermodynamic properties of ordinary water substance for general and scientific use. *Journal of Physical and Chemical Reference Data*, 31(2):387, 1999. doi: 10.1063/1.1461829. URL <http://dx.doi.org/10.1063/1.1461829>.
- Matthew Warkentin, James P. Sethna, and Robert E. Thorne. Critical droplet theory explains the glass formability of aqueous solutions. *Phys. Rev. Lett.*, 110(1), jan 2013. doi: 10.1103/physrevlett.110.015703. URL <http://dx.doi.org/10.1103/PhysRevLett.110.015703>.
- B.E. Warren. *X-Ray Diffraction*. Dover Books on Physics. Dover Publications,

2012. ISBN 9780486141619. URL [https://books.google.fr/books?id=cA\\\_EAgAAQBAJ](https://books.google.fr/books?id=cA\_EAgAAQBAJ).
- Gunnar Weck. *Etude des propriétés de l'oxygène sous haute pression et haute température*. PhD thesis, 2001. URL <http://www.theses.fr/2001PA066251>. Thèse de doctorat dirigée par Loubeyre, Paul Sciences des matériaux Paris 6 2001.
- Björn Wehinger, Dmitry Chernyshov, Michael Krisch, Sergey Bulat, Victor Ezhov, and Alexei Bosak. Diffuse scattering in ice. *Journal of Physics: Condensed Matter*, 26(26):265401, jun 2014. doi: 10.1088/0953-8984/26/26/265401. URL <http://dx.doi.org/10.1088/0953-8984/26/26/265401>.
- C. E. Weir, E. R. Lippincott, A. Van Valkenburg, and E. N. Bunting. Infrared studies in the 1-to 15-micron region to 30,000 atmospheres. *J. Res. Natl. Bur. Stand. A*, 63:55–62, 1959.
- J. S. Wettlaufer. ACCRETION IN PROTOPLANETARY DISKS BY COLLISIONAL FUSION. *ApJ*, 719(1):540–549, jul 2010. doi: 10.1088/0004-637x/719/1/540. URL <http://dx.doi.org/10.1088/0004-637x/719/1/540>.
- Edward Whalley, D. D. Klug, and Y. P. Handa. Entropy of amorphous ice. *Nature*, 342(6251):782–783, December 1989. URL <http://dx.doi.org/10.1038/342782a0>.
- contributors Wikipedia. *Water data page*. Wikimedia Foundation, 2015. URL [https://en.wikipedia.org/wiki/Water\\_\(data\\_page\)](https://en.wikipedia.org/wiki/Water_(data_page)).
- Georg Will. *Powder diffraction: The Rietveld method and the two stage method to determine and refine crystal structures from powder diffraction data*. Springer Science & Business Media, 2006.
- Thomas Williams, Colin Kelley, and many others. Gnuplot 4.6: an interactive plotting program. <http://gnuplot.sourceforge.net/>, February 2014.
- Christopher E. Wilmer, Michael Leaf, Chang Yeon Lee, Omar K. Farha, Brad G. Hauser, Joseph T. Hupp, and Randall Q. Snurr. Large-scale screening of hypothetical metal–organic frameworks. *Nature Chem*, 4(2):83–89, nov 2011. doi: 10.1038/nchem.1192. URL <http://dx.doi.org/10.1038/nchem.1192>.
- Herman Winick. *Synchrotron radiation sources : a primer*. World Scientific series on synchrotron radiation techniques and applications, vol. 1. World Scientific, 1994. ISBN 9810218567. URL <http://www.worldcat.org/isbn/9810218567>.

- K. Winkel, M. Seidl, T. Loerting, L. E. Bove, S. Imberti, V. Molinero, F. Bruni, R. Mancinelli, and M. A. Ricci. Structural study of low concentration licl aqueous solutions in the liquid, supercooled, and hyperquenched glassy states. *The Journal of Chemical Physics*, 134(2):024515, 2011a. doi: <http://dx.doi.org/10.1063/1.3528000>. URL <http://scitation.aip.org/content/aip/journal/jcp/134/2/10.1063/1.3528000>.
- Katrin Winkel, Marion Bauer, Erwin Mayer, Markus Seidl, Michael S Elsaesser, and Thomas Loerting. Structural transitions in amorphous h<sub>2</sub>o and d<sub>2</sub>o: the effect of temperature. *Journal of Physics: Condensed Matter*, 20(49):494212, nov 2008. doi: 10.1088/0953-8984/20/49/494212. URL <http://dx.doi.org/10.1088/0953-8984/20/49/494212>.
- Katrin Winkel, Erwin Mayer, and Thomas Loerting. Equilibrated high-density amorphous ice and its first-order transition to the low-density form. *J. Phys. Chem. B*, 115(48):14141–14148, dec 2011b. doi: 10.1021/jp203985w. URL <http://dx.doi.org/10.1021/jp203985w>.
- Marcin Wojdyr. Fityk : a general-purpose peak fitting program. *Journal of Applied Crystallography*, 43(5):1126–1128, sep 2010. doi: 10.1107/s0021889810030499. URL <http://dx.doi.org/10.1107/S0021889810030499>.
- Y Yoshimura and H Kanno. Pressure-induced amorphization of ice in aqueous licl solution. *Journal of Physics: Condensed Matter*, 14(44):10671, 2002.
- Yukihiro Yoshimura, Ho-kwang Mao, and Russell J Hemley. Transformation of ice in aqueous kcl solution to a high-pressure, low-temperature phase. *Chemical physics letters*, 400(4):511–514, 2004.



## **Étude du diagramme de phases des solutions d'électrolytes sous conditions extrêmes**

### Résumé :

L'étude des phases amorphes et cristallines de solutions permet est d'un fort intérêt pour la biologie et la planétologie.

Le but de cette thèse est l'exploration du diagramme de phase des solutions d'électrolytes (LiCl et NaCl dans l'eau) sous des conditions de pression et température typiques des corps glacés tels Europe et Ganymède (de 77 à 300 K et jusqu'à 5 GPa). Nous avons étudié des phases de glaces amorphes et cristallines pouvant incorporer des quantités considérables de sel (jusqu'à 10 % de masse de sel). En outre de la mise en évidence de phases de glace salées, nous avons caractérisé deux propriétés exotiques induites sous pression, à savoir le polyamorphisme et l'inclusion des ions dans le réseau de la glace.

Nous avons produit des échantillons de phase amorphe de solutions de NaCl dans l'eau par trempe rapide à 77 Kelvin. Nos expériences de diffraction de neutron et de rayons X montrent que la structure locale de cette phase amorphe est très similaire de celle de la phase haute densité de l'eau pure.

Nos expériences haute pression avec la presse Paris-Edinburgh et nos calculs de dynamique moléculaire montrent que la densité et la structure évoluent de manière continue en compression jusqu'à 4 GPa. La possibilité d'inclusion du sel (NaCl) dans le réseau de la glace VII sous pression dans nos expériences est analysée en comparaison avec des simulations utilisant la théorie de la densité fonctionnelle. La glace VII qui cristallise dans nos expériences est soit pure, soit elle contient une fraction faible des ions de la solution mère. Il est possible que des quantités de sel plus grandes puissent être incorporées à des pressions plus élevées.

Mots clefs : [ glace – sel – diffraction – haute pression – structure cristalline – amorphes ]

## **Exploring the phase diagram of electrolyte solutions under extreme conditions**

### Abstract :

The study of amorphous and crystalline phases of solutions gives essential insight on the behaviour of water under conditions relevant for biology and planetary science.

The aim of this work is the exploration of the phase diagram of common electrolyte solutions (LiCl-water, NaCl-water) under pressure and temperature conditions (from 77 K to 330 K and up to 5 GPa) relevant for icy bodies such as Europe and Ganymede. In experiments and simulations we search for crystalline phases of ice at high-pressure, which can contain considerable amounts of salt in their lattice (up to 10 % of by weight). We probe the existence of these salty ices, and characterize two exotic, pressure induced properties, polyamorphism and ionic inclusions in the ice lattice.

We have produced highly concentrated amorphous solutions of NaCl in water by fast quenching to liquid nitrogen temperature. Our neutron and X-ray diffraction experiments show that the local structure of this amorphous solution at ambient pressure is very similar to the high density amorphous structure of pure water. Our high-pressure experiments with the Paris-Edinburgh cell and our classical Molecular Dynamics calculations show only smooth structure and density changes during compression up to 4 GPa. We discuss the possibility of salt (NaCl) inclusions in the ice VII lattice at high pressure in our experiments by complementary calculations based on Density Functional Theory. The ice VII which crystallized in our experiments is either pure ice, or it contains only a small fraction of the ions from the solution. It may be possible that ions can be included in larger quantities at higher pressures.

Keywords : [ ice – salt diffraction – high-pressure – crystal structure – amorphous ]